Distribution Agreement

Astrochemistry in Star-forming Regions: Laboratory Millimeter–Submillimeter Spectroscopy and Broadband Astronomical Line Surveys

By

Luyao Zou
Doctor of Philosophy

Chemistry

Susanna L. Widicus Weaver, Ph.D
Advisor

Michael C. Heaven, Ph.D
Committee Member

Joel M. Bowman, Ph.D
Committee Member

Accepted:

Lisa A. Tedesco, Ph.D
Dean of the James T. Laney School of Graduate Studies

Date

Astrochemistry in Star-forming Regions: Laboratory Millimeter–Submillimeter Spectroscopy and Broadband Astronomical Line Surveys

By

Luyao Zou
Bachelor of Science, Fudan University, 2012

Advisor: Susanna L. Widicus Weaver, Ph.D

An abstract of
A dissertation submitted to the Faculty of the
James T. Laney School of Graduate Studies of Emory University
in partial fulfillment of the requirements for the degree of
Doctor of Philosophy
in Chemistry
2017

Abstract

Astrochemistry in Star-forming Regions: Laboratory Millimeter–Submillimeter Spectroscopy and Broadband Astronomical Line Surveys

By Luyao Zou

The interstellar medium in star-forming regions is highly molecular, evidenced by the detection of nearly 200 molecules via radio astronomy. Despite the confirmed chemical complexity in star-forming regions, mechanisms that drive the formation of this chemical complexity are far from well understood. The widely accepted overall picture is that ion-molecular reactions dominate the gas phase, while gas-grain chemistry dominate in the icy mantle on the dust surface. Still, when narrating reaction pathways leading to specific interstellar molecules, astronomical observations, laboratory experiments, and modeling often draw convoluted, even contradictory results and interpretations. Models suggest that ions and radicals, the unstable molecules under terrestrial conditions, play key roles in the gas-phase chemistry and ice chemistry, respectively. In order to elucidate these astrochemistry processes, it is insightful to combine perspectives from laboratory rotational spectroscopy and broadband astronomical line surveys. In this dissertation, I first describe a millimeter–submillimeter spectrometer and the development of a fast-sweep technique that facilitates the study of unstable molecules, and then demonstrate the application of these techniques to rotational spectroscopy and astronomy. The performance of the fast-sweep technique was fully evaluated, and its application was demonstrated by the spectral acquisition and analysis of *trans*-HO_3 radical and Ar–H_2O dimer. Meanwhile, quantitative abundance and temperature of interstellar molecules were determined from a global analysis of broadband astronomical line surveys of a large sample of star-forming regions. This analysis constructs the correlations between molecules in a variety of interstellar environment and evolutionary stage. It is also a first step to search for new interstellar molecules, preferably the reaction intermediates whose spectra can be measured using the laboratory millimeter–submillimeter spectroscopy described in this dissertation. The preliminary results of global analysis, as well as the search for *trans*-HO_3, were presented.

Astrochemistry in Star-forming Regions: Laboratory Millimeter–Submillimeter Spectroscopy and Broadband Astronomical Line Surveys

By

Luyao Zou
Bachelor of Science, Fudan University, 2012

Advisor: Susanna L. Widicus Weaver, Ph.D

A dissertation submitted to the Faculty of the
James T. Laney School of Graduate Studies of Emory University
in partial fulfillment of the requirements for the degree of
Doctor of Philosophy
in Chemistry
2017

Acknowledgement

Looking back to the long journey of graduate school, I cannot exaggerate enough how much I have grown as a researcher, a professional, and a mature adult. The progress I have achieved cannot happen without all the guidance and help I received from the people and the community who cared and supported me and whom I would like to sincerely acknowledge.

First and foremost, I would like to thank my advisor, Dr. Susanna L. Widicus Weaver, for your impassioned mentorship. You are not only an academic advisor, but also a life mentor, who taught me the attitude, ethics, methodology, and professionalism to be a researcher and an independent thinker. As an academic advisor, you lead me into the family of spectroscopists and astrochemists. You offered me the freedom to try and learn, but would also call me out when I lost my direction. With the countless advice, discussions, and comments on research strategies, scientific writing, and presentation and communication skills, you ensured that I was able to fulfill my research objectives. As a life mentor, you are always available, supportive, and empathetic. I greatly appreciate your help in introducing me to the job market, and your discussions with me about my career choice.

I would like to thank my committee members, Dr. Michael Heaven and Dr. Joel Bowman, for your constructive criticism on my research project, for your advice on my career development, and for your care on my success in general. Outside Emory, I thank Dr. Steve Shipman as a great mentor and friend. We had fun chats at conferences and during your visit at Emory. I also thank Dr. Mike McCarthy for your helpful discussion on discharge chemistry, and for offering the opportunity to visit your laboratory, which turned into some great results.

I would like to thank my peers and colleagues in the Widicus Weaver Group. You are great and lovely people, and I enjoyed working with you. Despite the succeeding generations over years, the Widicus Weaver Group maintained a positive, supportive group environment which cannot be made possible without the effort of each of you. I overlapped with Jake Laas and Brian Hays when I joined the group. You were both so patient to teach me the essential laboratory skills, and to tolerate all the mistakes I have made. Jake led me into Linux and coding, and these are the skills I would appreciate for my entire career. Brian, I enjoyed the time working closely with you developing our fast-sweep experimental techniques. I greatly appreciate your enthusiasm on those experiments, in addition to all the fun conversations we had. Nadine Wehres was the lab keeper, who kept everything organized and in track. I enjoyed working with you on the hollow cathode experiment, and thank you for your contribution to the analysis of all the CSO and HIFI line surveys. Then there were AJ Mesko and Morgan McCabe, who always brought joy and cheer to me. We worked so closely together in teaching and in the laboratory. I will miss all the conversations, full with joyfulness and deep thoughts, with you two. AJ, it was so much fun with you at the interferometer workshop in Socorro, NM. For our fresh blood Kevin Roenitz and Carson Powers, I greatly appreciate your enthusiasm and your hard work both in research and in keeping the group dynamics in a healthy track. The extensive responsibility on you may be overwhelming, but I believe in your perseverance and ability to succeed in graduate school. I also thank all the undergraduate students and high school trainees who I have met and worked with: Mary Rad, Jim Sanders III, Trevor Cross, Althea Roy, Anthony Chirillo, Mateo Correa, Houston Smith, Samuel Zinga, Elena Jordanov, Lindsay Rhoades, and Lina Zhang. It was my honor to know you in person.

I would like to thank the staff in the Department of Chemistry, who are devoted to build a strong and supportive program. My special thank goes to Steve Krebs and Clair Scott, who made all their effort to ensure our purchases got processed and our parcels got delivered. I could not remember how many times Steve saved us on the liquid helium Dewar that is the fuel of our bolometer detector. I would also thank Ann Dasher, who made sure I met all the annual requirements and stayed in good standing with my graduate program.

I would like to thank the resources and opportunities provided by the Department of Chemistry, the Laney Graduate School, and Emory. I specially thank Peggy Wagner and Heather Boldt, who were my English teachers in the English Language Support program. Without Peggy and Heather, I could not make such a noticeable progress in my language skills during my first year at Emory. These writing and oral communications skills, again, are not only beneficial to my study at Emory, but also to my entire career. I thank the Professional Development Support Funding from the Laney Graduate School, which allowed me to take unique training and research opportunities to Arecibo, VLA, and Havard University. I also thank the staff in the International Student and Scholar Service at Emory, who understood the special concerns of international students and offered their kind help whenever I needed.

Last but not least, I would like to express my love and gratitude to my family and my friends, for all your understanding and moral support, without which I could not survive in graduate school. I owe a big thank to Mom, who has always been positive and supportive after going through many tough years. Although I had chances to travel and visit, five years of me being overseas was a long time to endure. Dear Wenjun Liu, Sophia Xu, Chuan Yu, Lucy Wang, Zhiyu Qian, Yuanjun Dai, Lin Zhou, and especially Luyuan Xu, I treasure your friendship, for encouraging me when I felt hesitant, for pacifying me when I felt depressed, and for accompanying me when I felt lonely. I would also like to thank Zhihu.com, the online community that encouraged me to start my science communication writings.

Table of Contents

List of Figures

List of Tables

Chapter 1 Introduction

The interstellar medium (ISM) is the matter between stars and planets, and the physical environment in which the matter resides. It is highly heterogeneous and highly molecular, which is evidenced by the discovery of almost 200 molecules[1]. When new stars and planetary systems form, they recycle the materials ejected into the ISM by dead stars, and facilitate the chemical synthesis of new materials. It is believed that the astrochemical processes that occur during star formation shape the initial chemical inventory of protoplanetary disks, which may be preserved and delivered onto planets [1–3]. Nevertheless, understanding the interstellar chemistry in star formation is extremely difficult, and numerous questions have been raised. How does the physical environment of the ISM drive the chemistry, and in turn how do molecules trace the ISM environment? Will our understanding of these astrochemical processes lead us to the explanation of the origin of planetary materials, including those of our own solar system? In order to answer these questions, it is essential to bridge the perspectives of laboratory chemistry and astronomical observations. In this dissertation, I will present the development of laboratory rotational spectroscopy, and show how it facilitates the astrochemical analysis of star-forming regions.

1.1 Rotational spectroscopy

The rotational motion of molecules opens a spectroscopic window for studying molecular structure and chemical bonding. The quantized energy levels of this rotational motion are fully determined by the moments of inertia of the molecules. Each molecule, owing to its unique molecular geometry and structure, possesses 1–3 unique moment(s) of inertia that lead to unambiguous construction of the ladder of

[1] `http://www.astro.uni-koeln.de/cdms/molecules`

rotational levels. Dipole-allowed transitions connecting two adjacent rotational levels can be probed spectroscopically, provided that the molecule has a permanent electric or magnetic dipole moment. By assigning the rotational spectrum, namely recognizing the patterns of the rotational energy levels, one can reconstruct the energy ladder from which the moments of inertia of the molecule can be determined. The structure of the molecule, characterized by its bond lengths, bond angles and dihedral angles, can then be determined by solving an equation set using the moments of inertia values obtained from multiple isotopologues of the same molecule, if we assume the isotope substitution only changes the atomic masses but not the molecular structure.

The spacing between rotational energy levels is on the order of 10^{-23}–10^{-21} J. These energies correspond to photons ranging 10–10^3 GHz in frequency and 0.3–30 mm in wavelength, falling into the centimeter, millimeter, and submillimeter regime of light. Because the spacing between levels is in principle inversely proportional to the moment of inertia of the molecule, and proportional to the quantum number of the total rotational angular momentum, transitions from large molecules and low quantum numbers have longer wavelengths, and those from smaller molecules and high quantum numbers have shorter wavelengths. By accessing the full centimeter and millimeter–submillimeter regime, the "softness" of chemical bonds can be estimated from the systematic frequency deviation from an ideal rigid rotor, observed in a large sample of spectral lines connecting a wide range of rotational energy levels. The vibrational-rotational interaction and the internal motion of one part of a molecule with respect to the rest can also be observed as frequency shifts and line splittings in the rotational spectrum. Another advantage of rotational spectroscopy is that the Doppler width of spectral lines is on the order of 0.01–1 MHz. Therefore, under the Doppler broadening limit, fine and ultrafine structures can be resolved. These structures, caused by the coupling between the molecule's rotational angular momenta, electronic spins, and nuclear spins, send messages to us about the local chemical environment of the molecule. They are also characteristic features that can assist the assignment of spectral lines.

Our understanding of molecular properties is certainly incomplete without theoretical interpretations. Unstable molecules and molecular complexes are often ideal test grounds for modern computational chemistry. The laboratory measurements of these molecules and molecular complexes using millimeter–submillimeter spectroscopy provide theoreticians the empirical perspective and reliable benchmarks, upon which insightful theoretical models can be constructed.

1.2 The environment and chemistry in star-forming regions

The heterogeneous environment in the ISM is shaped by the competition and balance between heating and cooling processes. There are mainly three types of heat sources in the ISM. The stellar radiation predominantly heats up the interstellar material by photoprocesses. Its heating rate is strongly dependent on the radiation field, which can be attenuated by shielding, scattering, and photo-ionization of the interstellar material. The cosmic rays, which are mainly atomic nuclei and electrons with MeV energy, dissipate their energy into the surrounding material when they collide with or penetrate through the material. The cosmic ray flux distribution is roughly consistent throughout the ISM, although small variations, characterized by the cosmic ray ionization rate ζ_{H}, have been reported [4]. The interstellar material can also gain energy from gravitational contraction and acceleration. On the other hand, there are mainly two types of cooling mechanism in the ISM. First of all, radiative cooling is ubiquitous as long as the molecules are able to emit photons via spontaneous emission. The spontaneous emission rate is proportional to the Einstein A coefficient, and thus is molecule- and transition-dependent. Collisional deexcitation also transfers energies between molecules. If the density of molecules is significant for collisions to occur efficiently, local thermodynamic equilibrium (LTE) is reached. Since the heating and cooling processes compete with each other, the temperature of the ISM varies significantly in different regions.

The coldest regions in the ISM are dense molecular clouds, where significant amount of interstellar dust and molecular hydrogen, along with other small molecules, gather. The density of gas-phase molecules in dense clouds is about 10^3–10^6 cm^{-3} [5]. The photon flux in the core of dense clouds is minimal, because the dust efficiently absorbs and scatters the interstellar radiation field. Only a limited amount of secondary UV photons from atomic hydrogen excited by cosmic rays is available. On the other hand, considerable amount of diatomic and triatomic molecules and ions, such as CO, N_2H^+, HCN, and HNC, are ubiquitously found cohabitating with molecular hydrogen [6]. The radiative cooling by these molecules is much more efficient than the heating from cosmic rays and secondary UV photons, leading to a gas temperature below 10 K in dense cores.

When the mass of the dense cloud exceeds the Jeans limit, the gas starts to collapse due to its own gravity. The collapse converts the gravitational energy into heat. When this compressional heating rate beats the radiative cooling rate, the cloud core starts to warm up, and its center becomes a protostar. If the total mass of the cloud is above the hydrogen fusion limit, which is 0.08 $M_\odot$, the protostar eventually ignites and there forms a new star. During this protostellar phase, the dense core is no longer cold. Instead, it becomes a hot core, or hot corino if the mass of the protostar is comparable to the sun [7]. Hot cores and hot corinos usually have a density of $> 10^7$ cm^{-3} and a temperature of 100–300 K [7, 8]. Hot cores and hot corinos have by far the richest chemistry observed in the ISM; dozens of complex organic molecules (COMs), defined as molecules with 6 or more atoms, are discovered in hot cores and hot corinos [9]. The origin of such a rich chemistry in hot cores and hot corinos is not completely understood, because astrochemistry models cannot perfectly explain the abundances of COMs observed in these regions [10]. There is a consensus that pure gas-phase chemistry, although important [11], is not sufficient to explain all the observations. Instead, COMs may be formed on the ice mantles on dusts via photo processes, and then sublimate into the gas phase as the core warms up [12, 13]. Models suggest that radicals are important in the photochemistry in ice mantles, and may be responsible for the observed abundance of COMs, e.g., methyl formate [14–16]. Although extremely challenging, the direct observation in the gas phase of these key reaction intermediates, e.g. the methoxy radical [17, 18], will provide us with invaluable information about the astrochemistry processes occurred in hot cores and hot corinos.

1.3 Millimeter–submillimeter spectroscopy and its application to astrochemistry in star-forming regions

Millimeter–submillimeter spectroscopy serves as the main approach to probe gas-phase molecules in the ISM. The rotational lines of molecules are analytical fingerprints to decipher the molecular inventory of the ISM. Because astronomical sources are typically moving relative to Earth, frequencies of spectral lines are shifted by the Doppler effect. Accurate laboratory measurements of the rest frequencies of rotational lines are thus essential for the remote identification of molecular carriers in the forest of rotational lines: only those lines consistently agreeing with the laboratory dataset with the same Doppler shift arise from the same molecule. Such laboratory measurements are usually straightforward for stable molecules accessible from major chemical suppliers. From the chemistry perspective, however, stable molecules do not explain the complete picture of chemical processes in the ISM. As mentioned in Section 1.2, It is often the unstable molecules, as reaction intermediates, that drive the chemistry, especially the chemistry in star-forming regions where significant amount of photochemistry occurs [11, 15]. Laboratory spectroscopy of unstable molecules therefore plays a key role in understanding the interstellar chemistry.

The analysis of astronomical broadband line surveys is challenging due the complexity and volume of the datasets. The complexity mainly arises from the high density of rotational lines that increase exponentially with molecular complexity and temperature. This spectral complexity causes blended lines and ultimately results in a line confusion limit, beyond which individual spectral lines cannot be discerned. In the laboratory, one can prepare molecular samples in high purity to minimize the interference from impurities. Yet, 10^3–10^4 lines are routinely observed for in the range between 0.1–1 THz [19–22]. This is on average one line for every 0.1–1 GHz for a single COM. The spectral signatures for each COM present in an interstellar source are the superimposed in one complicated spectrum. In addition to the number of COMs, these gas-phase molecules in hot cores and hot corinos may have kinematic velocities on the order of 5 km$\cdot$s^{-1}, which corresponds to a full-width-half-maximum (FWHM) of 5 MHz at 300 GHz, and 17 MHz at 1 THz. In this case, it is highly likely that rotational lines from different molecules are blended, namely overlap with each other, in the same frequency window. Being blended, these overlapping lines increase the difficulty in spectral analysis. Eventually, when the signal-to-noise ratio is sufficiently high, every spectral channel becomes molecular flux, which is the line confusion limit.

1.4 Organization of this dissertation

This dissertation addresses both the laboratory millimeter–submillimeter spectroscopy and its applications in broadband astronomical line surveys. In the first part of this dissertation, I present the result of the laboratory millimeter–submillimeter spectroscopy of weakly bound radicals and molecular complexes using new millimeter–submillimeter spectroscopy techniques. In the second part, I present the identified COMs and their physical parameters in star-forming regions using the results from laboratory millimeter–submillimeter spectroscopy.

This dissertation is organized as following:

- Chapter 2 discusses the laboratory spectroscopy techniques used for these studies.
- Chapter 3 and 4 presents the millimeter–submillimeter spectroscopic study of the HO_3 radical and the Ar–H_2O van der Waals complex, respectively.
- Chapter 5 presents the numerical program "GOBASIC", which was developed for the spectral analysis of astronomical line surveys taking the advantage of laboratory spectroscopy results.
- Chapter 6 presents the spectroscopic analysis of 31 star-forming regions using GOBASIC. The chemical composition and physical conditions in these star-forming regions were determined by the LTE analysis of detected rotational lines. Correlations between COMs and the implications for astrochemistry processes in these star-forming regions are discussed.

Part of the content in this dissertation is reproduced with permission from the following sources:

- L. Zou, B. M. Hays, S. L. Widicus Weaver, *J. Phys. Chem. A.*, 120, 657 (2016). 2016 American Chemical Society.©
- L. Zou and S. L. Widicus Weaver, *J. Mol. Spectrosc.*, 324, 12 (2016). 2016 Elsevier Inc.©

Chapter 2 Experimental Design

The main experimental technique I used in this dissertaion is a supersonic expansion discharge source combined with a 7-pass millimeter–submillimeter spectrometer. This source prepares transient molecules to be discussed in this dissertation by high-voltage discharge. The rotational temperature of these molecules is jet-cooled in the expansion for millimeter–submillimeter spectroscopic detection. For clarity, the manufacturers and models of all instruments and parts used in my experiments are summarized in Table 2.1. The following sections will discuss the details of the experimental design.

2.1 The jet-cooled molecular source

2.1.1 Supersonic expansion

In gas-phase spectroscopy, the use of a supersonic expansion is a mature technique to prepare rotationally cooled molecules, especially transient molecules that are unstable or reactive. In a supersonic expansion, seeding molecules, diluted in buffer gas under high pressure, expand adiabatically into the vacuum through a small orifice. Upon the exit of the orifice, collisions between the seeding molecules and the buffer gas transfer the internal energy of these molecules into their translational velocity along the expansion axis. The rotational and vibrational temperatures of the molecules are thus reduced, resulting in less congested spectral lines. Reaction and dissociation channels are also quenched so that transient molecules can be stabilized and be probed with spectroscopic techniques.

In our experiments, gas mixtures were injected into the vacuum via a solenoid valve (Parker Hannifin, Series 9 general valve) running at a repetition rate of 10–50 Hz. The faceplate of the solenoid valve was adapted for better gas sealing: we expanded

Table 2.1: Models and manufactures of the instruments described in Chapter 2 and in Schematic 2.2.

Instrument	Manufacturer	Model & Part Number	Main Specifications
Millimeter–submillimeter system			
RF synthesizer	Agilent Technology	E8257D PSG (1EA, UNU, 550, & UNT)	0–50 GHz, max 5 dbm
Multiplier chain	Virginia Diodes, Inc.	S197(b) and S197(c)	70–1000 GHz, 30 mW (W band)
Teflon lenses	Thorlabs	LAT100, LAT300, LAT500	Ø=50 mm, f=100 mm, 300 mm, and 500 mm
Spherical mirrors	Edmund Optics	NT32-836	Ø=6″, f=6″ (15.2 cm)
Flip mirror mount	Thorlabs	TRF90	Ø=1″ (2.5 cm)
HeNe laser	Thorlabs	HRP020-1	633 nm, 2.0 mW
Vacuum and gas system			
Solenoid valve	Parker Hannifin	9S1-A1-P1-9B06	flange orifice Ø=0.038″ (1 mm) without cone
Pulsed valve driver	Parker Hannifin	Iota One	
Rotary vane pump	Œrlikon	Sogevac SV630 B(F)	755 $m^3 \cdot h^{-1}$
Gas flow controller	MKS	1179A	100–5000 sccm
Gas flow readout	MKS	Type 247	4 channel
Discharge system			
High voltage power supply	Spellman	SL2PN2000/208/3P	max 2 kV, 2 kW
High voltage pulser	Directed Energy Inc.	PVX-4150	max 1.5 kV, 150 W
Delay generator	Stanford Research Systems	DG645	4 channel
Ballast resistor	DALE	HL-100-06Z	1–10 kΩ, max 100 W
Detector and DAQ system			
Zero-biased detector	Virginia Diodes, Inc.	WR8.0 and WR10	2 kV/W
InSb hot-electron bolometer	QMC Ltd.	QFI/XBI	5 kV/W, 500 kHz bandwidth
Lock-in amplifier	Stanford Research Systems	SR830	
Digitizer card	National Instruments	PCI-5124	12 bit, 200 MS/s

the diameter of the central pinhole (1 mm) on the faceplate, so that a Nylon tube (3 mm outer diameter and 0.91 mm inner diameter) can be inserted in. We found this Nylon tube maintained the gas seal longer than the original manufacturer's design. The stagnation pressure behind the pulsed valve varied between 15 psig (2.0 bar) and 120 psig (9.3 bar), depending on the chemistry needed in the expansion for each experiment. To control the mixing ratios of gases, we used a set of mass flow controllers (MKS 1179A, 100 sccm for seeding gases and 5000 sccm for the buffer gas) and a four channel flow rate readout (MKS Type 247).

The vacuum chamber was pumped by a rotary-vane roots blower combination system (Œrlikon SV630 B(F)). The baseline pressure of the vacuum chamber was below 10 mTorr, and would equilibrate in the range of 30–60 mTorr when the valve was operating.

2.1.2 High voltage pulsed discharge source

In order to prepare transient molecules in the supersonic expansion, a high voltage discharge source was developed based on the design of McCarthy *et al.* [23, 24]. Schematic 2.1 draws the inner structure of our discharge source. The body of the discharge source is a Teflon cap with a length of 1.1″ (2.8 cm) and an inner diameter of 0.5″ (1.27 cm). The cap holds two copper electrodes insulated by Teflon spacers. The electrode closer to the pulsed valve (inner electrode) was always grounded, and the one closer to the source exit (outer electrode) was always applied with positive high voltage. The spacing between the two electrodes, their locations in the Teflon cap, and the size of the gas channel in the center of the spacers, are adjustable via creative combinations of customized parts. The length and the diameter of the pinhole gas channel controls the plasma chemistry by affecting the collision rate of molecules. The optimal configurations of the discharge source are described for each experiment in subsequent chapters.

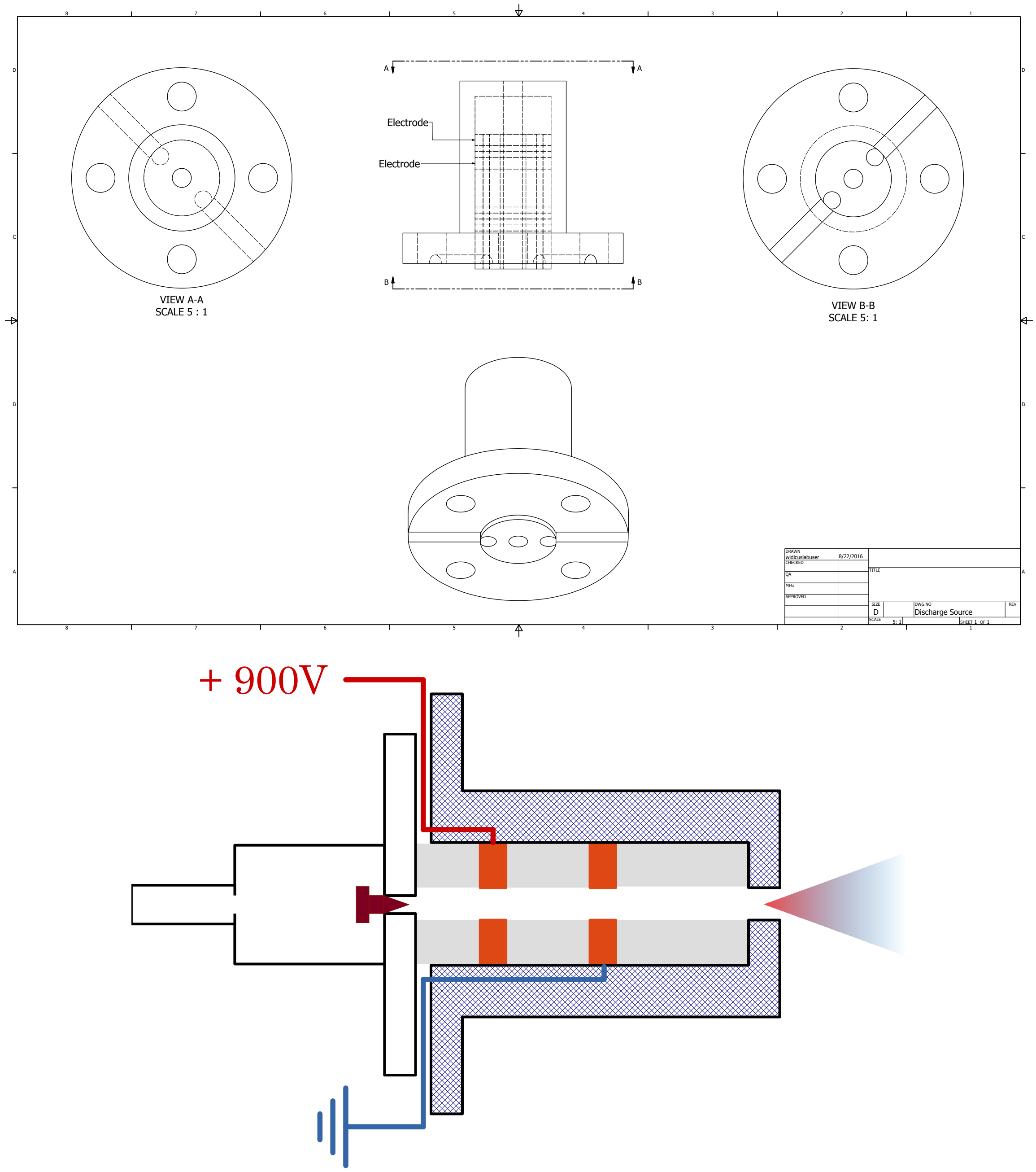

Schematic 2.1: Schematic of the high voltage discharge source. The CAD drawing is plotted in the top panel and the cartoon schematic is plotted in the bottom panel.

The pulsed high voltage was generated by a pulse generator (Directed Energy Inc., PVX-4150) backed by a high-voltage power supply (Spellman, SL2PN2000). The rising and falling time of the discharge was controlled by a 5 V TTL signal sent into the pulse generator. The maximum discharge current was constrained by ballast resistors.

2.2 The millimeter–submillimeter spectrometer

2.2.1 The multipass spectrometer

The main probe of the molecules is a multipass millimeter–submillimeter spectrometer. The millimeter–submillimeter radiation was generated by the up-conversion of microwave radiation, which was synthesized from am Agilent radio frequency (RF) synthesizer. Frequency bands from 70 GHz to 1 THz were accessed via a chain of Schottky diodes (Virginia Diodes Inc., S197(b) and S197(c)) listed in Table 2.2. The peak output power of the WR10 base band is about 30 mW. The power drops as the frequency band increases.

Table 2.2: Frequency bands of the Virginia Diodes Inc. S197 multiplier chain system.

Band	Diodes	Multiplication	Frequency Coverage (GHz)
3	WR10	3	70–115
4	WR8	3	90–140
5	WR10 + WR5.1	$3 \times 2 = 6$	140–230
6	WR10 + WR3.4	$3 \times 3 = 9$	215–335
7	WR10 + WR5.1 + WR2.2	$3 \times 2 \times 2 = 12$	320–450
8(a)	WR10 + WR5.1 + WR1.5	$3 \times 2 \times 3 = 18$	430–700
8(b)	WR10 + WR3.4 + WR1.5	$3 \times 3 \times 3 = 27$	650–800
9	WR10 + WR3.4 + WR1.0	$3 \times 3 \times 3 = 27$	700–1000

Two spherical mirrors (Edmund Optics, NT32-836) spaced roughly by 24″ (61 cm) created a multipass cell for the millimeter–submillimeter beam. This multipass design was based on the designs of Kaur *et al.* [25] in the infrared regime, as well as a smaller version in the millimeter–submillimeter regime [26]. Schematic 2.2 shows the design of this multipass cell, along with its controlling and data acquisition components, and the discharge source.

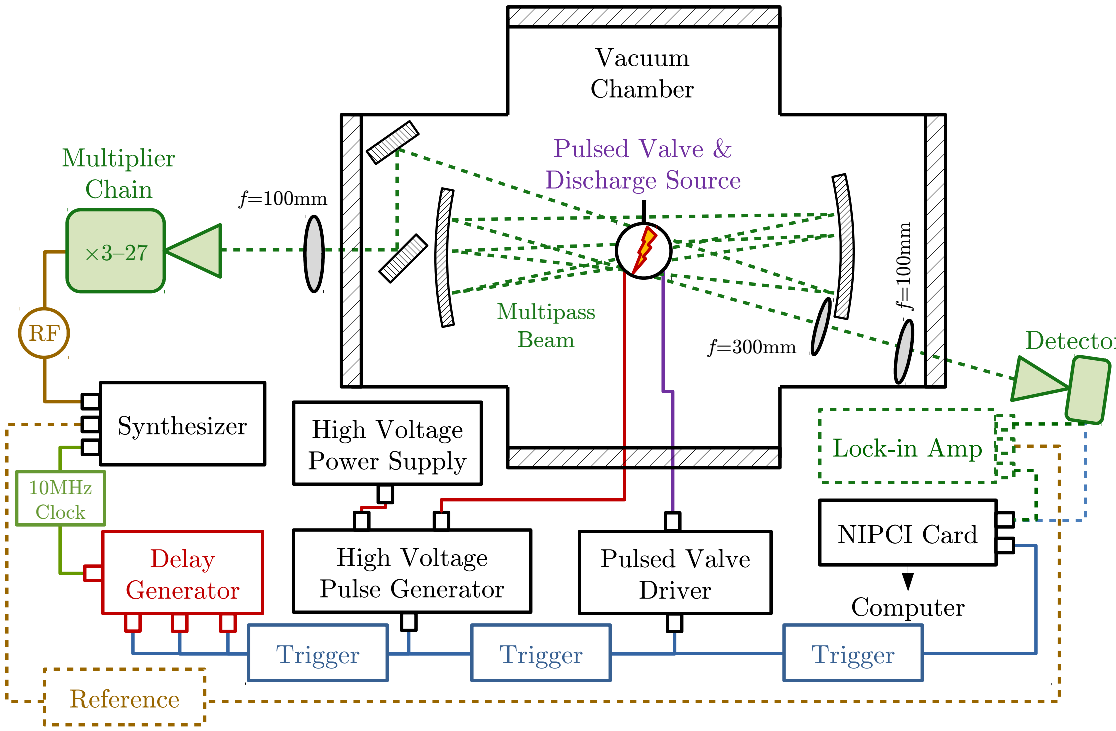

Schematic 2.2: Schematic of the millimeter–submillimeter spectrometer. The lock-in amplifier and the reference signal, drawn in dashed boxes, are optional. Reprinted with permission from Zou *et al.* [27].

In addition to the two spherical mirrors, three Teflon lenses were used to collimate and focus the millimeter–submillimeter beam. The collimation lens (f = 100 mm) was installed between the multiplier horn and the Plexiglass flange, at a distance of 3″–4″ (7.5–10 cm) from the horn. The lens was mounted on a translational stage with tuning micrometers, because the lens location is critical for receiving optimal millimeter–submillimeter power. After collimation, the millimeter–submillimeter beam passed the 1″ (2.5 cm) thick Plexiglass flange through a window of 1″ (2.5 cm) in diameter. The window was sealed by a 1/8″ (3.2 mm) thick polyethylene sheet and a square o-ring. Two guiding mirrors then redirected the millimeter–submillimeter beam to the proper incident angle for the multipass cell. A pair of Teflon lenses, one (f = 300 mm) before the edge of the spherical mirror, and another one (f = 100 mm) before the exit polyethylene window on the other flange, focused the millimeter–submillimeter beam down into the detector. The reason to use polyethylene windows is that Plexiglass of 1″ (2.5 cm) thick absorbs 30–40 % of the millimeter–submillimeter power. Polyethylene has a much lower transmission tangent than Plexiglass, therefore can reduce the total millimeter–submillimeter power loss from 60 % to below 10 %.

A HeNe laser (Thorlabs), pre-aligned with the millimeter–submillimeter beam, guided the alignment of the millimeter–submillimeter multipass. A control mirror, mounted on a 90° flip mount (Thorlabs TRF90), switches between the laser beam and the millimeter–submillimeter beam. The HeNe helped to initiate the location of the multipass cell, i.e., the two spherical mirrors and two plain mirrors drawn in Schematic 2.2, in the vacuum chamber to establish a 7-pass beam. After the coarse alignment, the millimeter–submillimeter beam was switched on for fine tuning. In the center of the two spherical mirrors, the millimeter–submillimeter beam focuses into a ∼5 cm area, and orients perpendicular to the molecular beam. The pulsed valve was positioned so that this area crossed the zone of silence in the supersonic expansion, where rotationally cooled molecules were located.

In Perry's infrared setup, they achieved as many as 57 passes between the two spherical mirrors. They proposed a relationship between the maximum number of passes $n_{\max}$ and the optical configuration [25], as

$$n_{\max} = \sqrt[3]{\frac{h^2\pi^4}{18L\lambda}} \tag{2.1}$$

where h is the height of spot pattern on each mirror, L is the mirror spacing, and λ is the wavelength of the light. In our millimeter–submillimeter version of the multipass, a significant difference is that the wavelength of the millimeter–submillimeter is two orders of magnitude longer than that of the infrared light. Using Perry's model, our optical setup is predicted to achieve a maximum of 6 passes at 300 GHz (1 mm wavelength). In practice, 7 passes were made possible by carefully adjusting the spacing between the two spherical mirrors. More passes were not allowed because of the constraint of the optical design, which is reflected by significant power loss from the millimeter–submillimeter beam clipping off the mirror edges.

Despite the smaller number of passes available in the millimeter–submillimeter regime than in the infrared, this optical design has been shown to improve the signal-to-noise ratio by a factor of 5 [26].

2.2.2 Detection of molecular signal

In our experiments, the absorption of the millimeter–submillimeter light by the rotational transitions of molecules was detected. For frequencies in Band 3 and Band 4 (see Table 2.2), we used zero-biased detectors (Virginia Diodes Inc., WR10 and WR8.0); for all frequency bands above 135 GHz, we used an InSb hot electron bolometer (QMC, Ltd., QFI/XBI). Detector signal can be sent into a digitizer card (National Instruments, PCI-5124) for digitizing and data storage, either directly or after the aid of a lock-in amplifier (SR830).

Data acquisition techniques and strategies involved in our experiments include a lock-in scheme using the lock-in amplifier and the digitizer card, a direct absorption scheme using solely the digitizer card, and most importantly, a fast-sweep data acquisition strategy which will be described in more detail in Section 2.3.

In the lock-in scan scheme, the RF generated by the synthesizer was internally frequency-modulated by a sine wave at a frequency of 30 kHz and a deviation of $\pm$75 kHz away from the carrier frequency. This modulation was imposed onto the millimeter–submillimeter radiation, and demodulated by the lock-in amplifier using a second harmonic detection scheme. The lock-in amplifier not only amplified the signal, but also removed any noise that did not resonant with the second harmonic frequency of the modulated signal. Because of this second harmonic detection, the spectrum displayed a second-derivative lineshape. In the direct absorption scheme, the millimeter–submillimeter radiation was directly measured by the detector and recorded by the digitizer card. Therefore, the absorption lineshape was maintained.

In both the lock-in scheme and the direct absorption scheme, the millimeter–submillimeter frequency was scanned at a fixed step size (usually between 0.05 MHz and 0.1 MHz), and the oscilloscope waveform was digitized and recorded by the NIPCI card at each frequency. A 3D plot, illustrated in Figure 2.3(a), was then reconstructed, taking the oscilloscope time as the x axis, the millimeter–submillimeter frequency as the y axis, and the signal intensity as the z axis. A integration of the signal intensity in a time window confined within the molecular absorption generates a plot of integrated intensity with respect to the millimeter–submillimeter frequency, namely, the expected molecular spectrum.

When using zero-biased detectors (ZBDs), the lock-in detection scheme was always applied, because the low output voltage of ZBDs did not favor the direct absorption scheme. When using the bolometer, all three detection techniques could be applied.

2.3 Fast-sweep data acquisition technique

2.3.1 Concept

The goal of the "fast-sweep" technique is to overcome the slow data acquisition by lock-in and direct absorption detections without introducing additional instrumentation. Both the lock-in and the direct absorption scheme (see Section 2.2.2) collects spectral frequencies point-by-point. The data acquisition speed is therefore constrained by the repetition rate of the pulsed valve, provided that the number of spectral averages remains constant. In typical experimental conditions, the pulsed valve runs at 10–50 Hz, which turns into a data collection time of 400—2000 seconds (7–33 minutes) for a 10 MHz spectral bandwidth with 0.05 MHz frequency resolution and 100 spectral averages. Searching for spectral lines in GHz-wide windows is then almost unfeasible because of the long acquisition time required.

The invention of the chirped-pulse technique in the microwave regime [28] revolutionized data acquisition in microwave spectroscopy. The chirped-pulse concept has been adopted into the millimeter–submillimeter wavelength range [29–31] for GHz-wide fast data collection. These techniques are time-domain, Fourier transform techniques that require Gs/s arbitrary waveform generators to generate frequency chirps of GHz widths within a microsecond, high power amplifiers of Watts to kilowatts, and Gs/s ultrafast digital oscilloscopes for time-domain data acquisition. The sales price of each single piece of these instruments lies at a few hundred thousand dollars. As a result, these techniques require significant financial investment in the laboratory instrumentation.

In our experiments, we applied a "fast-sweep" technique that enables faster data acquisition than the point-by-point scheme without requiring the purchase of expensive new equipment. The technique references the chirped-pulse concept, but adopts it in such a way that a slower frequency chirp of a narrower bandwidth is applied to the frequency-domain detection instead of the time-domain. Because frequency-domain detection is implemented, identical instruments, as described in Section 2.1, can be used in this technique, and there is no requirement for a strong radiation field or an ultrafast oscilloscope. Despite its simple concept, this technique increases the speed of spectral acquisition by 2 orders of magnitude compared to the point-by-point scans.

The preliminary concept of the fast-sweep technique was presented by Hays in his dissertation [32]. In Dr. Hays' dissertation, he described the experimental configuration of the fast-sweep technique for the $O(^1D)$ insertion reaction of methylamine. In that particular experiment, the technique was applied to a laser-induced molecular signal that was 50 μs long. The signal was compared to the point-by-point direct absorption scans.

In this dissertation, I present a comprehensive performance test on this fast-sweep technique, as applied to the supersonic expansion experiments. The concept of the fast-sweep technique is visualized in Figure 2.3. In Figure 2.3(a), the color map shows the oscilloscope waveforms across a frequency window where a CH_3OH transition is located. In the scheme of point-by-point scans, the millimeter–submillimeter frequency at each scanned point remains constant, and is stepped across the window. The spectrum of CH_3OH in this window, however, can be reconstructed with one single scan, if the millimeter–submillimeter frequency sweeps through the entire window, as the diagonal arrow shows in Figure 2.3(a).

To generate this sweep, an internal triangle-wave frequency modulation of the Agilent synthesizer is necessary. This triangle-wave modulation can output linear frequency sweeps that span a few MHz bandwidth in a period of several hundreds of microseconds. Multiplied by the multiplier chain, the sweep bandwidth expands into a few dozens of MHz in the millimeter–submillimeter regime. This linear frequency sweep can then be mapped to the time window where the pulsed valve is open and molecules are present. Therefore, the spectral information within the full bandwidth, i.e., a few dozens of MHz wide, can be collected in a single shot. The pulsed experiment also provides an advantage of background subtraction because a background sweep can be recorded immediately after the pulsed valve is closed, as illustrated in Figure 2.3(b).

Post-processing of the fast-sweep data is performed by a Python3.4 script using the Numpy1.8 and Scipy0.15 modules. The script code is included in Appendix A. The script first maps the oscilloscope time to the millimeter–submillimeter frequencies by combining the pre-recorded modulation output (i.e., the bottom trace in Figure 2.3(b)) and bandwidth information. The next step is to reshape the data array, taking one full sweep as the signal and another one as the background, and to subtract the background from the signal. Lastly, the background-subtracted sweeps at all center frequencies within the same data file (usually set at 1 GHz for convenience)

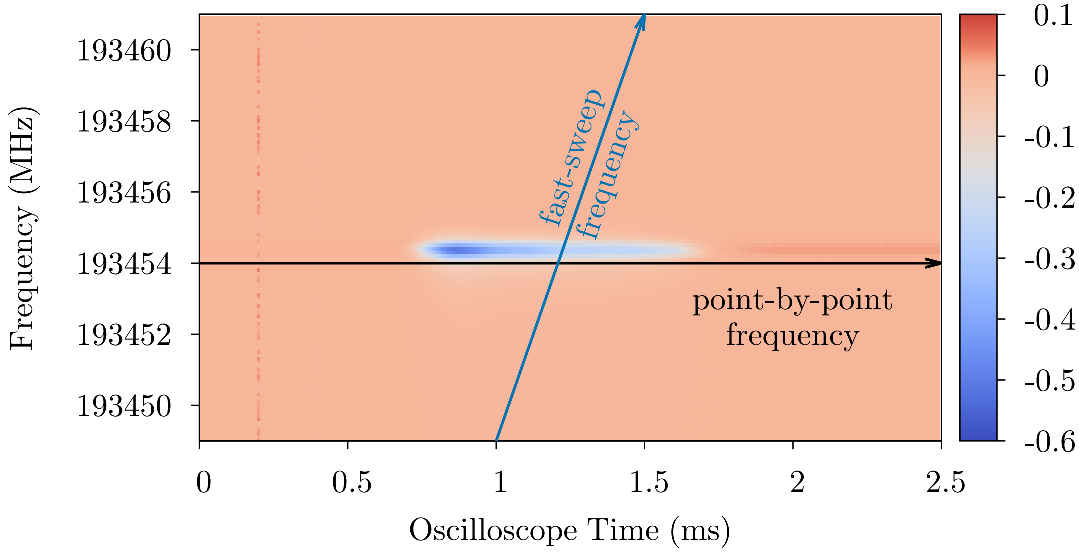

(a) A color map of the oscilloscope voltage across a CH_3OH transition.

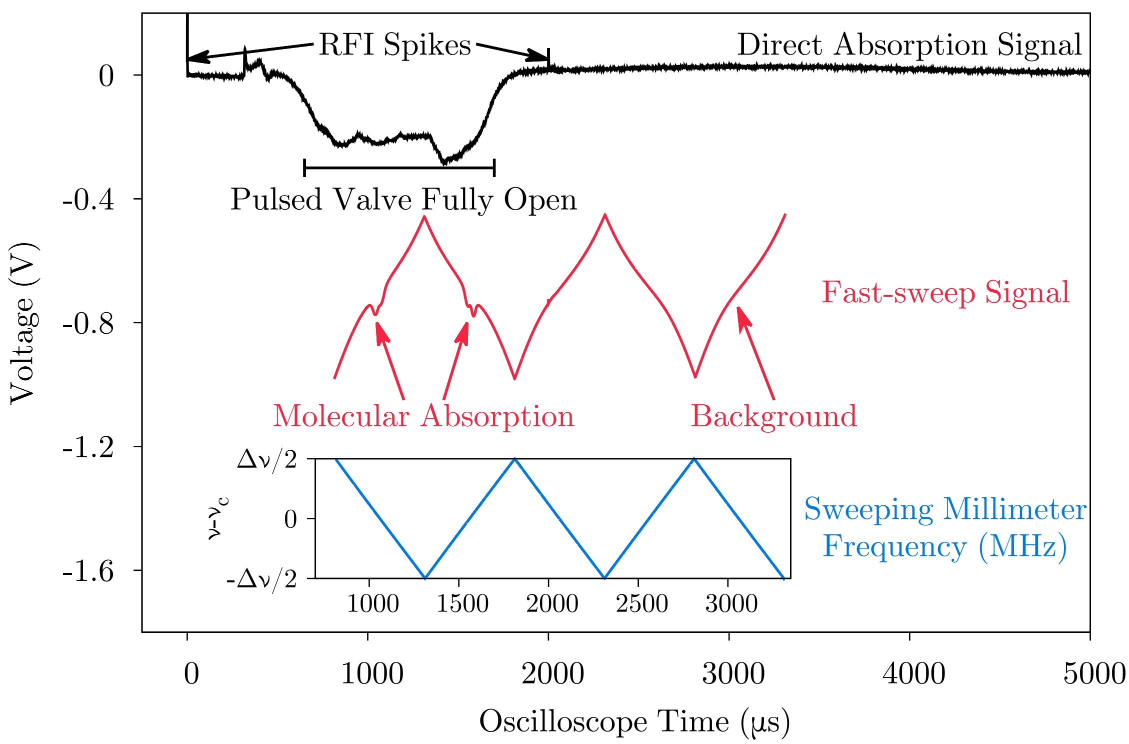

(b) (top) A molecular direct absorption signal; (middle) the fast-sweep signal of 5 cycles; (bottom) the graphical representation of the frequency deviation from the center frequency, $\nu - \nu_c$, in real time. $\Delta\nu$ is the full sweep bandwidth.

Figure 2.3: The concept of the fast-sweep technique.

were stitched together to create a spectrum. Additional linear and spline baseline removal options are available to suppress large intensity oscillations in the final spectrum, especially in the case of a discharge spectrum. More discussion on the effects of discharge on the fast-sweep spectra can be found in Section 2.3.4.

2.3.2 Instrument settings and practical consideration

There are a few practical considerations when applying the concept of fast-sweep. The synchronization between the pulsed valve, the digital oscilloscope, and the discharge firing is essential. The capacity of our instruments should also be tested in order to take the full advantage of this technique.

The synchronization of all pulsed instruments was achieved by phase-locking the four-channel delay generator (Stanford Research Systems, DG645) to the 10 MHz Rb clock output of the Agilent synthesizer. This ensured the phase stability of the frequency modulation with respect to the digitizer card trigger, which was controlled by the delay generator. Other pulse signals, including the triggers to the pulsed valve and discharge source, were also synchronized because they were all generated by the same delay generator.

Several frequencies, including the modulation frequency of the synthesizer (f_{RF}), the repetition frequency of the pulsed valve (f_{v}), and the sampling frequency of the digitizer card (f_{s}), need to match. Since a sweep was considered as a linear increase or decease of the RF, one triangle-wave modulation cycle contains two sweeps. That is to say, the sweep frequency is twice the triangle-wave modulation frequency. The sweep frequency must be divisible by the pulsed valve repetition frequency so that the phase of the triangle modulation is fixed in each molecular pulse. Then, the sampling frequency of the digitizer card needs to coordinate with the sample length (n) so that integer numbers of sweeps are recorded. Only a selection of 2 and 5 multiples are allowed to be set as the sampling frequency due to the manufacture settings on the digitizer card. The modulation bandwidth was manually set by the "modulation depth" option on the synthesizer. The "modulation depth" is the maximum frequency deviation from the center frequency ν_c. Therefore, the RF bandwidth $\delta\nu$ is twice the modulation depth. Moreover, since the modulation depth was set on the synthesizer, the total sweep bandwidth is equal to the product of twice the modulation depth and the frequency multiplication factor g, which varies in different frequency bands (See Table 2.2). Table 2.3 summarizes the key settings in the fast-sweep technique and their relations.

Table 2.3: Parameters and settings involved in the fast-sweep technique.

	Parameter	Relation	Recommended Setting
f_v	Pulsed valve repetition	–	≤ 50 Hz
f_{RF}	Modulation frequency	$f_{RF} \mod f_v \equiv 0$	≤ 10 kHz
f_s	Sampling frequency	$f_s = 2Rg\Delta\nu f_{RF}$	≤ 10 MHz
$\delta\nu/2$	Modulation depth (RF)	–	≤ 5 MHz
$\delta\nu$	Modulation bandwidth (RF)	–	≤ 10 MHz
$\Delta\nu$	Sweep bandwidth	$\Delta\nu = g\delta\nu$	$\leq 10g$ MHz
g	Multipler factor	–	3–27
ν_c	Center frequency	–	70 – 1000 GHz
n	Number of sweeps recorded	–	5
l	Sample length	$l = nf_s/(2f_{RF})$	≤ 10000 pts
R	Frequency resolution	$R = l/(n\Delta\nu)$	> 20 pts·MHz^{-1}
N	number of averages	–	$\leq 10,000$
t	Acquision time	$t = N/f_v$	≤ 5 min

The millimeter–submillimeter frequency is reconstructed under the assumption of the linearity of the frequency sweep centered at ν_c. The detector, however, is not sensitive to the "direction", i.e., the sign of the derivative of RF with respect to time, of the sweep. As a result, the sweep signal does not contain information about whether it starts with frequencies higher or lower than ν_c. In order to correctly reconstruct the millimeter–submillimeter frequency, we need to record the local frequency output, which resembles the modulation applied to the RF, from the synthesizer using the identical trigger settings of the sweep signal. The direction of the sweep can be determined from the waveform analysis of this local frequency signal.

Two modes were available in our data acquisition routine. The "oscilloscope" mode can average the digitizer card signal sitting on a given center frequency and save it as a one-column voltage array. The center frequency and sweep bandwidth themselves, however, are not saved in the file. Therefore, they need to be recorded manually, otherwise the center frequency will be set to a default value of 0 and the bandwidth at 1 MHz in the post-process code (See the code in Appendix A for a full option list). The "scan" mode scans the center frequency by a fixed frequency interval, and saves both the frequency array (1D) and the digitizer card voltage array (2D), in which each column corresponds to the waveform at a scanned frequency point. The frequency step in the scan mode should be set equal to the full sweep bandwidth to avoid frequency gap or frequency overlap. Since the frequency step is set in this way, both center frequencies and sweep bandwidth are recorded in digital files.

The odd sweeps and even sweeps are not perfect mirror images. This is caused by the imperfection of the internal modulation mode of the synthesizer, which has a limited ability of waveform manipulation. This imperfection, represented by the deviation of the local oscillator (LO) voltage from linearity (Figure 2.4), will lead to poor background subtraction if an odd sweep and an even sweep are used for the signal–background pair. Ordinal numbers of the same parity should always be used for background subtraction.

2.3.3 Benchmark with known methanol (CH_3OH) transitions

The performance of the "fast-sweep" technique was systematically tested with a grid of settings on the modulation bandwidth, the modulation frequency, the sampling rate, and the number of averages. The benchmark was a series of methanol transitions between 193.4 GHz and 193.6 GHz that have been well-characterized and well-documented in literature. The transition frequencies and quantum numbers of these lines were retrieved from the JPL spectroscopy catalog[1] (Version 3, updated in

[1] http://spec.jpl.nasa.gov/ftp/pub/catalog/catdir.html

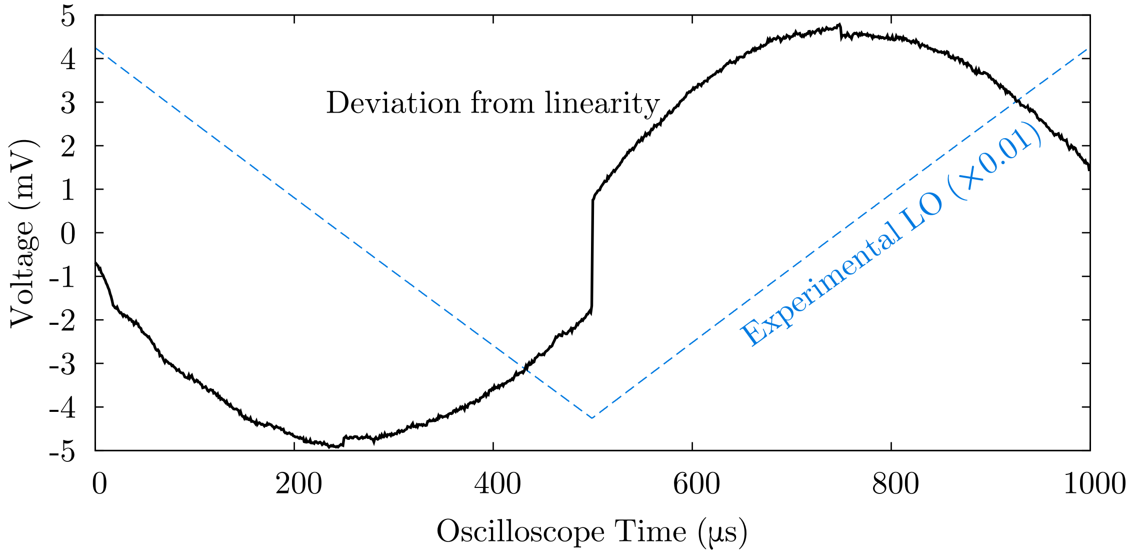

Figure 2.4: Imperfection of the triangle-wave modulation of the synthesizer, represented by the deviation of the local frequency voltage from linearity.

March 2010). The reason for choosing this set of lines is because within a narrow frequency range, they span a wide range of lower state energies that can be used to conveniently probe the rotational temperature of CH_3OH in the jet-expansion. The transition frequencies, lower state energies, and quantum numbers are listed in Table 2.4.

Table 2.4: Transition frequencies, lower state energies E_{low}, and quantum numbers of the benchmark CH_3OH transitions.

Transition (MHz)	E_{low} (cm^{-1})	Quantum Number (J_K)	Symmetry
193415.324	18.803	$4_0 \leftarrow 3_0$	E^+
193441.600	13.557	$4_1 \leftarrow 3_1$	E_2^-
193454.358	9.681	$4_0 \leftarrow 3_0$	A^+
193471.434	44.293	$4_3 \leftarrow 3_3$	A^+
193471.545	44.293	$4_3 \leftarrow 3_3$	A^-
193474.414	42.842	$4_3 \leftarrow 3_3$	$E_1^\pm$
193488.047	35.890	$4_2 \leftarrow 3_2$	A^-
193488.964	53.266	$4_3 \leftarrow 3_3$	$E_2^\pm$
193506.559	24.310	$4_1 \leftarrow 3_1$	E_1^-
193510.750	35.890	$4_2 \leftarrow 3_2$	A^+
193511.225	27.682	$4_2 \leftarrow 3_2$	E_2^+
193511.335	25.141	$4_2 \leftarrow 3_2$	E_1^+

Before fast-sweep tests, two spectra using the traditional point-by-point scan schemes were measured for reference. One is a direct absorption spectrum integrating the bolometer signal over the time duration of the molecular pulse, and the other is the second harmonic lock-in scan. Both scans were set at a frequency resolution of 0.1 MHz, 20 averages, and a bandwidth of 120 MHz starting from 193400 MHz. The lock-in amplifier was set at a time constant of 30 µs, an integration time of 60 ms, an FM frequency of 30 kHz, and an FM bandwidth of ±75 kHz on the RF signal. The pulsed valve was running at 50 Hz with a stagnation pressure of 20 psig (2.4 bar).

Both the direct absorption and the lock-in spectra are plotted in Figure 2.5. The

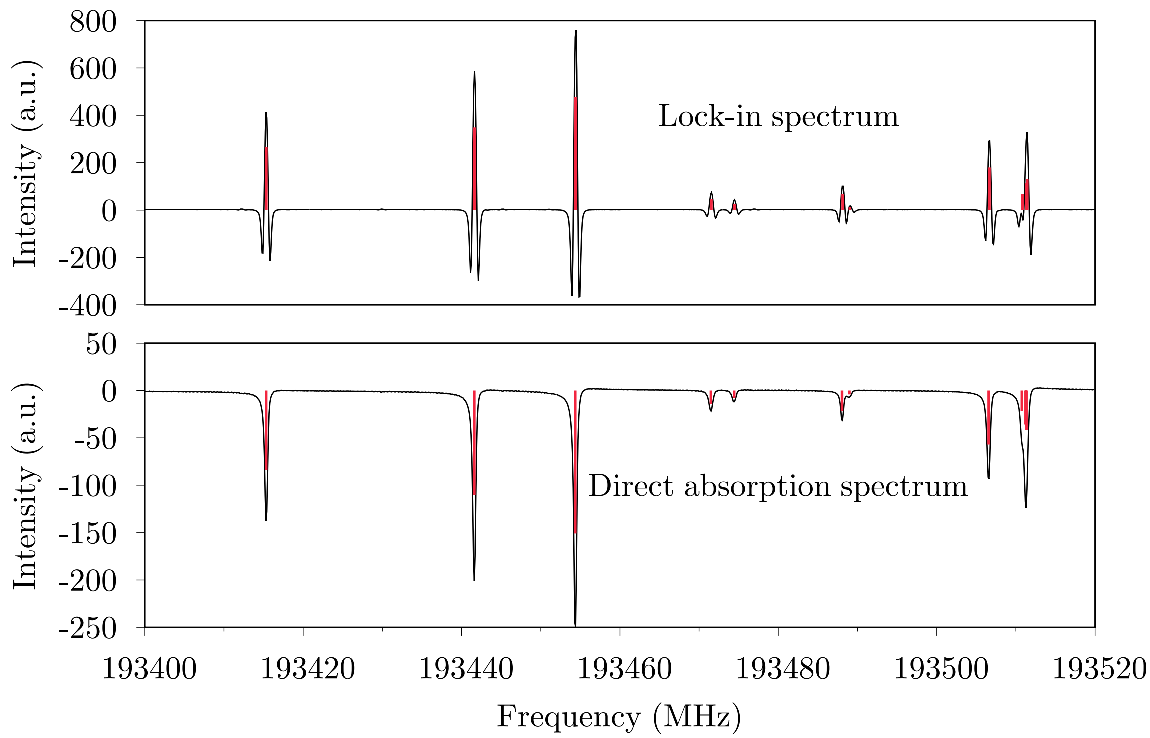

Figure 2.5: Point-by-point scan of the CH_3OH branch from 193400 MHz to 193520 MHz. The top panel shows the lock-in spectrum, and the bottom panel shows the direct absorption spectrum. Purple sticks represent simulated CH_3OH transitions from the JPL catalog assuming a rotational temperature of 22.5 K.

direction absorption scan shows the Gaussian lineshape, whereas the lock-in scan shows the second derivative of the Gaussian lineshape because of the second harmonic detection. Slight asymmetry of the lineshape is observed, likely due to the imperfect alignment of the expanding axis of the molecules with the millimeter–submillimeter beam. It causes uneven Doppler components that asymmetrically broadens the spectral lines.

A rotational temperature of 22.5 K was derived from these spectra using a Boltzmann analysis referred to as the "rotational diagram" method [26, 33]. The integrated line intensity is related to the rotational temperature of the molecule by

$$\int I \mathrm{d}\nu = \frac{hc^3}{8\pi k} \frac{Ag_\mathrm{u}}{\nu^2} \frac{N_\mathrm{T}}{Q(T_\mathrm{rot})} e^{-E_\mathrm{up}/kT_\mathrm{rot}} \tag{2.2}$$

The Ag_u/ν^2 term can be calculated from the JPL catalog by the conversion [34]

$$\frac{Ag_\mathrm{u}}{\nu^2} = \frac{10^{\mathrm{LOGINT}} Q(T_{300})}{e^{-E_\mathrm{up}/(300k)} - e^{-E_\mathrm{low}/(300k)}} \times 2.7964 \times 10^{-16} \tag{2.3}$$

in which the LOGINT is the documented base-10 logarithm of the line intensity. The lower state energy E_low and upper state degeneracy g_u are both listed in the catalog file, and the upper state energy E_up can be easily calculated from the lower state energy and the transition frequency. Subsituting Equation 2.3 into Equation 2.2, we have

$$\int I \mathrm{d}\nu = \frac{hc^3}{8\pi k} \frac{10^{\mathrm{LOGINT}}}{e^{-E_\mathrm{up}/(300k)} - e^{-E_\mathrm{low}/(300k)}} \frac{N_\mathrm{T} Q(T_{300})}{Q(T_\mathrm{rot})} e^{-E_\mathrm{up}/kT_\mathrm{rot}} \times 2.7964 \times 10^{-16} \tag{2.4}$$

The natural logarithm of the integrated intensity is then

$$\ln \int I \mathrm{d}\nu = \ln \mathrm{Const} + \ln N_\mathrm{T} - \ln Q(T_\mathrm{rot}) - \frac{E_\mathrm{up}}{kT_\mathrm{rot}} \tag{2.5}$$

which is proportional to the upper state energy E_up/k with a slope of $-1/T_\mathrm{rot}$. All fixed constants are packed into the single term $\ln \mathrm{Const}$, which introduces a vertical shift of the logarithm intensity. The number density and the partition function are reflected as the vertical intercept. Since calibration of the absolute number density is unnecessary for the determination of the rotational temperature, all data points were vertically shifted to generate a tight-fit plot, which is shown in Figure 2.6. Numerical integration was used to obtain the integrated intensities of the asymmetric CH_3OH lines, and the blended lines at 193488 MHz and 193511 MHz were omitted because of the difficulty in the numerical integration. The variation of the millimeter–submillimeter power was corrected by measuring the 1% amplitude-modulation voltage from the lock-in amplifier. The 3σ uncertainties are propagated based on the noise level of the spectra and the fluctuation of the power measurement, and a weighted linear least-square fit was used to derive the rotational temperature.

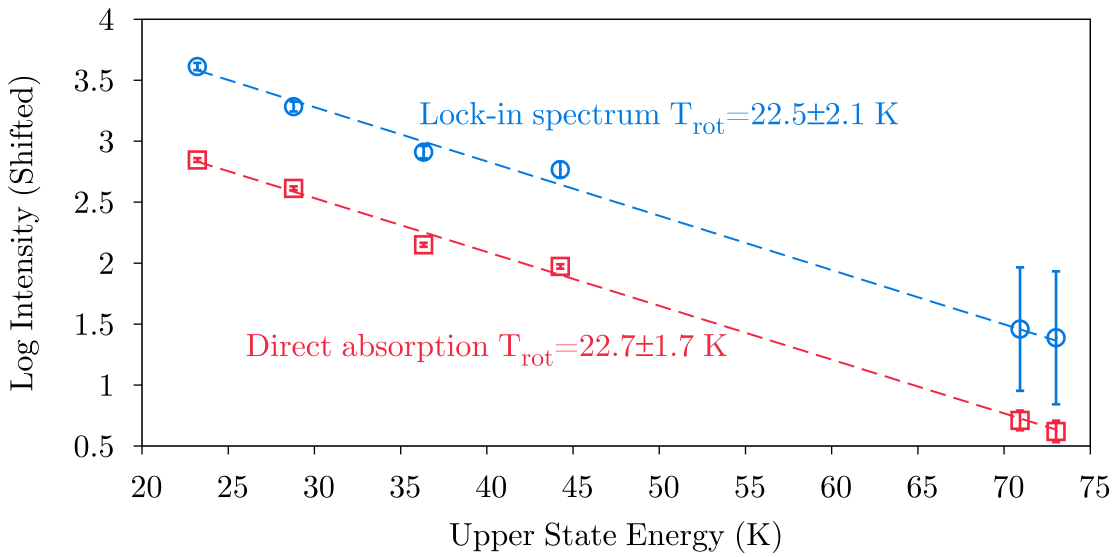

Figure 2.6: Rotational diagrams of CH_3OH from the direct absorption (red) and the lock-in (blue) spectra. The logarithm integrated intensity was vertically shifted to generate a tight-fit plot, since the intercept on the y axis does not affect the rotation temperature calculation. Error bars represent 3σ uncertainty of the intensity measurement. Weighted linear least-square fit was used to derive the dashed lines and the rotational temperature. Blended lines were omitted in this plot.

Both spectra, lock-in and direct absorption, present similar rotational temperatures around 22.5 K. This temperature was used to simulate the catalog spectrum of CH_3OH throughout this chapter. The simulated spectral intensity at this temperature agrees well with the experimental spectra, as shown in Figure 2.5.

Modulation bandwidth

The modulation bandwidth determines the frequency coverage of a sweep. The wider the bandwidth is, the faster a spectral scan will be. The increase of bandwidth, however, should not sacrifice the signal intensity and frequency accuracy of the spectrum. A series of modulation bandwidth from 0.4 to 80 MHz on the RF side, corresponding to 2.4 to 480 MHz at Band 5 for the CH_3OH benchmark, were tested at a modulation frequency of 1 kHz. The spectra from this series are plotted in Figure 2.7. The full plot stacks these fast-sweep spectra from the highest bandwidth (480 MHz) at the top to the lowest bandwidth (2.4 MHz) at the bottom. Two inset plots zoom into the center and edge of the spectra. Catalog frequencies are also plotted as red sticks for frequency references.

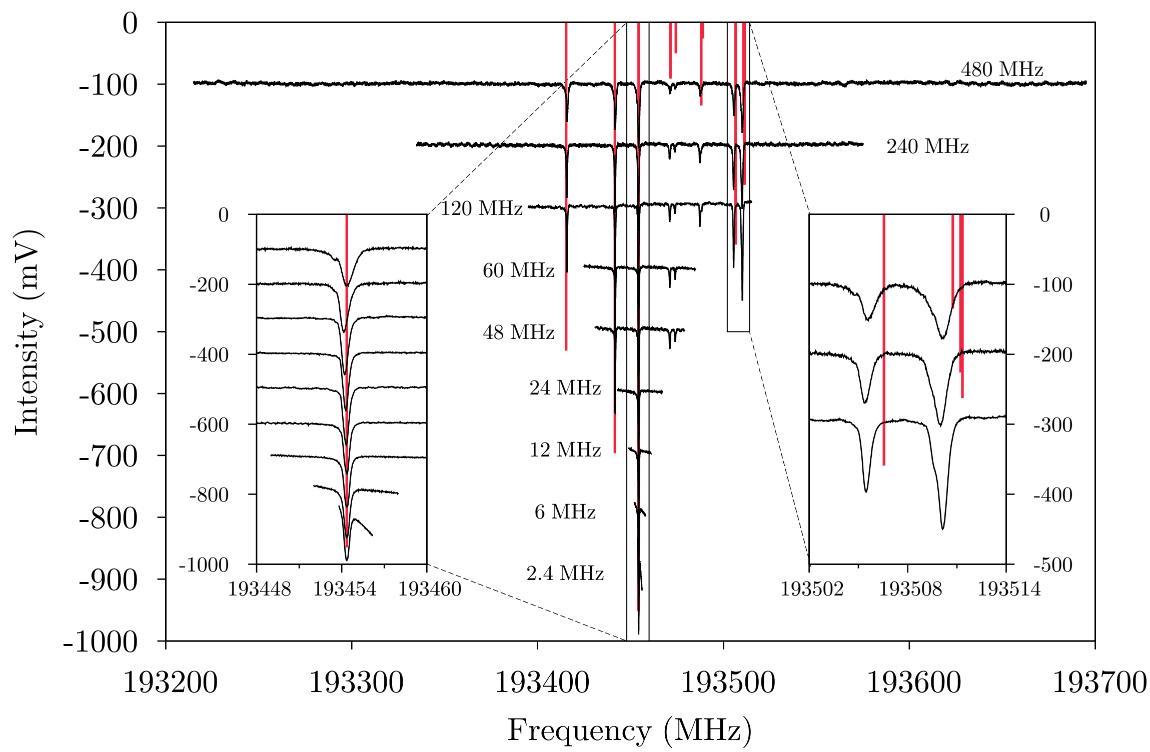

Figure 2.7: The effect of the fast-sweep bandwidth to the quality of the spectrum. The full-scale plot stacks spectra with decreasing total bandwidth from 480 MHz at the top to 2.4 MHz at the bottom. The center frequency was set at 193455 MHz. The left inset plot zooms in the center region of the spectra, while the right inset plot zooms in the right edge of the spectra. Purple sticks reference to the JPL catalog frequencies of CH_3OH transitions.

For these scans, the sampling rate and sampling length were adapted according to the bandwidth setting so that the frequency resolution was consistently at 500 points per RF MHz. A slight drop of the intensity and an increase of the noise level are observed for modulation bandwidths larger than 20 MHz. Systematic frequency shifts of the spectral lines are also observed, especially with high modulation bandwidths. The frequency shifts appear larger at the edge of the spectrum (1–2 MHz) than at the center of the spectrum (< 0.2 MHz). This is likely due to the imperfection of the triangle modulation, which does not fully cover the entire set bandwidth. The modulation bandwidth accuracy is $< \pm 3.5\%$ of the set FM bandwidth [35]. A 40 MHz RF sweep generates a maximum frequency deviation of 1.4 MHz, which can be multiplied into 12.4 MHz in the Band 5 system. Because of this imperfection, the spectra slightly "shrink", causing the observed transitions to shift towards the center frequency from the expected catalog frequency. The spectral lines also broaden at high modulation bandwidths, and turn asymmetric. This is likely caused by two factors: the instrumental limitation of the synthesizer, and the finite bandwidth of the bolometer. Under FM mode, the modulation resolution of the RF signal is ± 0.1 % of the total FM bandwidth or 1 Hz, whichever is the greater [35]. Therefore, when modulating at a RF bandwidth above 40 MHz, the frequency envelop of the millimeter–submillimeter wave approaches 0.04 MHz, which becomes visible in the spectrum as a broadened convolution with the spectral line profile. Another problem at high bandwidths is that the sweep rate pushes the limit of the detector. A 480 MHz sweep at a modulation rate of 1 kHz (0.5 ms per sweep) corresponds to a sweep rate of 0.96 MHz per µs. The rated response bandwidth of the detector is only 0.5 MHz [36]. As a result, the detector is too slow compared to the change of millimeter–submillimeter frequency, and the delay of the detector response becomes visible in the spectrum. In summary, to ensure the quality and accuracy of the fast-sweep spectrum, the RF modulation bandwidth should be constrained to values below 10 MHz (modulation depth ≤ 5 MHz).

Sampling rate

The quality of the fast-sweep spectra at various sampling rates was tested with a fixed sweep bandwidth of 12 MHz and a fixed modulation frequency of 1 kHz. Considering the full-width-half-maximum of the spectral line is on the order of 0.25 MHz, the Nyquist frequency of the spectral line signal at this modulation setting is $12/0.25 \times 1 = 48$ kHz. Therefore, a minimum sampling rate of 100 kHz is sufficient for signal acquisition. Theoretically, oversampling by increasing sampling rate improves the frequency resolution, and also provides the advantage of anti-alias. The result of a series of sampling rate from 100 kHz to 10 MHz is plotted in Figure 2.8.

The 40 kHz sampling rate is below the Nyquist frequency, and was therefore expected to fail to resolve the spectral line. The spectral feature is sufficiently sampled above 100 kHz; the best results, however, are those above 500 kHz that provide higher frequency resolution and lower noise. The noise level of the spectra with original sampling rate does not significantly change with an increase of sampling rate, as shown in Figure 2.8(a). A high-frequency sinusoidal contamination is observed in several spectra, especially those sampled at 2 MHz, 4 MHz, and 20 MHz. A Gaussian bandstop filter in the Fourier domain was applied to filter out this contamination prior to down-sampling. The effectiveness of down-sampling is presented in Figure 2.8(b), where all spectra are down-sampled to an equivalent 0.5 MHz sampling rate by algorithmic averaging. After down-sampling, the signal-to-noise ratio (SnR) is slightly improved, except for the "4 MHz" trace which still exhibits a sinusoidal contamination oscillating at a lower frequency. The SnR of the original spectra and the down-sampled spectrum is plotted in Figure 2.8(c). The SnR improvement to the original spectra is about a factor of 2, but has large uncertainties. Considering the cost of low maximum bandwidth and large data storage requirements, oversampling is not an optimal option for SnR improvement. The test, however, verifies that high sampling rate does not destroy the molecular signal.

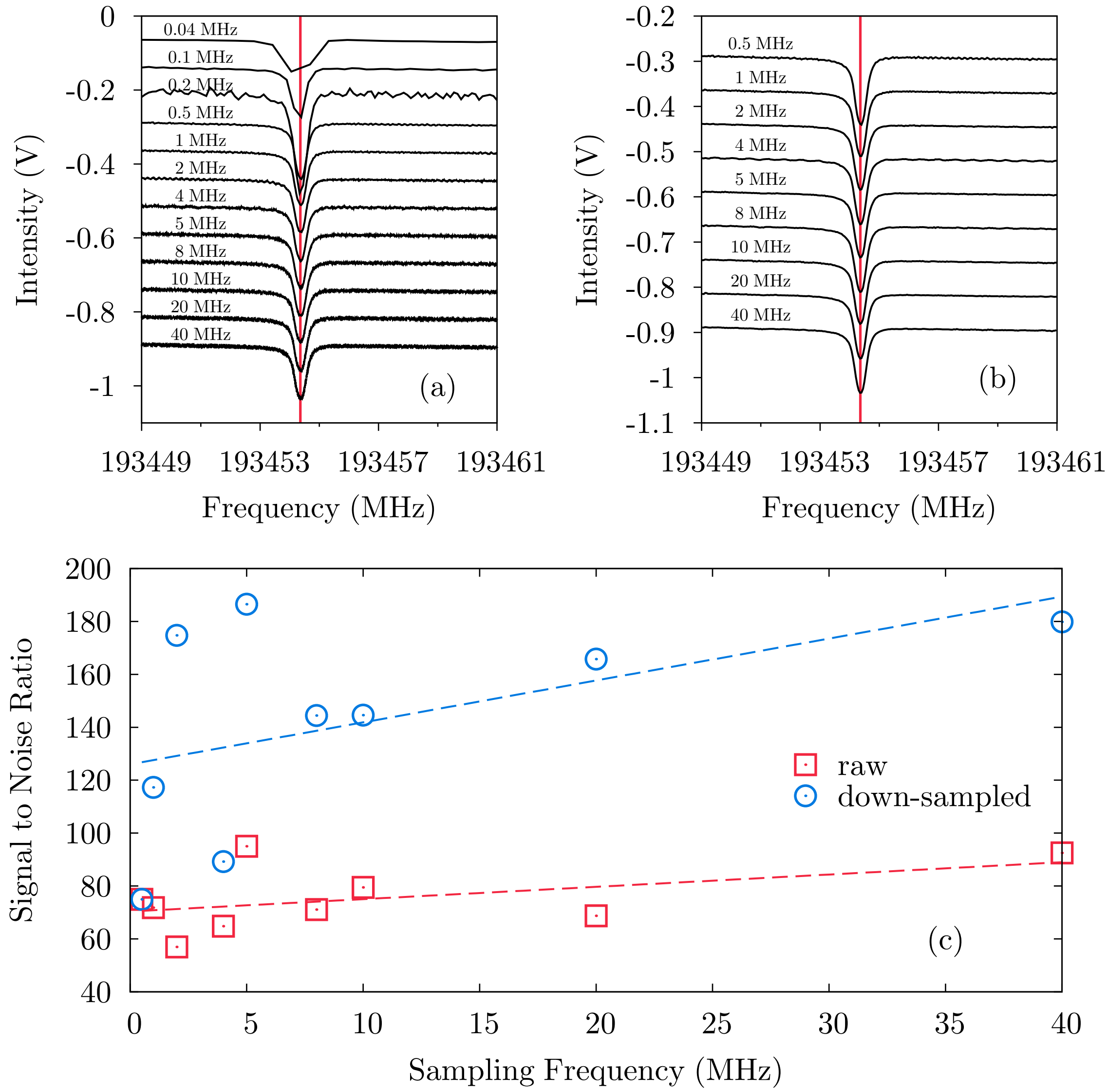

Figure 2.8: The quality of fast-sweep spectra under various sampling rates: (a) the processed spectra at the original sampling rates; (b) the down-sampled spectra with 0.5 MHz equivalent sampling rates; (c) the change of SnR under tested sampling rates with dashed lines indicating the least-square fits of the SnR trend. The red sticks in (a) and (b) refer to the catalog frequency of CH_3OH.

Modulation frequency

The modulation frequency determines the time duration of a single sweep. Faster modulation frequencies produce shorter sweeps, which can be applied to shorter molecular signals. This approach may also allow averaging multiple sweeps in a single molecular pulse, thus increasing the total number of spectral averages without longer data acquisition time. However, high modulation frequency causes problems similar to high modulation bandwidths: the sweep rate exceeds the limit of our detector bandwidth. Moreover, the quality of the triangle modulation drops at high modulation frequencies because of the limited instrumental ability of the RF synthesizer.

The left panel of Figure 2.9 stacks the spectra taken under increasing modulation frequencies with the same bandwidth of 12 MHz and identical frequency resolution. It shows that as the modulation frequency increases, the intensity of the spectrum drops, the width of the spectral line broadens, the purity of the spectral lines breaks down, and the line frequency starts to deviate from the reference frequency listed in the JPL catalog.

The cause of the line broadening, attributed to the limit of detector bandwidth, has been discussed in Section 2.3.3. The cause of the impurity and frequency shift is likely due to both the limitation of the RF synthesizer and the aligning of trigger signals. They are reflected in the right panel of Figure 2.9, which plots the raw data from the digitizer with respect to the oscilloscope time. The gray dash locates the turning point where one sweep ends and the next one starts. At low modulation frequencies, the waveform has sharp turns at the turning point. At high modulation frequencies, such as 40 and 50 kHz, the waveform turns become curved, which is an indication of the decreasing quality of the triangle wave. This quality decrease may introduce undesired impurities into the processed spectra. It is also more difficult to determine the actual turning point of the sweep with the curved edge, introducing

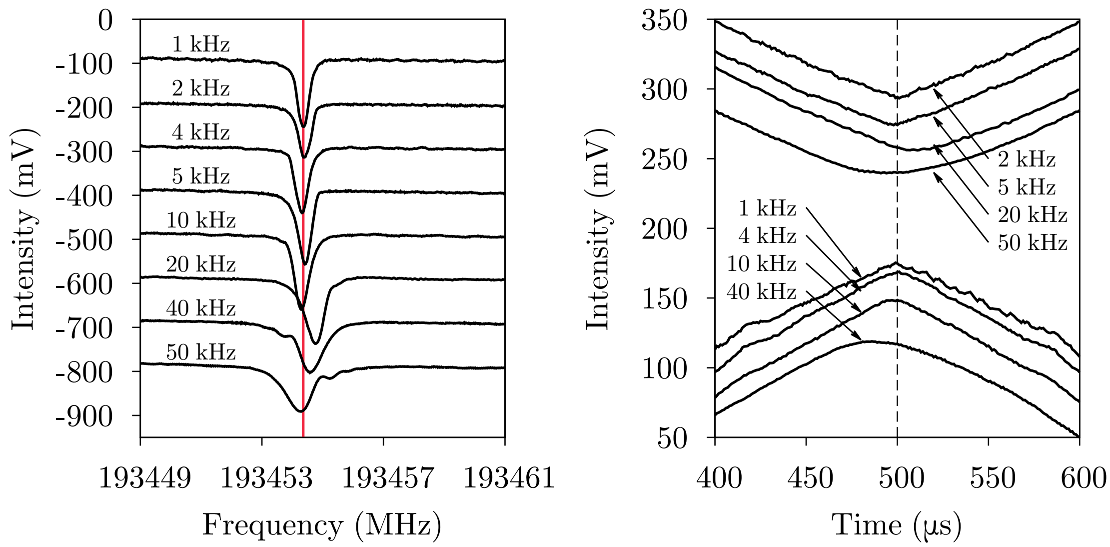

Figure 2.9: The effect of modulation frequency to the fast-sweep spectra. The left panel stacks the fast-sweep spectra at multiple modulation frequencies. The right panel plots the raw oscilloscope traces from which the fast-sweep spectra were reconstructed. The dashed line in the right panel draws the turning point of a frequency sweep.

more uncertainty in aligning the trigger signal with respect to the start of a sweep. As a result, frequency reconstruction becomes unreliable at these high modulation frequencies.

To maintain an acceptable spectral quality, the modulation frequency should be constrained within 10 kHz. 10 kHz modulation frequency corresponds to a 50 μs sweep, sufficiently short for all experiments reported in this dissertation, and also for most scenarios in jet-cooled experiments. 10 kHz was also the setting reported by Hays [32].

Signal to noise ratio

The goal of the fast-sweep technique is to achieve an equivalent SnR to that obtained by the point-by-point scan in a shorter spectral acquisition time. The spectral acquisition time increases linearly with the number of averages for both techniques. The difference is that the acquisition time of the point-by-point scan also scales linearly with the increase of spectral bandwidth and spectral resolution, whereas the fast-sweep technique does not.

The theoretical SnR is proportional to the square root of number of averages. Does the SnR of fast-sweep spectra follow this square root of N rule? Will the sweep bandwidth affect the noise level?

To test the SnR behavior of the fast-sweep spectra, both methanol and blank spectra, i.e., spectra without the pulsed valve running, were collected in a series of increasing numbers of averages. The noise levels for the blank spectra are determined by the standard deviation of the data points, and the SnR of each methanol spectrum is determined by the ratio between the peak intensity of the strongest line in the spectrum and the standard deviation of the local baseline around the spectral lines. To test the effect of sweep bandwidth on the SnR, three sweep bandwidths were chosen: 12 MHz, 60 MHz, and 240 MHz, which represent small, medium, and large bandwidth, respectively. All blank and methanol spectra are plotted in Figure 2.10.

The blank spectra of all three sweep bandwidths exhibit a systematic decrease of noise level as the number of averages increases. The noise level of the 240 MHz sweep, however, is visibly larger than those of the 12 MHz and the 60 MHz sweep. For all three sweep bandwidths, when the number of averages is above 1000, interference from the pulsed valve with the detector electronics starts to appear at the edges of the spectra. The baseline is also not completely flat: it shows a small increasing slope. Most of these impurities, however, can be removed by polynomial baseline fitting. Therefore, they do not cause unmanageable trouble in spectral line identification. The SnR behavior of blank spectra is further illustrated in Figure 2.11 by plotting the noise level with respect to the number of averages, as well as the corresponding data acquisition time, in base 10 logarithm scale. The noise level of both the full sweep and the center part (1/6–5/6) of the sweep are plotted in order to evaluate the impact of the pulsed valve impurity, which appears at the spectral edges. The impurity is reflected by the tail of the noise level at high Ns. Especially, the tail of

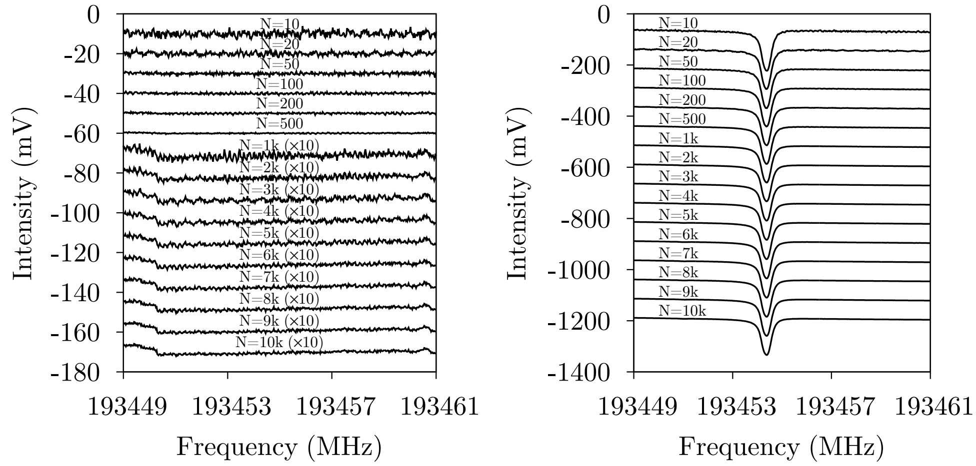

(a) Blank (left) and CH_3OH (right) spectra with 12 MHz sweep bandwidth.

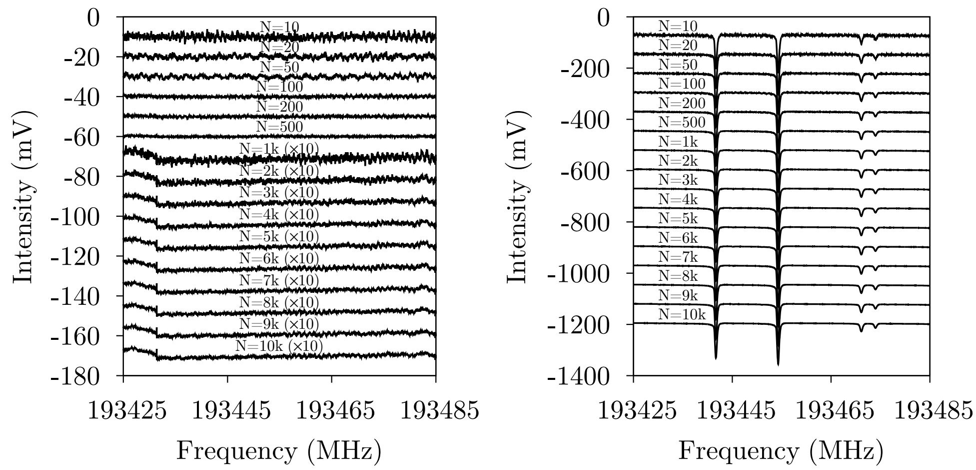

(b) Blank (left) and CH_3OH (right) spectra with 60 MHz sweep bandwidth.

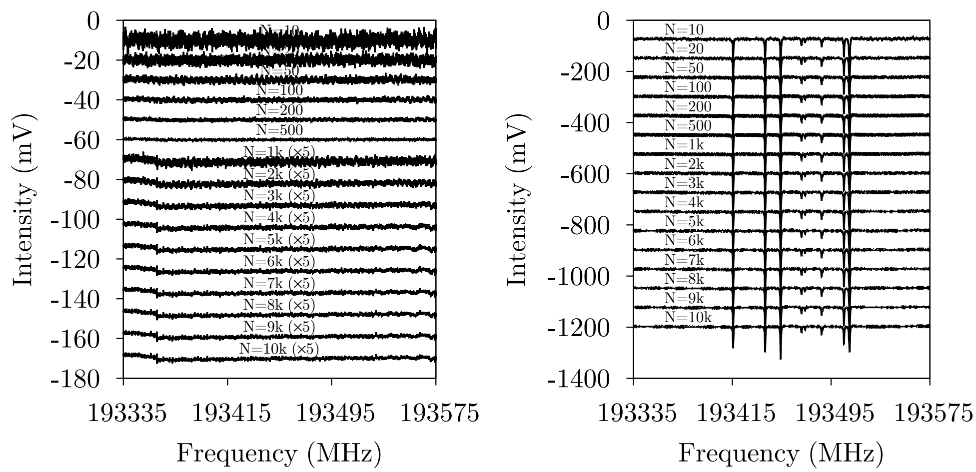

(c) Blank (left) and CH_3OH (right) spectra with 240 MHz sweep bandwidth.

Figure 2.10: Stacks of blank and CH_3OH spectra with increasing average numbers. The intensities of spectra above 1000 averages are multiplied by a factor of 10 for the 12 MHz and 60 MHz series, and a factor of 5 for the 240 MHz series.

the full spectrum is more severe than the one of the center part of the spectrum. The noise curve of the 240 MHz series also lies above the other two, in agreement with the visual conclusion drawn from Figure 2.10.

A least-square fit of the noise points with $N \leq 1000$ was used to verify the square root of N rule. The best fit equations for each sweep bandwidth are shown in the legend of Figure 2.11. The order on N agrees with the theoretical value of $-1/2$. The orders from the full spectra window deviate from $-1/2$ slightly more than the center part of the spectra, because of the impact of spectral impurity.

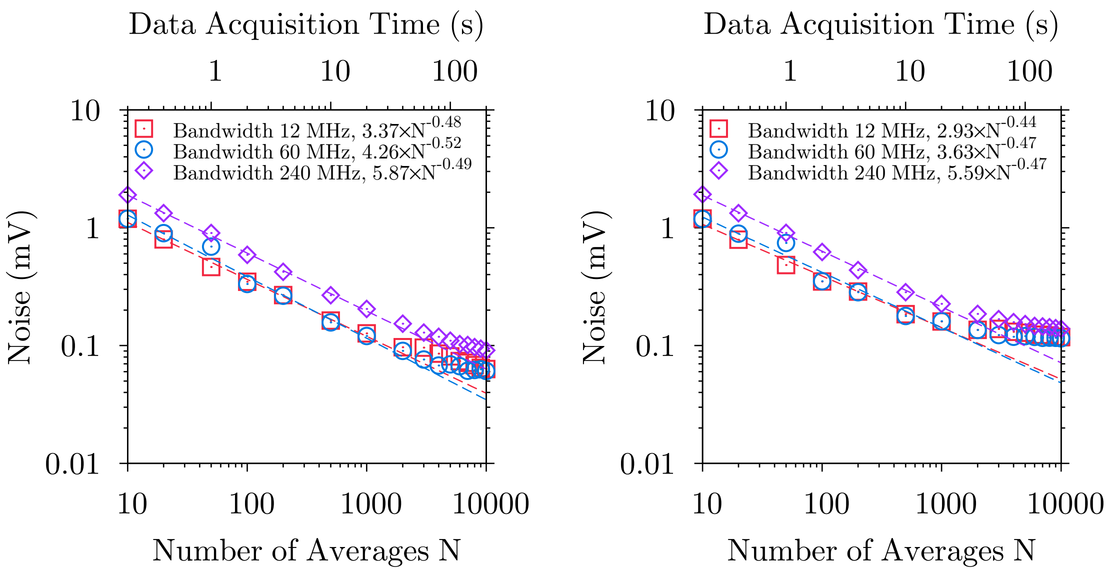

Figure 2.11: The noise level of blank sweeps with increasing number of averages at three sweep bandwidths: 12 MHz (red square), 60 MHz (blue circle), and 120 MHz (pink diamond). The noise level of the 1/6–5/6 section of the spectra is plotted on the left panel, while that of the full spectrum is plotted on the right panel.

For the molecular spectra, the increase of SnR with increasing spectral averages is also visible in Figure 2.10. The SnR is plotted in Figure 2.12. For all three sweep bandwidths, strong linearity to $\sqrt{N}$ is observed. The smallest sweep band, 12 MHz, shows the highest SnR, followed closely by the medium 60 MHz sweep. The SnR of the 240 MHz is significantly lower. This is consistent with the results from the blank spectra shown in Figure 2.11. The SnR of the 12 MHz and 60 MHz sweeps became similar at averages larger than 1000. Considering the data acquisition speed of the 60 MHz sweep is 5 times faster than the 12 MHz for a same frequency coverage, the slight sacrifice of the SnR seems reasonable. The SnR of the fast sweep spectra unambiguously beats the point-by-point direct absorption spectrum, but is slightly lower than the lock-in spectrum. Nevertheless, the frequency resolution of the sweep spectra is higher (12 kHz) than the lock-in scan (100 kHz). If the lock-in scan was set at the same frequency resolution and the bandwidth, it will take 2000 s, whereas the 60 MHz sweep only takes 200 s. A zoomed in spectral region is plotted on the right panel of Figure 2.12, from which the quality of the spectra is clearly seen. The spectral lines stand out more clearly in the 60 MHz sweep, owing to the fine frequency resolution, than in the lock-in spectrum, even though the statistical SnR of the 60 MHz sweep is slightly lower. The fine frequency resolution also offers room for down-sampling, which can improve the SnR slightly by a factor of 2, as shown in Figure 2.8.

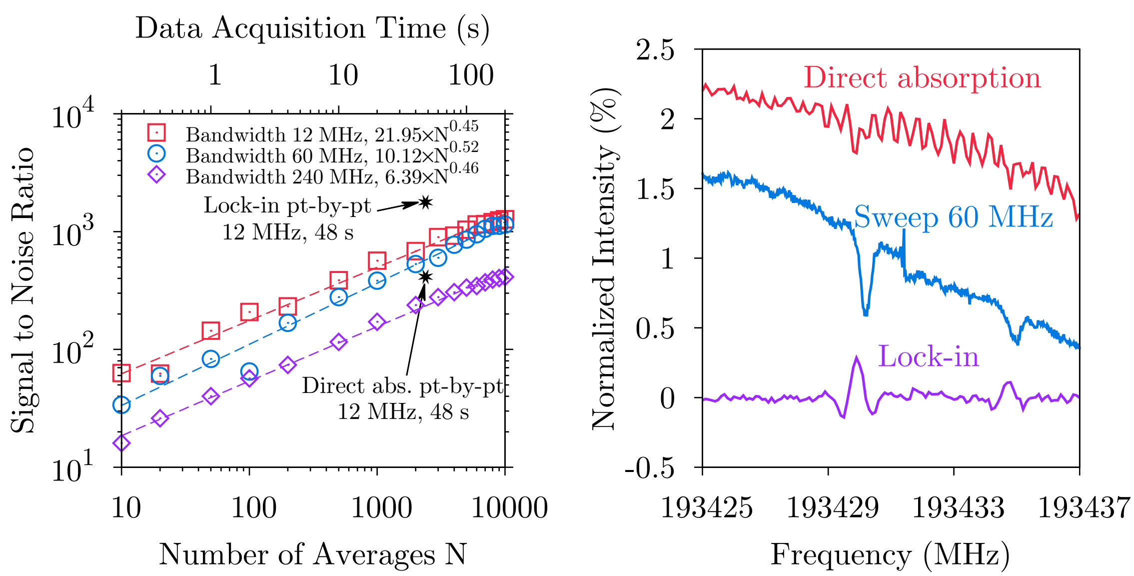

Figure 2.12: Signal to noise ratio (left panel) of the fast-sweep spectra as an increase of number of averages N, and the comparison to the SnR of the point-by-point lock-in and direct absorption scans, pointed by two stars. The right panel shows a zoomed-in region of the 60 MHz sweep with 10000 averages (200 s acquisition time), as well as two point-by-point scans (240 s acquisition time).

2.3.4 Concerns regarding radio frequency interference (RFI)

The radicals and ions studied in this dissertation were produced in a high-voltage plasma discharge on the throat of the supersonic expansion. Therefore, the applicability of the fast-sweep method to discharge experiments is crucial. There are a few concerns specifically applied to discharge experiments because of the additional interference from the pulsed high voltage field.

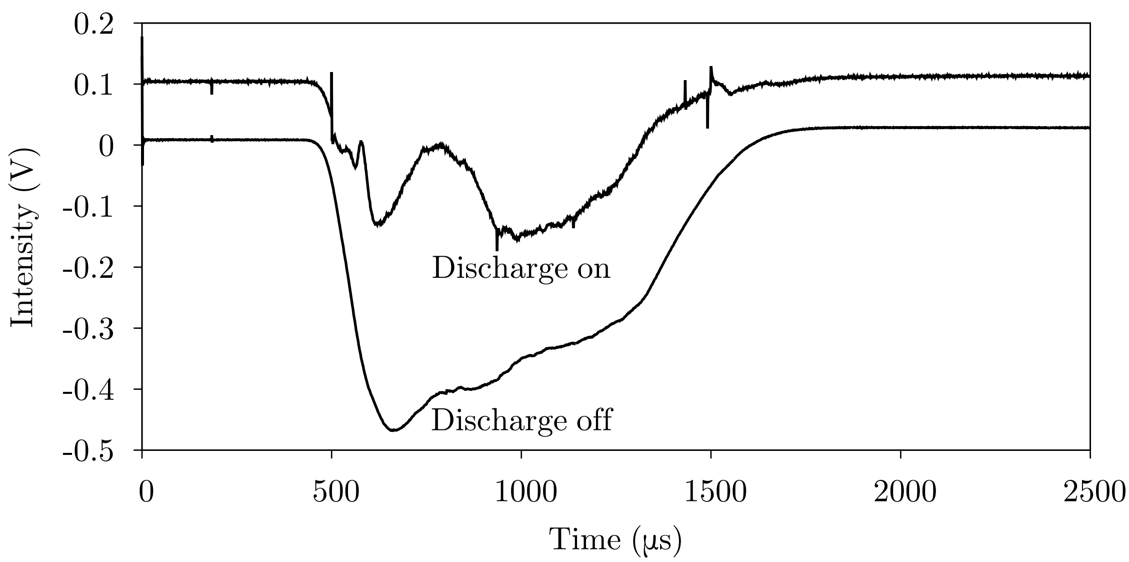

Figure 2.13: The discharge interference on the molecular signal, shown as multiple RFI spikes, and a change of the baseline and molecular absorption curve.

In a discharged experiment, RFI from the high voltage contaminates the signal. Figure 2.13 clearly shows multiple RFI spikes in addition to the ones from the solenoid valve. The curvature of the sweep is also strongly distorted by the high voltage plasma. The outcome is that the background subtraction in the fast-sweep method returns results of lower quality compared to the discharge-free experiments. In order to suppress this baseline as much as possible, we attempted to fit the baseline using a univariate spline interpolation method in the data processing. The use of this spline fit has pros and cons. While the spline fit can remove most of the curvature caused by the discharge RFI, the algorithm does not fully recognize spectral lines embedded in the noise except for the extremely strong ones. Therefore, spectral lines of weak to intermediate intensities also contributes in the spline fitting algorithm. The spectral contribution introduces baseline artifacts, and may cause the expected Gaussian absorption lineshape appear to be similar to a second-derivative lineshape.

2.4 Summary

This chapter discusses the spectrometer I used to produce and probe unstable molecules and molecular clusters. The spectrometer includes a Perry-style multipass millimeter–submillimeter cell, a supersonic expansion source, and a McCarthy-style discharge source. I specifically focused on the full performance test of the fast-sweep spectroscopic acquisition technique, which is able to facilitate the search for molecular transitions in the millimeter–submillimeter range. This fast-sweep technique is well-suited for spectral searches for unknown molecular transitions in a broad frequency range in the millimeter–submillimeter regime, and has a minimum impact on instrument investment.

This key technique, together with conventional point-by-point direct absorption and lock-in scan methods, was applied to all the molecules studied in this dissertation. In the next few chapters, I will show the success of this technique in the study of the HO_3 radical (Chapter 3) and the Ar–H_2O dimer (Chapter 4). The supersonic expansion source and the multipass optical arrangement were used throughout all experiments. Specific fast-sweep settings are described in the experimental section of each individual chapter.

Chapter 3 The Weakly Bound Radical: HO_3

This chapter, with minor adjustment, is reprinted with permission from L. Zou, B. M. Hays, S. L. Widicus Weaver, J. Phys. Chem. A. 120, 657 (2016). Copyright (2016) American Chemical Society.©

3.1 Introduction

Molecular oxygen has surprisingly only been detected in a few astronomical sources [37–41], despite the relatively large fractional elemental abundance of oxygen relative to hydrogen [42] in the universe. Identifying the carrier(s) of oxygen in dense molecular clouds encourages new reaction mechanisms to be proposed. Silicates, CO, and water ice are the major reservoirs of oxygen in these environments, but they do not fully explain the low observed molecular oxygen abundance in dense clouds [43]. Other possible oxygen reservoirs must be investigated. Here we explore whether weakly bound clusters could play important roles in the oxygen chemistry in interstellar clouds.

Strongly bound clusters, such as protonated molecular ions H_3^+, HCO^+, and N_2H^+, play central roles in both terrestrial and interstellar chemistry, and their existence has been unambiguously supported by astronomical observations [44]. Weakly bound clusters such as HO_3, however, are important reaction intermediates in terrestrial chemistry, but they have been discounted as important intermediates in interstellar chemistry because the low densities in interstellar clouds do not favor their formation. Nonetheless, the question of their possible existence in interstellar clouds is intriguing. Indeed, if a three-body collision is required to form such a cluster, as is typical under terrestrial conditions, such a reaction is unlikely in interstellar environments. Nevertheless, Klemperer and Vaida [44] suggest that weakly bound clusters whose binding energy is ∼5 kcal·mol^{-1} are still possible interstellar species because they can form via radiative association reactions, which are common in interstellar environments. In addition to radiative association in the gas phase, weakly bound clusters could also possibly form on interstellar or protoplanetary ices. Specifically for HO_3, experiments have shown that it can be produced in cold water ice rich in O_2 under proton [45] or electron [46] bombardment. The latest experimental upper limit of HO_3 binding energy is 3 kcal·mol^{-1} [47], whereas the theoretical estimation lies between 1.8 kcal·mol^{-1} [48] and 2.8 kcal·mol^{-1} [49]. HO_3 may therefore be produced within and survive the sublimation of interstellar ices below 100 K. If detected, clusters such as HO_3 could dramatically change our current understanding of the roles of three-body collisions, radiative association reactions, and sublimation in astrochemistry.

The identification of HO_3 via its rotational transitions cannot be achieved without supporting laboratory measurements. We focus here on the millimeter–submillimeter spectrum of HO_3. Although rotational spectra of *trans*-HO_3 are available in the microwave range [50], extrapolation to the millimeter–submillimeter wavelength range may be subject to large uncertainties. Therefore, our experimental measurements of HO_3 transitions at these wavelengths will aid in the search for this cluster in space. Once the HO_3 rotational spectrum is measured, we can apply similar techniques to examine other clusters of astrochemical interest.

In addition to its possible importance in astrochemistry, HO_3 is also of great interest in atmospheric chemistry and theoretical chemistry. It is a challenging target in both experimental and computational studies. In experimental studies, its potential role in shaping the HO_x cycle that controls the atmospheric O_2 budget was proposed (see Murray et al. [51] and references therein) but then discarded based on more accurate experimental results [47]. In computational studies, HO_3 is a sensitive benchmark for theoretical methods as its experimentally measured properties can rarely be simultaneously reproduced by a single theoretical method.

The experimental measurement of the dissociation energy of HO_3 determines its importance in atmospheric chemistry. The value 10(5) kcal·mol^{-1} determined from proton and electron transfer experiments [52, 53] was unreliable due to large experimental uncertainty and large discrepancy from theoretical calculations. From infrared–UV action spectroscopy, Derro *et al.* estimated the upper limit of the dissociation energy of HO_3 to be 5.32 kcal·mol^{-1}, by measuring the maximum energy of dissociated OH [54]. Le Picard *et al.* further refined the upper limit of the HO_3 dissociation energy to be 2.97(7) kcal·mol^{-1} [47], which was derived from a kinetics model based on laser-induced fluorescence (LIF) decay measurements of OH at various temperatures and O_2 concentrations. Therefore, the originally postulated contribution of HO_3 to atmospheric OH depletion was discarded.

Spectroscopic studies of HO_3 have been primarily conducted in the infrared. Early spectroscopic investigations of HO_3 after its first detection in mass spectrometry [55] include infrared experiments in an Ar matrix [56] and water ice [45, 46]. Rotationally resolved infrared spectra were first obtained by infrared-UV action spectroscopy in a supersonic jet [54, 57–59], where an infrared laser was used to pump the radical, while the dissociation product OH was probed via LIF from its UV excitation. Several rotationally resolved bands were unambiguously assigned to *trans*-HO_3 [54]. Vibrational bands of *trans*-DO_3 were also measured [54, 59].

Additional rotational spectroscopic studies using Fourier Transform Microwave (FTMW) Spectroscopy have shown that HO_3 possesses an extremely long center O–O bond [50, 60]. In these experiments, HO_3 was also formed in a pulsed discharge supersonic expansion comprised of a mixture of O_2 and water vapor or H_2 diluted in Ar. HO_3 and DO_3 were measured by Suma *et al.,* and spectra of its three ^{18}O isotopologues were measured by McCarthy *et al.,* who also reported a more efficient discharge production mechanism of HO_3 using H_2 instead of H_2O as a precursor.

Transitions for HO_3 were measured up to 80 GHz. Empirical structural information for *trans*-HO_3 was derived from the experimental rotational constants of the five isotopologues retrieved from the microwave spectra, by assuming a planar geometry [60]. The empirical center O–O bond was much longer (1.684 Å) than a normal O–O single bond (e.g., 1.474 Å in HOOH), while the O–H bond was much shorter (0.913 Å) than that in free OH (0.970 Å). As the authors pointed out, however, the empirical bond length r_0 is not directly comparable to the theoretical equilibrium value r_e, due to the effect of the vibrational wavefunction in the ground state. A recent dipole moment measurement for *trans*-HO_3 in a He nanodroplet further illustrated the large discrepancy between theoretical calculated properties with experimental measurements, as well as the sensitive dependence of the radical's property on its geometry estimation [61].

It is worthwhile to mention that the existence of *cis*-HO_3 is perplexing. Broad infrared bands containing no rotational structure were tentatively assigned to the *cis*-conformer [54, 57–59], but the validity of this assignment is questionable because both microwave studies claimed no detection of *cis*-HO_3 after careful searches [50, 60]. As Raston *et al.* suggested based on their He nanodroplet study, it is possible that there is only one vibrationally averaged structure of HO_3, and the broad infrared band arises from HO_3–$(O_2)_n$ complexes [62].

Along with these experimental efforts, theoretical calculations have been extensively conducted to reproduce the experimentally measured molecular geometry and dissociation energy, to construct the potential energy surface, and to analyze the dissociation channels of HO_3 [48, 49, 63–74]. Despite this fact, none of these studies can thus far simultaneously reproduce every experimentally measured aspect of this radical. This is not only due to the complexity of the HO_3 system itself, but also to the difficulty of direct comparison of theoretical results with experimental values. The comparison of geometry, dipole moment, and dissociation energy for the ground vibrational state of HO_3 relies greatly on the estimation of the anharmonic multidimensional potential energy surface as well as the vibrational–rotational interaction. For example, the torsional potential between the *trans* and *cis* conformer (if it does exist) of HO_3 largely determines the form of the rovibronic wavefunctions. The torsional barrier is estimated to be $\sim$340 cm^{-1}, based on the infrared-UV action spectroscopy results [54]. A more recent six-dimensional potential energy surface [48] showed strong coupling between multiple vibrational modes, which all have impact on the estimation of the difference between the theoretical equilibrium geometry and the empirical geometry. Much theoretical and experimental work remains to fully understand the HO_3 system.

In this dissertation, I report the measurement of pure rotational spectra of HO_3 and DO_3 from 70 GHz to 450 GHz. These new measurements were obtained using the aid of the fast-sweep technique described in Section 2.3. The measurements access more K_a levels than the microwave studies, thus providing sufficient information to empirically fit all quartic centrifugal distortion constants of HO_3 using a standard asymmetric top Hamiltonian. In addition to the observed HO_3 and DO_3 transitions, we found numerous lines arising from Ar–H_2O and other unidentified carrier(s). The spectral analysis of Ar–H_2O is described later in Chapter 4. The comparison of these experimental results with observational spectra to search for HO_3 in 32 star-forming regions is described in Section 6.6.

3.2 Experimental details

The overall experimental design has been described in Chapter 2, thus only specific conditions for producing the HO_3 radical are listed here.

The jet-cooled HO_3 radical was produced in our high-voltage discharge source (see Section 2.1.2) by discharging a gas mixture of O_2, H_2, and Ar (NexAir, ultrahigh purity). The seeding gases O_2 and H_2 were pre-mixed at a flow ratio of 3:2, and then diluted to 10% in Ar before being sent into the Parker Series 9 general valve. The valve operated at a repetition rate between 20 and 25 Hz with ∼1 ms opening time, which led to a total gas flow rate of 700–850 sccm and an equilibrium chamber pressure of ∼50 mTorr. The gas mixture was held at a stagnation pressure of 90 psig (720 kPa). The discharge source used two copper electrodes separated 0.2″ (4.8 mm) apart by Teflon washers. Additional Teflon spacers were used to fill the rest of the empty space in the Teflon cap of the discharge source. The gas channel was 0.1″ (2.5 mm) in diameter. A 900 V pulsed discharge was applied using a pulse generator (Directed Energy Inc., PVX-4150) backed by a high voltage power supply (Spellman, SL2PN2000). The voltage rose simultaneously with the pulsed valve trigger signal and lasted for 2.2–2.5 ms, and the current was constrained by a 10 kΩ ballast resistor. All pulses were triggered using a standard 5 V TTL output from a four-channel delay generator (Stanford Research Systems, DG645). DO_3 was produced under identical conditions, by using D_2 (Cambridge Isotopes Laboratories, 99.8% D_2 , 0.2% HD) in place of H_2.

The fast-sweep technique (see Section 2.3) was used to search for the millimeter transitions of HO_3. The triangle-wave modulation for the fast-sweep was set at 1 kHz with a RF deviation of ±1 MHz. Initial searches aimed at 1 GHz windows around the extrapolated frequencies from published microwave data [50]. Broader spectral windows were scanned after the discovery of new spectral features other than HO_3. Once the HO_3 transitions were located in the fast-sweep spectrum, point-by-point scans using a lock-in amplifier was used to verify the presence of these transitions, and to retrieve their line center frequencies. The DO_3 spectrum was collected using the same strategy. In general, 500 shots were averaged for the fast-sweep spectra, whereas 100 scans were averaged for the lock-in spectra. More averages were taken for a few weak lines to increase the SnR.

3.3 Results

3.3.1 HO_3 and DO_3 detection

The detection of HO_3 below 170 GHz was straightforward based on the extrapolation of transition frequencies from previous microwave studies [50, 60], once the discharge and gas mixture conditions were optimized for HO_3 production. The observed experimental transitions agree with the microwave extrapolation. The spectral search above 170 GHz was more difficult because of the large frequency disagreements between the extrapolation and experimental line centers. With the assistance of the fast-sweep technique, which allowed efficient search for these HO_3 transitions in a large frequency window, large frequency shifts from the extrapolation were observed. For transitions from 170 GHz to 320 GHz, the shift was $\sim$35 MHz, while for transitions above 320 GHz, the shift was $\sim$170 MHz. Sample spectra from the fast-sweep experiment are shown in Figure 3.1.

Each new transition observed in the fast-sweep scans was confirmed using a lock-in scan and then fitted by a second derivative Gaussian function to retrieve its transition frequency. Additionally, weaker HO_3 transitions that were ambiguous in the fast-sweep data were sought using the lock-in detection. A total of 38 new lines for HO_3 with 118 resolved hyperfine components were measured in the range of 70 GHz to 450 GHz. The highest J level observed was $J = 7$. The top panel of Figure 3.2 plots a computer generated stick spectrum showing all newly measured transitions of HO_3. The heights of the sticks are proportional to the integrated intensities of measured spectral lines, which are derived from the second-derivative Gaussian fit. DO_3 transitions were also measured using the same procedure. A total of 44 new lines were recorded. Unfortunately, because of the heavier nuclear mass of deuterium, the hyperfine splitting of most lines was not resolved, except for the partially resolved $2_{2,1} \leftarrow 2_{1,2}$ transition. The full stick spectrum of DO_3 is plotted in the bottom panel of

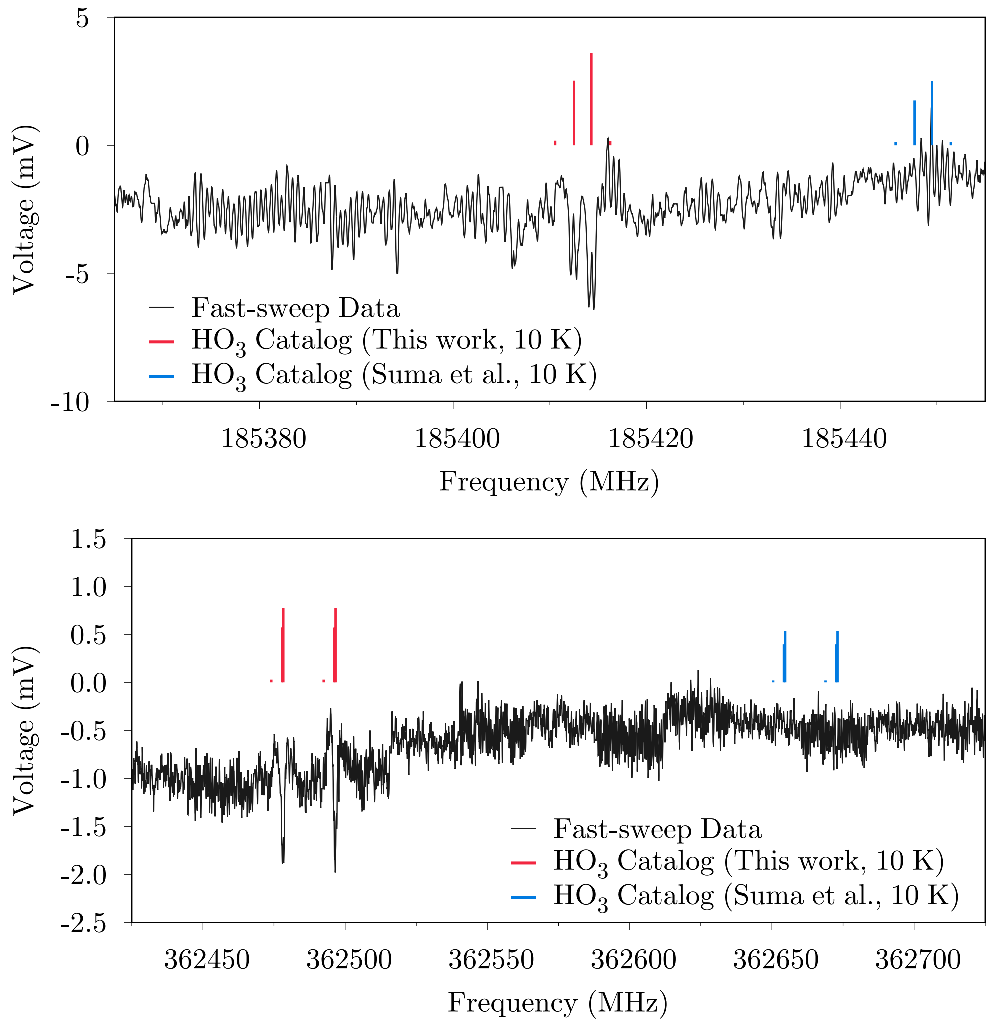

Figure 3.1: Fast-sweep detection of HO_3 at 185 GHz and 362 GHz. The spectral extrapolation from the previous microwave study is shown in blue, while the prediction based on the current study is shown in red. Simulations were generated at 10 K rotational temperature using reported molecular constants.

Figure 3.2. A scaling factor based on the lock-in amplifier sensitivity was considered for DO_3, but not HO_3. Since the experimental condition details varied day by day, the power fluctuation due to the standing waves in the spectrometer was difficult to calibrate. Therefore, no further power normalization was applied.

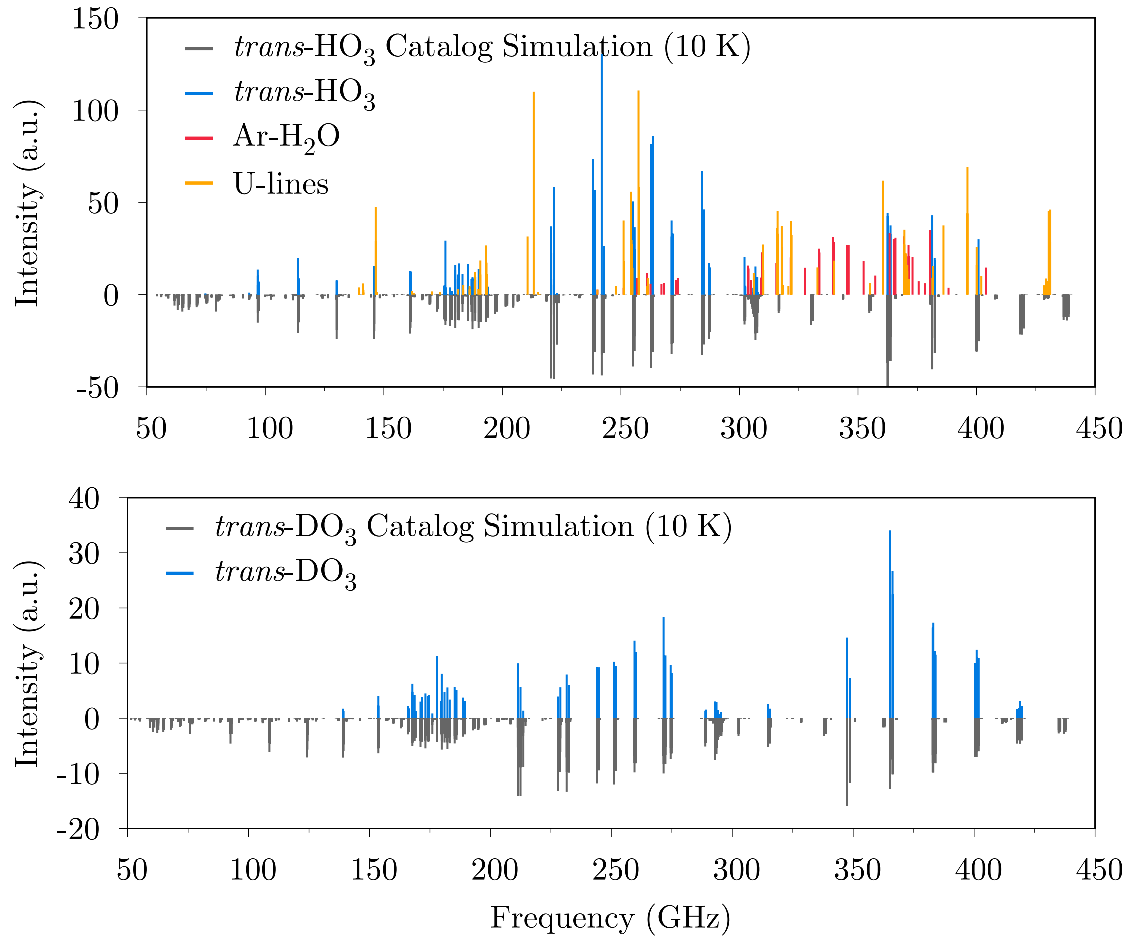

Figure 3.2: Stick spectra of all new measured HO_3 and DO_3 transitions. Transitions identified to be Ar-H_2O and unidentified lines are also included. Intensities are proportional to the integrated intensities of measured transitions and are calibrated for the sensitivity level of the lock-in amplifier for DO_3, but not HO_3. No power normalization was applied.

The molecular constants of HO_3 and DO_3 were fitted using the SPFIT program in the CALPGM suite [75]. We used a Watson-A reduced Hamiltonian that includes centrifugal distortion, spin-rotation interaction and associated centrifugal distortion, magnetic dipole-dipole hyperfine splitting, and electric quadrupole hyperfine splitting for deuterium. The hyperfine tensor element T_{cc} was fixed at $-T_{aa} - T_{bb}$, while χ_{cc} was fixed at $-\chi_{aa} - \chi_{bb}$ to ensure the traceless property of the T and χ matrices. For unresolved HO_3 hyperfine structure, the same center frequency was assigned to the two strongest hyperfine components. For DO_3, the strongest three hyperfine components were assigned to the same frequency. The transitions reported by Suma *et al.* [50] in the microwave range were also included in the fit. We assumed a uniform 5 kHz frequency uncertainty for the microwave data from Suma *et al.*, and a uniform 50 kHz frequency uncertainty for the data from this study based on the spectral resolution. The root-mean-square (rms) of the fit is 50 kHz for HO_3 and 51 kHz for DO_3, both of which agree well with the frequency uncertainty in this work. The molecular constants from this fit are compared to the previous results in Tables 3.1 and 3.2, for HO_3 and DO_3, respectively. The final fit files with complete spectral assignments for HO_3 and DO_3 are included in Appendix B.

Using the new spectroscopic constants determined in Table 3.1 and 3.2, we updated the HO_3 and DO_3 spectral predictions using the SPCAT program in the CALPGM suite [75]. For these predictions, the a and b components of the electric dipole moment were set at the experimental values of $\mu_a = 0.61$ D, $\mu_b = 1.48$ D for *trans*-HO_3, and $\mu_a = 0.62$ D, $\mu_b = 1.52$ D for *trans*-DO_3 [61]. These new spectral catalogs were used to simulate spectra assuming a rotational temperature of 10 K for comparison to the experimentally measured spectra, shown in Figure 3.1 and 3.2. The HO_3 catalog was also used to compare with astronomical observations, which will be discussed in more detail below.

3.3.2 New spectral features

Along with the detection of HO_3, we also found a set of new discharge-dependent spectral features using the fast-sweep technique. Follow-up lock-in detections were also conducted to confirm the discovery of new spectral lines. These lines are also

Table 3.1: Comparison of the spectroscopic parameters of *trans*-HO_3 from this study and the results from Suma *et al.* [50]. 1σ uncertainties in the unit of the last significant digit are included in parentheses.

Constants (MHz)	This Study	Suma *et al.* [50]	Difference
A_0	70781.11869(136)	70778.1652(24)	2.9535(28)
B_0	9987.3873(61)	9986.9501(11)	0.4372(62)
C_0	8749.7284(59)	8750.1580(11)	-0.4296(60)
$\Delta_N \times 10^3$	47.5200(223)	46.461(30)	1.059(37)
Δ_{NK}	0.149167(123)	0.15335(40)	-0.00418(42)
Δ_K	2.956094(237)	–	–
$\delta_N \times 10^3$	6.1406(116)	6.11(41)	0.031(43)
δ_K	0.21649(298)	–	–
ϵ_{aa}	-1252.6932(42)	-1252.5858(58)	-0.1074(72)
ϵ_{bb}	-106.25192(198)	-106.2551(26)	-0.0032(33)
ϵ_{cc}	-3.49564(187)	-3.4954(24)	-0.0002(30)
$\lvert\epsilon_{ab} + \epsilon_{ba}\rvert/2$	42.503(80)	42.45(11)	0.05(14)
a_F	3.66102(240)	3.6587(30)	0.0023(38)
T_{aa}	8.4792(46)	8.4828(59)	-0.0036(75)
T_{bb}	-6.8512(45)	-6.8533(56)	0.0021(72)
$\Delta_N^S \times 10^3$	0.987(75)	1.00(10)	-0.01(12)
Δ_{NK}^S	0.05626(85)	0.0544(15)	0.018(17)
Δ_K^S	0.10421(179)	–	–
Δ[a]	0.0176	0.0123	0.0053
fitted transitions	180	62	
rms (kHz)	50	5.4	

[a] Inertial defect (amu·Å^2)

Table 3.2: Comparison of the spectroscopic parameters of *trans*-DO_3 from this study and the results from Suma *et al.* [50]. 1σ uncertainties in the unit of the last significant digit are included in parentheses.

Constants (MHz)	This Study	Suma *et al.* [50]	Difference
A_0	67859.76412(114)	67857.3708(30)	2.3933(32)
B_0	9448.9011(46)	9448.5330(13)	0.3681(48)
C_0	8299.0882(45)	8299.4517(13)	-0.3635(47)
$\Delta_N \times 10^3$	37.3937(159)	36.573(37)	0.821(40)
Δ_{NK}	0.181509(111)	0.18544(51)	-0.00393(52)
Δ_K	2.394778(270)	–	–
$\delta_N \times 10^3$	4.5481(87)	4.566(49)	-0.018(50)
δ_K	0.18323(228)	–	–
ϵ_{aa}	-1224.7306(40)	-1224.611(80)	-0.120(80)
ϵ_{bb}	-101.53380(183)	-101.5335(32)	-0.0003(37)
ϵ_{cc}	-3.78785(174)	-3.7870(30)	0.0008(35)
$\lvert\epsilon_{ab} + \epsilon_{ba}\rvert/2$	41.154(74)	41.25(13)	-0.10(15)
a_F	0.46216(161)	0.4607(28)	0.0015(32)
T_{aa}	1.2970(32)	1.2972(55)	-0.0002(64)
T_{bb}	-1.08913(277)	-1.0893(47)	0.0002(55)
$\Delta_N^S \times 10^3$	0.788(64)	0.71(11)	0.08(13)
Δ_{NK}^S	0.04933(74)	0.0451(19)	0.0042(20)
Δ_K^S	0.10804(216)	–	–
χ_{aa}	0.0126(44)	-0.0042(78)	0.0168(90)
χ_{bb}	0.1556(48)	0.1376(74)	0.0180(88)
Δ[a]	-0.0372	-0.0422	0.0050
fitted transitions	153	74	
rms (kHz)	51	7.6	

[a] Inertial defect (amu·Å^2)

plotted in Figure 3.2 along with the HO_3 lines. One of the molecular carriers was identified to be the Ar–H_2O dimer; these lines, marked in purple in Figure 3.2, disappeared with substitution of He buffer gas in place of Ar. Ar–H_2O, however, does not fully explain all of the unidentified lines measured in this experiment. Additional analysis is required before the carrier(s) of these lines is identified. The full characterization of the Ar–H_2O spectrum is included in Chapter 4.

3.4 Discussion

The search for HO_3 transitions above 170 GHz was complicated due to the large frequency shifts relative to the extrapolation from the previous microwave work. The fast-sweep technique eased the search problem as it could cover a $\geq$1 GHz wide spectral range in less than an hour. The large shifts between the measured spectra and the extrapolation from microwave studies are primarily caused by the lack of inclusion of certain quartic centrifugal distortion constants in the analysis of the microwave spectra. This finding is supported by the terms listed in Table 3.1 and 3.2, where most of the spin-orbit interaction, magnetic dipole hyperfine interaction, and electric quadrupole hyperfine interaction terms remain unchanged within their respective statistical uncertainties. In the previous microwave studies, only $K_a = 1 \leftarrow 0$ transitions were detected, leading to the undetermined centrifugal distortion constants Δ_K and δ_K. Once higher K_a levels were accessed, these centrifugal distortion constants could be added in the spectral analysis. As shown in Table 3.1 and 3.2, the centrifugal distortion constants associated with the angular momentum operators on the primary axis $\hat{N}_a$, namely Δ_{NK}, Δ_K, δ_K, Δ^S_{NK} and Δ^S_K, are now well defined. The inclusion of these additional centrifugal distortion constants also led to significant changes in the rotational constants A, B and C, especially the A constant, from the values reported in previous studies. The compensation of the contribution to the energy levels of HO_3 from the centrifugal distortion constants over the rotational constants may be responsible for this large discrepancy. As expected, the change of the rotational constants also leads to a change in the inertial defect, but only by a small amount.

The centrifugal distortion constants Δ_K and δ_K are significantly larger compared to the other centrifugal distortion constants Δ_N, Δ_{NK} and δ_N. This result indicates the large dependency of the HO_3 geometry on the projection of its rotational angular momentum along its principle axis. A similar trend was observed in the *trans*-HOCO radical [76], though the C–O bond in HOCO was found to be much shorter than the O–O bond in HO_3. These large values for Δ_K and δ_K may provide additional benchmarks for theoretical calculations of the geometry and multi-dimensional potential energy surface for HO_3, since the distortion tensor relies on the estimation of the moment of inertia gradient and the force field.

The behavior of DO_3 is similar to that of HO_3. Because of the heavier deuterium nucleus, the shift of DO_3 constants in this work from the previous study is systematically smaller than the shift of HO_3 constants.

In addition to the interesting results for HO_3 and DO_3, additional spectral lines were observed for other species produced in the discharge. In the previous study by McCarthy *et al.,* OH, H_2O–OH, H_2O–O_2, $(H_2O)_2$ and O_3 were also detected [60] using similar discharge conditions to those used in our experiment. Our experiment is consistent with the previous results, as we saw strong transitions from HO_2, H_2O_2, O_3, H_2O, O_2 (both $^3\Sigma$ and $^1\Delta$), and Ar–H_2O dimer. The spectral features of these known species were excluded from the analysis of HO_3 spectrum, and are not plotted in Figure 3.2 (except for Ar–H_2O). In particular, the presence of Ar–H_2O was confirmed by a comparison with the spectra of a water and Ar mixture. The Ar–H_2O vibrational-rotational-tunneling spectra have been studied previously [77–81]. Unfortunately, no experimental data were available in the frequency range of this experiment. We therefore measured the Ar–H_2O spectra separately to clean up the list of unidentified lines in our HO_3 spectra. The details of the Ar–H_2O spectra are included in Chapter 4.

Despite the prevalence of Ar–H_2O lines in the spectrum, this dimer can only partially reproduce the unidentified lines shown in Figure 3.2. Consequently, it is likely that at least one additional species was created in the discharge. These spectral lines persisted when Ar was replaced by He, but also remained in a discharge with only H_2 and O_2 as precursors. As such, the carrier is not an Ar cluster nor a He cluster. The splitting pattern of these unidentified lines indicates an open-shell species. Future work will focus on determining the identity of this new species. Meanwhile, this new finding illustrates the capacity of the fast-sweep technique. Since this technique allows scanning for tens of GHz in a day under normal experimental conditions, it makes blind searches feasible even without any spectroscopic prediction. This opens up the possibility of discovering new spectral features in the millimeter-submillimeter range, which could not be done easily before with the conventional point-by-point spectral acquisition technique.

3.5 Summary

In this chapter, we have presented the measurement of the pure rotational transitions of HO_3 and DO_3 in the 70–450 GHz frequency range. A large discrepancy was found between these new experimental measurements and the spectral extrapolation from previous FTMW studies [50, 60]. This discrepancy was fully explained by the inclusion of a full list of quartic centrifugal distortion constants in the Hamiltonian. Molecular constants were fitted using the new experimental results and were used to generate a more reliable submillimeter spectral extrapolation for these two radicals. The updated spectral line catalogs based on new experimental measurements presented here are expected to guide astronomical searches in sources that have high expected abundances of HO_3.

Chapter 4 The Vibration-Rotation-Tunneling Spectrum of Ar–H_2O

This chapter, with minor adjustment, is reprinted with permission from L. Zou and S. L. Widicus Weaver, J. Mol. Spectrosc., 324, 12 (2016).

4.1 Introduction

The intermolecular interaction of van der Waals complexes is crucial to our understanding of the behavior of these complexes, and can be used to simulate the properties of larger systems such as bulk liquids and solvent-solute interaction [82]. Rich information on the intermolecular potential can be deduced from spectroscopic measurement of these complexes [83]. However, the complexity of the vibration-rotation-tunneling (VRT) spectrum arising from the anisotropic intermolecular potential of these complexes is a challenge even for a small dimer system.

Van der Waals complexes can be categorized into the semi-rigid regime or the free-rotor regime based on the barrier height of the intermolecular potential. In the semi-rigid regime, the intermolecular potential is high and the complex can be treated as a whole body with well-defined rotational constants. In the free-rotor regime, on the contrary, one monomer in the complex experiences a low intermolecular potential barrier, and thus rotates almost freely. The effect of the anisotropic intermolecular potential is reflected by the shift and split of rovibrational energy levels of the monomer.

Ar–H_2O dimer is one of the simplest atomic–asymmetric rotor dimers. Nevertheless, its spectrum is complicated. The first two reported VRT bands of Ar–H_2O (0.5–0.8 THz) were assigned by Cohen and coworkers based on a semi-rigid model [77].

The utility of this model was later depreciated after more bands were found both in the far-IR region (1–2 THz) [78, 79] and mid-IR region around the v_3 band (3780 cm^{-1}) [84, 85] and v_2 band (1620 cm^{-1}) [84, 86–88] of H_2O. The free-rotor model proposed by Hutson [89] was adopted to assign these bands with success, supporting the fact that the water moiety almost freely rotates. In addition to the Ar–H_2O bands, detection of Ar–D_2O bands in the millimeter region (280–460 GHz) [90] and around multiple H_2O vibration modes, $v_1 + v_2 + v_3$ (6536 cm^{-1}) [91] and v_2 (1190 cm^{-1}) [92, 93], also supports this dimer being in the free-rotor limit, assuming the intermolecular potential of Ar–D_2O is similar to that of Ar–H_2O. Several transitions were also observed in the microwave range where hyperfine structures were resolved [80, 81]. Combining all of these spectroscopic measurements from the microwave, far-IR, and IR regions, Cohen & Saykally fitted an accurate empirical 3-dimensional potential surface for Ar–H_2O [94].

Here we report the detection of three additional Ar–H_2O bands in the millimeter region. This dataset is complementary to the spectra from Cohen *et al.* [77]. An energy diagram for Ar–H_2O in the range of this experiment is shown in Figure 4.1, highlighting the bands observed by Cohen *et al.* and the bands detected in the present work. We also re-measured the bands reported by Cohen *et al.* with higher frequency resolution. Most importantly, to our knowledge, this is the first direct observation of the band origin of the $\Pi(1_{01}) \leftarrow \Sigma(1_{01})$ transitions, the value of which could only be indirectly determined from the difference of other infrared band origins [84]. These new measurements support the free-rotor model of Ar–H_2O, and allow us to determine the band heads with higher accuracy. We present these measurements and the associated analysis herein.

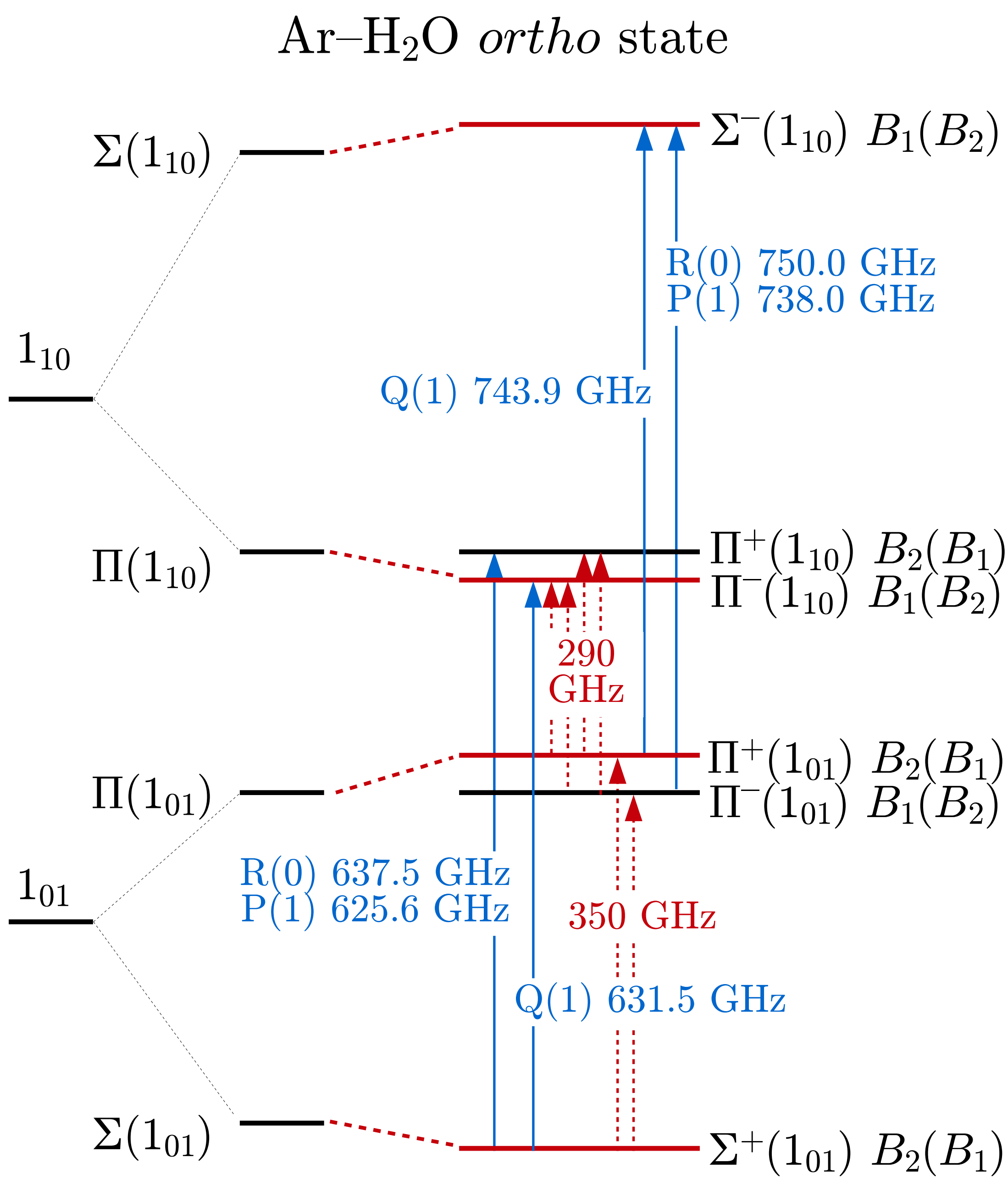

Figure 4.1: Ar–H_2O energy diagram in the 1_{01} and 1_{10} states region. Red arrows represent the bands detected in the present work. Blue arrows represent the bands reported by Cohen *et al.* [77]. These bands are also remeasured in the present work with higher frequency resolution. Band heads are labeled with their approximate transition frequencies. The relative position of these levels is only a qualitative approximation and does not accurately reflect the actual energy differences between states. Reprinted with permission from Zou & Widicus Weaver [95].

4.2 Experimental details

The Ar–H_2O spectrum was measured in a jet-cooled expansion using the millimeter–submillimeter spectrometer described in Chapter 2. This complex was detected during an experiment designed for probing HO_3, the details of which were reported previously [27] and can also be found in Chapter 3. This follow-up study measuring the spectrum of Ar–H_2O was conducted to confirm the presence of Ar–H_2O in the HO_3 spectrum.

The dimer was readily produced by expanding water vapor in Ar gas (NexAir, UHP) under ambient temperature into the vacuum. The Ar was bubbled through tap water, which was used without further purification. The backing pressure behind the valve was held at 24 psig (2.0 kTorr). The pulsed valve (Parker Series 9) was driven by a 0.8 ms TTL voltage repeated at a rate of 40 Hz for fast-sweep and 42 Hz for direct absorption.

Millimeter-submillimeter light was generated by passing cm-wave radiation (generated using an Agilent Technology E8257D PSG) through a frequency multiplier chain system (Viginia Diodes Inc., S197(c)). The spectrum of Ar–H_2O was initially searched using the fast-sweep method, and then confirmed using the direct absorption scheme. In both cases, the InSb hot electron bolometer (QMC Ltd., QFT/XBI) was used to detect the signal, which was recorded digitally via a digitizer card (National Instruments, PCI-5124). In the fast-sweep search scheme, the triangle wave modulation was set at 1 kHz with a RF deviation of ± 1 MHz. 100–200 spectral averages were taken. In the direct absorption confirmation scheme, the bolometer signal was directly integrated over the valve opening time as a function of the millimeter-submillimeter light frequency. Integrated intensity of the observed lines was then fitted to a Gaussian line shape. We estimated the uncertainty of the measured frequencies to be 0.1 MHz based on the Doppler width and the slight asymmetry of the line shape that was observed.

The power level at each transition frequency was also measured for the purpose of power normalization. It was achieved by recording the sine waveform of a ± 5 % depth amplitude modulation signal at these frequencies. These power measurements were recorded during the same run of the experiment to minimize power fluctuations. A sine function was fitted to the waveform and the fitted amplitude was interpreted to be 10 % of the power level, assuming a linear correlation between the modulation depth and the radiation power. Power normalization was applied to the integrated intensity of measured spectral lines so that transition intensities were qualitatively comparable.

Other works reported that a slit expansion source may be optimal for dimer yield [77, 84, 88, 90, 92]. Nonetheless, we found the pinhole source that had been optimized for HO_3 production [27] yielded sufficiently strong signal for the unambiguous detection of Ar–H_2O.

4.3 Model

The details of the model for Ar–H_2O have been thoroughly discussed in previous works [79, 89, 90], thus the details are not repeated here. Briefly, since the H_2O moiety in Ar–H_2O rotates nearly freely, it is possible to separate the Hamiltonian of the complex from the Hamiltonian of the H_2O monomer. The Hamiltonian of the monomer is then a standard Watson-A type Hamiltonian, and the Hamiltonian of the complex is in the form for a diatomic rotor. The rotational states are labeled with lowercase j_{k_a,k_c} for the monomer, and capital J and Ω for the complex. The presence of the anisotropic potential arising from the Ar atom splits the rotational states of H_2O into their projections Ω on the monomer–Ar axis. Analogous to the l-doubling in linear molecules, $|\Omega| = 0, 1, 2, \ldots$ are labeled as $\Sigma, \Pi, \Delta, \ldots$ states, respectively. Coriolis interaction further mixes the states of the complex of the same symmetry and H_2O rotational quantum number.

Because of the challenges in developing an effective model for Ar–H_2O, the Hamiltonian and notations used to describe the dimer are not consistent in the literature. In this paper, we chose to follow the model of Cohen & Saykally [79] to enable direct comparison with their results. Therefore, the rigid rotor energy of the complex is expressed as

$$E = v+B\big[J(J+1)-2\Omega^2\big]-D\big[J(J+1)-2\Omega^2\big]^2+H\big[J(J+1)-2\Omega^2\big]^3+L\big[J(J+1)-2\Omega^2\big]^4 \tag{4.1}$$

where v is the band head of each water state that is treated as an independent vibrational state. The Coriolis splitting on related energy levels is found by the perturbation matrix

$$\begin{bmatrix} E_1 & H_{\mathrm{Cor}} \\ H_{\mathrm{Cor}} & E_2 \end{bmatrix} \tag{4.2}$$

where $H_{\mathrm{Cor}} = 2\beta\sqrt{J(J+1)}$ is the Coriolis perturbation Hamiltonian for $j = 1$ states, and E_1 and E_2 (assuming $E_1 < E_2$) are the vibrational energies of two connected states. The shifted energies are

$$\begin{aligned} E_1' &= \frac{1}{2}\left[E_1 + E_2 - (E_2 - E_1)\sqrt{1 + 16J(J+1)\Big(\frac{\beta}{E_2 - E_1}\Big)^2}\,\right] \\ E_2' &= \frac{1}{2}\left[E_1 + E_2 + (E_2 - E_1)\sqrt{1 + 16J(J+1)\Big(\frac{\beta}{E_2 - E_1}\Big)^2)}\,\right] \end{aligned} \tag{4.3}$$

The lower state corresponds to the negative energy shift, while the upper state corresponds to the positive energy shift.

The symmetry and parity labels are shown in Figure. 4.1. For each state, the symmetry label outside the parentheses marks even J levels while that inside the parentheses marks odd J levels. We assign arbitrary signs of '+' to the states with $B_2(B_1)$ symmetry, and '−' to the states with $B_1(B_2)$ symmetry. Selection rules allow $B_1 \leftrightarrow B_2$ transitions [90]. Therefore, for P and R branches where $\Delta J = 1$, states with the same sign connect. For Q branches where $\Delta J = 0$, states with opposite signs connect.

We fitted the measured transition frequencies to the desired model by a weighted nonlinear least squares algorithm using the "lsqcurvefit" solver in Matlab[1]. Four microwave transitions from a previous study [80] were included in the fit. We assign an uncertainty of 0.005 MHz for the microwave transitions and 0.1 MHz uncertainty for our measurements; the relative weight is proportional to the reciprocal of the square of frequency uncertainties.

4.4 Result and discussion

4.4.1 Observed bands

Three new bands belonging to the *ortho*- states of Ar–H_2O were observed in the millimeter wavelength range using the fast-sweep method. Each band has P, Q, and R branches. One band is assigned to the transitions between the $\Pi^{+/-}(1_{01})$ and $\Sigma^+(1_{01})$ $B_2(B_1)$ states. The fast-sweep spectrum of the Q branch of this band is shown in Figure 4.2. Under our experimental conditions, only 35 min was required to collect the 20 GHz spectral window shown in Figure 4.2 using the fast-sweep method, whereas 132 h was necessary for the point-by-point direct absorption scan to cover the same frequency window with the same number of spectral averages. The other two bands are assigned to transitions between the $\Pi(1_{10})$ and $\Pi(1_{01})$ states, in which case the way to group P, Q, and R branches is somewhat arbitrary. We group the branches from the same lower state into one band, i.e., the P and R branches of the $\Pi^-(1_{01})$ band connect to the $\Pi^-(1_{10})$ state and its Q branch connects to the $\Pi^+(1_{10})$ state. Additionally, the two submillimeter bands originally measured by Cohen *et al.* [77] were re-measured with higher frequency resolution. In the previous experiment, the frequency uncertainty for their tunable far-IR lasers was 0.5 MHz. In our experiment, with high precision multiplier chains, we could constrain the frequency uncertainty of our measurements down to 0.1 MHz. All measured transition frequencies, their

[1]http://www.mathworks.com/help/optim/ug/lsqcurvefit.html

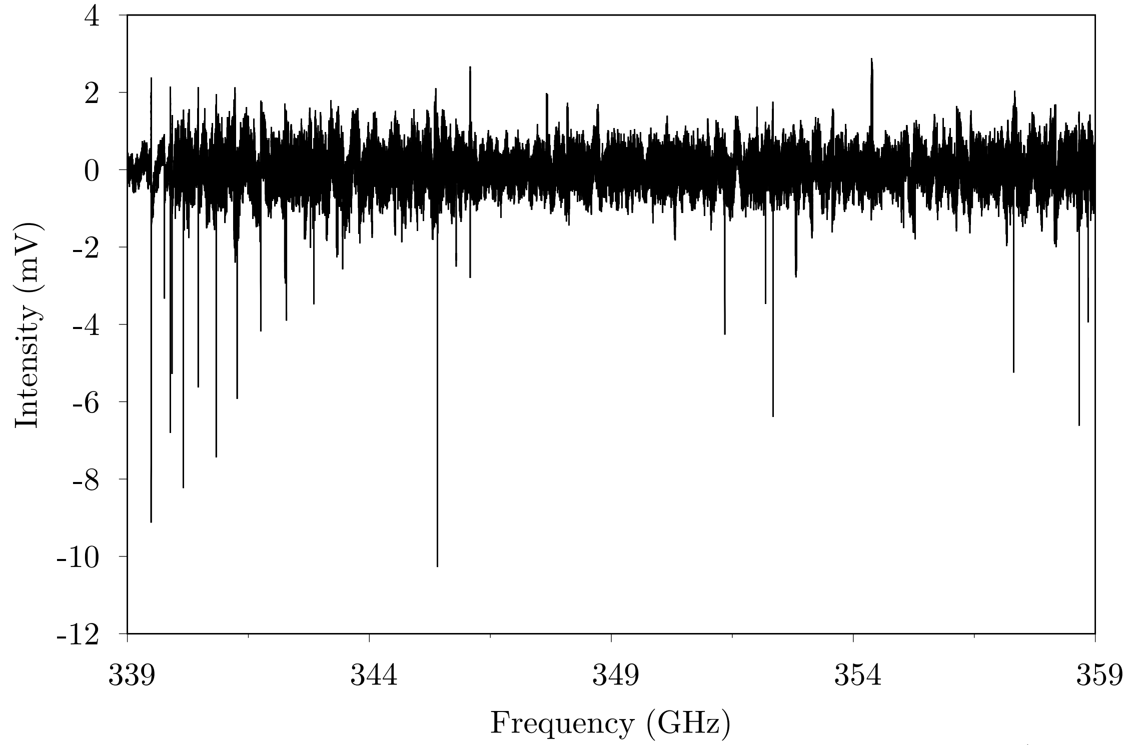

Figure 4.2: Fast-sweep spectrum of the Q branch of Ar–H_2O VRT band $\Pi^{+/-}(1_{01}) \leftarrow \Sigma^{+}(1_{01})$ $B_2(B_1)$.

assignments, and the observed−calculated residuals from the least squares fit are listed in Tables 4.1–4.5. The measurements reported by Cohen *et al.* [77] are also included in Tables 4.5 and 4.4 for comparison.

The full spectrum is plotted in Figure 4.3 where each stick is proportional to the power-normalized integrated intensity of the measured transition. The stick spectrum of each separated band is plotted in Figure 4.4. Characteristic spectral lines are shown in Figure 4.5. The weaker intensities of the $\Pi(1_{01}) \leftarrow \Sigma(1_{01})$ and $\Pi(1_{10}) \leftarrow \Pi(1_{01})$ bands relative to the stronger $\Pi(1_{10}) \leftarrow \Sigma(1_{01})$ and $\Sigma(1_{10}) \leftarrow \Pi(1_{01})$ bands support the assignment of the spectrum under the free-rotor model, because the forbidden transitions between the same H_2O rotational levels are only weakly relaxed in the anisotropic potential of the Ar–H_2O dimer [90].

Despite power normalization, the relative line intensities shown here are still qualitative. The correction is more reliable within a given frequency band from the same

Table 4.1: Transition frequencies of the $\Pi^{+/-}(1_{01}) \leftarrow \Sigma^{+}(1_{01})$ $B_2(B_1)$ band of Ar–H_2O. Δ is the difference between experimental measured values and the least-square fit values. Frequency units are MHz. Experimental uncertainty is estimated to be 0.1 MHz.

Transition	Exp.	Δ	Transition	Exp.	Δ
P(17)	275116.20	−0.07	Q(8)	342286.93	0.09
P(16)	277339.86	0.02	Q(9)	342854.51	0.03
P(15)	279687.54	0.03	Q(10)	343448.17	−0.01
P(14)	282175.49	0.00	Q(11)	344057.23	−0.08
P(13)	284819.92	−0.04	Q(12)	344670.52	−0.12
P(12)	287637.09	0.09	Q(13)	345276.39	−0.09
P(11)	290642.31	0.05	Q(14)	345862.73	−0.07
P(10)	293850.95	0.10	Q(15)	346417.42	0.06
P(9)	297277.26	0.12	Q(16)	346927.93	0.11
P(8)	300934.65	0.11	Q(17)	347381.93	0.02
P(7)	304835.44	0.07	R(0)	345795.42	−0.06
P(6)	308990.72	0.04	R(1)	352185.30	−0.06
P(5)	313410.06	0.00	R(2)	358850.72	−0.05
P(4)	318101.52	−0.01	R(3)	365784.16	−0.01
P(3)	323071.35	−0.07	R(4)	372976.06	−0.01
P(2)	328324.12	−0.08	R(5)	380415.19	0.00
Q(1)	339766.22	−0.06	R(6)	388088.48	0.03
Q(2)	339924.17	−0.02	R(7)	395981.20	−0.01
Q(3)	340157.82	0.00	R(8)	404077.33	0.00
Q(4)	340463.38	0.03	R(9)	412359.38	0.01
Q(5)	340835.78	0.06	R(10)	420808.71	−0.03
Q(6)	341268.87	0.11	R(11)	429405.85	−0.02
Q(7)	341755.33	0.10			

Table 4.2: Transition frequencies of the $\Pi^{+/-}(1_{10}) \leftarrow \Pi^{-}(1_{01})$ $B_1(B_2)$ band of Ar–H_2O. Δ is the difference between experimental measured values and the least-square fit values. Frequency units are MHz. Experimental uncertainty is estimated to be 0.1 MHz.

Transition	Exp.	Δ	Transition	Exp.	Δ
P(15)	209753.90	−0.13	Q(3)	292739.54	0.00
P(14)	214423.35	0.00	Q(4)	293437.84	−0.04
P(13)	219268.22	0.08	Q(5)	294320.19	−0.14
P(12)	224272.48	0.13	R(1)	303584.79	0.08
P(11)	229420.27	0.08	R(2)	309559.69	0.05
P(10)	234696.27	0.06	R(3)	315559.60	0.02
P(9)	240085.57	0.02	R(4)	321587.51	−0.03
P(8)	245574.04	−0.02	R(5)	327647.80	−0.04
P(7)	251148.48	−0.04	R(6)	333745.96	−0.08
P(6)	256796.67	−0.05	R(7)	339888.77	−0.10
P(5)	262507.50	−0.07	R(8)	346083.92	−0.11
P(4)	268271.22	−0.03	R(9)	352340.06	−0.08
P(3)	274079.23	0.00	R(10)	358666.51	−0.04
P(2)	279924.40	0.02	R(11)	365073.25	0.04
Q(1)	291876.27	0.03	R(12)	371570.50	0.09
Q(2)	292220.27	0.00	R(13)	378168.75	0.10

Table 4.3: Transition frequencies of the $\Pi^{+/-}(1_{10}) \leftarrow \Pi^{+}(1_{01})$ $B_2(B_1)$ band of Ar–H_2O. Δ is the difference between experimental measured values and the least-square fit values. Frequency units are MHz. Experimental uncertainty is estimated to be 0.1 MHz.

Transition	Exp.	Δ	Transition	Exp.	Δ
P(14)	207269.10	−0.10	Q(1)	291524.43	0.06
P(13)	212837.91	0.00	R(1)	303820.31	0.05
P(12)	218550.69	0.06	R(2)	309825.98	0.05
P(11)	224386.84	0.08	R(3)	315799.72	0.03
P(10)	230326.17	0.04	R(4)	321745.99	−0.01
P(9)	236349.25	0.02	R(5)	327671.20	0.01
P(8)	242437.50	0.02	R(6)	333583.29	−0.02
P(7)	248573.41	0.00	R(7)	339491.97	−0.04
P(6)	254740.83	−0.03	R(8)	345408.30	−0.05
P(5)	260925.14	−0.01	R(9)	351344.61	−0.03
P(4)	267113.20	0.00	R(10)	357314.25	0.02
P(3)	273293.71	0.03	R(11)	363331.30	0.01
P(2)	279457.16	0.01	R(12)	369410.56	0.06
Q(5)	289074.93	0.12	R(13)	375566.92	0.04
Q(4)	289933.29	0.06	R(14)	381815.36	0.00
Q(3)	290633.11	0.06	R(15)	388170.50	−0.02
Q(2)	291165.69	0.06	R(16)	394646.19	−0.03

Table 4.4: Transition frequencies of the $\Pi^{+/-}(1_{10}) \leftarrow \Sigma^{+}(1_{01})$ $B_2(B_1)$ band of Ar–H_2O. Δ is the difference between experimental measured values and the least-square fit values. Frequency units are MHz. Experimental uncertainty is estimated to be 0.1 MHz. Experimental values reported by Cohen *et al.* [77] (0.5 MHz uncertainty) are also included.

Transition	Exp.	Δ	Exp. [77]	Transition	Exp.	Δ	Exp. [77]
P(20)	564788.83	−0.03	564787.7	Q(10)	637204.47	−0.01	637204.1
P(19)	565529.94	0.04	565530.9	Q(11)	638387.72	−0.03	638388.0
P(18)	566549.12	−0.01	566550.2	Q(12)	639685.72	−0.04	639686.1
P(17)	567847.65	−0.01	567848.6	Q(13)	641099.85	−0.05	641099.5
P(16)	569425.55	−0.05	569427.5	Q(14)	642631.33	−0.05	642632.4
P(15)	571282.31	−0.04	571283.3	Q(15)	644281.12	−0.02	644281.8
P(14)	573416.69	−0.04	573417.7	Q(16)	646049.72	−0.01	646050.3
P(13)	575827.14	0.01	575828.1	Q(17)	647937.19	0.02	647937.5
P(12)	578511.75	0.01	578512.8	Q(18)	649942.85	0.02	649942.9
P(11)	581468.56	0.04	581469.6	Q(19)	652065.22	−0.01	652065.5
P(10)	584695.42	0.05	—	R(0)	637466.72	−0.04	637466.9
P(9)	588190.25	0.05	588191.4	R(1)	643791.47	−0.03	643791.6
P(8)	591951.01	0.05	591952.1	R(2)	650364.20	−0.06	650364.4
P(7)	595975.70	0.03	595976.8	R(3)	657183.52	−0.04	657184.1
P(6)	600262.42	−0.01	600263.6	R(4)	664247.81	−0.01	664249.2
P(5)	604809.42	−0.03	604810.7	R(5)	671555.47	−0.02	671556.6
P(4)	609614.99	−0.04	609615.4	R(6)	679104.95	0.08	679104.3
P(3)	614677.51	−0.04	614677.8	R(7)	686894.24	−0.03	686896.1
P(2)	619995.41	−0.06	619995.6	R(8)	694921.82	−0.03	694922.0
Q(1)	631495.57	−0.04	631495.1	R(9)	703185.60	−0.03	703187.0
Q(2)	631703.93	−0.02	631703.4	R(10)	711683.45	−0.03	711684.7
Q(3)	632016.93	0.01	632017.1	R(11)	720413.04	0.00	720414.6
Q(4)	632435.07	0.01	632435.0	R(12)	729371.63	0.01	729371.1
Q(5)	632959.13	0.03	632959.0	R(13)	738556.05	−0.06	738555.8
Q(6)	633589.98	0.05	633589.9	R(14)	747962.90	0.03	747963.3
Q(7)	634328.65	0.03	634328.7	R(15)	757587.70	0.08	757587.8
Q(8)	635176.40	0.03	635176.5	R(16)	767425.22	0.03	767425.6
Q(9)	636134.53	0.01	636134.6				

Table 4.5: Transition frequencies of the $\Sigma^-(1_{10})\ B_1(B_2) \leftarrow \Pi^{+/-}(1_{01})$ band of Ar–H_2O. Δ is the difference between experimental measured values and the least-square fit values. Frequency units are MHz. Experimental uncertainty is estimated to be 0.1 MHz. Experimental values reported by Cohen *et al.* [77] (0.5 MHz uncertainty) are also included.

Transition	Exp.	Δ	Exp. [77]	Transition	Exp.	Δ	Exp. [77]
P(10)	692100.92	0.26	692101.5	Q(6)	742834.32	0.01	742834.5
P(9)	696530.41	0.05	696532.2	Q(5)	743141.15	0.06	743141.2
P(8)	701135.89	−0.03	701135.9	Q(4)	743404.16	0.07	743404.2
P(7)	—	—	705915.4	Q(3)	743619.40	−0.02	743619.4
P(6)	710862.99	−0.01	710863.4	Q(2)	743783.87	0.02	743783.7
P(5)	715978.38	−0.05	715979.3	Q(1)	743894.84	−0.04	743894.8
P(4)	721257.54	−0.07	721259.0	R(1)	756202.88	−0.06	—
P(3)	726697.44	−0.01	726699.3	R(2)	762545.99	−0.01	762545.5
P(2)	732294.90	0.01	732294.3	R(3)	769030.48	0.05	769030.3
P(1)	738047.08	0.11	738046.8	R(4)	775653.81	−0.01	775654.5
Q(13)	739871.92	−0.03	—	R(5)	782413.71	−0.07	782413.3
Q(12)	740346.67	0.08	—	R(6)	789307.87	−0.03	789307.3
Q(11)	740812.25	0.00	740811.7	R(7)	796333.60	−0.09	796335.7
Q(10)	741264.36	-0.03	741264.1	R(8)	803488.30	−0.16	803488.0
Q(9)	741697.96	-0.02	741697.4	R(9)	810769.21	−0.08	810769.9
Q(8)	742107.78	0.08	742107.9	R(10)	818172.78	−0.03	818176.4
Q(7)	742488.28	0.06	742488.3				

multiplier, rather than near the band edges or between different multiplier bands. Near the band edges, the power correction did not fully account for the rapid power drop of multiplier output. In particular, for the undetected P(7) transition in the $\Sigma(1_{10}) \leftarrow \Pi(1_{01})$ band, the majority of radiation power was lost at the frequency of that transition.

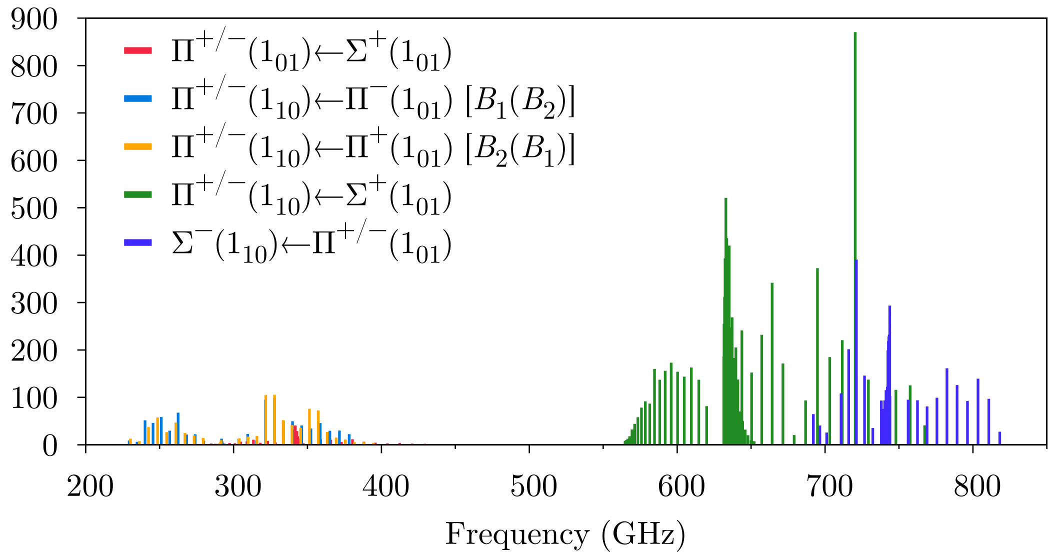

Figure 4.3: Full power-normalized stick spectrum of Ar–H_2O from 200 to 800 GHz. Reprinted with permission from Zou & Widicus Weaver [95].

4.4.2 Coriolis interaction

The Coriolis interaction between Σ and Π states is treated as a perturbation between two levels. The analytical eigenvalues of the two-level perturbation matrix are shown in Eq. 4.3. In previous studies, this interaction is approximated by the first order term of the Taylor series expansion of Equation 4.3:

$$
\begin{aligned}
E_1' &\approx E_1 - 4\beta^2 J(J+1)/(E_2 - E_1) \\
E_2' &\approx E_2 + 4\beta^2 J(J+1)/(E_2 - E_1)
\end{aligned}
\tag{4.4}
$$

under the assumption that $16\beta^2 J(J+1)/(E_2 - E_1)^2 \ll 1$. In the case of Ar–$H_2O$ *ortho-* states, the splitting of Σ and Π states is on the order of 300 GHz, while β is near 3 GHz. For high J levels (i.e., $J > 10$), the first order approximation starts to

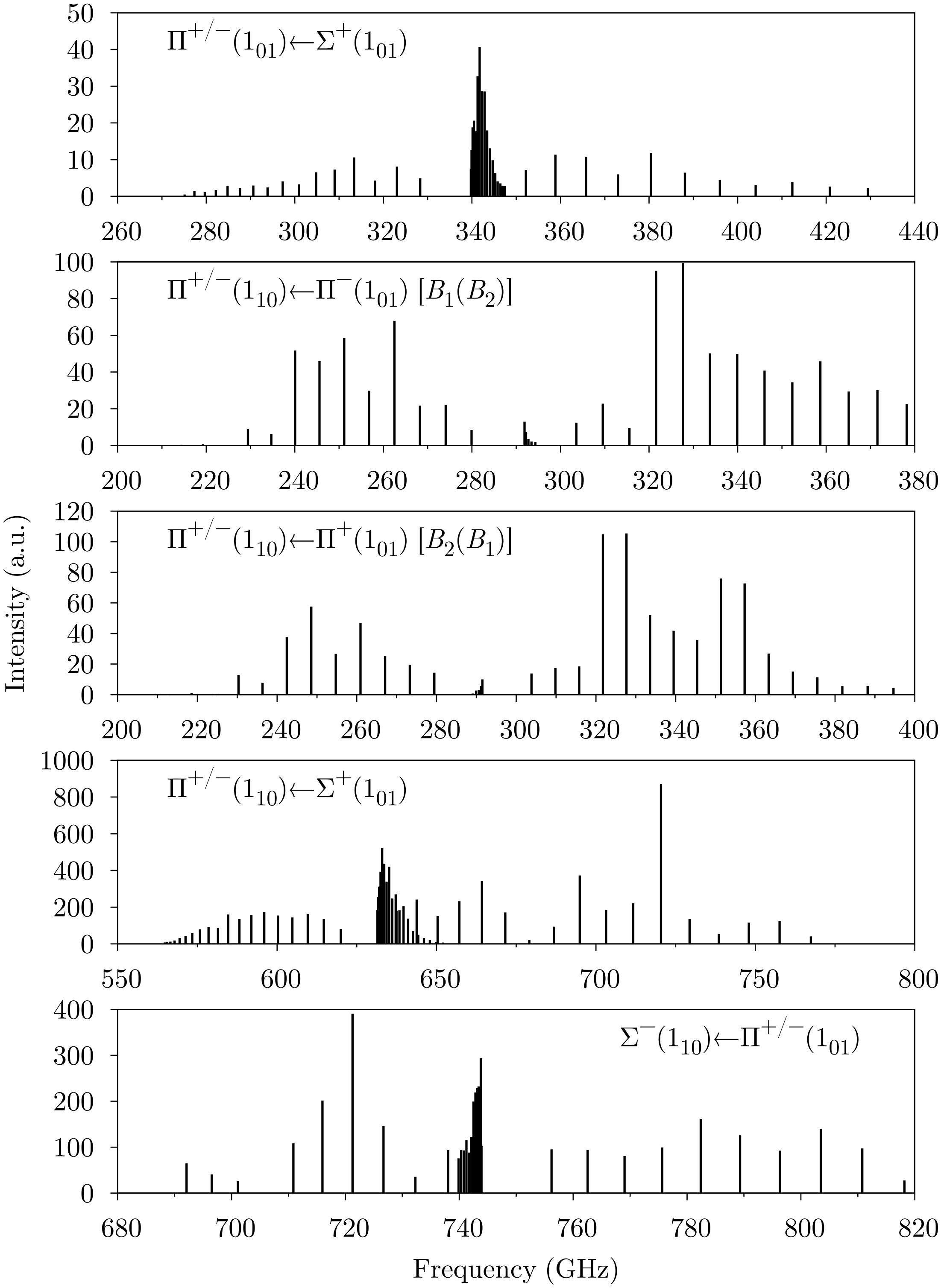

Figure 4.4: Power-normalized stick spectrum of each individual band of Ar–H_2O. Reprinted with permission from Zou & Widicus Weaver [95].

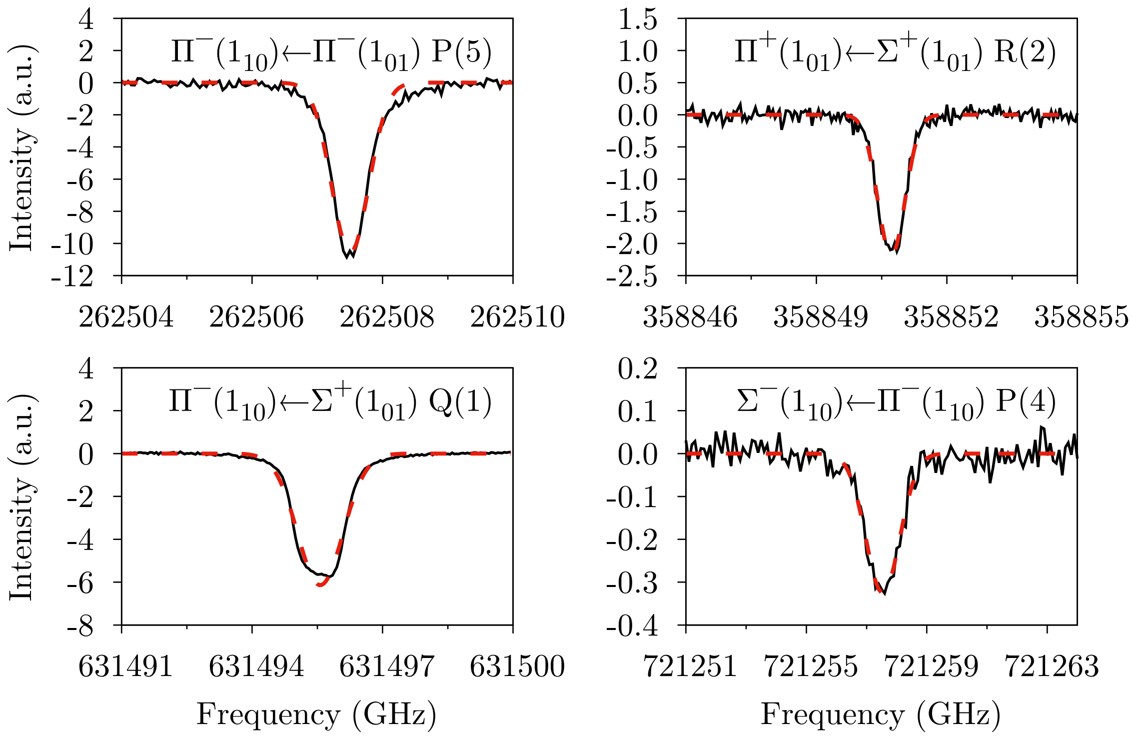

Figure 4.5: Characteristic spectral lines of Ar–H_2O. Black solid line is the experimental integrated intensity, and the red dash line is the Gaussian fit. Reprinted with permission from Zou & Widicus Weaver [95].

introduce a noticeable discrepancy as $16\beta^2 J(J+1)/(E_2-E_1)^2 > 0.1$. Our initial linear fit test reflected this trend by returning a r.m.s of 2.72 MHz if we only included the number of constants listed in the analysis of Cohen & Saykally [79]. This r.m.s did not reflect our experimental precision, and the difference between calculated frequencies and experimental frequencies was found to be systematically larger at higher J levels. Therefore, we performed a weighted nonlinear fit using the analytical equations of Coriolis terms (Equation 4.3), instead of approximating the square root term with the first order truncated Taylor series expansion. We observed a significant drop of r.m.s down to 0.30 MHz in the nonlinear fit with the same number of constants used in the linear fit. The fit was furthermore improved by adding higher order centrifugal distortion constants that have statistical significance. We included sextic and octic centrifugal constants for most of the states to achieve a final r.m.s of 0.06 MHz, consistent with the estimated uncertainty of our measurements.

The constants resulting from our nonlinear least square analysis are listed along with the result from Cohen & Saykally [79] in Table 4.6. Here we only fitted the reported transitions from the current study, along with the four microwave transitions from Fraser *et al.* [80]. Cohen & Saykally included two additional bands from the ground state to the intermolecular stretching state of Ar–H_2O. The exclusion of the transitions to these higher states, however, does not significantly affect the constants determined for lower states in our fit, since each water state is treated as an independent vibrational state. From Table 4.6, it can bee seen that the accuracy of the energies of the 1_{01} Σ and Π states is significantly improved because of the observation of the direct transitions between these two states. For the states unperturbed by Coriolis interaction, the constants in our analysis agree well with the results from Cohen & Saykally [79], but have a higher precision. For the states perturbed by the Coriolis interaction, i.e., $\Sigma^+(1_{01})$, $\Pi^+(1_{01})$, $\Pi^-(1_{10})$, and $\Sigma^-(1_{10})$ states, a systematic discrepancy of the centrifugal distortion constants is observed as compared to the results from Cohen & Saykally [79]. This is because our rigorous Coriolis fit prevents the contamination of the higher order coefficients from the Coriolis splitting into the centrifugal distortion constants. The Taylor series expansion of the Coriolis term in Eq. 4.3 up to the third order is

$$\mp \frac{\Delta E}{2}\sqrt{1+16J(J+1)\left(\frac{\beta}{\Delta E}\right)^2} = \\ \frac{\Delta E}{2} \pm \frac{4\beta^2}{\Delta E}J(J+1) \pm \frac{16\beta^4}{\Delta E^3}\big(J(J+1)\big)^2 \pm \frac{128\beta^6}{\Delta E^5}\big(J(J+1)\big)^3 \quad (4.5)$$

where $\Delta E = E_2 - E_1$ is the difference of corresponding vibrational energies. Substituting the β and ΔE values we obtained in our rigorous analysis, we can evaluate the amount of contamination that arises from the truncated Taylor series expansion. The calculated coefficients of the quadratic and cubic terms in Equation 4.5 for each water state are listed in Table 4.7. These coefficients are expected to agree with the difference between the constants fitted by Cohen & Saykally [79] and by this work, because our analysis has removed the effect of this Taylor series expansion from the centrifugal distortion constants. The results for the 1_{10} states quantitatively agree with the difference. The results for the 1_{01} states only qualitatively agree, indicating that there might be other effects we cannot account for in our analysis. After the removal of this contamination in our nonlinear fit, we found that the centrifugal distortion coefficients of the perturbed and unperturbed states are similar. This similarity indicates that the elongation of the bond length of the complex is not severely affected by the Coriolis effect.

The interpretation of each internal H_2O state energy v from the least squares analysis is model sensitive. The rigid rotor energy term we applied, following Cohen & Saykally [79], is $J(J+1) - 2\Omega^2$, i.e., $J(J+1)$ for Σ states and $J(J+1) - 2$ for Π states. Other models using $J(J+1)$ [90, 93] or $J(J+1) - \Omega^2$ [96] for all states have also been reported. Attention should be paid when comparing results retrieved from these other reports where different models were applied.

Table 4.6: Molecular constants fitted to Ar–H_2O $j = 1$ *ortho*- states (rms=0.060 MHz) and comparison with the results from Cohen & Saykally [79] (rms=0.623 MHz). The 1σ uncertainty of each constant is included in the parentheses.

	This Work		Cohen & Saykally [79]	
	$\Sigma(1_{01})$	$\Pi(1_{01})$	$\Sigma(1_{01})$	$\Pi(1_{01})$
ν (GHz)	0	345.590524(18)	0	345.587(18)
B (MHz)	3014.7865(17)	2951.6969(70)	3014.783(27)	2951.658(57)
$D(+)$ (kHz)	90.956(13)	115.713(20)	72.616(71)	135.49(40)
$D(-)$ (kHz)	—	114.8240(23)	—	114.76(35)
$H(+)$ (Hz)	−4.316(61)	−1.90(13)	1.25(20)	—
$L(+)$ (mHz)	−2.207(94)	1.85(27)	—	—
β (MHz)	2976.455(14)		2950.84(40)	
	$\Pi(1_{10})$	$\Sigma(1_{10})$	$\Pi(1_{10})$	$\Sigma(1_{10})$
ν (GHz)	637.466766(17)	1083.637495(35)	637.46708(43)	1083.634(18)
B (MHz)	3037.4887(13)	2953.1776(31)	3037.476(15)	2953.224(66)
$D(+)$ (kHz)	60.824(17)	—	60.44(13)	—
$D(-)$ (kHz)	65.149(14)	98.107(76)	51.42(14)	111.75(66)
$H(+)$ (Hz)	−18.796(92)	—	−21.45(28)	—
$H(-)$ (Hz)	−18.449(71)	−14.97(67)	−12.38(32)	−23.9(22)
$L(+)$ (mHz)	−4.54(16)	—	—	—
$L(-)$ (mHz)	−2.49(11)	−9.2(19)	—	—
β (MHz)	2862.862(17)		2880.78(33)	

Table 4.7: The contamination arising from the quadratic and cubic terms in the Taylor series expansion of Equation 4.5 for Coriolis perturbed states. The contamination is compared to the discrepancy between the analyses of ours and Cohen & Saykally [79].

Constant	State	Cohen & Saykally [79]	This work	Difference	Contamination (Eq. 4.5)
$-D$ (kHz)	$\Sigma^+(1_{01})$	−72.616(71)	−90.956(13)	18.340	30.4
$-D$ (kHz)	$\Pi^+(1_{01})$	−135.49(40)	−115.713(20)	−19.777	−30.4
H (Hz)	$\Sigma^+(1_{01})$	1.25(20)	−4.316(61)	5.566	18.0
H (Hz)	$\Pi^+(1_{01})$	—	−1.90(13)	1.90	−18.0
$-D$ (kHz)	$\Pi^-(1_{10})$	−51.42(14)	−65.149(14)	13.729	12.1
$-D$ (kHz)	$\Sigma^-(1_{10})$	−111.75(66)	−98.107(76)	−13.643	−12.1
H (Hz)	$\Pi^-(1_{10})$	−12.38(32)	−18.449(71)	6.069	4.0
H (Hz)	$\Sigma^-(1_{10})$	−23.9(22)	−14.97(67)	−8.93	−4.0

4.5 Summary

We have detected three additional vibrational-rotation-tunneling bands of the Ar–H_2O *ortho*- state in the millimeter wavelength range. One band is assigned to the $\Pi(1_{01}) \leftarrow \Sigma(1_{01})$ state and the other two are assigned to the $\Pi(1_{10}) \leftarrow \Pi(1_{01})$ states with allowed symmetry. In addition, we confirmed two bands reported by Cohen *et al.* [77] with higher frequency resolution. The spectrum agrees well with the free-rotor model of Ar–H_2O. The observed bands provide direct measurement of states that were only previously accessible from frequency differences of infrared bands, thus providing additional information of Ar–H_2O energy levels near the minimum of its intermolecular potential.

Chapter 5 Global Optimization Broadband Analysis Software for Interstellar Chemistry (GOBASIC)

Due to copyright restrictions from the publisher, the full content from the original publication cannot be reproduced in this dissertation. Therefore, only a brief outline of the GOBASIC program is presented here. The reader is encouraged to be directed to the original publication [97] for more details.

5.1 An outline of GOBASIC

GOBASIC is the "Global Optimization Broadband Analysis Software for Interstellar Chemistry". The main goal of GOBASIC is to address the challenge of line blending and line confusion in the broadband analysis of astronomical line surveys. The conventional Boltzmann diagram method [33] may suffer from unreliable estimation of the line intensity for blended lines, because in this method the intensity is estimated manually line by line. GOBASIC uses a different approach by simulating spectral lines from multiple molecules simultaneously. This approach results in a cumulative line intensity in which the contribution of all molecules is accounted for, and therefore provides more reliable treatment for blended lines. GOBASIC is also designed to speed up the analysis of broadband astronomical line surveys by automating the fitting process.

The basis assumptions in GOBASIC are local thermodynamic equilibrium (LTE) for each molecular component, Gaussian spectral lineshape, and the optically thin limit. LTE is a fair assumption in most hot cores and hot corinos because the density of gases is sufficiently high to support collisional deexcitation. It is necessary to point out that assuming a unique temperature for each molecular component is contradictory to the LTE assumption, if the molecules spatially cohabitate and collide with each other. Despite this contradiction,it has been shown that each molecular component does have its own unique temperature [98], which is an indirect evidence of spatial separation and segregation of different molecules in star-forming regions.

GOBASIC is able to load the molecular line catalogs in the JPL/CDMS format [34, 99], which is also the output format of the CALPGM spectral fitting program [75]. This feature of GOBASIC is designed to be user-friendly since the JPL/CDMS catalogs are the standard format for spectral line catalogs in the rotational spectroscopy community. GOBASIC is written in Matlab, and uses the "pattersearch" algorithm in Matlab's Global Optimization Toolbox to perform direct least-square optimization in a parallel computing environment.

As explained in Chapter 6, GOBASIC was used to analyze broadband spectral line surveys of a set of molecule-rich astronomical sources. Initial benchmarks of GOBASIC results was performed by comparison of the Orion-KL spectrum with the results of Blake *et al.* [98] (see the original publication for details). The details of the subsequent analyses are presented in Chapter 6.

The code of the latest GOBASIC program is deposited on `http://chemistry.emory.edu/faculty/widicusweaver/gobasic.html`.

Chapter 6 Broadband Line Surveys of Star-forming Regions Using the Caltech Submillimeter Observatory (CSO)

6.1 Introduction

Nearly 200 molecules have been detected in interstellar and circumstellar environments [99], and a great fraction of these are complex organic molecules (COMs). Here, following the convention of [9], we define a COM as one containing 6 or more atoms. Laboratory, observational, and modeling studies have revealed that very little is understood about the chemical and physical mechanisms driving complex molecule formation in the interstellar medium, despite the chemical diversity confirmed in space. In fact, calculations [10] and laboratory results [100] have shown that the textbook chemical mechanisms thought to lead to complex organics in the ISM — ion-molecule and electron recombination reactions — are actually quite inefficient processes for the formation of most complex molecules. Even simple molecules like methanol present a challenge, with ion-molecule reactions accounting for only a small percentage of the methanol observed in dense clouds [14], and neutral methanol comprising only $\sim$3% of the dissociative recombination products from protonated methanol [100].

Chemical modeling suggests that reactions of simple radicals on interstellar grain surfaces may be integral to COM formation [15, 16], and that grain surface reactions are the dominant formation mechanism for many of the most abundant COMs under typical interstellar cloud conditions. Based on this type of chemistry, many other uninvestigated COMs are also predicted to be present in high abundance in hot cores. Modeling studies must be compared with observations to test the robustness of the model. Unfortunately, the subset of sources for which extensive COM inventories have been compiled is quite small. Therefore, the modeling studies have initially focused on comparisons with the Sagittarius B2(N) hot molecular core, which has the highest number of detected molecules of any sightline studied to date [101]. It can be expected that with the increase in sensitivity and bandwidth offered by the Stratospheric Observatory for Infrared Astronomy (SOFIA) and the Atacama Large Millimeter Array (ALMA), more COMs will be detected in all interstellar environments.

Before a full understanding of interstellar organic chemistry can be obtained, we must test these models against observations to gain a comprehensive view of the possible chemical and physical parameter space for interstellar clouds. Previously, molecular searches largely consisted of targeted searches focusing on only the most abundant molecules, or on molecules that were high-priority targets. Unbiased, self-consistent, broadband spectral line surveys, however, are more effective in determining the true composition of interstellar clouds as they allow acquisition of spectral data over large frequency ranges and sample many transitions of each molecule. Such surveys will also guide observations at higher frequencies with the next generation of far-infrared telescopes such as SOFIA and ALMA by identifying the sources that have the richest chemical inventory.

We present here the first results from our molecular line survey observations using two broadband $\lambda = 1.3$ mm receivers at the Caltech Submillimeter Observatory (CSO). The goal of this program is to conduct deep, broadband spectral line surveys of interstellar clouds to probe the influence of physical environment on molecular complexity. We are observing a wide variety of sources in an attempt to correlate the relative abundances of organic molecules with the physical properties of the source (i.e., temperature, density, dynamics, etc.). Our broader research goal is to improve astrochemical models to the point where accurate predictions of complex molecular inventory can be made based on physical and chemical environment of a given source. The information gained from our observations will serve as a benchmark for these astrochemical models and holds the promise of significantly advancing our understanding of interstellar chemical processes. We report here on the details of the observations, the spectral analysis process, and the initial results for the molecular species that contribute significantly to the spectral line density in this spectral regime.

6.2 Observations and data reduction

The observations were performed with the 10.4 m Leighton Telescope at the Caltech Submillimeter Observatory[1] (CSO). Observations were performed between 2007 September and 2013 June. The nominal source positions and values for v_{lsr} assumed are listed in Table 6.1. Typical system temperatures (T_{sys}) during the observations were <400 K; T_{sys} was higher during periods of high opacity, but did not exceed 1100 K.

Observations were performed using two sets of receivers and spectrometers. The first was a prototype 230 GHz wideband receiver [102, 103], which was used with the facility acousto-optical spectrometer (AOS). The receiver has a 12 GHz bandwidth, but the total bandwidth for the observations was limited by the AOS to 4 GHz, with a channel width of ∼0.65 MHz. The second receiver was the facility 230 GHz wideband receiver [104], used with the facility Fast Fourier Transform Spectrometer (FFTS). The receiver is a fully synthesized, dual frequency, tuneless wide-IF bandwidth (4–8 GHz) system; the total bandwidth for the observations was limited by the FFTS to 4 GHz, with a channel width of ∼0.27 MHz.

All collected spectra were double sideband (DSB). A set of rest frequencies in the range 223.192 – 251.192 GHz were chosen, with each rest frequency setting being separated by 4 GHz. Each frequency point was sampled with a minimum redundancy of six to ensure sufficient sampling for deconvolution of the DSB spectra; most frequencies were sampled with a redundancy of eight. To achieve this redundancy, four IF

[1]The CSO was operated by the California Institute of Technology under contract from the National Science Foundation

Table 6.1: Sources, positions, and velocities used in the CSO observations.

Source Name	Source Type	α (J2000)	δ (J2000)	v_{lsr} (km·s^{-1})
W3(H_2O)	Hot core	2:27:04.61	+61:52:25.0	-47.0
L1448 MM-1	Outflow + Class 0	3:25:38.80	+30:44:05.0	0.0
NGC 1333 IRAS 2A	Hot corino	3:28:55.40	+31:14:35.0	7.8
NGC 1333 IRAS 2B	Hot corino	3:28:57.24	+31:11:14.0	7.0
NGC 1333 IRAS 4A	Hot corino	3:29:10.30	+31:13:31.0	6.8
NGC 1333 IRAS 4B	Hot corino	3:29:11.99	+31:13:08.9	5.0
B1-b	Pre-stellar core	3:33:20.80	+31:07:40.0	0.39
Orion-KL	Hot core	5:35:14.16	-05:22:21.5	8.0
NGC 2264 MM3	Hot core	6:41:12.00	+9:29:09.0	7.6
NGC6334-29	Class 0 protostar	17:19:57.00	-35:57:51.0	-5.0
NGC6334-38	Class 0 protostar	17:20:18.00	-35:54:42.0	-5.0
NGC6334-43	Class 0 protostar	17:20:23.00	-35:54:55.0	-2.6
NGC6334-I(N)	Class 0 protostar	17:20:55.00	-35:45:40.0	-2.6
Sgr B2(N-LMH)	Hot core	17:47:19.89	-28:22:19.3	64
GCM+0.693-0.027	Shocked region	17:47:21.86	-28:21:27.1	68.0
GAL 10.47+00.03	Hot core	18:08:38.40	-19:51:51.8	67.8
GAL 12.21-0.10	HII region	18:12:39.70	-18:24:20.9	24.0
GAL 12.91-00.26	Hot core	18:14:39.00	-17:52:0.30	37.5
HH 80-81	Outflow	18:19:12.30	-20:47:27.5	12.2
GAL 19.61-0.23	Hot core	18:27:37.99	-11:56:42.0	40.0
G24.33+00.11 MM1	Hot core	18:35:08.14	-7:35:01.1	113.4
GAL 24.78+0.08	Hot core	18:36:12.60	-7:12:11.0	111.0
GAL 31.41+0.31	Hot core	18:47:34.61	-1:12:42.8	97.0
GAL 034.3+00.2	Hot core	18:53:18.54	+1:14:57.9	58.0
GAL 45.47+0.05	Hot core	19:14:25.60	+11:09:26.0	62.0
W51	Hot core	19:23:43.50	+14:30:34.0	55.0
GAL 75.78+0.34	HII region	20:21:44.09	+37:26:39.8	4.0
W75N	Hot core	20:38:36.60	+42:37:32.0	10.0
DR21(OH)	Hot core	20:39:01.10	+42:22:49.1	-3.0
L1157-MM	Class 0 + outflow	20:39:06.20	+68:02:16.0	2.7
NGC 7538	Hot core	23:13:45.70	+61:28:21.0	-57.0

offsets (4.254, 6.754, 5.268, and 7.795 GHz) were applied to each rest frequency, and DSB spectra were collected at each of these frequency settings. Additional IF offsets of 6.283, 4.753, 5.767, and 7.269 GHz were applied to the two lowest rest frequency settings. The number of DSB spectra acquired for each source varied, depending on weather conditions and the amount of available observing time.

Spectral intensities for the raw data were calibrated using the standard chopper wheel calibration method and placed on the atmosphere-corrected temperature scale, T_a^*. The chopper settings used were either $70 \pm 8''$ of throw with a chopping frequency of 1.123 Hz or $90 \pm 8''$ of throw with a chopping frequency of 1.1 Hz. The estimated percent calibration error in antenna temperature is <20%, based on previous experience with this hardware. Integration times were adjusted based on the T_{sys} determined after tuning the receiver to a given frequency setting (i.e., for one set of rest frequency and IF values), such that the noise level achieved for a given frequency setting was ∼30 mK. Pointing was verified on average every two hours, and pointing offsets were consistent to within $\leq 5''$ over the course of a given night. As an independent verification of the pointing accuracy, each spectrum was checked against previous spectra recorded for consistency in spectral line intensity. The full-width-half-power beam size at 230 GHz was determined to be $33.4''$ for the prototype receiver, and $35.54''$ for the facility receiver.

Spectral cleaning and deconvolution was achieved using the CLASS software package included in the GILDAS suite of programs (Institut de Radioastronomie Millimétrique, Grenoble, France). Baselines were fitted and removed from each DSB spectrum using a first degree baseline function. In cases where line density precluded a reliable baseline fit, a constant offset was subtracted from the T_a^* scale. This offset was determined through comparison to the baseline in neighboring spectral windows. In addition to baseline subtraction, some spurious noise features were present in the spectra, but their identification was straightforward because they were significantly narrower than the spectral linewidths. Such noise features were removed from the spectra by blanking the affected channels prior to processing. After baseline subtraction and removal of noise features, the spectra were resampled at a uniform channel spacing of 1 MHz. The deconvolution was performed using the standard routine included in CLASS. An initial deconvolution was performed assuming no gain variations between the upper and lower sidebands. This was then used as an initial guess to constrain a second deconvolution allowing for varying gains between sidebands. Due to the nature of the algorithm used, extremely strong lines in the spectrum can produce ghosts visible above the final residual noise. Therefore, the CO line at 230.5 GHz and other strong spectral features with intensities above 2 K were masked during deconvolution and later stitched back into the spectrum to prevent the introduction of spurious features. After deconvolution was completed, it was found that a few strong features in the image sideband produced ghosts which appear as negative features in the deconvolved spectrum. These features were blanked in the deconvolved spectrum. After deconvolution, all intensities were corrected to the main beam temperature scale, T_{mb}, using the relation $T_{mb} = T_a^*/\eta_{mb}$. The root-mean-squared noise in the deconvolved spectra was determined to be ≤25 mK on the T_{mb} scale.

6.3 Line identification and analysis

The deconvolved spectra are near the line confusion limit for many of these sources. Detailed spectral analysis using the traditional Boltzmann diagram approach was therefore quite challenging. Such analyses are often unreliable because they are conducted one molecule at a time using a small set of lines for which line widths are determined independently and do not account for possible line blending. We have therefore developed a new program that analyzes all of the lines from one molecule across the entire broadband spectrum simultaneously. This Global Optimization and Broadband Analysis Software for Interstellar Chemistry (GOBASIC) is described in detail elsewhere [97]. In short, the software assumes local thermodynamic equilibrium (LTE) and Gaussian lineshapes, and conducts a simultaneous, multi-molecule, multi-component, broadband spectral analysis. We used published line surveys for Sgr B2(N) [105] and Orion-KL [98, 106, 107] to guide the initial list of molecules that were included for the analysis for this dataset. We imported spectral line catalogs from the Cologne Database for Molecular Spectroscopy (CDMS) [99] and the Jet Propulsion Laboratory (JPL) Spectral Line Catalog [34]. Unless combined in the JPL/CDMS catalog files, individual vibrational states were treated as unique molecular components. In the case where multiple databases contained information for a given molecule suitable for an LTE analysis, we used the catalog that had most recently been revised and updated according to the online documentation.

The partition function interpolation required for such an analysis is not trivial for many molecules. In order to match line intensities tabulated in the JPL/CDMS catalogs, we used the tabulated partition function values provided by these databases along with the molecular catalogs. These partition function values are determined from direct summations of Boltzmann factors of all accessible energy levels in the catalog. These values are provided in the documentation for each molecule at several specific temperature points spanning from 10 K to 300 K. Blake *et al.* showed that for either linear or nonlinear molecules, their pure rotational partition function $Q_{\mathrm{rot}}(T)$ is always proportional to T or $T^{3/2}$ [98]. Unfortunately, we discovered that this pure rotational model did not always describe the tabulated partition function values provided by JPL/CDMS, especially for molecules that possess significant internal motions, and for catalogs (and thus partition function values) merging multiple vibrational states together. Therefore, we adopted a general functional form

$$Q(T) = \alpha T^{\beta} \left[\gamma + \exp(\epsilon/T)\right] \tag{6.1}$$

for our partition function interpolation. This functional form consists of two terms: a pure Q_{rot} term, and a Q_{rot} combined with a Boltzmann factor for a vibrational state.

When fixing part of the 4 coefficients to specific values, this functional form reduces to simpler cases. For example, a pure $Q_{\rm rot}$ term is derived when $\gamma = \epsilon = 0$. For each molecule to be analyzed, we minimized the coefficients to be fitted in Equation 6.1, only adding additional terms if necessary to obtain a reliable fit. Since the partition function values span several orders of magnitude, the residual may not be reliable to evaluate the goodness of the interpolation. Instead, we simply examined the range of the relative deviation between the interpolated values and the tabulated values. This relative deviation is defined as $\delta = Q_{\rm interpolated}/Q_{\rm tabulated} - 1$. The line catalogs, their databases and versions, the coefficients for the partition function interpolation, and the relative deviation range of our interpolation, are summarized in Table 6.2.

Table 6.2: Summary of the line catalog information. The molecules are sorted alphabetically by their chemical names.

Molecule	Formula	Database	Version
Acetaldehyde	CH_3CHO	JPL	Jan 2012
Acetone	CH_3COCH_3	JPL	Mar 2008
Carbon Monosulfide	CS	CDMS	Oct 2008
Carbon Monosulfide	^{13}CS	CDMS	Jan 2004
Carbon Monosulfide	$^{13}C^{34}S$	CDMS	Jan 2004
Carbon Monosulfide	$C^{33}S$	CDMS	Jan 2004
Carbon Monosulfide	$C^{34}S$	CDMS	Jan 2004
Carbon Monoxide Ion	CO^+	CDMS	Aug 2013
Carbonyl Sulfide	OCS	CDMS	Nov 2005
Carbonyl Sulfide	$OC^{34}S$	CDMS	Apr 2005
Cyanide Radical	CN ($^2\Sigma^+$)	CDMS	May 2005
Diazenylium	N_2D^+	CDMS	Mar 2009
Dimethyl Ether	CH_3OCH_3	CDMS	Nov 2011
Ethanol	C_2H_5OH	JPL	Apr 2008
Ethenone (Ketene)	H_2CCO	CDMS	Nov 2003
Ethenone (Ketene)	HDCCO	CDMS	Jan 2006
Ethenone (Ketene)	D_2CCO	CDMS	Jan 2006
Ethyl Cyanide	C_2H_5CN	JPL	Jul 2009
Ethynyl	CCH	CDMS	Jul 2010
Formaldehyde	$H_2^{13}CO$	JPL	Oct 2005
Formaldehyde	H_2CO	CDMS	Aug 2005
Formaldehyde	HDCO	CDMS	Feb 2000
Formamide	$NH_2CH(O)$	CDMS	Apr 2003

Continued on next page

Table 6.2 – *Continued from previous page*

Molecule	Chemical Formula	Database	Version
Formic Acid	*trans*-HCOOH	CDMS	Jul 2003
Formyl Cation	HCO^+	CDMS	Oct 2007
Formyl Cation	$HC^{18}O^+$	JPL	Dec 1983
Formyl Cation	$H^{13}CO^+$	CDMS	Oct 2007
Formyl Radical	HCO	JPL	Aug 1983
Hydrogen Cyanide	HCN	CDMS	May 2007
Hydrogen Cyanide	$H^{13}CN$	CDMS	Nov 2014
Hydrogen Cyanide	$HC^{15}N$	CDMS	Aug 2005
Hydrogen Isocyanide	$HN^{13}C$	JPL	Dec 1979
Hydrogen Sulfide	H_2S	CDMS	Oct 2008
Isocyanic Acid	HNCO	CDMS	May 2009
Isocyanide	DNC	CDMS	Sep 2009
Methanethiol	CH_3SH	CDMS	Jan 2012
Methanol	CH_3OH	JPL	Mar 2010
Methanol	CH_2DOH	JPL	Jun 2012
Methanol	$^{13}CH_3OH$	CDMS	Dec 2002
Methenamine	CH_2NH	JPL	Jan 1981
Methyl Cyanide	CH_3CN	CDMS	Nov 2016
Methyl Cyanide	CH_3CN ($v_8 = 1$)	CDMS	Nov 2016
Methyl Cyanide	$CH_3^{13}CN$	CDMS	Dec 2009
Methyl Cyanide	$^{13}CH_3CN$	CDMS	Dec 2009
Methyl Formate	$HCOOCH_3$	JPL	Apr 2009
Methylamine	CH_3NH_2	JPL	Jan 2009
Nitric Oxide	NO	JPL	Oct 2010
Nitrogen Sulfide	NS	JPL	Feb 1995
Nitrogen Sulfide	$N^{34}S$	CDMS	Aug 2011
Propyne	CH_3CCH	CDMS	Aug 2008
Propyne	CH_3CCD	CDMS	Apr 2002
Propyne	CH_2DCCH	CDMS	Apr 2002
Propynenitrile	HCCCN	CDMS	Oct 2000
Propynenitrile	HCCCN ($v_7 = 1$)	CDMS	Oct 2000
Propynenitrile	$H^{13}CCCN$	JPL	Dec 1979
Propynenitrile	$HC^{13}CCN$	JPL	Dec 1979
Propynenitrile	$HCC^{13}CN$	JPL	Dec 1979
Silicon Monoxide	SiO	JPL	Jan 1984
Sulfur Dioxide	SO_2	CDMS	Jul 2005
Sulfur Dioxide	$^{33}SO_2$	JPL	Nov 1996
Sulfur Dioxide	$^{34}SO_2$	JPL	Nov 1996
Sulfur Monoxide	SO	CDMS	Aug 1998
Sulfur Monoxide	^{33}SO	CDMS	Aug 1998
Sulfur Monoxide	^{34}SO	CDMS	Aug 1998
Sulfur Monoxide Ion	SO^+	JPL	Dec 1996

Continued on next page

Table 6.2 – *Continued from previous page*

Molecule	Chemical Formula	Database	Version
Thioformaldehyde	H_2CS	CDMS	Feb 2008
Thioformaldehyde	HDCS	CDMS	May 2004
Thioformaldehyde	$H_2C^{34}S$	CDMS	Feb 2006
Thiomethylium	HCS^+	CDMS	Jun 2003
Vinyl Cyanide	C_2H_3CN	JPL	Oct 2009
Water	HDO	JPL	Oct 1989

Table 6.3: Interpolated coefficients and relative deviations from catalogs for molecules listed in Table 6.2 using the partition function form Eq. 6.1.

Chemical Formula	α	β	γ	ϵ	$\delta_{\rm min}$ (%)	$\delta_{\rm max}$ (%)
CH_3CHO	17.1065	1.5	0.5489	-256.2868	-0.51	0.27
CH_3COCH_3	15274.522	1.5	0.0165	-527.2334	-12.48	27.87
CS	0.8510	1	0	0.3957	-0.10	0.06
^{13}CS	1.8034	1	0	0.3631	-0.07	0.04
$^{13}C^{34}S$	0.9171	1	0	0.3593	-0.04	0.03
$C^{33}S$	3.4325	1	0	0.3845	-0.04	0.03
$C^{34}S$	0.8650	1	0	0.3790	-0.07	0.04
CO^+	0.7105	1	0	0.9603	-4.04	0.63
OCS	3.4361	1	0	0	-0.75	0.21
$OC^{34}S$	3.5220	1	0	0	-0.73	0.21
CN ($^2\Sigma^+$)	2.2040	1	0	0.9449	-0.26	0.33
N_2D^+	4.9476	1	0	0	-4.80	1.51
CH_3OCH_3	91.2742	1.5	0	0	-1.80	4.00
C_2H_5OH	6.6674	1.5	0.4972	-59.8213	-0.11	0.17
H_2CCO	1.0186	1.5	1	-3.8746	-8.45	11.59
HDCCO	1.2928	1.5	0	0	-1.03	0.32
D_2CCO	2.4272	1.5	0	0.0000	-2.79	0.63
C_2H_5CN	7.1989	1.5	0	0	-0.38	0.17
CCH	1.9078	1	0	0.7175	-0.13	0.16
H_2CO	0.2791	1.5	1	-2.1456	-9.43	14.90
HDCO	0.3694	1.5	0	0.7692	-2.54	3.62
$H_2^{13}CO$	0.2903	1.5	1	-2.7718	-4.11	2.85
$NH_2CH(O)$	1.8945	1.5	0	0	-4.55	1.15
trans-HCOOH	1.7189	1.5	0	0	-1.20	0.38
HCO^+	0.4671	1	0	0.7344	-0.14	0.17
$HC^{18}O^+$	0.4894	1	0	0.6847	-0.01	0.02
$H^{13}CO^+$	0.4802	1	0	0.7143	-0.12	0.15
HCO	0.5697	1.5	0	1.8171	-2.27	4.02
HCN	1.4357	1	0	0	-5.69	1.55

Continued on next page

Table 6.3 – *Continued from previous page*

Chemical Formula	α	β	γ	ϵ	$\delta_{\min}$ (%)	$\delta_{\max}$ (%)
$H^{13}CN$	1.4489	1	0	0.6870	-0.12	0.05
$HC^{15}N$	0.4892	1	0	0	-2.64	0.78
$HN^{13}C$	0.4889	1	0	0	-5.20	1.95
H_2S	0.1015	1.5	0	0	-5.25	2.55
HNCO	0.4451	1.5242	0	2.8006	-7.77	5.17
DNC	0.5460	1	0	0.6251	-0.09	0.11
CH_3SH	46.0687	1.7072	0.1085	-1244.7174	-16.44	29.21
CH_3OH	1.8680	1.7336	0.2229	-1005.6869	-3.17	3.14
CH_2DOH	0.5941	1.7821	0	0	-4.97	5.51
$^{13}CH_3OH$	1.2810	1.7314	0.3372	-929.5959	-3.12	3.13
CH_2NH	1.1497	1.5	0	0	-3.52	1.19
CH_3CN	1.9286	1.5	0	1.2952	-1.94	2.11
CH_3CN ($v_8 = 1$)	0.1464	2.1176	0	-481.7178	-10.57	5.61
CH^{13}_3CN	1.9251	1.5	0	1.2743	-1.28	1.79
$^{13}CH_3CN$	2.0506	1.5	0	0	-10.77	2.30
$HCOOCH_3$	25.2869	1.5	0.9900	-190.5726	-0.30	0.22
CH_3NH_2	23.9534	1.5	0	0	-0.20	0.23
NO	0.9345	1.2435	0	6.2186	-4.16	3.89
NS	2.6639	1.1673	0	3.1202	-4.17	4.36
$N^{34}S$	3.9120	1.0988	0	1.6296	-6.92	8.19
CH_3CCH	1.0301	1.5	1	2.4731	-1.02	1.57
CH_3CCD	1.1330	1.5	1	2.4383	-1.02	1.57
CH_2DCCH	1.8964	1.5	0	0	-0.91	0.29
HCCCN	4.6073	1	0	0	-2.07	0.53
HCCCN ($v_7 = 1$)	9.1357	1	0	-321.0257	-0.01	0.00
$H^{13}CCCN$	14.2113	1	0	0	-0.53	0.20
$HC^{13}CCN$	13.8318	1	0	0	-0.54	0.21
$HCC^{13}CN$	13.8295	1	0	0	-0.56	0.21
SiO	0.9693	1	0	0	-2.69	1.25
SO_2	1.1492	1.5	0	0	-3.94	1.01
$^{33}SO_2$	4.6045	1.5	0	0	-0.95	0.30
$^{34}SO_2$	1.1608	1.5	0	0	-0.95	0.30
SO	1.4598	1	1	-16.7494	-1.19	1.95
^{33}SO	5.8908	1	1	-16.7632	-0.89	2.16
^{34}SO	1.4851	1	1	-16.7767	-0.83	2.36
SO^+	1.9142	1	0	0.0914	-8.00	5.28
H_2CS	0.5848	1.5	1	-3.2965	-9.84	13.46
HDCS	0.7709	1.5	0	0	-1.73	0.55
$H_2C^{34}S$	0.6004	1.5	1	-3.6703	-4.28	3.12
HCS^+	0.9871	1	0	0	-2.55	0.90
C_2H_3CN	29.1521	1.5	0.5212	-396.4232	-0.31	0.21
HDO	0.0273	1.5	0	4.7166	-2.85	5.14

The values for the source velocity, v_{lsr}, were set to those listed in Table 6.1 based on information available in the literature. The column density (N_{T}), rotational temperature (T_{rot}), line width (characterized as the full-width-half-maximum (FWHM)), and red shift δV with respect to the source v_{lsr} were determined iteratively for each molecule using the procedures outlined in [97]. In brief, 4 steps were followed for each source. Firstly, spectral lines from CO, ^{13}CO, C^{17}O, and C^{18}O were flagged in GOBASIC because of their large intensity and non-Gaussian line shapes. Data in the frequency windows of these 4 lines were omitted in the least-squares fit. Secondly, strong spectral features arising from ubiquitous small molecules, such as CS, CN, CCH, and HCN, were fitted with arbitrary temperature and column density in GOBASIC to achieve only a best fit model for the emission. These molecules only present a few lines in the observed frequency range, and therefore the information is not sufficient to perform an LTE analysis. Nonetheless, their flux was properly accounted for in the analysis by using the arbitrarily fitted parameters. After that, each target molecule was fit using GOBASIC with the inclusion of the results from the second step. In this process, we determined which molecules were unambiguously detected in a source, and we obtained a coarse estimation of their LTE parameters. In the final step, all detected target molecules were fit simultaneously in GOBASIC, using their LTE parameters obtained from the third step as the initial guess. The convergence requirement for the change of r.m.s of the residual and the change of parameter vector were both set to $< 10^{-6}$ in GOBASIC, with the exception of a few extremely complex sources such as Orion-KL and GAL 10.47+00.03, to which a looser requirement was applied. Caution was taken to make sure the final results did not hit boundaries of the searching parameter space, with the exception of those cases that are specified later in the text. Spectral lines with uncertainties over 1 MHz in the catalog were discarded in our analysis to avoid unreliable assignments. Not all sources listed in Table 6.1 have interferometric data available in the 1.3 mm band. As a consequence, for consistency, beam dilution effect was not accounted for in our analysis, despite the ability of GOBASIC to do so. Uncertainties for the final parameters were determined from the quality of the fit as described by [97], using 10^{-3} as the grid size for its numerical gradient calculation.

6.4 Results

Due to the highly collaborative nature of this project, many others have contributed to the observations and reduction of the raw data. The discussion here will therefore only focus on the results of the analysis that I performed, rather than give a comprehensive comparison to the literature and discussion of the astrophysical implications. Those additional aspects of this project go well beyond the scope of this dissertation.

The baseline-subtracted, deconvolved spectra for the 31 star-forming regions are shown in Figure 6.1. The spectra are plotted with intensity in the unit of antenna temperature, and sorted from high flux on the top to low flux on the bottom. The spectral coverage is 220–267 GHz in general, with individual variations up to 10 GHz depending on the specific spectral coverage obtained for that source. The Orion-KL survey is particularly short relative to the others, because it was used only as a benchmark to test receiver operation and deconvolution reliability. Given the extensive literature related to Orion-KL [107–128], no new astrochemical information was expected to be gained from its analysis. Likewise, although Sgr B2(N) is included here, a full analysis was not performed, because it has been so extensively studied by other groups [105, 129–146].

In all sources, the CO isotopologue lines, including CO at 230.5 GHz, ^{13}CO at 220.4 GHz, $C^{17}O$ at 224.7 GHz, and $C^{18}O$ at 219.6 GHz, are ubiquitously observed. Other strong spectral features include the H_2CO $3_{1,2} \rightarrow 2_{1,1}$ line at 225.7 GHz, the CN

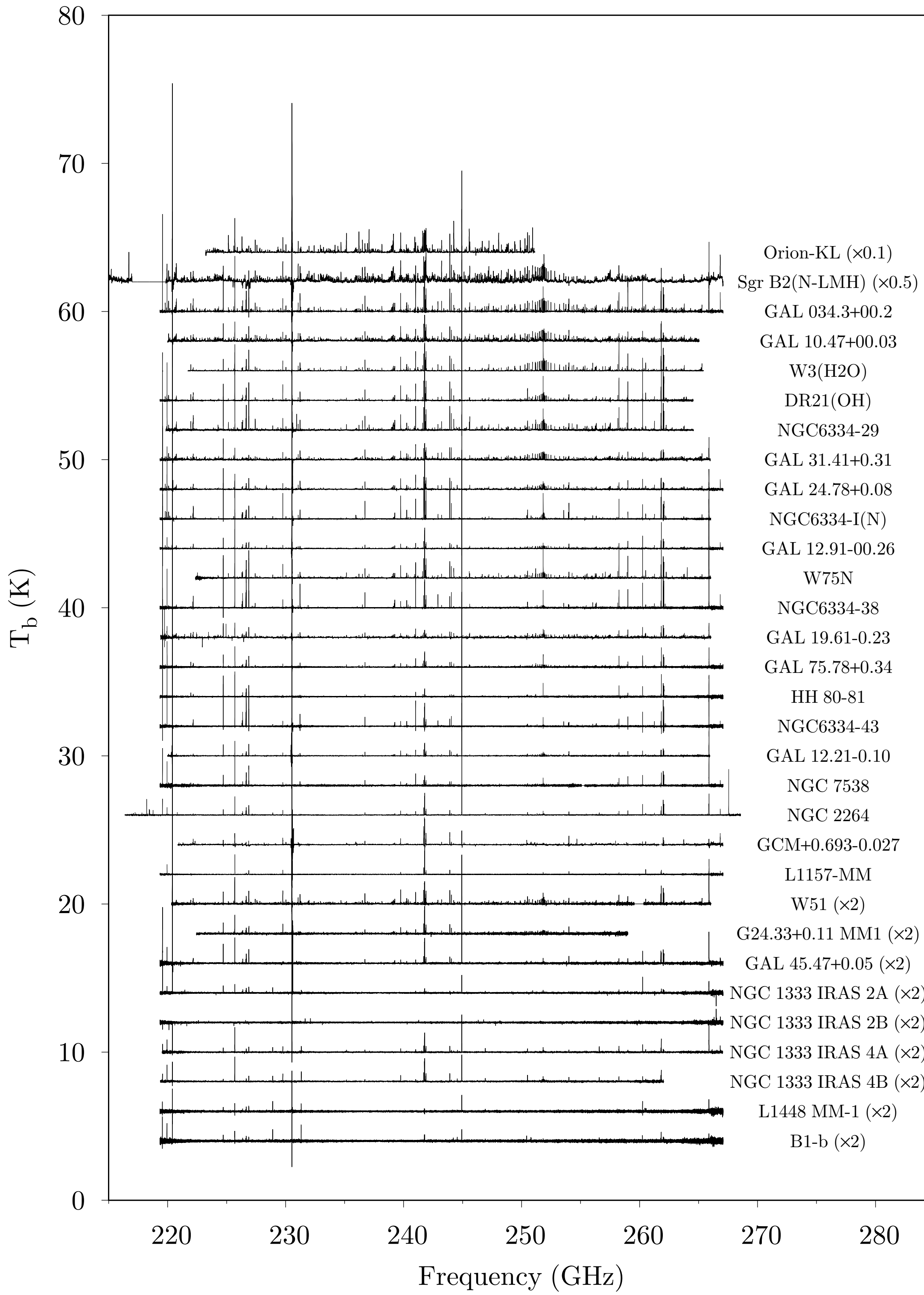

Figure 6.1: Deconvolved CSO spectra of 31 star-forming regions.

$N = 2 \rightarrow 1$ hyperfine lines at 226 GHz, the methyl cyanide $J = 13 \rightarrow 12$ Q-branch at 239 GHz, the CS $J = 5 \rightarrow 4$ line at 244.9 GHz, methanol $J = 5 \rightarrow 4$ Q-branch around 242 GHz and $K_a = 3 \rightarrow 2$ R-branch around 252 GHz, the CCH $N = 3 \rightarrow 2$ hyperfine lines at 262.1 GHz, and the HCN $J = 3 \rightarrow 2$ line at 265.9 GHz. Because of the source-to-source variation of the spectral coverage, molecules such as HCN and HCO^+ are undetected in some sources simply because their lines are outside of the observed spectral window. This non-detection due to the limited spectral range is distinguished from the non-detection due to weak spectral intensity, which impacts the interpretation of the chemistry in these sources.

The full result of the LTE analysis of all detected molecules in the 31 sources (i.e., excluding Sgr B2(N)) is presented in Table 6.4, which is printed in a machine-readable format in Appendix C. The four LTE parameters for each detected molecule are the column density N_T in cm^{-2}, the rotational temperature T_rot in K, the FWHM in km·s^{-1}, and the red shift with respect to v_{lsr}, δv, in km·s^{-1}. Only molecules with more than three clean lines at different upper state energies can be fit to a reliable T_rot. Other small molecules are fit with arbitrary N_T and T_rot, and their associated uncertainties may be unphysically large. Figure 6.2 shows a sample frequency window, in which the molecular components fitted in the global LTE analysis are plotted. The spectrum from NGC 1333 IRAS 2B is omitted because we did not find any molecular lines in this source.

Due to the complexity of the physical environment in most of these sources, molecules have a wide range of rotational temperatures and FWHMs. It is to be expected given that many of these sources have been shown through interferometric studies to have multiple kinematic components [122, 147, 148]. Therefore, no upper-limit calculations were performed on undetected molecules. Instead, we simply report a non-detection. It is important to mention that these non-detections can be interpreted in various ways. The insufficient spectral line intensity could come from a low

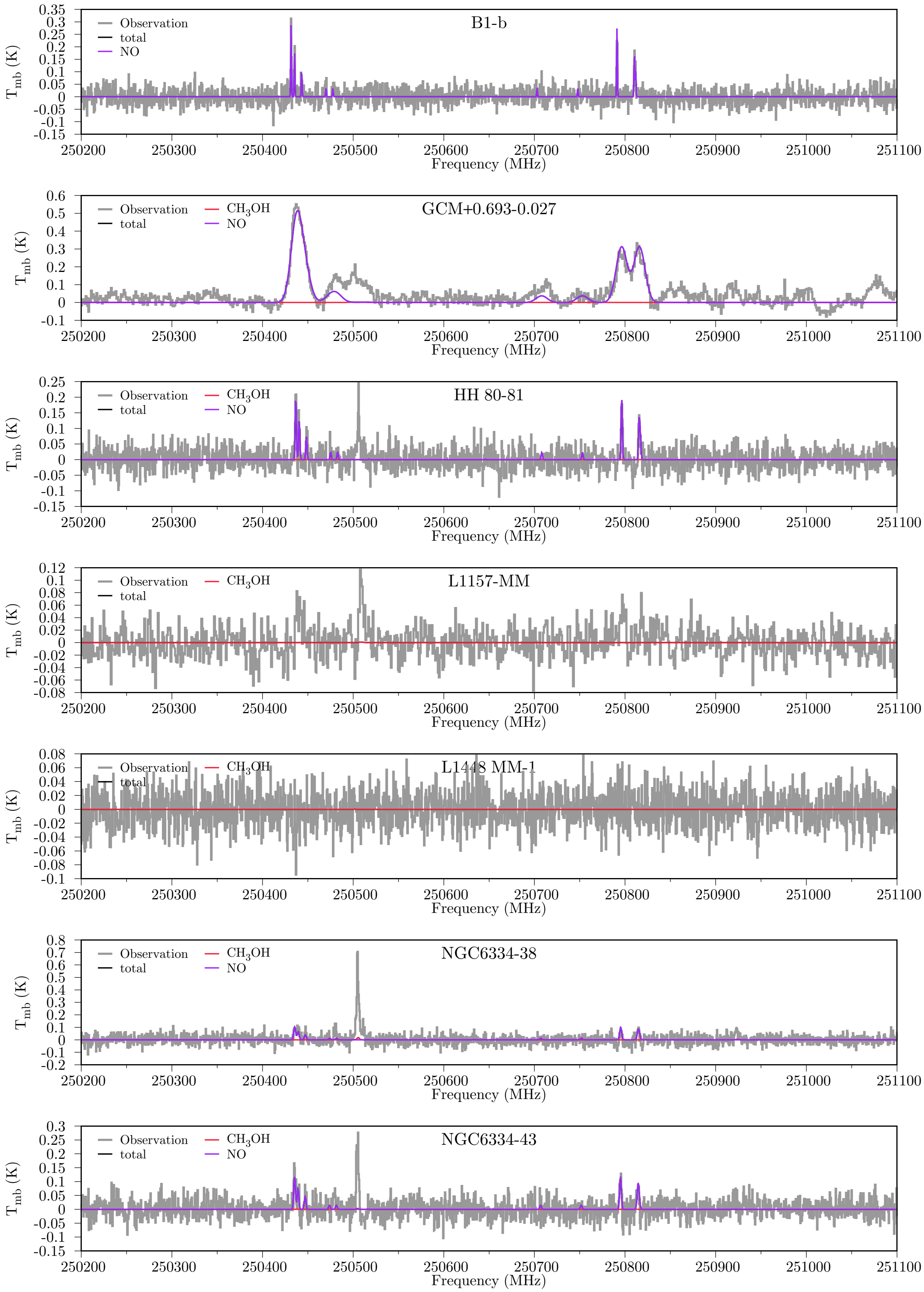

Figure 6.2: Sample frequency window of molecular components fitted in the global LTE analysis. The CH_3OH line at 250510 MHz is non-LTE. *Continued on next page.*

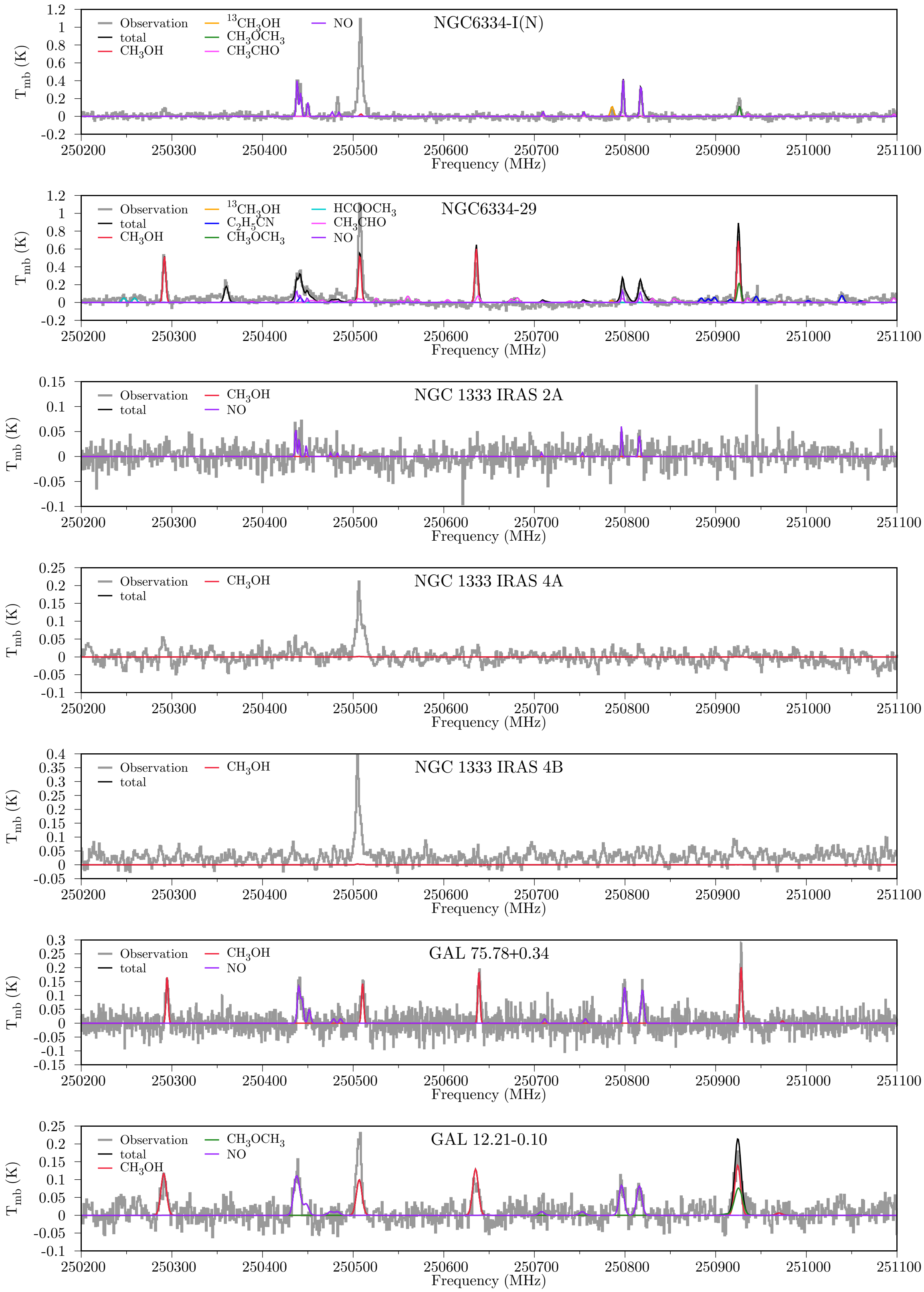

Figure 6.2: Sample frequency window of molecular components fitted in the global LTE analysis. The CH_3OH line at 250510 MHz is non-LTE. *Continued on next page.*

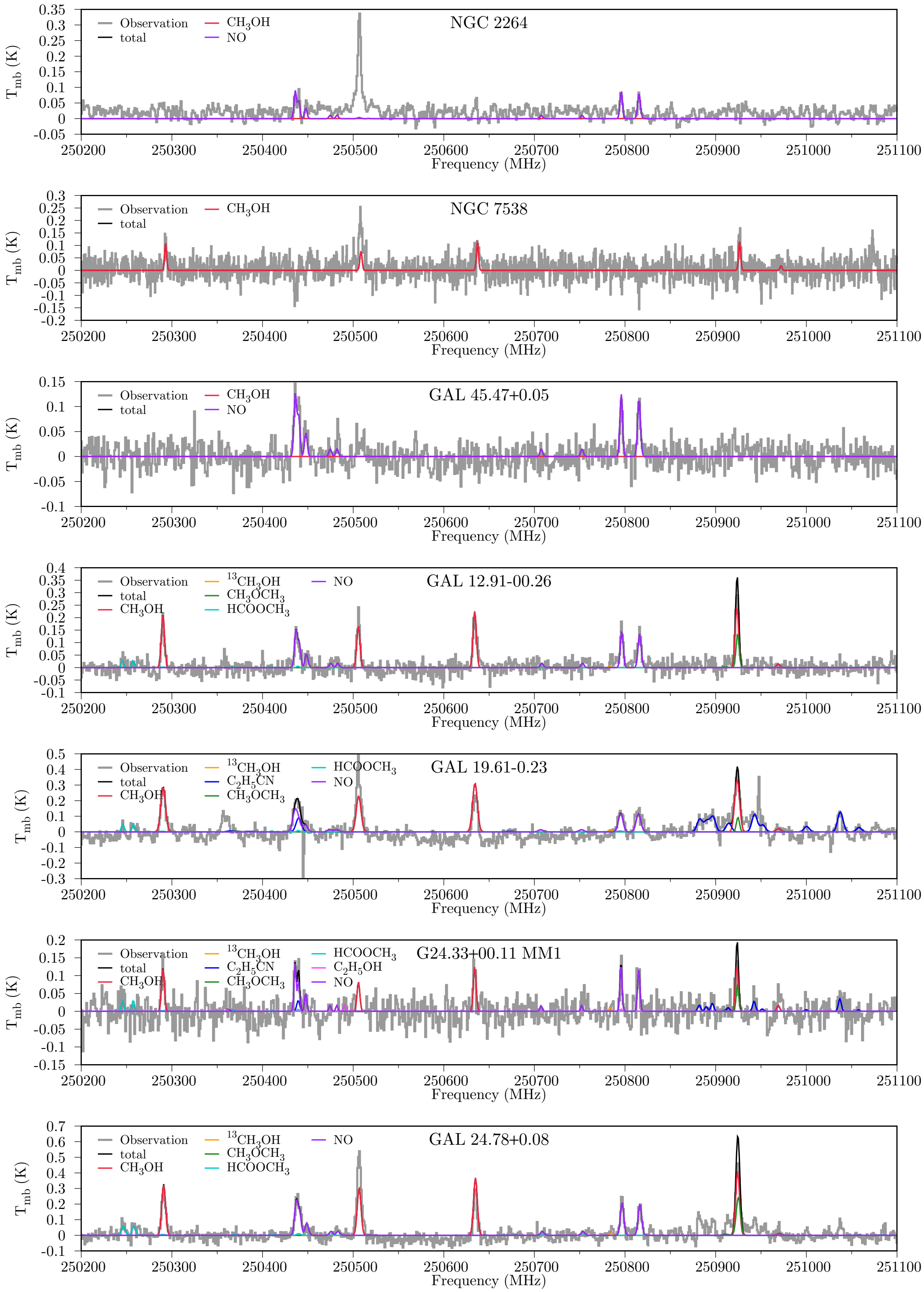

Figure 6.2: Sample frequency window of molecular components fitted in the global LTE analysis. The CH_3OH line at 250510 MHz is non-LTE. *Continued on next page.*

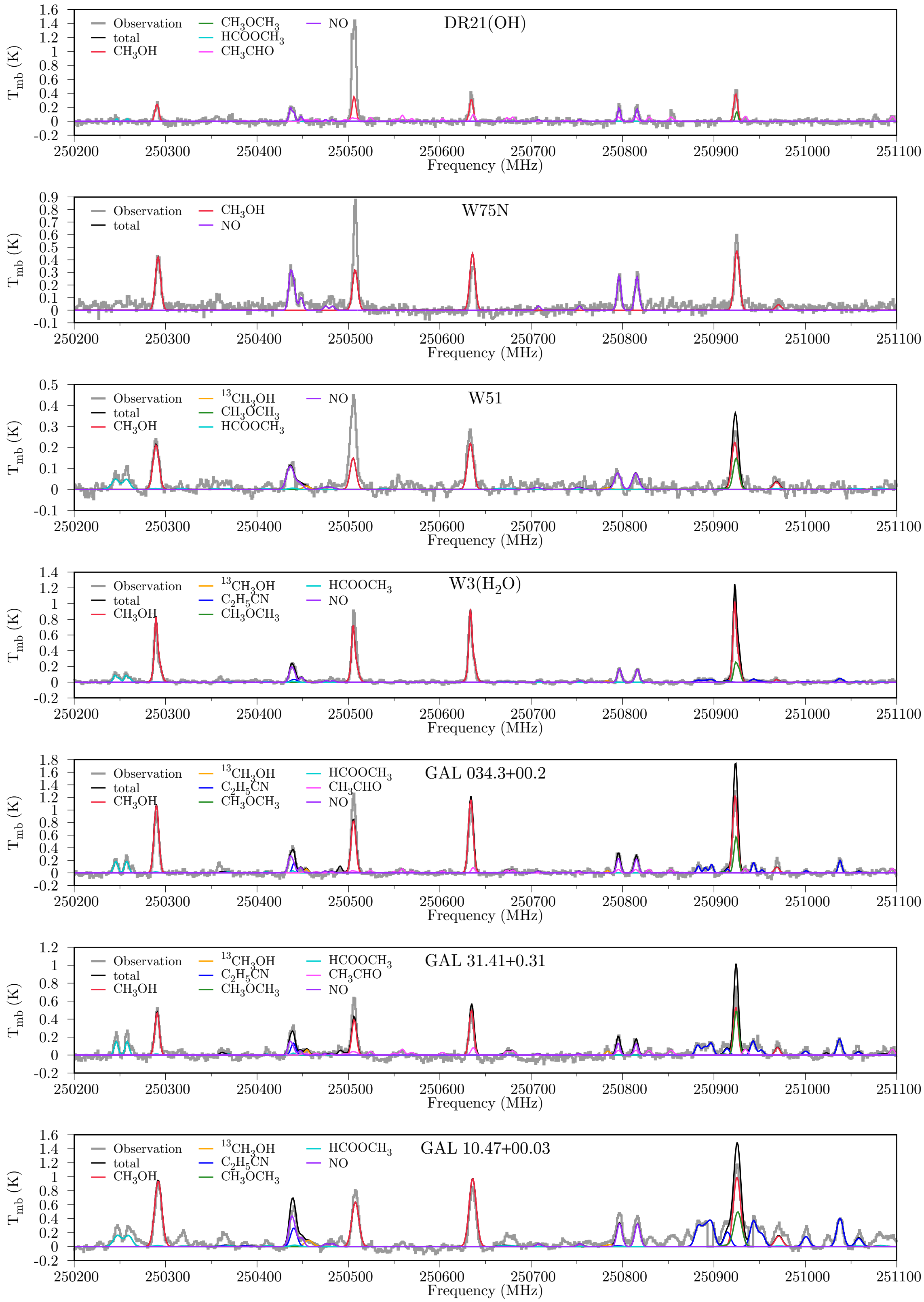

Figure 6.2: Sample frequency window of molecular components fitted in the global LTE analysis. The CH_3OH line at 250510 MHz is non-LTE. *Continued on next page.*

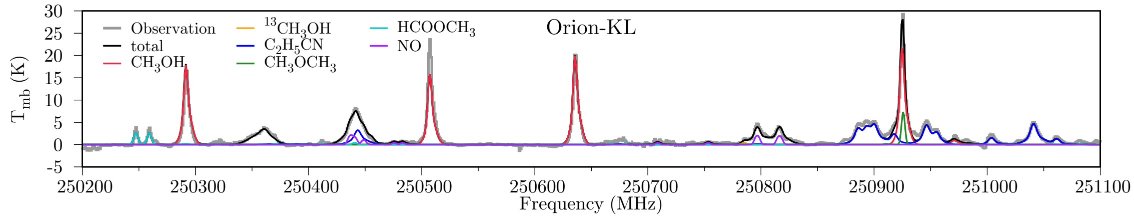

Figure 6.2: Sample frequency window of molecular components fitted in the global LTE analysis. The CH_3OH line at 250510 MHz is non-LTE.

Table 6.4: Detected molecules in 31 sources, their LTE parameters, and associated 1σ uncertainties. The four LTE parameters are the column density N_T in cm^{-2}, the rotational temperature T_{rot} in K, the FWHM in $km{\cdot}s^{-1}$, and the red shift with respect to v_{lsr}, δv, in $km{\cdot}s^{-1}$. Only molecules with more than three clean lines at different upper state energies can be fit to a reliable T_{rot}. Other small molecules are fit with arbitrary N_T and T_{rot}, and their associated uncertainties may be unphysically large.[a]

Source	Molecule	N_T (cm^{-2})	T_{rot} (K)	FWHM ($km{\cdot}s^{-1}$)	δv ($km{\cdot}s^{-1}$)
B1-b	SO	$6 \pm 1 \times 10^{13}$	9.9 ± 0.5	1.2 ± 0.0	6.7 ± 0.0
DR21(OH)	CH_3CCH	$124 \pm 4 \times 10^{13}$	36.8 ± 1.0	5.0 ± 0.2	0.1 ± 0.1
DR21(OH)	CH_3CHO	$8 \pm 1 \times 10^{13}$	139 ± 24	5.5 ± 0.4	0.2 ± 0.1
DR21(OH)	CH_3CN	$231 \pm 5 \times 10^{11}$	56.7 ± 2.1	5.4 ± 0.2	0.6 ± 0.1
DR21(OH)	CH_3OH	$176 \pm 2 \times 10^{13}$	18.2 ± 0.3	5.6 ± 0.1	0.3 ± 0.0
DR21(OH)	CH_3OH	$152 \pm 3 \times 10^{13}$	92.8 ± 2.4	5.9 ± 0.2	0.8 ± 0.0
DR21(OH)	CH_3OCH_3	$35 \pm 2 \times 10^{13}$	60.0 ± 4.9	4.1 ± 0.4	0.3 ± 0.2
DR21(OH)	H_2CCO	$30 \pm 3 \times 10^{12}$	58.0 ± 9.7	4.8 ± 0.8	0.4 ± 0.2
DR21(OH)	H_2CS	$148 \pm 2 \times 10^{12}$	53.7 ± 1.6	5.6 ± 0.1	0.6 ± 0.0
DR21(OH)	HCCCN	$10 \pm 2 \times 10^{12}$	79 ± 12	6.0 ± 0.3	0.4 ± 0.1
DR21(OH)	$HCOOCH_3$	$107 \pm 7 \times 10^{12}$	81 ± 26	4.1 ± 0.4	0.2 ± 0.2
DR21(OH)	HDCO	$12 \pm 6 \times 10^{12}$	79 ± 42	4.8 ± 0.6	0.6 ± 0.2
DR21(OH)	OCS	$4 \pm 1 \times 10^{14}$	42.3 ± 8.5	5.4 ± 0.4	0.6 ± 0.1
DR21(OH)	SO	$431 \pm 2 \times 10^{12}$	36.2 ± 0.5	6.5 ± 0.0	0.9 ± 0.0
DR21(OH)	SO_2	$288 \pm 7 \times 10^{12}$	75.6 ± 2.6	7.7 ± 0.2	1.6 ± 0.1
DR21(OH)	^{33}SO[b]	$6 \pm 86 \times 10^{14}$	9.7 ± 35.8	5.8 ± 10.9	1.9 ± 2.8
DR21(OH)	^{34}SO[b]	$29 \pm 8 \times 10^{12}$	39 ± 76	6.3 ± 1.7	1.4 ± 0.6

[a] The full table in a machine-readable format is printed verbatim in Appendix C.

[b] The unphysically large uncertainties indicate the spectral lines of this molecule are detected, but they are insufficient to perform a reliable LTE analysis.

abundance of the carrier molecule in that source, or from beam dilution if the carrier molecule's spatial distribution is compact compared to the single-dish beam.

6.5 Discussion

Given that this set of sources was targeted because they are known to be rich in COMs, it does not come as a surprise that many of these sources have extremely rich chemistry. Nonetheless, some surprises are still found in the results from these observations. Additionally, trends can be discerned that offer insight into chemical pathways that have long been assumed for star-forming regions. An overview of the results in graphical form is given in Figure 6.3. Here we plot the column density for a set of molecules as colored circles. The area of each circle was scaled to the magnitude of the column density. The color of each circle corresponds to the temperature, the scale for which is shown on the right. Sources are sorted on the horizontal axis by type, and within each type the chemical complexity of the sources is arranged to increase from left to right. The molecules are sorted on the vertical axis, grouped into the O-bearing, N-bearing, and S-bearing species. Within each group, molecules on the top are more frequently detected in the sources. As such, trends are easily discernable in the dataset. For molecules with multiple temperature and velocity components, we plot concentric circles with each ring representing one component. The column density of molecules in Orion-KL was divided by 10 before plotting.

Here we will not attempt a detailed discussion of each molecule detected in each source and the corresponding implications, but rather will save that level of detail for subsequent papers that examine a particular chemical or physical subset from this dataset. Nonetheless, we can immediately find general trends in these results that offer glimpses into the power of such comprehensive observational studies. The most striking features of these results as gleaned from Figure 6.3 are as follows:

1. Most sources are chemically complex. Among different source types, hot cores

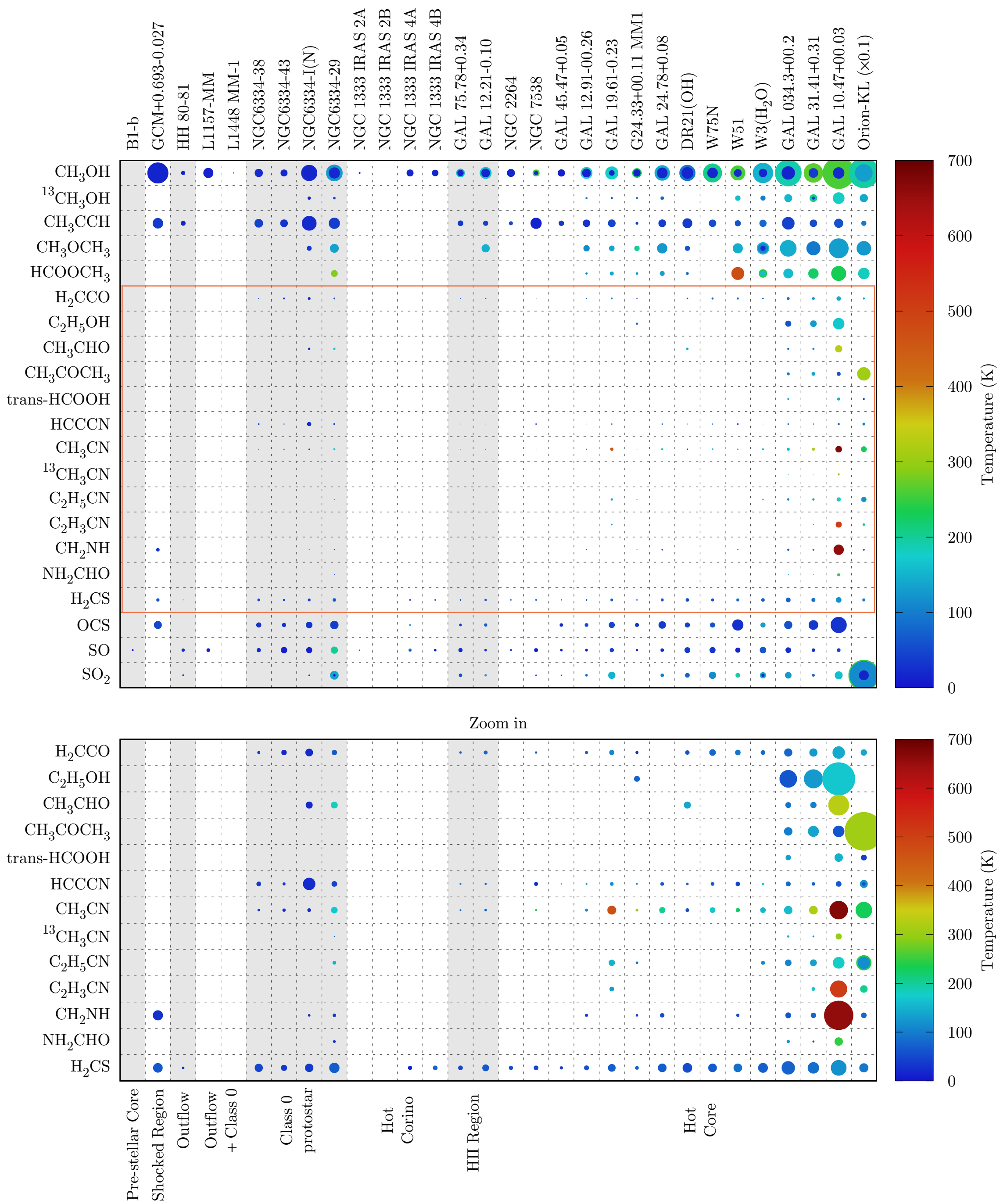

Figure 6.3: Visualization of Table 6.4: Column density and LTE temperature. Sources are on the horizontal axis, and molecules are on the vertical axis. Areas of the circles are proportional to the column density of molecules. Circles for Orion-KL are shrunk by a factor of 10 in area to fit the overall scale of the plot. For molecules with multiple temperature components, concentric circles are drawn, with each ring stands for one particular component. The color of the circles maps the LTE temperature of the molecules. The full scale plot is presented on the top panel, and the zoomed-in region, highlighted by the orange frame, is presented on the bottom panel.

present the most complex chemistry, indicated by the large number of COMs observed in these sources. Protostars present some level of complexity. Hot corinos are quiet in this survey, likely due to their small source sizes and therefore severe beam dilution effect. Some observed complexity is not inherently a surprise, given that these sources were chosen because COMs had already been detected in previous observations. But the level of complexity in many of these sources is comparable to that of Orion-KL, and that is a surprise. The most striking case is that of GAL 10.47+00.03, which displays a remarkable array of COMs at abundances rivaling those observed in Orion-KL.

2. Methanol, CH_3CCH, H_2CS, OCS, SO, and SO_2 are nearly ubiquitous in this sample set. Methanol, SO, and SO_2 are known to be indicators of grain mantle disruption [149–151]. Hence it is possible that these other ubiquitous molecules are also indicators of this process. It is particularly striking that all of the major sulfur-bearing species are on this list.

3. CH_3OH is, not surprisingly, ubiquitous. For most hot cores, two CH_3OH temperature components can be found: a cold one of 10–30 K, and a warm one whose temperature ranges from 100 to 300 K, a variable dependent on the size and evolutionary stage of the central star. The ratio between the $^{13}CH_3OH$ and CH_3OH isotopologues seems to be consistent at $\sim$0.1. Therefore $^{13}CH_3OH$ was only detected in massive star-forming regions with a high CH_3OH abudance.

4. CH_3CCH is nearly as ubiquitous and abundant as CH_3OH, and it is always cold. The abundance of CH_3CCH is surprising. It is thought to be a convenient tracer for dense clouds [152].

5. It is not surprising that the S-bearing molecules, H_2CS, OCS, SO, and SO_2 are nearly ubiquitous in this sample set, since they are simpler than COMs, and therefore have stronger spectral lines. S-bearing molecules are proposed to

be the indicators of grain-mantle disruption and material injection into the gas phase during the star-formation process, and therefore can be used as a chemical clock to trace the evolutionary stage of the source [149–151]. Wakelam *et al.*, however, argued that this chemical clock approach is not that straightforward [153].

In our surveys, it appears that SO is always present. It is definitively detected in Orion-KL. SO and OCS are definitely detected in Orion-KL, but not listed as detections because the narrower spectral coverage for Orion-KL provides insufficient information to perform LTE analysis on these molecules. H_2CS correlates well with SO across our sources, while OCS and SO_2 do not always coexists. In NGC 1333 IRAS 4A, NGC6334-38, NGC6334-43, and G24.33+00.11 MM1, we only detected OCS but not SO_2. Since SO_2 is generally less abundant than OCS and SO in other sources, the non-detection of SO_2 in NGC 1333 IRAS 2A may simply be caused by its low spectral intensity, which is below our detection limit. NGC6334-38, NGC6334-43, and G24.33+00.11 MM1, however, present significant OCS abundances. In HH 80-81 and NGC 7538 IRS 1, we only detect SO_2 but not OCS. For sources where all 4 S-bearing molecules are detected, the abundance ratios vary dramatically from source to source. For example, GAL 10.47+00.03 and W51, compared to other hot cores, have significantly more OCS than the rest of S-bearing molecules. Orion-KL is the anomaly on the other extreme: it has extensive amount of SO_2, which is as abundant as CH_3OH. In general, we conclude that the abundance of S-bearing small molecules cannot be explained by a simple correlation to the evolutionary stage of the star-forming region. Our observations agree with the argument addressed by Wakelam *et al.*

6. Nearly all molecules detected that have a CN group are found at elevated temperatures relative to O-bearing COMs. Despite the prevalence of these species in

these sources, they are present at much lower abundances than their O-bearing counterparts. The variation of the CH_3CN temperature across sources is also large. Unlike CH_3CCH which is always cold, or CH_3OCH_3 and $HCOOCH_3$ which are always warm but only present in chemically evolved sources, CH_3CN is nearly ubiquitously detected, and its temperature correlates with the source type. C_2H_3CN and C_2H_5CN, the two "interstellar weeds" thought to be ubiquitous in the ISM, are only detected in a handful of massive star-forming regions with the richest chemistry and most elevated temperatures. It is possible that the cyanides larger than CH_3CN are both warm and compact, and therefore beam diluted. The abundance of C_2H_5CN is surprisingly low relative to CH_3CN, despite their nearly equal abundance in Orion-KL.

7. There may be a chemical link between dimethyl ether and methyl formate during grain-surface chemistry (see Garrod *et al.* for a lengthy discussion [15]). Based on our results, although these two species are often both present in a given star-forming region, there is no clear correlation between their abundances. In general, CH_3OCH_3 is more abundant and colder than $HCOOCH_3$. The ratio between CH_3OCH_3 and $HCOOCH_3$ column density is not consistent throughout our sample set. This result is surprising, given that they are both presumed to form from grain-surface processes involving CH_3O radicals. Beam dilution can contribute to this inconsistency if CH_3OCH_3 and $HCOOCH_3$ have different spatial distributions. It is unclear if scaling by the spatial scale of the emission would result in column densities that are correlated; additional interferometric observations are warranted.

8. Previous interferometric studies of methyl formate in Orion indicate that it is formed on grain-surfaces and detected in the colder, extended regions rather than in the hot core [122, 125]. Surprisingly, methyl formate is shown here to

be present at warmer temperatures than CH_3OCH_3 and most of the other O-bearing COMs that are detected. The reason for this is unclear. In Orion-KL, methyl formate, similar to methanol, has both an extended, cold component and a hot, compact component [122]. It is possible that we could sufficiently describe its spectral intensity with one temperature component due to its weaker overall line intensities, and this temperature is in fact an averaged value from two different temperatures. If the warm component can be found in multiple sources, it is not impossible that the gas-phase formation mechanisms for $HCOOCH_3$ [10] are still relevant, although they do not account for all the observed $HCOOCH_3$ abundance. Further interferometric investigation of its spatial distribution as a function of temperature is warranted.

9. Complex O-bearing species such as C_2H_5OH, CH_3CHO, *trans*-HCOOH, and NH_2CHO are not highly abundant in these sources. They are only detected in a few sources. Indeed, complex molecules are more difficult to find, because of their weaker line intensities and their lower abundances. But our result has huge implications for more complex chemistry, as many of these species are thought to be chemical precursors to more complex molecules. If these molecules are even less abundant than what was anticipated before, the formation routes for more complex molecules are uncertain.

10. Interstellar acetone has only been detected in Sgr B2 (N-LMH) [130] and Orion-KL [112]. It is now detected in two additional sources, GAL 31.41+0.31 and GAL 034.4+00.2, where detections had not been reported before.

11. The complexity of chemistry may not be directly correlated with elevated temperature. NGC6334-29 and NGC6334-I(N) have similar chemistry, but NGC6334-I(N) is significantly colder than NGC6334-29. In NGC6334-I(N), CH_3OCH_3 and CH_3CHO are present at 35 K and 20 K, respectively. In NGC6334-

29, CH_3OCH_3 and CH_3CHO are present at 135 K and 182 K, respectively. The cold CH_3OCH_3 and CH_3CHO indicates the gas-grain chemistry origin of these O-bearing molecules, but what unique process causes their sublimation into the gas-phase in NGC6334-I(N) in such a cold environment is not clear. Likewise, GAL 034.3+0.02 presents similar chemical complexity to GAL 31.41+0.31, but its averaged temperature of COMs is lower.

12. The non-LTE CH_3OH emissions, $8_{-1,8} \rightarrow 7_{0,7}$ ($E_{\rm low}$ = 78 K) at 229.76 GHz, and $11_{0,11} \rightarrow 10_{1,10}$ ($E_{\rm low}$ = 141 K) at 250.51 GHz are found primarily in shocks and HII regions. These two non-LTE lines do not appear in B1-b, GAL 12.91-00.26, G24.33+00.11 MM1, GAL 45.47+0.05, GAL 75.78+0.34, L1448 MM-1, NGC 1333 IRAS 2A, and W3(H_2O). In all other sources, they are observed in flux much larger than the CH_3OH simulation by the LTE model.

6.6 Search for HO_3 in star-forming regions

The content in this section is reprinted with permission from L. Zou, B. M. Hays, S. L. Widicus Weaver, J. Phys. Chem. A. 120, 657 (2016). Copyright (2016) American Chemical Society.©

After the LTE analysis of COMs in the 31 CSO surveys, we can search for HO_3 using the laboratory spectra obtained in Chapter 3. We used the SPCAT program in CALPGM suite [75] to simulate a line catalog using the molecular parameters given in Table3.1. The partition function was interpolated using the equation $Q(T) = \alpha T^{1.5}$. The rotational temperature $T_{\rm rot}$ and FWHM of the trial fit of HO_3 was constrained to the weighted average of these values found for other molecules in that source, with the weighting set as the reciprocal of their estimated uncertainty. Unfortunately, no transitions of *trans*-HO_3 were found in any of these observational line surveys. Therefore, the fitted column density was interpreted as an upper limit for HO_3 column density in each source, without the correction for beam dilution. The results of this analysis are summarized in Table 6.5. No information is included here for Sgr B2(N), because severe line confusion and blending precluded analysis for HO_3.

Table 6.5: Estimation of column density upper limits of HO_3 in astronomical sources. The listed $T_{\rm rot}$ and FWHM are the weighted average values from other molecules fitted in each source, and were fixed during the analysis for HO_3.

Source	Column Density (cm^{-2})	$T_{\rm rot}$ (K)	FWHM ($km \cdot s^{-1}$)
W3(H_2O)	$\leq 6.9 \times 10^{13}$	48.9	6.6
L1448 MM-1	$\leq 2.4 \times 10^{12}$	17.7	1.3
NGC 1333 IRAS 2A	$\leq 3.2 \times 10^{12}$	22.4	3.4
NGC 1333 IRAS 2B	$\leq 9.0 \times 10^{11}$	10[a]	1[b]
NGC 1333 IRAS 4A	$\leq 2.2 \times 10^{12}$	18.9	9.6
NGC 1333 IRAS 4B	$\leq 3.2 \times 10^{13}$	20.0	5.5
B1-b	$\leq 1.8 \times 10^{14}$	9.9	1.2
Orion-KL	$\leq 1.2 \times 10^{15}$	80.6	9.4
NGC 2264 MM3	$\leq 3.1 \times 10^{13}$	20.4	4.5
NGC6334-29	$\leq 4.1 \times 10^{13}$	49.6	5.4
NGC6334-38	$\leq 5.2 \times 10^{12}$	26.4	3.5
NGC6334-43	$\leq 1.3 \times 10^{13}$	16.0	3.1
NGC6334-I(N)	$\leq 8.8 \times 10^{13}$	20.2	3.9
GCM+0.693-0.027	$\leq 3.0 \times 10^{15}$	10[a]	14.1[c]
GAL 10.47+00.03	$\leq 2.1 \times 10^{14}$	62.0	10.8
GAL 12.21-0.10	$\leq 2.0 \times 10^{13}$	28.9	8.2
GAL 12.91-00.26	$\leq 4.9 \times 10^{12}$	29.4	4.9
HH 80-81	$\leq 1.5 \times 10^{12}$	19.0	2.4
GAL 19.61-0.23	$\leq 5.2 \times 10^{13}$	53.7	9.0
G24.33+00.11 MM1	$\leq 1.9 \times 10^{12}$	18.2	4.7
GAL 24.78+0.08	$\leq 2.1 \times 10^{13}$	38.0	7.2
GAL 31.41+0.31	$\leq 2.7 \times 10^{13}$	79.1	7.4
GAL 034.3+00.2	$\leq 3.7 \times 10^{13}$	45.8	6.8
GAL 45.47+0.05	$\leq 5.2 \times 10^{11}$	15.1	4.6
W51	$\leq 6.7 \times 10^{13}$	49.0	9.2
GAL 75.78+0.34	$\leq 4.2 \times 10^{12}$	28.0	4.2
W75N	$\leq 1.2 \times 10^{14}$	42.7	5.6
DR21(OH)	$\leq 3.4 \times 10^{13}$	39.0	6.0
L1157-MM	$\leq 1.7 \times 10^{13}$	14.3	5.8
NGC 7538	$\leq 3.1 \times 10^{11}$	19.0	3.7

[a] No temperature information is available. The temperature was assumed to be 10 K.
[b] FWHM assumed to be 3 times the channel width, which is $\sim$1 $km \cdot s^{-1}$.
[c] FWHM of CS.

The results of this initial search for HO_3 are not surprising, especially given that this particular source sample focused on warmer regions of star formation, where weakly-bound clusters might not be prevalent. Nonetheless, there are several cold pre-stellar cores included in this sample, and yet HO_3 was not detected in any of them. An estimate of expected HO_3 abundance reveals the challenge of such a search. We estimate the HO_3 fractional abundance in dense interstellar clouds to be $\sim 10^{-14}$ with respect to the abundance of molecular hydrogen. This estimate assumes that the dominant loss mechanism would be photodissociation, and uses typical dark cloud abundances for OH and O_2 [154]. Based on this estimated abundance, the brightest HO_3 rotational line at 20 K would result in an observational signal intensity of $\sim$0.01 mK. This is well below the detection limit for these observations, where the noise level is $\leq$25 mK.

Despite this lack of detection, there is still a possibility for HO_3 detection in future observations. Recent advances in radio interferometry lead to sensitivity levels that approach what is required for HO_3 detection. For example, a 10 min integration of ALMA array at 240 GHz with 1 MHz bandwidth would achieve a noise level of 10 mK;[2] additional integration time has the potential of achieving the desire sensitivity. Therefore, detection of HO_3 at this signal intensity would be challenging even for the most sensitive observations, but is not completely ruled out. It should be noted that our abundance predictions are highly conservative, and HO_3 may be detectable in other regions with higher O_2 abundance such as O-rich stellar envelopes.

6.7 Summary

We conducted broadband spectral line surveys of 31 star-forming regions in the 1.3 mm band (220–267 GHz) using the 10.4 m Leighton Telescope at the Caltech Submillimeter Observatory. The deconvovled spectra are presented. For each spectrum, we performed a global LTE analysis for molecules with sufficient number of spectral

[2]Calculated by ALMA sensitivity calculator at https://almascience.eso.org/about-alma/proposing/sensitivity-calculator

lines and intensities, using the GOBASIC program. The result of this analysis indicates a series of expected and unexpected trends. Some molecular tracers, such as CH_3OH, CH_3CCH, and SO, are ubiquitously detected in these sources. The difference in chemical complexity between hot cores, hot corinos, and class 0 protostars is verified. Within each type of star-forming regions, however, unexpected variations on the molecular complexity, abundance, and temperatures, are present. No straightforward correlations between different COMs can be drawn. It seems that each source demonstrates a unique chemistry. Because of the large size of the single-dish beam, line intensities are diluted, and spatial distribution of different molecules cannot be resolved. To reveal the details of astrochemistry in these star-forming regions, more information from interferometric studies on these sources is required so that source size can be properly included in the analysis.

Once the global LTE analysis is performed, we can search for potential interstellar molecules using their laboratory spectra, which allow reliable line catalog simulation. To address the possible importance of weakly bound clusters like HO_3 in the astrochemistry of star-forming regions, we attempted a preliminary search for HO_3 in these sources. Unfortunately, no HO_3 was detected in these line surveys, likely due to the presumably low abundance of HO_3. Nonetheless, upper limits were estimated for each of these sources. Additionally, the updated spectral line catalog based on new experimental measurements presented here is expected to guide new astronomical searches in other sources that have high expected abundances of HO_3.

Chapter 7 Conclusion and Future Outlook

In this dissertation, I presented the laboratory and astronomical perspectives of astrochemistry questions. To unravel the details of reaction mechanisms in star-forming regions, searches for unstable molecules in the sources based on precisely measured laboratory rotational spectra are of particular importance. Chapter 2 describes the spectrometer design and the supersonic expansion source that was implemented for studying unstable molecules using plasma discharge chemistry. This chapter demonstrates the performance of the fast-sweep technique, the preliminary concept for which was described in [32]. Chapter 3 and 4 illustrate the application of this fast-sweep technique in searching for spectral lines of unstable molecules, using the example of the weakly-bound radical *trans*-HO_3 and the van der Waals dimer Ar–H_2O. Chapter 5 and 6 presented the global analysis of broadband astronomical line surveys on 32 star-forming regions, from which insightful trends about the chemical complexity in these sources were drawn. The laboratory measurement of *trans*-HO_3 enabled a search for this molecule in these sources after the analysis presented in Chapter 6. The upper limit of *trans*-HO_3 column density was determined.

The results presented in this dissertation lead to the future work on the astrochemistry of star-forming regions. The future work may include these directions:

- The concept of fast-sweep can be generalized and applied to the search for other astrochemically relevant radicals, ions, and molecular clusters.

- The broadband analysis approach can be further improved to combine single-dish line surveys and interferometric images, which are able to reveal the spatial distribution of molecules. Being able to resolve the structure of star-forming regions provides more reliable estimation of the column density and temperature of molecules, and kinematics can be studied.

- The GOBASIC program can be upgraded to model non-Gaussian lineshapes, non-LTE spectral emissions, and temperature gradients.

Appendix A Python Script for the Fast-sweep Technique

```
# encoding = utf8
''' This script processes the linear-sweep data for pulsed experiment.
It is REQUIRED that the data takes full cycles of sweeps. '''

import argparse
import numpy as np
import re
from scipy import interpolate
from scipy.optimize import leastsq

# ------------------------------------------
# ------ MESSAGE CONSTANT DECLARATION ------
# ------------------------------------------
FILE_ERR_MSG = {0: '',                                   # Silent
                1: '{:s} does not exist',                # FileNotFoundError
                2: '{:s} format is not supported',       # Format Issue
                3: '{:s} contains an object array that is not allowed to load'
                # npy allow_pickle=False exception
                }

# -------------------------------------------------------
# ------ Function Declaration (Alphabetical Order) ------
# -------------------------------------------------------

def analyze_txt_fmt(file_name):
    ''' Analyze the data text format: delimiter and header

    Arguments:
    file_name -- data file name, str

    Returns:
    delm -- delimiter, str
    hd   -- number of header rows, int
    eof  -- end of file, boolean
    '''

    hd = 0
    delm = None
    a_file = open(file_name, 'r')
    # match two numbers and a delimiter
    pattern = re.compile(
              '(-?\d+\.?\d*(e|E.?\d+)?)( |\t|,)+(-?\d+\.?\d*(e|E.?\d+)?)')

    for a_line in a_file:
        if re.match('-?\d+\.?\d*(e|E)?.?\d+ *$', a_line):
```

```
            # if the first line is a pure number
            delm = ','
            break
        else:
            try:
                delm = pattern.match(a_line).group(3)
                break
            except AttributeError:
                hd += 1

    # check if end of the file is reached
    eof = (a_file.read() == '')

    a_file.close()

    return delm, hd, eof


def avg_inten(inten, pts, fg):
    ''' Average all intensity sweeps with the same parity to fg togethere.

    Arguments:
    inten -- intensity waveform, 1D/2D np.array
    pts   -- number of data points in a single sweep, int
    fg    -- signal ordinal number, int

    Returns:
    inten_avg -- averaged intenisity array, 1D/2D np.array
    '''

    # determine fg parity and total number of sweeps
    parity = fg % 2
    sweep_num = inten.shape[0] // pts

    # generate ordinal numbers than match the fg parity
    ordinal = np.arange(sweep_num) + 1
    match_parity = ordinal[ordinal % 2 == parity]

    # Extract cycles and sum up
    if len(inten.shape)==1:
        inten_ext = np.zeros(pts)
        for i in match_parity:
            inten_ext += inten[(i-1)*pts:i*pts]
    else:
        inten_ext = np.zeros((pts, inten.shape[1]))
        for i in match_parity:
            inten_ext += inten[(i-1)*pts:i*pts, :]

    # return the average
    return inten_ext / len(match_parity)


def box_car(x, win):
    ''' Boxcar smooth.
```

```
    Arguments:
    x   -- x frequency array, np.array
    win -- box-car window, integer

    Returns:
    x_new -- new x array, np.array
    '''

    if win == 1:
        return x
    else:
        x_new = np.convolve(x, np.ones(win), 'valid')/win
        return x_new


def box_win(win):
    ''' Verify boxcar window.

    Arguments:
    win -- box-car window, integer

    Returns:
    win_verified -- verified box-car window, odd integer
    '''

    win_verified = abs(win)
    if win_verified == 0:
        return 1
    elif not (win_verified % 2):
        return win_verified + 1
    else:
        return win_verified


def check_type(var):
    ''' Check data type of variables. If var is None, exit the program '''

    if isinstance(var, type(None)):
        exit()
    else:
        pass


def delay_inten(inten, delay):
    ''' Delay intensity array.

    Arguments:
    inten -- intensity array, nd.array
    delay -- delay number of points.

    Returns:
    inten_new -- delayed intensity array
    '''
```

```
    dim = inten.shape[0]
    # check the dimension of intensity array
    if len(inten.shape)==1:
        inten_new = np.roll(inten, dim - delay)
    else:
        inten_new = np.roll(inten, dim - delay, axis=0)

    return inten_new


def db_poly(y, deg=1):
    ''' Polynomial baseline clean.

    Arguments:
    y -- input array, 1D np.array

    Returns:
    y_db -- debaselined array, 1D np.array
    '''

    x = np.arange(len(y)) / (len(y)-1)
    popt = np.polyfit(x, y, deg)

    return y - np.polyval(popt, x)


def db_spline(y):
    ''' Background subtraction by fitting spline to the baseline.

    Arguments:
    y -- input array, 1D np.array

    Returns:
    y_db -- debaselined array, 1D np.array
    '''

    # Because of the discharge disturbance, the background does not exactly
    # match the signal. This creates a curved baseline after background
    # subtraction. Try to fit a B-spline to the baseline.
    x = np.arange(len(y)) / (len(y)-1)
    # Construct weight
    weight = weight_spline(y)
    w_nonzero = np.not_equal(weight, 0)
    # Interpolate spline
    spline = interpolate.UnivariateSpline(x, y, w=weight, k=5)
    # Remove spline
    y_db = y - spline(x)
    # Remove linear feature
    ppoly = np.polyfit(x[w_nonzero], y_db[w_nonzero], 1)
    y_db = y_db - np.polyval(ppoly, x)

    return y_db
```

```
def err_msg_str(f, err_code, msg=FILE_ERR_MSG):
    ''' Generate file error message string

    Arguments:
    f        -- file name, str
    err_code -- error code, int
    msg      -- error message, dict

    Returns:
    msg_str -- formated error message, str
    '''

    return (msg[err_code]).format(f)


def extract_fg(inten, fg, pts):
    ''' Background subtraction routine.

    Arguments:
    inten -- intensity waveform, 1D/2D np.array
    fg    -- ordinal number of the signal sweep, int
    pts   -- number of data points in a single sweep, int

    Returns:
    inten_sig -- Extracted array, 1D/2D np.array
    '''

    if len(inten.shape)==1:     # if intensity is 1D array
        inten_sig = inten[(fg-1):fg*pts]
    else:                       # if intensity is 2D array
        inten_sig = inten[(fg-1)*pts:fg*pts, :]

    return inten_sig


def flat_wave(freq, inten, nobase=False):
    ''' Flatten frequency and intensity arrays.

    Arguments:
    freq  -- frequency array, 1D/2D np.array
    inten -- intensity array, 1D/2D np.array
    nobase -- input argument option (do not perform intensity stitch)

    Returns:
    freq_flat  -- flattened frequency array, 1D np.array
    inten_flat -- flattened intensity array, 1D np.array
    '''

    if len(inten.shape)==1:
        # sort frequency
        sort_index = np.argsort(freq)
        return freq[sort_index], inten[sort_index]
    else:
```

```
        # Flatten frequency and intensity matrices into vector waveforms
        #freq_flat_index = np.argsort(freq.flatten('F'))
        #freq_flat = freq.flatten('F')[freq_flat_index]
        #inten_flat = inten.flatten('F')[freq_flat_index]

        # check frequency array: decreasing freq or increasing freq
        up_bool = freq[0, 0] < freq[-1, 0]

        if up_bool:
            pass
        else:   # flip freq and inten array upside down
            freq = np.flipud(freq)
            inten = np.flipud(inten)

        freq_flat = freq.flatten('F')
        if nobase:      # no stitch intensity
            inten_flat = inten.flatten('F')
        else:
            inten = glue_sweep(inten)
            inten_flat = inten.flatten('F')

        return freq_flat, inten_flat


def flip(signal, ordinal):
    ''' Flip signal array upside down if is even ordinal sweep.

    Arguments:
    signal -- signal array, 1D/2D np.array
    ordinal -- ordinal number, int

    Returns:
    flipped -- flipped signal if necessary, 1D/2D np.array
    '''

    if (ordinal % 2):
        return signal
    else:
        return np.flipud(signal)


def glue_sweep(y):
    ''' shift each sweep intensity to make the end of the previous sweep is
    equal to the start of the next sweep, so that the spectrum is
    continuous.

    Arguments:
    y -- intensity array, 2D np.array

    Returns:
    y_stitched -- stitched intensity array, 2D np.array
    '''

    # Get the difference of the end of col and the start of col+1
```

```
    col_shift = np.roll(y[-1, :], 1) - y[0, :]
    col_shift[0] = 0
    col_shift_accum = np.cumsum(col_shift)

    # Apply shift correction to all columns
    y_stitched = y + np.tile(col_shift_accum, (y.shape[0], 1))

    return y_stitched


def load_data(args):
    ''' Load all data files specified from input arguments. Perform background
    subtraction and data truncation according to input specifications.

    Arguments:
    args -- input argument, argparse Object

    Returen:
    freq -- frequency waveform, np.array 1D
    inten -- intensity waveform, np.array 1D/2D
    '''

    # load intensity file
    inten = load_single_file(args.inten[0])
    # exit if intensity file is not loaded correctly
    check_type(inten)

    # load lo file if available
    if args.lo:
        lo = load_single_file(args.lo[0])
        check_type(lo)
        sweep_num = np.count_nonzero(np.delete(lo*np.roll(lo, 1), 0) < 0)
        # check the direction of the first sweep
        sweep_up = lo[0] < 0
    else:
        # no lo file, invoke interactive interface
        sweep_num, sweep_up = interactive()

    # number of points in a single sweep
    pts = inten.shape[0] // sweep_num

    # set bandwidth
    if args.bdwth:
        bdwth = args.bdwth[0]
    else:
        bdwth = 1.

    # reconstruct frequency array
    if args.cf:
        try:
            center_freq = float(args.cf[0])
        except ValueError:
            center_freq = load_single_file(args.cf[0])
            bdwth = center_freq[1] - center_freq[0]
```

```
    else:
        center_freq = 0

    # get signal sweep number
    if args.fg:
        fg = args.fg[0]
    else:
        fg = 1

    # invert sweep_up for even sweeps
    if fg % 2:
        pass
    else:
        sweep_up = not sweep_up

    # reconstruct frequency array
    freq = reconstr_freq(center_freq, pts, sweep_up=sweep_up, bdwth=bdwth)

    # get background sweep number
    if args.bg:
        bg = args.bg[0]
        if fg == bg:    # fg==bg, extract fg without background subtraction
            inten = extract_fg(inten, fg, pts)
        else:           # fg!=bg, perform background subtraction
            inten = sub_bg(inten, fg, bg, pts)
    else:       # average intensity if -bg not specified
        inten = avg_inten(inten, pts, fg)

    # roll the intensity array if detector delay is specified
    if args.delay:
        inten = delay_inten(inten, args.delay[0])
    else:
        pass

    # truncate freq & inten array if delay is specified
    if args.delay:
        freq, inten = trunc(freq, inten, args.delay[0])

    return freq, inten


def load_single_file(file_name):
    ''' Load single data file & raise exceptions.

    Arguments:
    file_name -- input file name, str

    Returns:
    data -- np.array
    '''

    # test if the file is .npy binary
    if re.search('\.npy$', file_name):
        try:
```

```
            data = np.load(file_name, mmap_mode='r', allow_pickle=False)
            return data
        except IOError:
            print(err_msg_str(file_name, 2))
            return None
        except ValueError:
            print(err_msg_str(file_name, 3))
            return None
    else:
        try:
            delm, hd, eof = analyze_txt_fmt(file_name)
            if eof or isinstance(delm, type(None)):
                print(err_msg_str(file_name, 2))
            else:
                data = np.loadtxt(file_name, delimiter=delm, skiprows=hd)
                return data
        except FileNotFoundError:
            print(err_msg_str(file_name, 1))
            return None
        except ValueError:
            print(err_msg_str(file_name, 2))
            return None


def interactive():
    ''' Command line interactive interface for sweep information input.
    For mode 0, i.e. no LO data available only.

    Returns:
    sweep_num -- number of full sweeps, int
    sweep_up -- first sweep increases in frequency, boolean
    '''

    while True:     # Get number of sweeps from user input & Error handling
        try:
            typed = input('Input number of full sweeps: ').split()
            sweep_num = int(typed[0])
            break
        except ValueError:
            typed = input('''Must be an integer! Retype: ''').split()

    # Ask if the first sweep goes up
    typed = input('Does the first sweep go up? Y|n ')
    sweep_up = typed in ('y', 'Y', 'yes', 'Yes', 'YES')

    return sweep_num, sweep_up


def proc_nb(freq, inten, args):
    ''' Process narrow band (single sweep) according to input specifications.
        Inclues: box-car smooth in each sweep;
                 linear correction of baseline in each sweep;

    Arguments:
```

```
    freq  -- freuency array, 1D/2D np.array
    inten -- intensity array, 1D/2D np.array
    args  -- input arguments, argparse Object

    Returns:
    freq_b  -- processed frequency array, 1D/2D np.array
    inten_p/b -- processed intensity array, 1D/2D np.array
    '''

    if args.box:    # do box-car smooth
        box_win = (args.box[0])
        if len(inten.shape)==1:
            freq_b = box_car(freq, box_win)
            inten_b = box_car(inten, box_win)
        else:
            freq_b = np.apply_along_axis(box_car, 0, freq, box_win)
            inten_b = np.apply_along_axis(box_car, 0, inten, box_win)
    else:
        freq_b = freq
        inten_b = inten

    if args.nobase:     # if no baseline removal is specified
        return freq_b, inten_b
    else:
        # Apply linear correction on each sweep
        inten_p = np.apply_along_axis(db_poly, 0, inten_b, 1)
        if args.spline:
            inten_p = np.apply_along_axis(db_spline, 0, inten_b)
        return freq_b, inten_p


def proc_wb(x, y, args):
    ''' Process wide band (full stiched spectrum).

    Arguments:
    x    -- x frequency data array, 1D np.array
    y    -- y intensity data array, 1D np.array
    args -- input arguments, argparse Object

    Returns:
    y_db -- debaselined, 1D np.array
    '''

    if args.nobase:
        y_db = y
    else:
        y_db = db_poly(y, deg=1)
        if args.spline:
            y_db = db_spline(y_db)
        else:
            pass

    return y_db
```

```
def reconstr_freq(center_freq, pts, sweep_up=True, bdwth=1.):
    ''' Reconstruct frequency array.

    Arguments:
    center_freq -- center frequency of each sweep. float or np.array
    pts -- dimension of the frequency array. int
    **sweep_up -- first sweep frequency increases. defautl True. boolean
    **bdwth -- sweep bandwidth (MHz), default 1. float

    Returns:
    freq -- frequency array, np.array 1D/2D
    '''

    if sweep_up:
        single_band = bdwth * (np.arange(pts)/(pts-1) - 0.5)
    else:
        single_band = bdwth * (0.5 - np.arange(pts)/(pts-1))

    if isinstance(center_freq, np.ndarray):
        freq = np.tile(single_band, (len(center_freq), 1)).transpose() + \
               np.tile(center_freq, (pts, 1))
    else:
        freq = single_band + center_freq

    return freq


def save_output(data, args):
    ''' Output data in csv format.

    Arguments:
    data -- output xy data, 2D np.array
    args -- input arguments, argparse Object

    Returns: None
    '''

    if args.o:
        out_name = args.o[0]
    else:
        out_name = 'SPlot_' + args.inten[0]

    np.savetxt(out_name, data, header='freq,inten', delimiter=',',
               newline='\n', fmt='%.10g', comments='')
    print('-- {:s} Saved --'.format(out_name))

    return None


def sub_bg(inten, fg, bg, pts):
    ''' Background subtraction routine.

    Arguments:
```

```
    inten -- intensity waveform, 1D/2D np.array
    fg    -- ordinal number of the signal sweep, int
    bg    -- ordinal number of the background sweep, int
    pts   -- number of data points in a single sweep, int

    Returns:
    inten_db -- background subtracted array, 1D/2D np.array
    '''

    if len(inten.shape)==1:     # if intensity is 1D array
        inten_sig = inten[(fg-1)*pts:fg*pts]
        inten_bg = inten[(bg-1)*pts:bg*pts]
    else:                       # if intensity is 2D array
        inten_sig = inten[(fg-1)*pts:fg*pts, :]
        inten_bg = inten[(bg-1)*pts:bg*pts, :]

    return inten_sig - flip(inten_bg, fg - bg + 1)


def trunc(freq, inten, delay):
    ''' Truncate frequency and intensity array if delay is specified.

    Arguments:
    freq  -- frequency array, 1D/2D np.array
    inten -- intensity array, 1D/2D np.array
    delay -- number of data points delayed in inten, inten

    Returns:
    freq_tr  -- truncated frequency, 1D/2D np.array
    inten_tr -- truncated intensity, 1D/2D np.array
    '''

    if len(inten.shape)==1:
        freq_tr = freq[:-delay]
        inten_tr = inten[delay:]
    else:
        freq_tr = freq[:-delay, :]
        inten_tr = inten[delay:, :]

    return freq_tr, inten_tr


def weight_spline(y):
    ''' Generate weight for spline interpolation.

    Arguments:
    y -- intensity array, 1D np.array

    Returns:
    weight -- weighting array, 1D np.array
    '''

    # shift y_min to 0 and rescale to range [0, 1]
    weight = y - y.min()
```

```
    weight = weight / weight.ptp()

    # test strong peak: the median will be falling on the edge of [0, 1]
    if np.median(weight) > 0.9:  # negative peak
        weight[weight<0.9] = 0
    elif np.median(weight) < 0.1: # positive peak
        weight[weight>0.1] = 0
    else:                   # most baseline
        weight = np.ones_like(weight)

    return weight


# ---------------- Input Argument Parser ----------------
def arg():
    ''' Input arguments parser. Returns: argparse Object.'''

    parser = argparse.ArgumentParser(description=__doc__,
             epilog='--- Luyao Zou @ https://github.com/luyaozou/ ---')
    parser.add_argument('inten', nargs=1, help='Intensity data file')
    parser.add_argument('-fg', nargs=1, type=int,
                        help='''The ordinal number of the signal sweep.
                                Default is 1. ''')
    parser.add_argument('-bg', nargs=1, type=int,
                        help='''The ordinal number of the background sweep. If
                                bg == fg, simply extract the fg sweep without
                                background subtraction. If not specified, all
                                sweeps with the same parity of fg are averaged
                                together. ''')
    parser.add_argument('-cf', nargs=1,
                        help='''Single center frequency (MHz) or a file listing
                                several center frequencies. If neither
                                specified, set at 0, and assume intensity is
                                a single sweep scan.''')
    parser.add_argument('-bdwth', nargs=1, type=float,
                        help='''Full frequency sweep band width (MHz).
                                If not specified while freq file is available,
                                get sweep window from the difference of the
                                first two data points in the freq file,
                                assuming frequency data points are evenly spaced
                                and matches the band width. Default is 1.''')
    parser.add_argument('-box', nargs=1, type=int,
                        help='Boxcar smooth window. Must be an odd integer.')
    parser.add_argument('-lo', nargs=1,
                        help='''LO file. If not specified, command line
                                interactive questions will be invoked.''')
    parser.add_argument('-o', nargs=1,
                        help='''Output file name. If not specified,
                                default name will be used.''')
    parser.add_argument('-delay', nargs=1, type=int,
                        help=''' Delay of detector response by number of
                                 data points. Default is 0.''')
    parser.add_argument('-spline', action='store_true',
                        help='Fit spline to subtract baseline. Optional')
```

```
    parser.add_argument('-nobase', action='store_true',
                        help='Disable ALL baseline removal functionality.')

    return parser.parse_args()


# ---------------- main routine ----------------
if __name__ == '__main__':

    input_args = arg()
    freq, inten = load_data(input_args)
    freq, inten = proc_nb(freq, inten, input_args)
    freq_flat, inten_flat = flat_wave(freq, inten, input_args.nobase)
    inten_flat = proc_wb(freq_flat, inten_flat, input_args)
    save_output(np.column_stack((freq_flat, inten_flat)), input_args)
```

Appendix B SPFIT Assignment and Output File for HO_3 and DO_3

B.1 SPFIT assignment and output file for HO_3

```
hooo predictions                                        Fri Sep 25 14:50:19 2015
LINES REQUESTED=  202 NUMBER OF PARAMETERS= 20 NUMBER OF ITERATIONS= 10
  MARQUARDT PARAMETER = 0.0000E+00 max (OBS-CALC)/ERROR =1.0000E+06
                              PARAMETERS - A.PRIORI ERROR
     1      1         10000   7.0781119276763E+04    1.000000E+10  A
     2      2         20000   9.9873872649628E+03    1.000000E+11  B
     3      3         30000   8.7497288142301E+03    1.000000E+11  C
     4      4           200  -4.7537800747846E-02    9.702165E+10  -DN
     5      5          1100  -1.4915714704417E-01    1.000000E+11  -DNK
     6      6          2000  -2.9561174306797E+00    1.000000E+10  -DK
     7      7         40100  -6.1459872189222E-03    1.000000E+11  -dN
     8      8         41000  -2.1629036345966E-01    1.000000E+10  -dK
     9      9      10010000  -1.2526939239286E+03    5.762869E+10  eaa
    10     10      10020000  -1.0623815010345E+02    6.632208E+10  ebb
    11     11      10030000  -3.4831374211852E+00    6.288901E+10  ecc
    12     12      10610000  -4.2245212137638E+01    6.288901E+10  (eab+eba)
    13     13     120000000   3.6602647802840E+00    5.007459E+10  a_F
    14     14     120010000   8.4831445222214E+00    3.642117E+10  Taa
    15     14    -120030000  -8.4831445222214E+00       -1.000000  Tcc
    16     15     120020000  -6.8505998785507E+00    5.970145E+10  Tbb
    17     15    -120030000   6.8505998785507E+00       -1.000000  Tcc
    18     16       1000100   2.0192703529843E-03    1.000000E+10  DNS
    19     17      10010100   5.8543709699932E-02    1.000000E+10  DNKS
    20     18      10011000   1.0278092438995E-01    1.000000E+10  DKS
20 parameters read, 18 independent parameters
NUMBER OF PARAMETERS EXCLUDED IF INDEX < 0 =    2
ENERGY SORT OF WANG SUB-BLOCKS
PROLATE ROTOR
    V KMIN KMAX WTPL WTMN ESYMWT NSYM SPINS
    0    0    9    1    1    999    2  0.5  0.5
BLOCK - WT - SYM - V - TSP - N  -  other quanta  (rel. to F=0 )
    1    1    x    0    0  -1.0  -0.5
    1    1    c    0    0  -1.0  -0.5
    1    1    x    0    1   0.0   0.5
    1    1    c    0    1   0.0   0.5
    1    1    x    0    2   0.0  -0.5
    1    1    c    0    2   0.0  -0.5
    1    1    x    0    3   1.0   0.5
    1    1    c    0    3   1.0   0.5
    2    1    b    0    0  -1.0  -0.5
    2    1    a    0    0  -1.0  -0.5
    2    1    b    0    1   0.0   0.5
    2    1    a    0    1   0.0   0.5
    2    1    b    0    2   0.0  -0.5
    2    1    a    0    2   0.0  -0.5
    2    1    b    0    3   1.0   0.5
    2    1    a    0    3   1.0   0.5
Maximum Dimension for Hamiltonian = 40
                                           EXP.FREQ.  -  CALC.FREQ. -   DIFF.  - EXP.ERR.- EST.ERR.-AVG. CALC.FREQ. -  DIFF. - WT.
    1:   3  1  2  4  4  3  1  3  4  4          7341.26700    7341.26030    0.00670    0.00500   0.00317
    2:   3  1  2  4  3  3  1  3  4  3          7342.23420    7342.23095    0.00325    0.00500   0.00313
    3:   3  1  2  3  2  3  1  3  3  2          7520.84760    7520.84472    0.00288    0.00500   0.00341
    4:   3  1  2  3  3  3  1  3  3  3          7522.67210    7522.66555    0.00655    0.00500   0.00336
    5:   4  0  4  4  3  3  1  3  3  2         16838.76800   16838.77287   -0.00487    0.00500   0.00280
    6:   4  0  4  4  4  3  1  3  3  3         16840.11640   16840.12805   -0.01165    0.00500   0.00281
    7:   4  0  4  5  5  3  1  3  4  4         17061.82110   17061.82323   -0.00213    0.00500   0.00298
    8:   4  0  4  5  4  3  1  3  4  3         17062.82350   17062.82638   -0.00288    0.00500   0.00300
    9:   1  0  1  2  1  0  0  0  1  1         18707.65160   18707.65575   -0.00415    0.00500   0.00174
   10:   1  0  1  2  2  0  0  0  1  1         18709.04950   18709.05347   -0.00397    0.00500   0.00100
   11:   1  0  1  2  1  0  0  0  1  0         18711.30490   18711.31661   -0.01171    0.00500   0.00143
   12:   1  0  1  1  0  0  0  0  1  1         18787.54880   18787.55065   -0.00185    0.00500   0.00274
   13:   1  0  1  1  1  0  0  0  1  1         18792.07590   18792.07116    0.00474    0.00500   0.00175
   14:   1  0  1  1  1  0  0  0  1  0         18795.72520   18795.73202   -0.00682    0.00500   0.00257
   15:   1  1  1  2  1  2  0  2  3  2         23068.50590   23068.50207    0.00383    0.00500   0.00218
   16:   1  1  1  2  2  2  0  2  3  3         23071.12390   23071.10896    0.01494    0.00500   0.00216
   17:   1  1  1  2  2  2  0  2  3  2         23071.92500   23071.91868    0.00632    0.00500   0.00241
   18:   1  1  1  1  1  2  0  2  2  2         23881.08610   23881.08407    0.00203    0.00500   0.00253
   19:   1  1  1  1  1  2  0  2  2  1         23883.04530   23883.04747   -0.00217    0.00500   0.00255
   20:   1  1  1  1  0  2  0  2  2  1         23888.83720   23888.83455    0.00265    0.00500   0.00311
   21:   2  1  2  2  1  1  1  1  1  0         35953.77430   35953.76934    0.00496    0.00500   0.00219
   22:   2  1  2  2  2  1  1  1  1  1         35958.65260   35958.65165    0.00095    0.00500   0.00174
   23:   2  1  2  3  3  1  1  1  2  2         36321.69300   36321.68971    0.00329    0.00500   0.00144
   24:   2  1  2  3  2  1  1  1  2  1         36323.17390   36323.15513    0.01877    0.00500   0.00152
```

25:	2	0	2	3	2	1	0	1	2	2	37426.08000	37426.07448	0.00552	0.00500	0.00164			
26:	2	0	2	3	3	1	0	1	2	2	37426.87000	37426.88420	−0.01420	0.00500	0.00114			
27:	2	0	2	3	2	1	0	1	2	1	37427.47590	37427.47219	0.00371	0.00500	0.00120			
28:	2	0	2	2	2	1	0	1	1	1	37480.33690	37480.33503	0.00187	0.00500	0.00101			
29:	2	0	2	2	1	1	0	1	1	0	37482.89330	37482.89215	0.00115	0.00500	0.00160			
30:	2	0	2	2	2	1	0	1	2	2	37563.35480	37563.35273	0.00207	0.00500	0.00293			
31:	3	1	3	3	2	2	1	2	2	1	54251.90670	54251.90288	0.00382	0.00500	0.00133			
32:	3	1	3	3	3	2	1	2	2	2	54252.47310	54252.47342	−0.00032	0.00500	0.00133			
33:	3	1	3	3	2	2	1	2	2	2	54252.81020	54252.80766	0.00254	0.00500	0.00246			
34:	3	1	3	4	3	2	1	2	3	3	54374.36890	54374.36644	0.00246	0.00500	0.00188			
35:	3	1	3	4	4	2	1	2	3	3	54375.77330	54375.77200	0.00130	0.00500	0.00142			
36:	3	1	3	4	3	2	1	2	3	2	54376.31530	54376.31764	−0.00234	0.00500	0.00142			
37:	3	0	3	4	3	2	0	2	3	3	56104.80880	56104.81535	−0.00655	0.00500	0.00169			
38:	3	0	3	4	4	2	0	2	3	3	56105.36800	56105.35984	0.00816	0.00500	0.00126			
39:	3	0	3	4	3	2	0	2	3	2	56105.62980	56105.62508	0.00472	0.00500	0.00128			
40:	3	0	3	3	2	2	0	2	2	2	56155.62460	56155.63562	−0.01102	0.00500	0.00238			
41:	3	0	3	3	3	2	0	2	2	2	56156.96490	56156.96984	−0.00494	0.00500	0.00189			
42:	3	0	3	3	2	2	0	2	2	1	56157.58650	56157.59902	−0.01252	0.00500	0.00193			
43:	1	1	0	2	1	1	0	1	2	2	61706.35800	61706.36882	−0.01082	0.00500	0.00221			
44:	1	1	0	2	2	1	0	1	2	2	61709.12100	61709.12649	−0.00549	0.00500	0.00164			
45:	1	1	0	1	1	1	0	1	1	1	62650.40400	62650.40539	−0.00139	0.00500	0.00248			
46:	2	1	1	3	2	2	0	2	3	3	63050.60000	63050.59820	0.00180	0.00500	0.00236			
47:	2	1	1	3	2	2	0	2	3	2	63051.41200	63051.40792	0.00408	0.00500	0.00208			
48:	2	1	1	3	3	2	0	2	3	3	63051.68200	63051.68492	−0.00292	0.00500	0.00205			
49:	2	1	1	3	3	2	0	2	3	2	63052.49400	63052.49464	−0.00064	0.00500	0.00259			
50:	2	1	1	2	1	2	0	2	2	2	63626.60400	63626.59955	0.00445	0.00500	0.00251			
51:	2	1	1	2	2	2	0	2	2	2	63627.83600	63627.82323	0.01277	0.00500	0.00210			
52:	4	1	4	4	3	3	1	3	3	2	72389.27160	72389.25501	0.01659	0.00500	0.00200			
53:	4	1	4	4	4	3	1	3	3	3	72389.40540	72389.38594	0.01946	0.00500	0.00200			
54:	4	1	4	5	5	3	1	3	4	4	72443.05310	72443.04408	0.00902	0.00500	0.00215			
55:	4	1	4	5	4	3	1	3	4	3	72443.32130	72443.31513	0.00617	0.00500	0.00215			
56:	4	0	4	5	5	3	0	3	4	4	74725.09630	74725.03407	0.06223	0.05000	0.00249	74725.10511	−0.00881	0.5000
57:	4	0	4	5	4	3	0	3	4	3	74725.09630	74725.17614	−0.07984	0.05000	0.00249	74725.10511	−0.00881	0.5000
58:	4	0	4	4	4	3	0	3	3	3	74775.36800	74775.36735	0.00065	0.00500	0.00265			
59:	4	0	4	4	3	3	0	3	3	2	74775.68290	74775.68062	0.00228	0.00500	0.00265			
60:	1	1	1	2	1	0	0	0	1	1	79203.63190	79203.63002	0.00188	0.00500	0.00232			
61:	1	1	1	2	2	0	0	0	1	1	79207.03970	79207.04663	−0.00693	0.00500	0.00190			
62:	1	1	1	2	1	0	0	0	1	0	79207.28570	79207.29087	−0.00517	0.00500	0.00212			
63:	1	1	1	1	1	0	0	0	1	1	80153.48500	80153.49026	−0.00526	0.00500	0.00273			
64:	1	1	1	1	0	0	0	0	1	1	80159.27290	80159.27735	−0.00445	0.00500	0.00291			
65:	5	0	5	6	6	4	0	4	5	5	93266.88880	93266.85268	0.03612	0.05000	0.00533	93266.89217	−0.00337	0.5000
66:	5	0	5	6	5	4	0	4	5	4	93266.88880	93266.93166	−0.04286	0.05000	0.00533	93266.89217	−0.00337	0.5000
67:	2	1	2	3	2	1	0	1	2	2	96817.77730	96817.73168	0.04562	0.05000	0.00230			
68:	2	1	2	3	2	1	0	1	2	1	96819.12770	96819.12939	−0.00169	0.05000	0.00209			
69:	2	1	2	3	3	1	0	1	2	2	96819.66940	96819.68287	−0.01347	0.05000	0.00204			
70:	2	1	2	2	2	1	0	1	1	1	97320.03150	97320.07075	−0.03925	0.05000	0.00221			
71:	2	1	2	2	1	1	0	1	1	1	97321.04420	97320.97552	0.06868	0.05000	0.00264			
72:	2	1	2	2	1	1	0	1	1	0	97325.49120	97325.49604	−0.00484	0.05000	0.00260			
73:	3	1	3	4	3	2	0	2	3	2	113767.99790	113767.97484	0.02306	0.05000	0.00254			
74:	3	1	3	4	4	2	0	2	3	3	113768.56980	113768.57067	−0.00087	0.05000	0.00253			
75:	3	1	3	3	3	2	0	2	2	2	114092.16910	114092.20914	−0.04004	0.05000	0.00257			
76:	3	1	3	3	2	2	0	2	2	1	114094.52610	114094.50677	0.01933	0.05000	0.00248			
77:	4	1	4	5	4	3	0	3	4	3	130105.64750	130105.66489	−0.01739	0.05000	0.00342			
78:	4	1	4	5	5	3	0	3	4	4	130106.23650	130106.25492	−0.01842	0.05000	0.00342			
79:	4	1	4	4	4	3	0	3	3	3	130324.60700	130324.62524	−0.01824	0.05000	0.00341			
80:	4	1	4	4	3	3	0	3	3	2	130326.17700	130326.16277	0.01423	0.05000	0.00332			
81:	5	1	5	6	5	4	0	4	5	4	145879.42700	145879.45063	−0.02363	0.05000	0.00574			
82:	5	1	5	6	6	4	0	4	5	5	145880.02170	145880.02630	−0.00460	0.05000	0.00576			
83:	5	1	5	5	5	4	0	4	4	4	146024.10020	146024.09386	0.00634	0.05000	0.00580			
84:	5	1	5	5	4	4	0	4	4	3	146025.28650	146025.29005	−0.00355	0.05000	0.00572			
85:	6	1	6	7	6	5	0	5	6	5	161145.15710	161145.22284	−0.06574	0.05000	0.01103			
86:	6	1	6	7	7	5	0	5	6	6	161145.75720	161145.77897	−0.02177	0.05000	0.01104			
87:	6	1	6	6	6	5	0	5	5	5	161234.68870	161234.65644	0.03226	0.05000	0.01076			
88:	6	1	6	6	5	5	0	5	5	4	161235.57960	161235.65543	−0.07583	0.05000	0.01072			
89:	5	2	3	6	5	5	1	4	6	5	175385.24560	175385.29610	−0.05050	0.05000	0.01240			
90:	5	2	3	6	6	5	1	4	6	6	175386.24530	175386.30239	−0.05709	0.05000	0.01240			
91:	5	2	3	5	5	5	1	4	5	5	175937.63940	175937.73037	−0.09097	0.05000	0.01267			
92:	5	2	3	5	4	5	1	4	5	4	175939.19340	175939.21946	−0.02606	0.05000	0.01269			
93:	7	1	7	8	7	6	0	6	7	6	175970.59120	175970.45824	0.13296	0.05000	0.02042	175970.72419	−0.13299	0.5000
94:	7	1	7	8	8	6	0	6	7	7	175970.59120	175970.99015	−0.39895	0.05000	0.02042	175970.72419	−0.13299	0.5000
95:	7	1	7	7	7	6	0	6	6	6	176016.68620	176016.66034	0.02586	0.05000	0.02011			
96:	7	1	7	7	6	6	0	6	6	5	176017.46670	176017.52492	−0.05822	0.05000	0.02008			
97:	4	2	2	5	4	4	1	3	5	4	177995.61150	177995.66262	−0.05112	0.05000	0.00652			
98:	4	2	2	5	5	4	1	3	5	5	177996.87040	177996.92544	−0.05504	0.05000	0.00652			
99:	4	2	2	4	4	4	1	3	4	4	178715.86300	178715.90628	−0.04328	0.05000	0.00662			
100:	4	2	2	4	3	4	1	3	4	3	178717.88770	178717.93120	−0.04350	0.05000	0.00663			
101:	3	2	1	4	3	3	1	2	4	3	180161.00220	180161.01435	−0.01215	0.05000	0.00408			
102:	3	2	1	4	4	3	1	2	4	4	180162.68550	180162.72373	−0.03823	0.05000	0.00408			
103:	3	2	1	3	3	3	1	2	3	3	181139.50460	181139.53303	−0.02843	0.05000	0.00416			
104:	3	2	1	3	2	3	1	2	3	2	181142.58930	181142.63855	−0.04925	0.05000	0.00410			
105:	2	2	0	3	2	2	1	1	3	2	181770.91130	181770.94904	−0.03774	0.05000	0.00521			
106:	2	2	0	3	3	2	1	1	3	3	181773.58670	181773.60263	−0.01593	0.05000	0.00528			
107:	2	2	0	2	2	2	1	1	2	2	183204.73590	183204.76078	−0.02488	0.05000	0.00559			
108:	2	2	1	3	2	2	1	2	3	2	185412.41280	185412.49219	−0.07939	0.05000	0.00464			
109:	2	2	1	3	3	2	1	2	3	3	185414.24620	185414.28979	−0.04359	0.05000	0.00470			
110:	2	2	1	2	2	2	1	2	2	2	186973.48500	186973.50528	−0.02028	0.05000	0.00549			
111:	2	2	1	2	1	2	1	2	2	1	186977.33330	186977.45607	−0.12277	0.05000	0.00602			
112:	3	2	2	4	3	3	1	3	4	3	187411.67050	187411.70890	−0.03840	0.05000	0.00419			
113:	3	2	2	4	4	3	1	3	4	4	187412.43830	187412.47178	−0.03348	0.05000	0.00422			
114:	3	2	2	3	3	3	1	3	3	3	188566.66860	188566.68748	−0.01888	0.05000	0.00432			
115:	3	2	2	3	2	3	1	3	3	2	188568.01490	188568.01898	−0.00408	0.05000	0.00461			
116:	4	2	3	5	4	4	1	4	5	4	189980.22090	189980.08009	0.14081	0.05000	0.00677	189980.21667	0.00423	0.5000

117:	4	2	3	5	5	4	1	4	5	5	189980.22090	189980.35325	-0.13235	0.05000	0.00677	189980.21667	0.00423 0.5000
118:	5	2	4	6	5	5	1	5	6	5	193150.80590	193150.74393	0.06197	0.05000	0.01271	193150.74454	0.06136 0.5000
119:	5	2	4	6	6	5	1	5	6	6	193150.80590	193150.74516	0.06074	0.05000	0.01271	193150.74454	0.06136 0.5000
120:	5	2	4	5	5	5	1	5	5	5	193968.43630	193968.52382	-0.08752	0.05000	0.01228	193968.52691	-0.09061 0.5000
121:	5	2	4	5	4	5	1	5	5	4	193968.43630	193968.53001	-0.09371	0.05000	0.01228	193968.52691	-0.09061 0.5000
122:	2	2	1	3	2	1	1	0	2	1	220523.83720	220523.85505	-0.01785	0.05000	0.00451		
123:	2	2	1	3	3	1	1	0	2	2	220524.85220	220524.84617	0.00603	0.05000	0.00451		
124:	2	2	1	2	2	1	1	0	1	1	221643.19450	221643.17065	0.02385	0.05000	0.00503		
125:	2	2	1	2	1	1	1	0	1	0	221645.73300	221645.72243	0.01057	0.05000	0.00522		
126:	2	2	1	2	1	1	1	0	1	1	221648.06100	221648.02621	0.03479	0.05000	0.00562		
127:	2	2	0	3	2	1	1	1	2	1	221754.07850	221753.85489	0.22361	0.05000	0.00442	221754.01674	0.06176 0.5000
128:	2	2	0	3	3	1	1	1	2	2	221754.07850	221754.17859	-0.10009	0.05000	0.00442	221754.01674	0.06176 0.5000
129:	2	2	0	2	2	1	1	1	1	1	222951.42560	222951.49994	-0.07434	0.05000	0.00495		
130:	2	2	0	2	1	1	1	1	1	1	222956.20070	222956.33399	-0.13329	0.05000	0.00534		
131:	3	2	2	4	3	2	1	1	3	2	238128.27230	238128.27582	-0.00352	0.05000	0.00495		
132:	3	2	2	4	4	2	1	1	3	3	238129.34990	238129.35753	-0.00763	0.05000	0.00493		
133:	3	2	2	3	3	2	1	1	2	2	239031.07150	239031.07339	-0.00189	0.05000	0.00433		
134:	3	2	2	3	2	2	1	1	2	1	239033.98900	239033.96280	0.02620	0.05000	0.00431		
135:	3	2	1	4	3	2	1	2	3	2	241879.70370	241879.56295	0.14075	0.05000	0.00456	241879.65949	0.04421 0.5000
136:	3	2	1	4	4	2	1	2	3	3	241879.70370	241879.75603	-0.05233	0.05000	0.00456	241879.65949	0.04421 0.5000
137:	3	2	1	3	3	2	1	2	2	2	242914.64170	242914.67200	-0.03030	0.05000	0.00467		
138:	3	2	1	3	2	2	1	2	2	1	242915.18570	242915.38615	-0.20045	0.05000	0.00503		
139:	4	2	3	5	4	3	1	2	4	3	255081.17890	255081.16426	0.01464	0.05000	0.00643		
140:	4	2	3	5	5	3	1	2	4	4	255082.18200	255082.13704	0.04496	0.05000	0.00642		
141:	4	2	3	4	4	3	1	2	3	3	255789.43070	255789.41785	0.01285	0.05000	0.00605		
142:	4	2	3	4	3	3	1	2	3	2	255791.54050	255791.53053	0.00997	0.05000	0.00604		
143:	4	2	2	5	5	3	1	3	4	4	262698.74400	262698.67764	0.06636	0.05000	0.00787	262698.69990	0.04410 0.5000
144:	4	2	2	5	4	3	1	3	4	3	262698.74400	262698.72217	0.02183	0.05000	0.00787	262698.69990	0.04410 0.5000
145:	4	2	2	4	4	3	1	3	3	3	263596.68290	263596.59419	0.08871	0.05000	0.00783	263596.70107	-0.01817 0.5000
146:	4	2	2	4	3	3	1	3	3	2	263596.68290	263596.80796	-0.12506	0.05000	0.00783	263596.70107	-0.01817 0.5000
147:	5	2	4	6	5	4	1	3	5	4	271389.92550	271389.96139	-0.03589	0.05000	0.01003		
148:	5	2	4	6	6	4	1	3	5	5	271390.83030	271390.84250	-0.01220	0.05000	0.01003		
149:	5	2	4	5	5	4	1	3	4	4	271952.08840	271952.05783	0.03057	0.05000	0.00916		
150:	5	2	4	5	4	4	1	3	4	3	271953.69400	271953.71616	-0.02216	0.05000	0.00916		
151:	5	2	3	6	6	4	1	4	5	5	284292.49880	284292.33556	0.16324	0.05000	0.01483	284292.45100	0.04780 0.5000
152:	5	2	3	6	5	4	1	4	5	4	284292.49880	284292.56643	-0.06763	0.05000	0.01483	284292.45100	0.04780 0.5000
153:	5	2	3	5	4	4	1	4	4	3	285103.53400	285103.48459	0.04941	0.05000	0.01463	285103.55330	-0.01930 0.5000
154:	5	2	3	5	5	4	1	4	4	4	285103.53400	285103.62201	-0.08801	0.05000	0.01463	285103.55330	-0.01930 0.5000
155:	6	2	5	7	6	5	1	4	6	5	287065.92180	287065.98957	-0.06777	0.05000	0.01531		
156:	6	2	5	7	7	5	1	4	6	6	287066.73980	287066.80519	-0.06539	0.05000	0.01532		
157:	6	2	5	6	6	5	1	4	5	5	287514.23830	287514.21606	0.02224	0.05000	0.01397		
158:	6	2	5	6	5	5	1	4	5	4	287515.56330	287515.60103	-0.03773	0.05000	0.01397		
159:	7	2	6	8	7	6	1	5	7	6	302119.78510	302119.44544	0.33966	0.05000	0.02361	302119.82973	-0.04463 0.5000
160:	7	2	6	8	8	6	1	5	7	7	302119.78510	302120.21401	-0.42891	0.05000	0.02361	302119.82973	-0.04463 0.5000
161:	7	2	6	7	7	6	1	5	6	6	302475.43730	302475.42618	0.01112	0.05000	0.02196		
162:	7	2	6	7	6	6	1	5	6	5	302476.63160	302476.63465	-0.00305	0.05000	0.02196		
163:	5	3	2	6	5	5	2	3	6	5	305866.36330	305865.73682	0.62648	0.05000	0.01417	305866.22546	0.13784 0.5000
164:	5	3	2	6	6	5	2	3	6	6	305866.36330	305866.71411	-0.35081	0.05000	0.01417	305866.22546	0.13784 0.5000
165:	3	3	0	4	3	3	2	1	4	3	306028.93130	306029.10574	-0.17444	0.05000	0.01559		
166:	3	3	0	4	4	3	2	1	4	4	306031.21810	306031.16529	0.05281	0.05000	0.01562		
167:	4	3	1	5	4	4	2	2	5	4	306035.96990	306036.02902	-0.05912	0.05000	0.01301		
168:	4	3	1	5	5	4	2	2	5	5	306037.32960	306037.38446	-0.05486	0.05000	0.01300		
169:	3	3	1	4	3	3	2	2	4	3	306120.50870	306120.47126	0.03744	0.05000	0.01553		
170:	3	3	1	4	4	3	2	2	4	4	306122.52810	306122.50671	0.02139	0.05000	0.01555		
171:	4	3	2	5	4	4	2	3	5	4	306310.09890	306310.15417	-0.05527	0.05000	0.01324		
172:	4	3	2	5	5	4	2	3	5	5	306311.44390	306311.46326	-0.01936	0.05000	0.01324		
173:	6	2	4	7	7	5	1	5	6	6	306758.47790	306758.27117	0.20673	0.05000	0.02722	306758.45924	0.01866 0.5000
174:	6	2	4	7	6	5	1	5	6	5	306758.47790	306758.64732	-0.16942	0.05000	0.02722	306758.45924	0.01866 0.5000
175:	5	3	2	5	5	5	2	3	5	5	306966.62590	306966.70903	-0.08313	0.05000	0.01281		
176:	5	3	2	5	4	5	2	3	5	4	306968.19620	306968.11910	0.07710	0.05000	0.01281		
177:	4	3	1	4	4	4	2	2	4	4	307386.56250	307386.34456	0.21794	0.05000	0.01273		
178:	4	3	1	4	3	4	2	2	4	3	307388.39770	307388.44730	-0.04960	0.05000	0.01270		
179:	6	2	4	6	5	5	1	5	5	4	307518.56600	307518.43916	0.12684	0.05000	0.02690	307518.62539	-0.05939 0.5000
180:	6	2	4	6	6	5	1	5	5	5	307518.56600	307518.81162	-0.24562	0.05000	0.02690	307518.62539	-0.05939 0.5000
181:	4	3	2	4	4	4	2	3	4	4	307669.55560	307669.59568	-0.04008	0.05000	0.01285		
182:	4	3	2	4	3	4	2	3	4	3	307671.74960	307671.62085	0.12875	0.05000	0.01283		
183:	3	3	1	3	3	3	2	2	3	3	307854.94260	307854.81541	0.12719	0.05000	0.01697		
184:	3	3	1	3	2	3	2	2	3	2	307858.38960	307858.34673	0.04287	0.05000	0.01690		
185:	3	3	1	4	3	2	2	0	3	2	362478.12890	362477.79804	0.33086	0.05000	0.01394	362478.02982	0.09908 0.5000
186:	3	3	1	4	4	2	2	0	3	3	362478.12890	362478.26161	-0.13271	0.05000	0.01394	362478.02982	0.09908 0.5000
187:	3	3	0	4	3	2	2	1	3	2	362496.50460	362496.17651	0.32809	0.05000	0.01394	362496.40402	0.10058 0.5000
188:	3	3	0	4	4	2	2	1	3	3	362496.50460	362496.63152	-0.12692	0.05000	0.01394	362496.40402	0.10058 0.5000
189:	3	3	1	3	3	2	2	0	2	2	363681.32520	363681.12802	0.19718	0.05000	0.01430	363681.30952	0.01568 0.5000
190:	3	3	1	3	2	2	2	0	2	1	363681.32520	363681.49102	-0.16582	0.05000	0.01430	363681.30952	0.01568 0.5000
191:	3	3	0	3	3	2	2	1	2	2	363700.85300	363700.65264	0.20036	0.05000	0.01429	363700.82331	0.02969 0.5000
192:	3	3	0	3	2	2	2	1	2	1	363700.85300	363700.99399	-0.14099	0.05000	0.01429	363700.82331	0.02969 0.5000
193:	4	3	2	5	4	3	2	1	4	3	381230.59710	381230.30408	0.29302	0.05000	0.01306	381230.59033	0.00677 0.5000
194:	4	3	2	5	5	3	2	1	4	4	381230.59710	381230.87657	-0.27947	0.05000	0.01306	381230.59033	0.00677 0.5000
195:	4	3	1	5	4	3	2	2	4	3	381323.33640	381323.04229	0.29411	0.05000	0.01330	381323.31631	0.02009 0.5000
196:	4	3	1	5	5	3	2	2	4	4	381323.33640	381323.59032	-0.25392	0.05000	0.01330	381323.31631	0.02009 0.5000
197:	4	3	2	4	4	3	2	1	3	3	382319.49370	382319.48050	0.01320	0.05000	0.01194		
198:	4	3	2	4	3	3	2	1	3	2	382320.52630	382320.51283	0.01347	0.05000	0.01194		
199:	4	3	1	4	4	3	2	2	3	3	382416.18160	382416.25127	-0.06967	0.05000	0.01219		
200:	4	3	1	4	3	3	2	2	3	2	382417.14990	382417.23628	-0.08638	0.05000	0.01219		
201:	5	3	3	5	5	4	2	2	4	4	400858.40890	400858.11412	0.29478	0.05000	0.01403	400858.57875	-0.16985 0.5000
202:	5	3	3	5	4	4	2	2	4	3	400858.40890	400859.04338	-0.63448	0.05000	0.01403	400858.57875	-0.16985 0.5000

NORMALIZED DIAGONAL:

1	1.00000E+00	2	3.25373E-01	3	3.20359E-02	4	9.15845E-01	5	4.98154E-01	6	7.37702E-01
7	4.04461E-01	8	9.96237E-01	9	7.57263E-01	10	8.03340E-01	11	8.45857E-01	12	9.51777E-01
13	9.89956E-01	14	9.19739E-01	15	9.95738E-01	16	9.99999E-01	17	5.56068E-01	18	9.93145E-01

MARQUARDT PARAMETER = 0, TRUST EXPANSION = 1.00

NEW PARAMETER (EST. ERROR) -- CHANGE THIS ITERATION

```
  1        10000          A      70781.11869(136)        -0.00000
  2        20000          B        9987.3873( 61)         0.0000
  3        30000          C        8749.7284( 59)        -0.0000
  4          200        -DN      -0.0475200(223)      -0.0000000
  5         1100       -DNK       -0.149167(123)        0.000000
  6         2000        -DK       -2.956094(237)        0.000000
  7        40100        -dN         -6.1406(116)E-03       0.0000E-03
  8        41000        -dK         -0.21649(298)        -0.00000
  9     10010000        eaa       -1252.6932( 42)        -0.0000
 10     10020000        ebb       -106.25192(198)        -0.00000
 11     10030000        ecc         -3.49564(187)         0.00000
 12     10610000  (eab+eba)          -42.503( 80)          0.001
 13    120000000        a_F          3.66102(240)        -0.00000
 14    120010000        Taa           8.4792( 46)        -0.0000
 15    120020000        Tbb          -6.8512( 45)         0.0000
 16      1000100        DNS            0.987( 75)E-03       0.000E-03
 17     10010100       DNKS          0.05626( 85)        -0.00000
 18     10011000        DKS          0.10421(179)         0.00000
 MICROWAVE AVG =       -0.007747 MHz, IR AVG =       0.00000
 MICROWAVE RMS =        0.049902 MHz, IR RMS =       0.00000
 END OF ITERATION  2 OLD, NEW RMS ERROR=       1.30478        1.30478
  1  2  0.108433  1  3 -0.090888  1  4 -0.042153  1  5 -0.337406  1  6 -0.220440  1  7  0.030166  1  8 -0.102742  1  9  0.124191
  1 10  0.000449  1 11  0.118669  1 12  0.237908  1 13  0.139761  1 14  0.112065  1 15  0.061610  1 16 -0.033070  1 17 -0.021927
  1 18 -0.027975  2  1  0.108433  2  3 -0.994220  2  4 -0.788965  2  5  0.453918  2  6 -0.174299  2  7 -0.045712  2  8 -0.995231
  2  9 -0.000007  2 10  0.025557  2 11  0.014671  2 12 -0.013414  2 13  0.045193  2 14  0.002942  2 15  0.010033  2 16  0.000558
  2 17  0.029861  2 18 -0.031318  3  1 -0.090888  3  2 -0.994220  3  4  0.727680  3  5 -0.441525  3  6  0.169784  3  7 -0.000230
  3  8  0.997972  3  9 -0.009427  3 10 -0.011093  3 11 -0.010365  3 12 -0.015231  3 13 -0.026903  3 14  0.003377  3 15 -0.010478
  3 16 -0.005422  3 17 -0.034956  3 18  0.038389  4  1 -0.042153  4  2 -0.788965  4  3  0.727680  4  5 -0.482079  4  6  0.145133
  4  7  0.396484  4  8  0.736442  4  9  0.066108  4 10 -0.106199  4 11 -0.026945  4 12  0.256019  4 13 -0.093883  4 14 -0.019717
  4 15 -0.000281  4 16  0.061161  4 17  0.010533  4 18 -0.024845  5  1 -0.337406  5  2  0.453918  5  3 -0.441525  5  4 -0.482079
  5  6 -0.603695  5  7  0.123276  5  8 -0.447509  5  9 -0.101579  5 10  0.032511  5 11 -0.036858  5 12 -0.168878  5 13 -0.008803
  5 14 -0.015536  5 15 -0.025674  5 16 -0.006315  5 17  0.067989  5 18  0.004545  6  1 -0.220440  6  2 -0.174299  6  3  0.169784
  6  4  0.145133  6  5 -0.603695  6  7 -0.209456  6  8  0.177777  6  9 -0.020608  6 10  0.000059  6 11 -0.022353  6 12 -0.006374
  6 13 -0.030953  6 14 -0.041361  6 15 -0.001050  6 16  0.007437  6 17 -0.003865  6 18  0.034862  7  1  0.030166  7  2 -0.045712
  7  3 -0.000230  7  4  0.396484  7  5  0.123276  7  6 -0.209456  7  8 -0.032818  7  9  0.064722  7 10 -0.057610  7 11  0.014851
  7 12  0.240159  7 13 -0.036472  7 14 -0.028603  7 15  0.008289  7 16  0.035352  7 17  0.033811  7 18 -0.031706  8  1 -0.102742
  8  2 -0.995231  8  3  0.997972  8  4  0.736442  8  5 -0.447509  8  6  0.177777  8  7 -0.032818  8  9 -0.009091  8 10 -0.012955
  8 11 -0.015179  8 12 -0.016326  8 13 -0.034178  8 14  0.002352  8 15 -0.011487  8 16 -0.005179  8 17 -0.035068  8 18  0.037860
  9  1  0.124191  9  2 -0.000007  9  3 -0.009427  9  4  0.066108  9  5 -0.101579  9  6 -0.020608  9  7  0.064722  9  8 -0.009091
  9 10  0.215055  9 11  0.231960  9 12  0.071332  9 13 -0.010900  9 14  0.023143  9 15 -0.178951  9 16  0.012553  9 17 -0.228702
  9 18 -0.200462 10  1  0.000449 10  2  0.025557 10  3 -0.011093 10  4 -0.106199 10  5  0.032511 10  6  0.000059 10  7 -0.057610
 10  8 -0.012955 10  9  0.215055 10 11  0.273352 10 12 -0.020130 10 13  0.076311 10 14 -0.035322 10 15  0.038026 10 16 -0.531160
 10 17  0.130400 10 18 -0.068578 11  1  0.118669 11  2  0.014671 11  3 -0.010365 11  4 -0.026945 11  5 -0.036858 11  6 -0.022353
 11  7  0.014851 11  8 -0.015179 11  9  0.231960 11 10  0.273352 11 12  0.176355 11 13  0.024669 11 14  0.059830 11 15 -0.117348
 11 16 -0.511751 11 17 -0.065504 11 18  0.064820 12  1  0.237908 12  2 -0.013414 12  3 -0.015231 12  4  0.256019 12  5 -0.168878
 12  6 -0.006374 12  7  0.240159 12  8 -0.016326 12  9  0.071332 12 10 -0.020130 12 11  0.176355 12 13 -0.027251 12 14  0.064408
 12 15 -0.000304 12 16 -0.244252 12 17  0.266188 12 18 -0.201818 13  1  0.139761 13  2  0.045193 13  3 -0.026903 13  4 -0.093883
 13  5 -0.008803 13  6 -0.030953 13  7 -0.036472 13  8 -0.034178 13  9 -0.010900 13 10  0.076311 13 11  0.024669 13 12 -0.027251
 13 14  0.323762 13 15  0.017340 13 16  0.024078 13 17  0.010779 13 18 -0.004034 14  1  0.112065 14  2  0.002942 14  3  0.003377
 14  4 -0.019717 14  5 -0.015536 14  6 -0.041361 14  7 -0.028603 14  8  0.002352 14  9  0.023143 14 10 -0.035322 14 11  0.059830
 14 12  0.064408 14 13  0.323762 14 15 -0.166802 14 16 -0.065252 14 17 -0.080125 14 18  0.066156 15  1  0.061610 15  2  0.010033
 15  3 -0.010478 15  4 -0.000281 15  5 -0.025674 15  6 -0.001050 15  7  0.008289 15  8 -0.011487 15  9 -0.178951 15 10  0.038026
 15 11 -0.117348 15 12 -0.000304 15 13  0.017340 15 14 -0.166802 15 16 -0.010456 15 17  0.066062 15 18 -0.019244 16  1 -0.033070
 16  2  0.000558 16  3 -0.005422 16  4  0.061161 16  5 -0.006315 16  6  0.007437 16  7  0.035352 16  8 -0.005179 16  9  0.012553
 16 10 -0.531160 16 11 -0.511751 16 12 -0.244252 16 13  0.024078 16 14 -0.065252 16 15 -0.010456 16 17 -0.205805 16 18  0.061386
 17  1 -0.021927 17  2  0.029861 17  3 -0.034956 17  4  0.010533 17  5  0.067989 17  6 -0.003865 17  7  0.033811 17  8 -0.035068
 17  9 -0.228702 17 10  0.130400 17 11 -0.065504 17 12  0.266188 17 13  0.010779 17 14 -0.080125 17 15  0.066062 17 16 -0.205805
 17 18 -0.699477 18  1 -0.027975 18  2 -0.031318 18  3  0.038389 18  4 -0.024845 18  5  0.004545 18  6  0.034862 18  7 -0.031706
 18  8  0.037860 18  9 -0.200462 18 10 -0.068578 18 11  0.064820 18 12 -0.201818 18 13 -0.004034 18 14  0.066156 18 15 -0.019244
 18 16  0.061386 18 17 -0.699477
hooo predictions                                   Fri Sep 25 14:50:19 2015
```

B.2 SPFIT assignment and output file for DO_3

```
DOOO predictions                                   Fri Sep 25 15:24:05 2015
LINES REQUESTED=  301 NUMBER OF PARAMETERS= 24 NUMBER OF ITERATIONS= 10
  MARQUARDT PARAMETER = 0.0000E+00 max (OBS-CALC)/ERROR =1.0000E+06
                              PARAMETERS - A.PRIORI ERROR
     1      1         10000   6.7859739201555E+04    1.000000E+10  A
     2      2         20000   9.4489017469189E+03    1.000000E+11  B
     3      3         30000   8.2990874338975E+03    1.000000E+11  C
     4      4           200  -3.7396588701691E-02    9.702165E+10  -DN
     5      5          1100  -1.8145831961274E-01    1.000000E+11  -DNK
     6      6          2000  -2.3948473083639E+00    1.000000E+10  -DK
     7      7         40100  -4.5480442535809E-03    1.000000E+11  -dN
     8      8         41000  -1.8387445320612E-01    1.000000E+10  -dK
     9      9      10010000  -1.2247319768010E+03    5.762869E+10  eaa
    10     10      10020000  -1.0153511524435E+02    6.632208E+10  ebb
    11     11      10030000  -3.7869174272997E+00    6.288901E+10  ecc
    12     12      10610000   4.1141821217462E+01    6.288901E+10  (eab+eba)
    13     13     120000000   4.6222570298589E-01    5.007459E+10  a_F
    14     14     120010000   1.2969095065145E+00    3.642117E+10  Taa
    15     14    -120030000  -1.2969095065145E+00       -1.000000  Tcc
    16     15     120020000  -1.0891261460888E+00    5.970145E+10  Tbb
```

```
    17     15    -120030000   1.0891261460888E+00       -1.000000  Tcc
    18     16       1000100   7.9925781199592E-04    1.000000E+10  DNS
    19     17      10010100   8.0668962271289E-01    1.000000E+10  DNKS
    20     18      10011000   1.5783872306555E-01    1.000000E+10  DKS
    21     19     220010000   1.2556538735062E-02    1.000000E+10  chi_aa
    22     19    -220030000  -1.2556538735062E-02       -1.000000  chi_cc
    23     20     220020000   1.5569700755351E-01    1.000000E+10  chi_bb
    24     20    -220030000  -1.0373674996675E-01       -0.666273  chi_cc
24 parameters read, 20 independent parameters
NUMBER OF PARAMETERS EXCLUDED IF INDEX < 0 =     2
ENERGY SORT OF WANG SUB-BLOCKS
PROLATE ROTOR
    V KMIN KMAX WTPL WTMN ESYMWT NSYM SPINS
    0    0    9    1    1    999    2  0.5  1.0
BLOCK - WT - SYM - V - TSP - N  -  other quanta  (rel. to F=0 )
    1    1    x    0    0  -1.5  -1.0
    1    1    c    0    0  -1.5  -1.0
    1    1    x    0    1  -0.5   0.0
    1    1    c    0    1  -0.5   0.0
    1    1    x    0    2  -0.5  -1.0
    1    1    c    0    2  -0.5  -1.0
    1    1    x    0    3   0.5   1.0
    1    1    c    0    3   0.5   1.0
    1    1    x    0    4   0.5   0.0
    1    1    c    0    4   0.5   0.0
    1    1    x    0    5   1.5   1.0
    1    1    c    0    5   1.5   1.0
    2    1    b    0    0  -1.5  -1.0
    2    1    a    0    0  -1.5  -1.0
    2    1    b    0    1  -0.5   0.0
    2    1    a    0    1  -0.5   0.0
    2    1    b    0    2  -0.5  -1.0
    2    1    a    0    2  -0.5  -1.0
    2    1    b    0    3   0.5   1.0
    2    1    a    0    3   0.5   1.0
    2    1    b    0    4   0.5   0.0
    2    1    a    0    4   0.5   0.0
    2    1    b    0    5   1.5   1.0
    2    1    a    0    5   1.5   1.0
Maximum Dimension for Hamiltonian = 60
                                                    EXP.FREQ.  -  CALC.FREQ. -   DIFF.  - EXP.ERR.- EST.ERR.-AVG. CALC.FREQ. -  DIFF. - WT.
    1:   1  0  1  2  2  0  0  0  1  2        17721.19540   17721.19441    0.00099    0.00500   0.00176
    2:   1  0  1  2  3  0  0  0  1  2        17721.35780   17721.36881   -0.01101    0.00500   0.00102
    3:   1  0  1  2  1  0  0  0  1  1        17721.79450   17721.79103    0.00347    0.00500   0.00152
    4:   1  0  1  2  2  0  0  0  1  1        17721.86240   17721.88765   -0.02525    0.00500   0.00179
    5:   1  0  1  1  1  0  0  0  1  2        17799.54830   17799.55180   -0.00350    0.00500   0.00255
    6:   1  0  1  1  1  0  0  0  1  1        17800.24720   17800.24504    0.00216    0.00500   0.00276
    7:   1  0  1  1  2  0  0  0  1  2        17800.61770   17800.62028   -0.00258    0.00500   0.00192
    8:   1  0  1  1  2  0  0  0  1  1        17801.31780   17801.31352    0.00428    0.00500   0.00260
    9:   2  0  2  3  4  1  0  1  2  3        35452.05770   35452.03589    0.02181    0.00500   0.00110
   10:   2  0  2  3  3  1  0  1  2  2        35452.13960   35452.14128   -0.00168    0.00500   0.00111
   11:   2  0  2  3  2  1  0  1  2  1        35452.21550   35452.19281    0.02269    0.00500   0.00114
   12:   2  0  2  2  3  1  0  1  1  2        35503.57650   35503.55860    0.01790    0.00500   0.00102
   13:   2  0  2  2  3  1  0  1  2  3        35582.80360   35582.81006   -0.00646    0.00500   0.00303
   14:   3  0  3  4  5  2  0  2  3  4        53147.67860   53147.68171   -0.00311    0.00500   0.00108
   15:   3  0  3  4  4  2  0  2  3  3        53147.71530   53147.72574   -0.01044    0.00500   0.00108
   16:   3  0  3  4  3  2  0  2  3  2        53147.74550   53147.75215   -0.00665    0.00500   0.00109
   17:   3  0  3  3  3  2  0  2  2  3        53197.14550   53197.14652   -0.00102    0.00500   0.00230
   18:   3  0  3  3  2  2  0  2  2  2        53197.35430   53197.35954   -0.00524    0.00500   0.00256
   19:   3  0  3  3  4  2  0  2  2  3        53197.41930   53197.42526   -0.00596    0.00500   0.00164
   20:   3  0  3  3  3  2  0  2  2  2        53197.55260   53197.56092   -0.00832    0.00500   0.00170
   21:   4  0  4  5  6  3  0  3  4  5        70790.87650   70790.86218    0.01432    0.00500   0.00172
   22:   4  0  4  5  5  3  0  3  4  4        70790.88860   70790.88534    0.00326    0.00500   0.00172
   23:   4  0  4  5  4  3  0  3  4  3        70790.89800   70790.89920   -0.00120    0.00500   0.00173
   24:   4  0  4  4  5  3  0  3  3  4        70839.44750   70839.44075    0.00675    0.00500   0.00246
   25:   4  0  4  4  4  3  0  3  3  3        70839.50610   70839.50358    0.00252    0.00500   0.00245
   26:   1  1  1  2  1  0  0  0  1  2        75841.14880   75841.15564   -0.00684    0.00500   0.00255
   27:   1  1  1  2  2  0  0  0  1  2        75841.55660   75841.56404   -0.00744    0.00500   0.00223
   28:   1  1  1  2  3  0  0  0  1  2        75842.10090   75842.10854   -0.00764    0.00500   0.00165
   29:   1  1  1  2  1  0  0  0  1  1        75841.84000   75841.84888   -0.00888    0.00500   0.00194
   30:   1  1  1  2  2  0  0  0  1  1        75842.25100   75842.25728   -0.00628    0.00500   0.00218
   31:   1  1  1  1  1  0  0  0  1  2        76771.12960   76771.14012   -0.01052    0.00500   0.00273
   32:   1  1  1  1  2  0  0  0  1  2        76769.81040   76769.81993   -0.00953    0.00500   0.00276
   33:   1  1  0  2  3  1  0  1  2  3        59245.57960   59245.58818   -0.00858    0.00500   0.00170
   34:   1  1  0  2  2  1  0  1  2  3        59245.13240   59245.11587    0.01653    0.00500   0.00193
   35:   1  1  1  2  3  2  0  2  3  4        22668.70190   22668.70383   -0.00193    0.00500   0.00217
   36:   1  1  1  2  2  2  0  2  3  3        22668.21650   22668.22835   -0.01185    0.00500   0.00259
   37:   1  1  1  2  1  2  0  2  3  2        22667.86850   22667.86505    0.00345    0.00500   0.00258
   38:   1  1  1  1  2  2  0  2  2  2        23466.05300   23466.05546   -0.00246    0.00500   0.00243
   39:   1  1  1  1  2  2  0  2  2  3        23465.63470   23465.64105   -0.00635    0.00500   0.00273
   40:   1  1  1  1  1  2  0  2  2  1        23467.62750   23467.62421    0.00329    0.00500   0.00316
   41:   1  1  1  1  1  2  0  2  2  2        23467.37250   23467.37565   -0.00315    0.00500   0.00275
   42:   2  1  1  3  4  2  0  2  3  4        60497.23190   60497.23642   -0.00452    0.00500   0.00193
   43:   2  1  1  3  3  2  0  2  3  4        60497.08750   60497.07873    0.00877    0.00500   0.00220
   44:   2  1  1  3  4  2  0  2  3  3        60497.30410   60497.30544   -0.00134    0.00500   0.00241
   45:   2  1  1  3  3  2  0  2  3  3        60497.13800   60497.14775   -0.00975    0.00500   0.00211
   46:   2  1  1  3  2  2  0  2  3  2        60497.16760   60497.16882   -0.00122    0.00500   0.00213
   47:   2  1  1  2  3  2  0  2  2  3        61059.94670   61059.94833   -0.00163    0.00500   0.00203
   48:   2  1  1  2  2  2  0  2  2  3        61059.62120   61059.61257    0.00863    0.00500   0.00235
   49:   2  1  1  2  3  2  0  2  2  2        61060.36390   61060.36274    0.00116    0.00500   0.00216
   50:   2  1  1  2  2  2  0  2  2  2        61060.02880   61060.02697    0.00183    0.00500   0.00193
   51:   2  1  1  2  1  2  0  2  2  2        61059.91640   61059.90701    0.00939    0.00500   0.00280
```

52:	4	0	4	5	6	3	1	3	4	5	15298.49350	15298.49236	0.00114	0.00500	0.00236		
53:	4	0	4	5	5	3	1	3	4	4	15298.62930	15298.63418	-0.00488	0.00500	0.00246		
54:	4	0	4	5	4	3	1	3	4	3	15298.82310	15298.82903	-0.00593	0.00500	0.00238		
55:	4	0	4	4	5	3	1	3	3	4	15077.58710	15077.59778	-0.01068	0.00500	0.00254		
56:	4	0	4	4	4	3	1	3	3	3	15077.30210	15077.31261	-0.01051	0.00500	0.00250		
57:	4	0	4	4	3	3	1	3	3	2	15077.16570	15077.17461	-0.00891	0.00500	0.00273		
58:	3	1	3	4	4	2	1	2	3	4	51541.23720	51541.24077	-0.00357	0.00500	0.00248		
59:	3	1	3	4	4	2	1	2	3	3	51541.48380	51541.48797	-0.00417	0.00500	0.00137		
60:	3	1	3	4	3	2	1	2	3	3	51541.28720	51541.28831	-0.00111	0.00500	0.00248		
61:	3	1	3	4	3	2	1	2	3	2	51541.54670	51541.54981	-0.00311	0.00500	0.00136		
62:	3	1	3	3	3	2	1	2	2	3	51420.16450	51420.16449	0.00001	0.00500	0.00227		
63:	3	1	3	3	4	2	1	2	2	3	51420.09480	51420.09523	-0.00043	0.00500	0.00138		
64:	3	1	3	3	3	2	1	2	2	2	51419.98700	51419.98501	0.00199	0.00500	0.00138		
65:	3	1	2	4	5	3	1	3	4	5	6819.48040	6819.47915	0.00125	0.00500	0.00298		
66:	3	1	2	4	4	3	1	3	4	4	6819.56630	6819.57656	-0.01026	0.00500	0.00317		
67:	3	1	2	4	3	3	1	3	4	3	6819.83950	6819.83284	0.00666	0.00500	0.00300		
68:	3	1	2	3	4	3	1	3	3	4	6991.36430	6991.35934	0.00496	0.00500	0.00326		
69:	3	1	2	3	3	3	1	3	3	3	6990.92520	6990.92032	0.00488	0.00500	0.00308		
70:	4	1	4	5	6	3	1	3	4	5	68667.43430	68667.43523	-0.00093	0.00500	0.00186		
71:	4	1	4	5	5	3	1	3	4	4	68667.48360	68667.48495	-0.00135	0.00500	0.00186		
72:	4	1	4	4	5	3	1	3	3	4	68614.52340	68614.50801	0.01539	0.00500	0.00190		
73:	4	1	4	4	4	3	1	3	3	3	68614.50410	68614.48514	0.01896	0.00500	0.00189		
74:	4	1	4	4	3	3	1	3	3	2	68614.47340	68614.46767	0.00573	0.00500	0.00188		
75:	5	1	5	6	5	4	0	4	5	4	139153.20170	139153.09341	0.10829	0.05000	0.00547	139153.21044	-0.00874 0.3333
76:	5	1	5	6	6	4	0	4	5	5	139153.20170	139153.23701	-0.03531	0.05000	0.00547	139153.21044	-0.00874 0.3333
77:	5	1	5	6	7	4	0	4	5	6	139153.20170	139153.30090	-0.09920	0.05000	0.00547	139153.21044	-0.00874 0.3333
78:	5	1	5	5	6	4	0	4	4	5	139297.71660	139297.51127	0.20533	0.05000	0.00566	139297.72198	-0.00538 0.3333
79:	5	1	5	5	5	4	0	4	4	4	139297.71660	139297.76941	-0.05281	0.05000	0.00566	139297.72198	-0.00538 0.3333
80:	5	1	5	5	4	4	0	4	4	3	139297.71660	139297.88528	-0.16868	0.05000	0.00566	139297.72198	-0.00538 0.3333
81:	6	1	6	7	6	5	0	5	6	5	153671.03410	153670.95139	0.08271	0.05000	0.01084	153671.06338	-0.02928 0.3333
82:	6	1	6	7	7	5	0	5	6	6	153671.03410	153671.08962	-0.05552	0.05000	0.01084	153671.06338	-0.02928 0.3333
83:	6	1	6	7	8	5	0	5	6	7	153671.03410	153671.14913	-0.11503	0.05000	0.01084	153671.06338	-0.02928 0.3333
84:	6	1	6	6	7	5	0	5	5	6	153761.85940	153761.68369	0.17571	0.05000	0.01056	153761.86259	-0.00319 0.3333
85:	6	1	6	6	6	5	0	5	5	5	153761.85940	153761.90380	-0.04440	0.05000	0.01056	153761.86259	-0.00319 0.3333
86:	6	1	6	6	5	5	0	5	5	4	153761.85940	153762.00027	-0.14087	0.05000	0.01056	153761.86259	-0.00319 0.3333
87:	6	2	4	7	6	6	1	5	7	6	165942.51130	165942.37438	0.13692	0.05000	0.01660	165942.52377	-0.01247 0.3333
88:	6	2	4	7	7	6	1	5	7	7	165942.51130	165942.54417	-0.03287	0.05000	0.01660	165942.52377	-0.01247 0.3333
89:	6	2	4	7	8	6	1	5	7	8	165942.51130	165942.65276	-0.14146	0.05000	0.01660	165942.52377	-0.01247 0.3333
90:	6	2	4	6	7	6	1	5	6	7	166371.89780	166371.67567	0.22213	0.05000	0.01756	166371.87891	0.01889 0.3333
91:	6	2	4	6	6	6	1	5	6	6	166371.89780	166371.91590	-0.01810	0.05000	0.01756	166371.87891	0.01889 0.3333
92:	6	2	4	6	5	6	1	5	6	5	166371.89780	166372.04516	-0.14736	0.05000	0.01756	166371.87891	0.01889 0.3333
93:	7	1	7	8	7	6	0	6	7	6	167774.06960	167774.06345	0.00615	0.05000	0.01993	167774.16999	-0.10039 0.3333
94:	7	1	7	8	8	6	0	6	7	7	167774.06960	167774.19553	-0.12593	0.05000	0.01993	167774.16999	-0.10039 0.3333
95:	7	1	7	8	9	6	0	6	7	8	167774.06960	167774.25100	-0.18140	0.05000	0.01993	167774.16999	-0.10039 0.3333
96:	7	1	7	7	8	6	0	6	6	7	167822.87630	167822.68413	0.19217	0.05000	0.01944	167822.84116	0.03514 0.3333
97:	7	1	7	7	7	6	0	6	6	6	167822.87630	167822.87810	-0.00180	0.05000	0.01944	167822.84116	0.03514 0.3333
98:	7	1	7	7	6	6	0	6	6	5	167822.87630	167822.96126	-0.08496	0.05000	0.01944	167822.84116	0.03514 0.3333
99:	5	2	3	6	5	5	1	4	6	5	168697.77240	168697.59148	0.18092	0.05000	0.00891	168697.76810	0.00430 0.3333
100:	5	2	3	6	6	5	1	4	6	6	168697.77240	168697.78814	-0.01574	0.05000	0.00891	168697.76810	0.00430 0.3333
101:	5	2	3	6	7	5	1	4	6	7	168697.77240	168697.92469	-0.15229	0.05000	0.00891	168697.76810	0.00430 0.3333
102:	4	2	2	5	4	4	1	3	5	4	171134.10790	171133.83684	0.27106	0.05000	0.00470	171134.05269	0.05521 0.3333
103:	4	2	2	5	5	4	1	3	5	5	171134.10790	171134.07015	0.03775	0.05000	0.00470	171134.05269	0.05521 0.3333
104:	4	2	2	5	6	4	1	3	5	6	171134.10790	171134.25106	-0.14316	0.05000	0.00470	171134.05269	0.05521 0.3333
105:	4	2	2	4	5	4	1	3	4	5	171842.20360	171841.94177	0.26183	0.05000	0.00537	171842.28544	-0.08184 0.3333
106:	4	2	2	4	4	4	1	3	4	4	171842.20360	171842.34258	-0.13898	0.05000	0.00537	171842.28544	-0.08184 0.3333
107:	4	2	2	4	3	4	1	3	4	3	171842.20360	171842.57198	-0.36838	0.05000	0.00537	171842.28544	-0.08184 0.3333
108:	3	2	1	4	3	3	1	2	4	3	173149.00280	173148.67178	0.33102	0.05000	0.00378	173148.95362	0.04918 0.3333
109:	3	2	1	4	4	3	1	2	4	4	173149.00280	173148.96362	0.03918	0.05000	0.00378	173148.95362	0.04918 0.3333
110:	3	2	1	4	5	3	1	2	4	5	173149.00280	173149.22547	-0.22267	0.05000	0.00378	173148.95362	0.04918 0.3333
111:	3	2	1	3	4	3	1	2	3	4	174109.58570	174109.14572	0.43998	0.05000	0.00455	174109.66793	-0.08223 0.3333
112:	3	2	1	3	3	3	1	2	3	3	174109.58570	174109.75380	-0.16810	0.05000	0.00455	174109.66793	-0.08223 0.3333
113:	3	2	1	3	2	3	1	2	3	2	174109.58570	174110.10429	-0.51859	0.05000	0.00455	174109.66793	-0.08223 0.3333
114:	2	2	0	3	2	2	1	1	3	2	174641.26450	174640.68911	0.57539	0.05000	0.00535	174641.10621	0.15829 0.3333
115:	2	2	0	3	3	2	1	1	3	3	174641.26450	174641.09422	0.17028	0.05000	0.00535	174641.10621	0.15829 0.3333
116:	2	2	0	3	4	2	1	1	3	4	174641.26450	174641.53531	-0.27081	0.05000	0.00535	174641.10621	0.15829 0.3333
117:	2	2	0	2	3	2	1	1	2	3	176045.80590	176045.87657	-0.07067	0.05000	0.00723		
118:	2	2	1	3	2	2	1	2	3	2	178023.52620	178023.23196	0.29424	0.05000	0.00493	178023.46269	0.06351 0.3333
119:	2	2	1	3	3	2	1	2	3	3	178023.52620	178023.40185	0.12435	0.05000	0.00493	178023.46269	0.06351 0.3333
120:	2	2	1	3	4	2	1	2	3	4	178023.52620	178023.75427	-0.22807	0.05000	0.00493	178023.46269	0.06351 0.3333
121:	2	2	1	2	3	2	1	2	2	3	179549.24940	179549.25519	-0.00579	0.05000	0.00730		
122:	2	2	1	2	2	2	1	2	2	2	179550.24680	179549.95642	0.29038	0.05000	0.00744	179550.20473	0.04207 0.5000
123:	2	2	1	2	1	2	1	2	2	1	179550.24680	179550.45304	-0.20624	0.05000	0.00744	179550.20473	0.04207 0.5000
124:	3	2	2	4	3	3	1	3	4	3	179886.35280	179886.26598	0.08682	0.05000	0.00379	179886.34939	0.00341 0.3333
125:	3	2	2	4	4	3	1	3	4	4	179886.35280	179886.30770	0.04510	0.05000	0.00379	179886.34939	0.00341 0.3333
126:	3	2	2	4	5	3	1	3	4	5	179886.35280	179886.47448	-0.12168	0.05000	0.00379	179886.34939	0.00341 0.3333
127:	3	2	2	3	4	3	1	3	3	4	181014.76410	181014.61069	0.15341	0.05000	0.00462	181014.80187	-0.03777 0.3333
128:	3	2	2	3	3	3	1	3	3	3	181014.76410	181014.79063	-0.02653	0.05000	0.00462	181014.80187	-0.03777 0.3333
129:	3	2	2	3	2	3	1	3	3	2	181014.76410	181015.00429	-0.24019	0.05000	0.00462	181014.80187	-0.03777 0.3333
130:	4	2	3	5	5	4	1	4	5	5	182275.14650	182275.09673	0.04977	0.05000	0.00519	182275.13230	0.01420 0.3333
131:	4	2	3	5	4	4	1	4	5	4	182275.14650	182275.11999	0.02651	0.05000	0.00519	182275.13230	0.01420 0.3333
132:	4	2	3	5	6	4	1	4	5	6	182275.14650	182275.18016	-0.03366	0.05000	0.00519	182275.13230	0.01420 0.3333
133:	4	2	3	4	5	4	1	4	4	5	183194.98920	183194.93658	0.05262	0.05000	0.00548	183194.97867	0.01053 0.3333
134:	4	2	3	4	4	4	1	4	4	4	183194.98920	183194.94965	0.03955	0.05000	0.00548	183194.97867	0.01053 0.3333
135:	4	2	3	4	3	4	1	4	4	3	183194.98920	183195.04979	-0.06059	0.05000	0.00548	183194.97867	0.01053 0.3333
136:	5	2	4	6	6	5	1	5	6	6	185221.79520	185221.69341	0.10179	0.05000	0.00979	185221.72671	0.06849 0.3333
137:	5	2	4	6	7	5	1	5	6	7	185221.79520	185221.73228	0.06292	0.05000	0.00979	185221.72671	0.06849 0.3333
138:	5	2	4	6	5	5	1	5	6	5	185221.79520	185221.75445	0.04075	0.05000	0.00979	185221.72671	0.06849 0.3333
139:	5	2	4	5	5	5	1	5	5	5	186018.61500	186018.57062	0.04438	0.05000	0.00998	186018.60527	0.00973 0.3333
140:	5	2	4	5	4	5	1	5	5	4	186018.61500	186018.61472	0.00028	0.05000	0.00998	186018.60527	0.00973 0.3333
141:	5	2	4	5	6	5	1	5	5	6	186018.61500	186018.63048	-0.01548	0.05000	0.00998	186018.60527	0.00973 0.3333
142:	6	2	5	7	7	6	1	6	7	7	188743.43200	188743.27360	0.15840	0.05000	0.01843	188743.30606	0.12594 0.3333
143:	6	2	5	7	8	6	1	6	7	8	188743.43200	188743.28577	0.14623	0.05000	0.01843	188743.30606	0.12594 0.3333

144:	6	2	5	7	6	6	1	6	7	6	188743.43200	188743.35880	0.07320	0.05000	0.01843	188743.30606	0.12594	0.3333
145:	6	2	5	6	6	6	1	6	6	6	189463.19730	189463.15047	0.04683	0.05000	0.01862	189463.18726	0.01004	0.3333
146:	6	2	5	6	5	6	1	6	6	5	189463.19730	189463.16295	0.03435	0.05000	0.01862	189463.18726	0.01004	0.3333
147:	6	2	5	6	7	6	1	6	6	7	189463.19730	189463.24835	-0.05105	0.05000	0.01862	189463.18726	0.01004	0.3333
148:	2	2	1	3	2	1	1	0	2	1	211328.74560	211328.51503	0.23057	0.05000	0.00468	211328.70863	0.03697	0.3333
149:	2	2	1	3	3	1	1	0	2	2	211328.74560	211328.74178	0.00382	0.05000	0.00468	211328.70863	0.03697	0.3333
150:	2	2	1	3	4	1	1	0	2	3	211328.74560	211328.86910	-0.12350	0.05000	0.00468	211328.70863	0.03697	0.3333
151:	2	2	0	3	2	1	1	1	2	1	212470.00720	212469.99288	0.01432	0.05000	0.00462	212470.02480	-0.01760	0.3333
152:	2	2	0	3	3	1	1	1	2	2	212470.00720	212470.01362	-0.00642	0.05000	0.00462	212470.02480	-0.01760	0.3333
153:	2	2	0	3	4	1	1	1	2	3	212470.00720	212470.06790	-0.06070	0.05000	0.00462	212470.02480	-0.01760	0.3333
154:	2	2	0	2	3	1	1	1	1	2	213640.16150	213640.18385	-0.02235	0.05000	0.00649			
155:	3	2	2	4	4	2	1	1	3	3	228029.12110	228029.13685	-0.01575	0.05000	0.00428	228029.11531	0.00579	0.3333
156:	3	2	2	4	3	2	1	1	3	2	228029.12110	228028.91950	0.20160	0.05000	0.00428	228029.11531	0.00579	0.3333
157:	3	2	2	4	5	2	1	1	3	4	228029.12110	228029.28959	-0.16849	0.05000	0.00428	228029.11531	0.00579	0.3333
158:	3	2	2	3	4	2	1	1	2	3	228914.29310	228913.93058	0.36252	0.05000	0.00451	228914.41989	-0.12679	0.3333
159:	3	2	2	3	3	2	1	1	2	2	228914.29310	228914.51555	-0.22245	0.05000	0.00451	228914.41989	-0.12679	0.3333
160:	3	2	2	3	2	2	1	1	2	1	228914.29310	228914.81353	-0.52043	0.05000	0.00451	228914.41989	-0.12679	0.3333
161:	3	2	1	4	4	2	1	2	3	3	231510.05280	231510.02815	0.02465	0.05000	0.00386	231510.05721	-0.00441	0.3333
162:	3	2	1	4	3	2	1	2	3	2	231510.05280	231510.05442	-0.00162	0.05000	0.00386	231510.05721	-0.00441	0.3333
163:	3	2	1	4	5	2	1	2	3	4	231510.05280	231510.08904	-0.03624	0.05000	0.00386	231510.05721	-0.00441	0.3333
164:	3	2	1	3	4	2	1	2	2	3	232520.69730	232520.60028	0.09702	0.05000	0.00469	232520.68804	0.00926	0.3333
165:	3	2	1	3	3	2	1	2	2	2	232520.69730	232520.65913	0.03817	0.05000	0.00469	232520.68804	0.00926	0.3333
166:	3	2	1	3	2	2	1	2	2	1	232520.69730	232520.80472	-0.10742	0.05000	0.00469	232520.68804	0.00926	0.3333
167:	4	2	3	5	4	3	1	2	4	3	244123.04090	244122.80443	0.23647	0.05000	0.00505	244122.98193	0.05897	0.3333
168:	4	2	3	5	5	3	1	2	4	4	244123.04090	244123.00513	0.03577	0.05000	0.00505	244122.98193	0.05897	0.3333
169:	4	2	3	5	6	3	1	2	4	5	244123.04090	244123.13624	-0.09534	0.05000	0.00505	244122.98193	0.05897	0.3333
170:	4	2	3	4	5	3	1	2	3	4	244818.40260	244818.08525	0.31735	0.05000	0.00522	244818.44573	-0.04313	0.3333
171:	4	2	3	4	4	3	1	2	3	3	244818.40260	244818.51447	-0.11187	0.05000	0.00522	244818.44573	-0.04313	0.3333
172:	4	2	3	4	3	3	1	2	3	2	244818.40260	244818.73746	-0.33486	0.05000	0.00522	244818.44573	-0.04313	0.3333
173:	4	2	2	5	5	3	1	3	4	4	251190.04520	251189.98928	0.05592	0.05000	0.00501	251190.02144	0.02376	0.3333
174:	4	2	2	5	6	3	1	3	4	5	251190.04520	251190.01855	0.02665	0.05000	0.00501	251190.02144	0.02376	0.3333
175:	4	2	2	5	4	3	1	3	4	3	251190.04520	251190.05650	-0.01130	0.05000	0.00501	251190.02144	0.02376	0.3333
176:	4	2	2	4	4	3	1	3	3	3	252065.32990	252065.28736	0.04254	0.05000	0.00544	252065.32219	0.00771	0.3333
177:	4	2	2	4	5	3	1	3	3	4	252065.32990	252065.31530	0.01460	0.05000	0.00544	252065.32219	0.00771	0.3333
178:	4	2	2	4	3	3	1	3	3	2	252065.32990	252065.36391	-0.03401	0.05000	0.00544	252065.32219	0.00771	0.3333
179:	5	2	4	6	5	4	1	3	5	4	259617.68590	259617.45722	0.22868	0.05000	0.00804	259617.62025	0.06565	0.3333
180:	5	2	4	6	6	4	1	3	5	5	259617.68590	259617.64548	0.04042	0.05000	0.00804	259617.62025	0.06565	0.3333
181:	5	2	4	6	7	4	1	3	5	6	259617.68590	259617.75804	-0.07214	0.05000	0.00804	259617.62025	0.06565	0.3333
182:	5	2	4	5	6	4	1	3	4	5	260170.66320	260170.36599	0.29721	0.05000	0.00808	260170.65218	0.01102	0.3333
183:	5	2	4	5	5	4	1	3	4	4	260170.66320	260170.70786	-0.04466	0.05000	0.00808	260170.65218	0.01102	0.3333
184:	5	2	4	5	4	4	1	3	4	3	260170.66320	260170.88268	-0.21948	0.05000	0.00808	260170.65218	0.01102	0.3333
185:	5	2	3	6	6	4	1	4	5	5	271584.00620	271583.90579	0.10041	0.05000	0.00815	271583.93983	0.06637	0.3333
186:	5	2	3	6	7	4	1	4	5	6	271584.00620	271583.90930	0.09690	0.05000	0.00815	271583.93983	0.06637	0.3333
187:	5	2	3	6	5	4	1	4	5	4	271584.00620	271584.00442	0.00178	0.05000	0.00815	271583.93983	0.06637	0.3333
188:	5	2	3	5	5	4	1	4	4	4	272373.05540	272373.00660	0.04880	0.05000	0.00854	272373.04692	0.00848	0.3333
189:	5	2	3	5	4	4	1	4	4	3	272373.05540	272373.03669	0.01871	0.05000	0.00854	272373.04692	0.00848	0.3333
190:	5	2	3	5	6	4	1	4	4	5	272373.05540	272373.09746	-0.04206	0.05000	0.00854	272373.04692	0.00848	0.3333
191:	6	2	5	7	7	5	1	4	6	6	274523.92570	274523.91058	0.01512	0.05000	0.01326	274523.88386	0.04184	0.3333
192:	6	2	5	7	6	5	1	4	6	5	274523.92570	274523.73115	0.19455	0.05000	0.01326	274523.88386	0.04184	0.3333
193:	6	2	5	7	8	5	1	4	6	7	274523.92570	274524.00986	-0.08416	0.05000	0.01326	274523.88386	0.04184	0.3333
194:	6	2	5	6	7	5	1	4	5	6	274966.12500	274965.83901	0.28599	0.05000	0.01315	274966.08106	0.04394	0.3333
195:	6	2	5	6	6	5	1	4	5	5	274966.12500	274966.12988	-0.00488	0.05000	0.01315	274966.08106	0.04394	0.3333
196:	6	2	5	6	5	5	1	4	5	4	274966.12500	274966.27429	-0.14929	0.05000	0.01315	274966.08106	0.04394	0.3333
197:	7	2	6	8	7	6	1	5	7	6	288851.21150	288851.03371	0.17779	0.05000	0.02158	288851.17894	0.03256	0.3333
198:	7	2	6	8	8	6	1	5	7	7	288851.21150	288851.20667	0.00483	0.05000	0.02158	288851.17894	0.03256	0.3333
199:	7	2	6	8	9	6	1	5	7	8	288851.21150	288851.29644	-0.08494	0.05000	0.02158	288851.17894	0.03256	0.3333
200:	7	2	6	7	8	6	1	5	6	7	289203.75800	289203.49615	0.26185	0.05000	0.02130	289203.70996	0.04804	0.3333
201:	7	2	6	7	7	6	1	5	6	6	289203.75800	289203.75473	0.00327	0.05000	0.02130	289203.70996	0.04804	0.3333
202:	7	2	6	7	6	6	1	5	6	5	289203.75800	289203.87898	-0.12098	0.05000	0.02130	289203.70996	0.04804	0.3333
203:	6	2	4	7	8	5	1	5	6	7	292780.58980	292780.40930	0.18050	0.05000	0.01427	292780.46130	0.12850	0.3333
204:	6	2	4	7	7	5	1	5	6	6	292780.58980	292780.42522	0.16458	0.05000	0.01427	292780.46130	0.12850	0.3333
205:	6	2	4	7	6	5	1	5	6	5	292780.58980	292780.54938	0.04042	0.05000	0.01427	292780.46130	0.12850	0.3333
206:	6	2	4	6	5	5	1	5	5	4	293518.32690	293518.30015	0.02675	0.05000	0.01472	293518.34519	-0.01829	0.3333
207:	6	2	4	6	6	5	1	5	5	5	293518.32690	293518.30103	0.02587	0.05000	0.01472	293518.34519	-0.01829	0.3333
208:	6	2	4	6	7	5	1	5	5	6	293518.32690	293518.43438	-0.10748	0.05000	0.01472	293518.34519	-0.01829	0.3333
209:	5	3	2	6	5	5	2	3	6	5	293822.30290	293822.25640	0.04650	0.05000	0.01264	293822.40541	-0.10251	0.3333
210:	5	3	2	6	6	5	2	3	6	6	293822.30290	293822.40102	-0.09812	0.05000	0.01264	293822.40541	-0.10251	0.3333
211:	5	3	2	6	7	5	2	3	6	7	293822.30290	293822.55880	-0.25590	0.05000	0.01264	293822.40541	-0.10251	0.3333
212:	3	3	0	4	3	3	2	1	4	3	293955.04070	293954.66238	0.37832	0.05000	0.01762	293954.96683	0.07387	0.3333
213:	3	3	0	4	4	3	2	1	4	4	293955.04070	293954.94343	0.09727	0.05000	0.01762	293954.96683	0.07387	0.3333
214:	3	3	0	4	5	3	2	1	4	5	293955.04070	293955.29469	-0.25399	0.05000	0.01762	293954.96683	0.07387	0.3333
215:	4	3	1	5	4	4	2	2	5	4	293970.36190	293970.11988	0.24202	0.05000	0.01387	293970.32328	0.03862	0.3333
216:	4	3	1	5	5	4	2	2	5	5	293970.36190	293970.31257	0.04933	0.05000	0.01387	293970.32328	0.03862	0.3333
217:	4	3	1	5	6	4	2	2	5	6	293970.36190	293970.53739	-0.17549	0.05000	0.01387	293970.32328	0.03862	0.3333
218:	3	3	1	4	3	3	2	2	4	3	294037.12760	294036.75248	0.37512	0.05000	0.01761	294037.05207	0.07553	0.3333
219:	3	3	1	4	4	3	2	2	4	4	294037.12760	294037.02740	0.10020	0.05000	0.01761	294037.05207	0.07553	0.3333
220:	3	3	1	4	5	3	2	2	4	5	294037.12760	294037.37633	-0.24873	0.05000	0.01761	294037.05207	0.07553	0.3333
221:	4	3	2	5	4	4	2	3	5	4	294216.65450	294216.49434	0.16016	0.05000	0.01385	294216.68856	-0.03406	0.3333
222:	4	3	2	5	5	4	2	3	5	5	294216.65450	294216.67546	-0.02096	0.05000	0.01385	294216.68856	-0.03406	0.3333
223:	4	3	2	5	6	4	2	3	5	6	294216.65450	294216.89587	-0.24137	0.05000	0.01385	294216.68856	-0.03406	0.3333
224:	5	3	3	6	5	5	2	4	6	5	294396.01340	294395.90977	0.10363	0.05000	0.01254	294396.04411	-0.03071	0.3333
225:	5	3	3	6	6	5	2	4	6	6	294396.01340	294396.03591	-0.02251	0.05000	0.01254	294396.04411	-0.03071	0.3333
226:	5	3	3	6	7	5	2	4	6	7	294396.01340	294396.18664	-0.17324	0.05000	0.01254	294396.04411	-0.03071	0.3333
227:	6	3	4	7	6	6	2	5	7	6	294616.27740	294616.20192	0.07548	0.05000	0.01525	294616.29854	-0.02114	0.3333
228:	6	3	4	7	7	6	2	5	7	7	294616.27740	294616.29255	-0.01515	0.05000	0.01525	294616.29854	-0.02114	0.3333
229:	6	3	4	7	8	6	2	5	7	8	294616.27740	294616.40116	-0.12376	0.05000	0.01525	294616.29854	-0.02114	0.3333
230:	5	3	2	5	6	5	2	3	5	6	294901.27530	294901.03399	0.24131	0.05000	0.01463	294901.25880	0.01650	0.3333
231:	5	3	2	5	5	5	2	3	5	5	294901.27530	294901.27713	-0.00183	0.05000	0.01463	294901.25880	0.01650	0.3333
232:	5	3	2	5	4	5	2	3	5	4	294901.27530	294901.46529	-0.18999	0.05000	0.01463	294901.25880	0.01650	0.3333
233:	4	3	1	4	5	4	2	2	4	5	295292.73070	295292.36360	0.36710	0.05000	0.01742	295292.69990	0.03080	0.3333
234:	4	3	1	4	4	4	2	2	4	4	295292.73070	295292.72983	0.00087	0.05000	0.01742	295292.69990	0.03080	0.3333
235:	4	3	1	4	3	4	2	2	4	3	295292.73070	295293.00627	-0.27557	0.05000	0.01742	295292.69990	0.03080	0.3333

236:	7	2	5	8	9	6	1	6	7	8	314880.54880	314880.22737	0.32143	0.05000	0.02531	314880.29691	0.25189 0.3333
237:	7	2	5	8	8	6	1	6	7	7	314880.54880	314880.25850	0.29030	0.05000	0.02531	314880.29691	0.25189 0.3333
238:	7	2	5	8	7	6	1	6	7	6	314880.54880	314880.40486	0.14394	0.05000	0.02531	314880.29691	0.25189 0.3333
239:	7	2	5	7	6	6	1	6	6	5	315591.51540	315591.47510	0.04030	0.05000	0.02599	315591.54544	-0.03004 0.3333
240:	7	2	5	7	7	6	1	6	6	6	315591.51540	315591.49810	0.01730	0.05000	0.02599	315591.54544	-0.03004 0.3333
241:	7	2	5	7	8	6	1	6	6	7	315591.51540	315591.66312	-0.14772	0.05000	0.02599	315591.54544	-0.03004 0.3333
242:	3	3	1	4	3	2	2	0	3	2	347425.06600	347424.98287	0.08313	0.05000	0.01545	347425.06117	0.00483 0.3333
243:	3	3	1	4	4	2	2	0	3	3	347425.06600	347425.07003	-0.00403	0.05000	0.01545	347425.06117	0.00483 0.3333
244:	3	3	1	4	5	2	2	0	3	4	347425.06600	347425.13061	-0.06461	0.05000	0.01545	347425.06117	0.00483 0.3333
245:	3	3	0	4	3	2	2	1	3	2	347441.53660	347441.48484	0.05176	0.05000	0.01544	347441.56134	-0.02474 0.3333
246:	3	3	0	4	4	2	2	1	3	3	347441.53660	347441.56973	-0.03313	0.05000	0.01544	347441.56134	-0.02474 0.3333
247:	3	3	0	4	5	2	2	1	3	4	347441.53660	347441.62946	-0.09286	0.05000	0.01544	347441.56134	-0.02474 0.3333
248:	3	3	1	3	4	2	2	0	2	3	348601.91710	348601.73263	0.18447	0.05000	0.02011	348601.76924	0.14786 0.3333
249:	3	3	1	3	3	2	2	0	2	2	348601.91710	348601.73698	0.18012	0.05000	0.02011	348601.76924	0.14786 0.3333
250:	3	3	1	3	2	2	2	0	2	1	348601.91710	348601.83811	0.07899	0.05000	0.02011	348601.76924	0.14786 0.3333
251:	3	3	0	3	3	2	2	1	2	2	348619.46580	348619.28666	0.17914	0.05000	0.02013	348619.32015	0.14565 0.3333
252:	3	3	0	3	4	2	2	1	2	3	348619.46580	348619.28740	0.17840	0.05000	0.02013	348619.32015	0.14565 0.3333
253:	3	3	0	3	2	2	2	1	2	1	348619.46580	348619.38639	0.07941	0.05000	0.02013	348619.32015	0.14565 0.3333
254:	4	3	2	5	4	3	2	1	4	3	365190.74200	365190.62699	0.11501	0.05000	0.01243	365190.71686	0.02514 0.3333
255:	4	3	2	5	5	3	2	1	4	4	365190.74200	365190.71696	0.02504	0.05000	0.01243	365190.71686	0.02514 0.3333
256:	4	3	2	5	6	3	2	1	4	5	365190.74200	365190.80664	-0.06464	0.05000	0.01243	365190.71686	0.02514 0.3333
257:	4	3	1	5	4	3	2	2	4	3	365273.99640	365273.91039	0.08601	0.05000	0.01240	365273.99533	0.00107 0.3333
258:	4	3	1	5	5	3	2	2	4	4	365273.99640	365273.99415	0.00225	0.05000	0.01240	365273.99533	0.00107 0.3333
259:	4	3	1	5	6	3	2	2	4	5	365273.99640	365274.08146	-0.08506	0.05000	0.01240	365273.99533	0.00107 0.3333
260:	4	3	2	4	5	3	2	1	3	4	366256.31000	366256.07753	0.23247	0.05000	0.01539	366256.23805	0.07195 0.3333
261:	4	3	2	4	4	3	2	1	3	3	366256.31000	366256.24689	0.06311	0.05000	0.01539	366256.23805	0.07195 0.3333
262:	4	3	2	4	3	3	2	1	3	2	366256.31000	366256.38973	-0.07973	0.05000	0.01539	366256.23805	0.07195 0.3333
263:	4	3	1	4	5	3	2	2	3	4	366343.27120	366343.06821	0.20299	0.05000	0.01546	366343.22022	0.05098 0.3333
264:	4	3	1	4	4	3	2	2	3	3	366343.27120	366343.22656	0.04464	0.05000	0.01546	366343.22022	0.05098 0.3333
265:	4	3	1	4	3	3	2	2	3	2	366343.27120	366343.36588	-0.09468	0.05000	0.01546	366343.22022	0.05098 0.3333
266:	5	3	3	6	5	4	2	2	5	4	382879.60440	382879.53015	0.07425	0.05000	0.01180	382879.61167	-0.00727 0.3333
267:	5	3	3	6	6	4	2	2	5	5	382879.60440	382879.61123	-0.00683	0.05000	0.01180	382879.61167	-0.00727 0.3333
268:	5	3	3	6	7	4	2	2	5	6	382879.60440	382879.69362	-0.08922	0.05000	0.01180	382879.61167	-0.00727 0.3333
269:	5	3	2	6	5	4	2	3	5	4	383131.20720	383131.14083	0.06637	0.05000	0.01164	383131.21294	-0.00574 0.3333
270:	5	3	2	6	6	4	2	3	5	5	383131.20720	383131.21007	-0.00287	0.05000	0.01164	383131.21294	-0.00574 0.3333
271:	5	3	2	6	7	4	2	3	5	6	383131.20720	383131.28793	-0.08073	0.05000	0.01164	383131.21294	-0.00574 0.3333
272:	5	3	3	5	4	4	2	2	4	3	383819.13630	383819.24675	-0.11045	0.05000	0.01335	383819.11131	0.02499 0.3333
273:	5	3	3	5	5	4	2	2	4	4	383819.13630	383819.12241	0.01389	0.05000	0.01335	383819.11131	0.02499 0.3333
274:	5	3	3	5	6	4	2	2	4	5	383819.13630	383818.96477	0.17153	0.05000	0.01335	383819.11131	0.02499 0.3333
275:	5	3	2	5	6	4	2	3	4	5	384079.35280	384079.19486	0.15794	0.05000	0.01352	384079.32704	0.02576 0.3333
276:	5	3	2	5	5	4	2	3	4	4	384079.35280	384079.33408	0.01872	0.05000	0.01352	384079.32704	0.02576 0.3333
277:	5	3	2	5	4	4	2	3	4	3	384079.35280	384079.45219	-0.09939	0.05000	0.01352	384079.32704	0.02576 0.3333
278:	6	3	4	7	6	5	2	3	6	5	400442.40010	400442.34158	0.05852	0.05000	0.01462	400442.41430	-0.01420 0.3333
279:	6	3	4	7	7	5	2	3	6	6	400442.40010	400442.41499	-0.01489	0.05000	0.01462	400442.41430	-0.01420 0.3333
280:	6	3	4	7	8	5	2	3	6	7	400442.40010	400442.48632	-0.08622	0.05000	0.01462	400442.41430	-0.01420 0.3333
281:	6	3	3	7	6	5	2	4	6	5	401032.82790	401032.78177	0.04613	0.05000	0.01414	401032.83930	-0.01140 0.3333
282:	6	3	3	7	7	5	2	4	6	6	401032.82790	401032.83605	-0.00815	0.05000	0.01414	401032.83930	-0.01140 0.3333
283:	6	3	3	7	8	5	2	4	6	7	401032.82790	401032.90008	-0.07218	0.05000	0.01414	401032.83930	-0.01140 0.3333
284:	6	3	4	6	7	5	2	3	5	6	401271.84950	401271.77274	0.07676	0.05000	0.01507	401271.89678	-0.04728 0.3333
285:	6	3	4	6	6	5	2	3	5	5	401271.84950	401271.90721	-0.05771	0.05000	0.01507	401271.89678	-0.04728 0.3333
286:	6	3	4	6	5	5	2	3	5	4	401271.84950	401272.01040	-0.16090	0.05000	0.01507	401271.89678	-0.04728 0.3333
287:	6	3	3	6	7	5	2	4	5	6	401878.68880	401878.65909	0.02971	0.05000	0.01521	401878.76163	-0.07283 0.3333
288:	6	3	3	6	6	5	2	4	5	5	401878.68880	401878.76609	-0.07729	0.05000	0.01521	401878.76163	-0.07283 0.3333
289:	6	3	3	6	5	5	2	4	5	4	401878.68880	401878.85972	-0.17092	0.05000	0.01521	401878.76163	-0.07283 0.3333
290:	7	3	5	8	7	6	2	4	7	6	417822.18060	417822.16816	0.01244	0.05000	0.02112	417822.23491	-0.05431 0.3333
291:	7	3	5	8	8	6	2	4	7	7	417822.18060	417822.23719	-0.05659	0.05000	0.02112	417822.23491	-0.05431 0.3333
292:	7	3	5	8	9	6	2	4	7	8	417822.18060	417822.29940	-0.11880	0.05000	0.02112	417822.23491	-0.05431 0.3333
293:	7	3	5	7	8	6	2	4	6	7	418558.07670	418558.16155	-0.08485	0.05000	0.02092	418558.26889	-0.19219 0.3333
294:	7	3	5	7	7	6	2	4	6	6	418558.07670	418558.27911	-0.20241	0.05000	0.02092	418558.26889	-0.19219 0.3333
295:	7	3	5	7	6	6	2	4	6	5	418558.07670	418558.36602	-0.28932	0.05000	0.02092	418558.26889	-0.19219 0.3333
296:	7	3	4	8	7	6	2	5	7	6	419008.43830	419008.48959	-0.05129	0.05000	0.02022	419008.53408	-0.09578 0.3333
297:	7	3	4	8	8	6	2	5	7	7	419008.43830	419008.53056	-0.09226	0.05000	0.02022	419008.53408	-0.09578 0.3333
298:	7	3	4	8	9	6	2	5	7	8	419008.43830	419008.58207	-0.14377	0.05000	0.02022	419008.53408	-0.09578 0.3333
299:	7	3	4	7	8	6	2	5	6	7	419772.16660	419772.29244	-0.12584	0.05000	0.02089	419772.36986	-0.20326 0.3333
300:	7	3	4	7	7	6	2	5	6	6	419772.16660	419772.37187	-0.20527	0.05000	0.02089	419772.36986	-0.20326 0.3333
301:	7	3	4	7	6	6	2	5	6	5	419772.16660	419772.44527	-0.27867	0.05000	0.02089	419772.36986	-0.20326 0.3333

NORMALIZED DIAGONAL:

1	1.00000E+00	2	2.99390E-01	3	3.83324E-02	4	9.88521E-01	5	4.77356E-01	6	7.46718E-01
7	4.71398E-01	8	9.99777E-01	9	7.67727E-01	10	7.45390E-01	11	8.60250E-01	12	9.15974E-01
13	9.09383E-01	14	9.88267E-01	15	9.94510E-01	16	9.99214E-01	17	5.51359E-01	18	9.99978E-01
19	9.16992E-01	20	9.82007E-01								

MARQUARDT PARAMETER = 0, TRUST EXPANSION = 1.00

			NEW PARAMETER (EST. ERROR)	-- CHANGE THIS ITERATION
1	10000	A	67859.76412(114)	-0.00000
2	20000	B	9448.9011(46)	-0.0000
3	30000	C	8299.0882(45)	0.0000
4	200	-DN	-0.0373937(159)	0.0000000
5	1100	-DNK	-0.181509(111)	-0.000000
6	2000	-DK	-2.394778(270)	0.000000
7	40100	-dN	-4.5481(87)E-03	-0.0000E-03
8	41000	-dK	-0.18323(228)	0.00000
9	10010000	eaa	-1224.7306(40)	0.0000
10	10020000	ebb	-101.53380(183)	-0.00000
11	10030000	ecc	-3.78785(174)	-0.00000
12	10610000	(eab+eba)	41.154(74)	-0.000
13	120000000	a_F	0.46216(161)	-0.00000
14	120010000	Taa	1.2970(32)	0.0000
15	120020000	Tbb	-1.08913(277)	-0.00000
16	1000100	DNS	0.788(64)E-03	0.000E-03
17	10010100	DNKS	0.04933(74)	-0.00000
18	10011000	DKS	0.10804(216)	0.00000
19	220010000	chi_aa	0.0126(44)	-0.0000

```
 20     220020000     chi_bb           0.1556( 48)           0.0000
 MICROWAVE AVG =        0.003759 MHz, IR AVG =        0.00000
 MICROWAVE RMS =        0.051022 MHz, IR RMS =        0.00000
 END OF ITERATION  3 OLD, NEW RMS ERROR=        1.56394         1.56394
  1  2 -0.022094  1  3  0.037605  1  4  0.080635  1  5 -0.258150  1  6 -0.165095  1  7  0.126779  1  8  0.022394  1  9  0.036632
  1 10 -0.047851  1 11  0.040043  1 12 -0.238034  1 13  0.184718  1 14  0.065397  1 15  0.026565  1 16 -0.051480  1 17  0.098079
  1 18 -0.071896  1 19  0.083727  1 20  0.016780  2  1 -0.022094  2  3 -0.991206  2  4 -0.706759  2  5  0.640423  2  6 -0.260912
  2  7  0.165373  2  8 -0.994867  2  9 -0.028986  2 10  0.009439  2 11  0.006369  2 12  0.005298  2 13  0.005449  2 14  0.009114
  2 15  0.006959  2 16 -0.007103  2 17  0.005976  2 18  0.035349  2 19  0.004535  2 20  0.003147  3  1  0.037605  3  2 -0.991206
  3  4  0.617713  3  5 -0.601933  3  6  0.243412  3  7 -0.182125  3  8  0.996430  3  9  0.017017  3 10  0.006694  3 11 -0.007666
  3 12  0.030134  3 13 -0.001511  3 14 -0.003126  3 15 -0.010405  3 16  0.009569  3 17 -0.012768  3 18 -0.029014  3 19 -0.005712
  3 20 -0.006062  4  1  0.080635  4  2 -0.706759  4  3  0.617713  4  5 -0.699840  4  6  0.267628  4  7  0.080065  4  8  0.648077
  4  9  0.073117  4 10 -0.101809  4 11  0.013252  4 12 -0.288834  4 13  0.005008  4 14 -0.017027  4 15  0.006726  4 16 -0.020318
  4 17  0.062487  4 18 -0.075577  4 19  0.002338  4 20  0.006586  5  1 -0.258150  5  2  0.640423  5  3 -0.601933  5  4 -0.699840
  5  6 -0.684195  5  7  0.066353  5  8 -0.613585  5  9 -0.063631  5 10  0.056432  5 11 -0.025722  5 12  0.226206  5 13 -0.040772
  5 14 -0.001983  5 15  0.000125  5 16  0.035354  5 17 -0.063918  5 18  0.110288  5 19 -0.008458  5 20 -0.002848  6  1 -0.165095
  6  2 -0.260912  6  3  0.243412  6  4  0.267628  6  5 -0.684195  6  7 -0.122357  6  8  0.251281  6  9  0.042743  6 10 -0.013688
  6 11  0.008047  6 12 -0.074117  6 13 -0.019267  6 14 -0.014875  6 15 -0.010382  6 16 -0.008995  6 17  0.039816  6 18 -0.116475
  6 19 -0.021424  6 20 -0.003513  7  1  0.126779  7  2  0.165373  7  3 -0.182125  7  4  0.080065  7  5  0.066353  7  6 -0.122357
  7  8 -0.229856  7  9  0.015979  7 10 -0.017737  7 11  0.028747  7 12 -0.154769  7 13  0.041184  7 14  0.005769  7 15 -0.014888
  7 16 -0.067329  7 17  0.024400  7 18  0.005759  7 19 -0.037628  7 20 -0.013978  8  1  0.022394  8  2 -0.994867  8  3  0.996430
  8  4  0.648077  8  5 -0.613585  8  6  0.251281  8  7 -0.229856  8  9  0.020861  8 10  0.000949  8 11 -0.009451  8 12  0.025419
  8 13 -0.006527  8 14 -0.004773  8 15 -0.004947  8 16  0.012537  8 17 -0.012239  8 18 -0.030563  8 19  0.000210  8 20 -0.002027
  9  1  0.036632  9  2 -0.028986  9  3  0.017017  9  4  0.073117  9  5 -0.063631  9  6  0.042743  9  7  0.015979  9  8  0.020861
  9 10  0.189202  9 11  0.141457  9 12 -0.036272  9 13  0.033112  9 14  0.073957  9 15 -0.166131  9 16  0.044017  9 17 -0.171037
  9 18 -0.247177  9 19 -0.105355  9 20  0.059662 10  1 -0.047851 10  2  0.009439 10  3  0.006694 10  4 -0.101809 10  5  0.056432
 10  6 -0.013688 10  7 -0.017737 10  8  0.000949 10  9  0.189202 10 11  0.317847 10 12  0.088821 10 13 -0.037326 10 14 -0.106779
 10 15  0.005396 10 16 -0.548286 10 17  0.080695 10 18 -0.014812 10 19 -0.069225 10 20 -0.038383 11  1  0.040043 11  2  0.006369
 11  3 -0.007666 11  4  0.013252 11  5 -0.025722 11  6  0.008047 11  7  0.028747 11  8 -0.009451 11  9  0.141457 11 10  0.317847
 11 12 -0.238013 11 13 -0.033595 11 14 -0.032229 11 15 -0.043378 11 16 -0.540724 11 17  0.094240 11 18 -0.016456 11 19  0.033763
 11 20  0.043320 12  1 -0.238034 12  2  0.005298 12  3  0.030134 12  4 -0.288834 12  5  0.226206 12  6 -0.074117 12  7 -0.154769
 12  8  0.025419 12  9 -0.036272 12 10  0.088821 12 11 -0.238013 12 13 -0.039772 12 14 -0.090737 12 15 -0.005041 12 16  0.283097
 12 17 -0.310019 12 18  0.207572 12 19 -0.016791 12 20 -0.003971 13  1  0.184718 13  2  0.005449 13  3 -0.001511 13  4  0.005008
 13  5 -0.040772 13  6 -0.019267 13  7  0.041184 13  8 -0.006527 13  9  0.033112 13 10 -0.037326 13 11 -0.033595 13 12 -0.039772
 13 14  0.367331 13 15 -0.015102 13 16  0.020856 13 17  0.030701 13 18 -0.033354 13 19  0.107199 13 20 -0.160517 14  1  0.065397
 14  2  0.009114 14  3 -0.003126 14  4 -0.017027 14  5 -0.001983 14  6 -0.014875 14  7  0.005769 14  8 -0.004773 14  9  0.073957
 14 10 -0.106779 14 11 -0.032229 14 12 -0.090737 14 13  0.367331 14 15 -0.087597 14 16  0.019182 14 17 -0.041564 14 18  0.019074
 14 19  0.167286 14 20 -0.038479 15  1  0.026565 15  2  0.006959 15  3 -0.010405 15  4  0.006726 15  5  0.000125 15  6 -0.010382
 15  7 -0.014888 15  8 -0.004947 15  9 -0.166131 15 10  0.005396 15 11 -0.043378 15 12 -0.005041 15 13 -0.015102 15 14 -0.087597
 15 16 -0.000193 15 17  0.017873 15 18  0.010763 15 19  0.158957 15 20  0.069307 16  1 -0.051480 16  2 -0.007103 16  3  0.009569
 16  4 -0.020318 16  5  0.035354 16  6 -0.008995 16  7 -0.067329 16  8  0.012537 16  9  0.044017 16 10 -0.548286 16 11 -0.540724
 16 12  0.283097 16 13  0.020856 16 14  0.019182 16 15 -0.000193 16 17 -0.215375 16 18  0.031389 16 19  0.008538 16 20  0.031772
 17  1  0.098079 17  2  0.005976 17  3 -0.012768 17  4  0.062487 17  5 -0.063918 17  6  0.039816 17  7  0.024400 17  8 -0.012239
 17  9 -0.171037 17 10  0.080695 17 11  0.094240 17 12 -0.310019 17 13  0.030701 17 14 -0.041564 17 15  0.017873 17 16 -0.215375
 17 18 -0.714164 17 19 -0.004727 17 20  0.002443 18  1 -0.071896 18  2  0.035349 18  3 -0.029014 18  4 -0.075577 18  5  0.110288
 18  6 -0.116475 18  7  0.005759 18  8 -0.030563 18  9 -0.247177 18 10 -0.014812 18 11 -0.016456 18 12  0.207572 18 13 -0.033354
 18 14  0.019074 18 15  0.010763 18 16  0.031389 18 17 -0.714164 18 19  0.018934 18 20 -0.014071 19  1  0.083727 19  2  0.004535
 19  3 -0.005712 19  4  0.002338 19  5 -0.008458 19  6 -0.021424 19  7 -0.037628 19  8  0.000210 19  9 -0.105355 19 10 -0.069225
 19 11  0.033763 19 12 -0.016791 19 13  0.107199 19 14  0.167286 19 15  0.158957 19 16  0.008538 19 17 -0.004727 19 18  0.018934
 19 20 -0.297141 20  1  0.016780 20  2  0.003147 20  3 -0.006062 20  4  0.006586 20  5 -0.002848 20  6 -0.003513 20  7 -0.013978
 20  8 -0.002027 20  9  0.059662 20 10 -0.038383 20 11  0.043320 20 12 -0.003971 20 13 -0.160517 20 14 -0.038479 20 15  0.069307
 20 16  0.031772 20 17  0.002443 20 18 -0.014071 20 19 -0.297141
D000 predictions                                 Fri Sep 25 15:24:05 2015
```

Appendix C Full Analysis Result for the CSO Surveys in a Machine-readable Format

Source	Molecule	Log10(NT)	1sigma	NT(cm^-2)	1sigma	T_rot(K)	1sigma	FWHM(km/s)	1sigma	dv(km/s)	1sigma
B1-b	CCH	13.27	0.09	1.871e+13	3.744e+12	38.62	18.29	1.19	0.16	6.63	0.06
B1-b	CN	15.04	0.08	1.086e+15	1.958e+14	2.71	0.04	1.03	0.07	6.33	0.04
B1-b	CS	12.97	2.84	9.298e+12	6.077e+13	10.81	29.92	1.37	0.18	6.48	0.04
B1-b	H2CO	13.43	0.15	2.718e+13	9.473e+12	6.66	0.57	1.64	0.31	6.37	0.10
B1-b	HCN	17.66	0.83	4.519e+17	8.645e+17	3.48	0.04	0.93	0.10	7.37	0.03
B1-b	N2D+	12.28	0.06	1.923e+12	2.460e+11	38.51	11.02	1.45	0.05	6.34	0.03
B1-b	NO	14.64	0.57	4.348e+14	5.726e+14	14.62	37.61	1.12	0.11	6.33	0.05
B1-b	SO	13.67	0.07	4.627e+13	6.955e+12	9.89	0.53	1.16	0.04	6.66	0.02
DR21(OH)	C-13-S	13.36	1.46	2.294e+13	7.689e+13	17.45	59.57	4.49	0.75	0.34	0.23
DR21(OH)	CCH	15.55	0.06	3.522e+15	4.711e+14	8.24	0.27	4.29	0.21	0.52	0.06
DR21(OH)	CH3CCH	15.09	0.01	1.236e+15	3.685e+13	36.81	0.95	4.98	0.16	0.12	0.07
DR21(OH)	CH3CHO	13.88	0.08	7.513e+13	1.360e+13	138.86	24.20	5.53	0.41	0.19	0.14
DR21(OH)	CH3CN	13.36	0.01	2.307e+13	5.062e+11	56.67	2.06	5.35	0.20	0.63	0.09
DR21(OH)	CH3OCH3	14.54	0.03	3.498e+14	2.412e+13	60.05	4.90	4.08	0.40	0.31	0.15
DR21(OH)	CH3OH	15.18	0.01	1.515e+15	3.177e+13	92.79	2.42	5.89	0.20	0.78	0.04
DR21(OH)	CH3OH	15.25	0.00	1.764e+15	1.768e+13	18.19	0.35	5.63	0.09	0.34	0.02
DR21(OH)	CN	14.08	0.62	1.201e+14	1.727e+14	6.36	3.59	2.24	2.62	-2.69	0.59
DR21(OH)	CN	14.33	0.49	2.124e+14	2.401e+14	5.71	1.60	1.96	3.06	2.90	0.78
DR21(OH)	CS	14.10	0.05	1.251e+14	1.467e+13	34.46	12.22	2.75	0.08	-1.44	0.04
DR21(OH)	CS	14.11	0.15	1.274e+14	4.391e+13	29.51	27.96	4.15	0.41	2.00	0.09
DR21(OH)	CS	14.37	0.07	2.355e+14	3.817e+13	10.00	0.59	12.12	0.49	-2.00	0.44
DR21(OH)	CS-33	13.05	1.66	1.117e+13	4.258e+13	15.31	44.31	5.01	1.93	0.63	0.61
DR21(OH)	CS-34	13.68	0.69	4.777e+13	7.558e+13	19.33	34.23	5.24	0.37	0.61	0.13
DR21(OH)	DNC	12.00	1.26	1.002e+12	2.911e+12	58.08	257.98	2.68	2.00	-1.68	0.98
DR21(OH)	DNC	12.00	9.81	1.000e+12	2.258e+13	68.56	2303.59	2.69	2.49	1.85	1.07
DR21(OH)	H2C-13-O	13.11	2.98	1.288e+13	8.849e+13	100.00	584.91	3.02	2.03	0.34	0.78
DR21(OH)	H2CCO	13.48	0.05	3.038e+13	3.157e+12	57.97	9.65	4.80	0.79	0.43	0.23
DR21(OH)	H2CO	13.40	1.09	2.540e+13	6.378e+13	84.89	191.79	1.00	0.36	2.00	0.24
DR21(OH)	H2CO	13.57	0.10	3.731e+13	8.694e+12	13.85	0.34	1.72	0.52	-2.00	0.15
DR21(OH)	H2CO	14.51	0.06	3.202e+14	4.511e+13	9.55	0.79	7.19	0.32	0.32	0.21
DR21(OH)	H2CS	14.17	0.01	1.477e+14	2.545e+12	53.69	1.55	5.59	0.09	0.56	0.04
DR21(OH)	H2CS-34	13.03	1.24	1.070e+13	3.049e+13	100.00	356.12	5.94	9.21	0.41	2.91
DR21(OH)	HC-13-N	13.14	0.11	1.380e+13	3.375e+12	41.95	27.21	6.00	0.29	0.23	0.13
DR21(OH)	HC-13-O+	13.00	0.04	1.005e+13	9.711e+11	16.32	1.86	4.67	0.19	0.23	0.08
DR21(OH)	HCCCN	13.02	0.07	1.039e+13	1.713e+12	79.05	11.73	6.01	0.28	0.37	0.13
DR21(OH)	HCN-15	12.75	0.60	5.598e+12	7.754e+12	88.93	169.26	5.95	1.33	0.62	0.49
DR21(OH)	HCO-18+	12.00	83.98	1.000e+12	1.934e+14	50.62	19580.05	5.37	2.59	0.93	1.25
DR21(OH)	HCOOCH3	14.03	0.03	1.072e+14	7.445e+12	80.81	25.78	4.11	0.41	0.16	0.16
DR21(OH)	HCS+	13.02	19.38	1.048e+13	4.677e+14	17.48	529.79	5.35	2.61	0.82	0.84
DR21(OH)	HDCO	13.09	0.22	1.217e+13	6.249e+12	79.16	41.64	4.83	0.64	0.55	0.23
DR21(OH)	HDCS	13.92	3.75	8.270e+13	7.132e+14	9.37	19.08	5.08	11.65	0.65	2.61
DR21(OH)	HNC-13	12.46	0.76	2.852e+12	4.991e+12	14.02	31.90	5.32	2.76	0.21	0.85
DR21(OH)	HNCO	13.87	0.20	7.349e+13	3.378e+13	29.39	10.42	8.00	11.53	2.31	2.54
DR21(OH)	NO	15.01	0.16	1.021e+15	3.649e+14	22.94	32.04	4.33	1.82	0.26	0.75
DR21(OH)	NS	13.23	1.02	1.689e+13	3.947e+13	66.17	298.01	4.81	1.75	1.50	0.60
DR21(OH)	OCS	14.55	0.16	3.544e+14	1.331e+14	42.26	8.46	5.39	0.35	0.56	0.13
DR21(OH)	S-33-O	13.81	5.86	6.389e+13	8.622e+14	9.68	35.80	5.84	10.93	1.89	2.81
DR21(OH)	S-34-O	13.46	0.12	2.913e+13	7.777e+12	39.32	75.83	6.34	1.67	1.35	0.63
DR21(OH)	SO	14.63	0.00	4.312e+14	1.658e+12	36.17	0.51	6.52	0.02	0.92	0.01
DR21(OH)	SO2	14.46	0.01	2.885e+14	7.046e+12	75.57	2.62	7.73	0.15	1.55	0.06
DR21(OH)	SiO	13.01	0.08	1.012e+13	1.750e+12	66.37	25.97	7.79	0.67	0.99	0.36
G24.33+00.11_MM1	C-13-H3OH	13.78	0.08	5.976e+13	1.120e+13	81.64	8.36	3.54	1.00	1.20	0.17
G24.33+00.11_MM1	C-13-S	12.23	0.10	1.694e+12	4.035e+11	44.81	18.10	4.03	0.85	0.68	0.46
G24.33+00.11_MM1	C2H5CN	13.06	0.05	1.153e+13	1.356e+12	88.42	13.08	4.58	0.40	1.11	0.18
G24.33+00.11_MM1	C2H5OH	13.74	0.08	5.436e+13	1.047e+13	76.02	10.43	3.37	0.95	0.97	0.24
G24.33+00.11_MM1	CH2NH	12.99	0.05	9.672e+12	1.221e+12	43.40	7.07	3.43	0.39	0.99	0.19
G24.33+00.11_MM1	CH3CCH	14.04	0.11	1.096e+14	2.654e+13	41.11	8.82	3.42	0.48	0.95	0.23
G24.33+00.11_MM1	CH3CN	13.13	0.07	1.358e+13	2.111e+12	301.71	42.38	4.96	0.41	1.18	0.18
G24.33+00.11_MM1	CH3CNv8	12.89	0.26	7.757e+12	4.601e+12	149.62	78.33	3.42	1.16	1.22	0.50
G24.33+00.11_MM1	CH3OCH3	14.58	0.05	3.783e+14	4.763e+13	200.29	24.68	3.92	0.42	1.28	0.20
G24.33+00.11_MM1	CH3OH	14.72	0.02	5.211e+14	2.320e+13	233.10	8.32	4.40	0.12	1.22	0.07
G24.33+00.11_MM1	CH3OH	14.83	0.01	6.711e+14	1.186e+13	13.83	0.19	4.82	0.05	0.96	0.02
G24.33+00.11_MM1	CN	15.71	0.11	5.139e+15	1.253e+15	2.75	0.04	2.33	0.12	0.25	0.06
G24.33+00.11_MM1	CS	13.27	0.02	1.853e+13	8.482e+11	41.51	8.20	4.09	0.11	0.62	0.04
G24.33+00.11_MM1	CS	13.50	0.22	3.160e+13	1.629e+13	17.34	8.34	16.70	0.69	1.34	0.24
G24.33+00.11_MM1	CS-34	12.55	0.12	3.534e+12	9.835e+11	27.65	27.01	4.33	0.55	0.64	0.23
G24.33+00.11_MM1	H2CCO	13.20	0.21	1.598e+13	7.788e+12	32.02	13.76	3.55	0.57	0.66	0.27
G24.33+00.11_MM1	H2CO	13.21	0.14	1.626e+13	5.217e+12	36.38	15.87	14.29	1.35	2.20	0.65
G24.33+00.11_MM1	H2CO	13.77	0.06	5.925e+13	8.497e+12	99.98	11.48	4.73	0.25	0.83	0.07
G24.33+00.11_MM1	H2CS	13.36	0.04	2.286e+13	1.877e+12	74.35	7.96	3.81	0.20	0.68	0.10
G24.33+00.11_MM1	HCCCN	12.66	0.24	4.599e+12	2.515e+12	73.09	33.51	8.76	0.68	0.61	0.42
G24.33+00.11_MM1	HCN-15	11.99	0.27	9.682e+11	6.019e+11	100.00	71.06	5.67	1.12	3.32	0.64
G24.33+00.11_MM1	HCOOCH3	13.97	0.04	9.301e+13	9.212e+12	124.27	15.11	3.54	0.32	1.11	0.12
G24.33+00.11_MM1	HNCO	13.90	0.13	7.861e+13	2.332e+13	23.23	3.96	10.00	2.59	3.00	0.27
G24.33+00.11_MM1	NO	15.14	0.17	1.392e+15	5.607e+14	95.80	39.77	3.33	0.46	1.13	0.21
G24.33+00.11_MM1	NS	12.78	0.44	6.060e+12	6.095e+12	15.42	6.73	2.79	3.22	1.63	0.32
G24.33+00.11_MM1	OCS	14.31	0.39	2.035e+14	1.845e+14	33.94	12.08	6.23	0.56	0.62	0.28

G24.33+00.11_MM1	SO	13.83	0.50	6.786e+13	7.817e+13	12.77	5.03	5.42	0.45	1.75	0.24
GAL_034.3+00.2	C-13-H3CN	12.90	0.11	7.979e+12	1.970e+12	149.91	45.21	5.25	0.85	-0.03	0.38
GAL_034.3+00.2	C-13-H3OH	14.91	0.02	8.086e+14	4.233e+13	154.88	6.81	5.55	0.26	1.36	0.10
GAL_034.3+00.2	C-13-S	13.75	0.10	5.599e+13	1.248e+13	100.00	31.58	5.31	0.35	0.37	0.18
GAL_034.3+00.2	C-13-S-34	12.88	5.79	7.499e+12	1.000e+14	88.56	1869.76	7.33	5.90	1.13	2.52
GAL_034.3+00.2	C2H5CN	13.81	0.02	6.416e+13	2.512e+12	107.06	7.35	5.27	0.21	-0.12	0.09
GAL_034.3+00.2	C2H5OH	14.68	0.02	4.734e+14	2.363e+13	61.10	2.45	5.74	0.35	0.85	0.14
GAL_034.3+00.2	CCH	15.03	0.23	1.062e+15	5.531e+14	13.15	5.64	5.96	0.41	0.76	0.11
GAL_034.3+00.2	CH2NH	13.71	0.06	5.125e+13	7.407e+12	64.33	10.83	6.22	0.59	0.11	0.27
GAL_034.3+00.2	CH3CCH	15.31	0.01	2.041e+15	4.625e+13	44.35	1.20	6.25	0.22	0.38	0.07
GAL_034.3+00.2	CH3CHO	13.72	0.06	5.248e+13	6.822e+12	90.89	11.90	5.73	0.95	0.36	0.28
GAL_034.3+00.2	CH3CN	14.04	0.01	1.107e+14	2.479e+12	160.07	3.79	7.11	0.13	0.82	0.05
GAL_034.3+00.2	CH3CNv8	13.53	0.17	3.420e+13	1.351e+13	128.34	50.89	4.87	0.94	-0.37	0.25
GAL_034.3+00.2	CH3COCH3	14.05	0.16	1.116e+14	4.025e+13	99.47	26.43	5.84	0.71	1.30	0.22
GAL_034.3+00.2	CH3OCH3	15.55	0.01	3.576e+15	9.262e+13	144.78	3.61	6.54	0.21	1.00	0.07
GAL_034.3+00.2	CH3OH	15.36	0.00	2.292e+15	2.432e+13	16.46	0.17	5.79	0.05	0.44	0.02
GAL_034.3+00.2	CH3OH	15.84	0.00	6.965e+15	6.178e+13	190.17	1.55	7.39	0.05	1.50	0.02
GAL_034.3+00.2	CS	14.02	0.11	1.037e+14	2.676e+13	37.48	0.59	6.17	0.75	0.83	0.32
GAL_034.3+00.2	CS	14.14	0.04	1.382e+14	1.262e+13	38.29	1.09	3.98	0.10	-1.24	0.09
GAL_034.3+00.2	CS	14.25	0.12	1.778e+14	4.794e+13	76.10	16.78	11.33	0.42	1.30	0.19
GAL_034.3+00.2	CS-33	13.00	0.85	1.000e+13	1.960e+13	50.50	79.46	3.97	2.77	0.50	0.77
GAL_034.3+00.2	CS-33	13.10	0.56	1.251e+13	1.605e+13	33.96	15.81	9.08	8.61	0.82	1.52
GAL_034.3+00.2	CS-34	13.70	0.11	5.037e+13	1.226e+13	35.60	0.96	7.14	1.20	0.62	0.26
GAL_034.3+00.2	CS-34	13.75	0.47	5.586e+13	5.994e+13	12.14	3.39	3.22	0.52	0.49	0.20
GAL_034.3+00.2	DNC	12.20	0.42	1.591e+12	1.532e+12	32.01	97.26	5.72	3.17	1.27	1.38
GAL_034.3+00.2	H2CCO	14.03	0.02	1.071e+14	5.648e+12	80.03	6.28	6.68	0.44	0.82	0.15
GAL_034.3+00.2	H2CO	14.00	0.08	1.000e+14	1.798e+13	26.01	12.55	9.55	0.82	1.11	0.60
GAL_034.3+00.2	H2CO	14.00	0.31	1.000e+14	7.122e+13	60.53	61.07	3.43	0.84	-1.91	0.73
GAL_034.3+00.2	H2CO	14.06	0.50	1.160e+14	1.334e+14	99.98	108.89	3.01	0.88	0.05	0.59
GAL_034.3+00.2	H2CS	14.45	0.01	2.798e+14	6.521e+12	74.91	2.27	6.41	0.10	0.99	0.05
GAL_034.3+00.2	HC-13-N	12.88	0.16	7.588e+12	2.711e+12	23.61	6.87	13.66	4.06	1.54	1.30
GAL_034.3+00.2	HC-13-N	13.14	0.10	1.366e+13	3.121e+12	30.19	20.37	5.08	0.54	-0.12	0.17
GAL_034.3+00.2	HC-13-O+	12.69	0.34	4.936e+12	3.836e+12	25.53	2.27	7.30	2.21	1.58	1.17
GAL_034.3+00.2	HC-13-O+	13.00	0.61	1.000e+13	1.408e+13	88.88	101.88	4.43	0.82	0.06	0.42
GAL_034.3+00.2	HCCCN	13.56	0.04	3.644e+13	3.403e+12	80.96	7.27	7.58	0.17	0.97	0.08
GAL_034.3+00.2	HCCCNv7	13.08	0.15	1.204e+13	4.296e+12	95.54	46.61	5.57	0.53	-0.20	0.27
GAL_034.3+00.2	HCN	13.59	0.17	3.852e+13	1.492e+13	11.76	0.88	8.00	0.99	-3.33	0.39
GAL_034.3+00.2	HCN	13.64	0.20	4.404e+13	2.064e+13	12.49	4.63	3.46	0.79	-2.64	0.06
GAL_034.3+00.2	HCN-15	13.01	0.24	1.026e+13	5.663e+12	71.91	59.21	6.10	0.64	0.61	0.30
GAL_034.3+00.2	HCO-18+	12.26	0.51	1.827e+12	2.159e+12	38.80	137.66	5.58	2.08	1.81	0.85
GAL_034.3+00.2	HCOOCH3	15.10	0.01	1.272e+15	4.037e+13	160.34	5.70	6.47	0.13	1.14	0.05
GAL_034.3+00.2	HCS+	13.00	1.14	1.004e+13	2.631e+13	99.41	444.46	5.59	1.86	1.12	0.92
GAL_034.3+00.2	HDO	14.54	0.11	3.446e+14	8.620e+13	100.00	80.23	5.60	2.02	0.11	0.64
GAL_034.3+00.2	HNC-13	12.75	2.26	5.624e+12	2.924e+13	87.22	640.03	4.97	1.23	0.50	0.53
GAL_034.3+00.2	HNCO	13.98	0.05	9.475e+13	1.069e+13	34.78	3.84	6.00	0.55	0.31	0.25
GAL_034.3+00.2	NH2CHO	13.23	0.07	1.697e+13	2.685e+12	122.29	22.07	6.04	0.73	-0.10	0.27
GAL_034.3+00.2	NO	15.52	0.48	3.274e+15	3.647e+15	68.67	87.73	6.12	3.17	1.07	0.93
GAL_034.3+00.2	NS	13.97	0.95	9.410e+13	2.061e+14	15.12	19.17	6.07	0.71	1.06	0.30
GAL_034.3+00.2	OCS	14.93	0.06	8.437e+14	1.230e+14	60.32	8.48	7.27	0.20	0.89	0.09
GAL_034.3+00.2	S-33-O	13.09	0.92	1.242e+13	2.645e+13	100.00	338.97	4.63	7.55	1.22	2.89
GAL_034.3+00.2	S-34-O	13.69	1.20	4.954e+13	1.373e+14	100.00	480.06	5.77	1.20	0.90	0.56
GAL_034.3+00.2	SO	14.62	0.01	4.212e+14	5.758e+12	25.87	0.54	6.88	0.05	0.59	0.02
GAL_034.3+00.2	SO2	14.73	0.01	5.390e+14	1.839e+13	126.90	4.50	6.41	0.14	0.54	0.06
GAL_034.3+00.2	SiO	13.06	0.09	1.146e+13	2.341e+12	72.61	24.19	10.02	1.17	2.21	0.68
GAL_034.3+00.2	t-HCOOH	13.66	0.21	4.524e+13	2.177e+13	132.90	79.94	4.65	1.09	0.66	0.49
GAL_10.47+00.03	C-13-H3CN	13.76	0.05	5.809e+13	6.944e+12	298.91	32.94	11.00	0.45	-0.18	0.24
GAL_10.47+00.03	C-13-H3OH	15.25	0.01	1.790e+15	5.903e+13	178.79	4.81	11.54	0.25	-1.35	0.15
GAL_10.47+00.03	C2H3CN	14.66	0.02	4.534e+14	1.639e+13	507.57	15.49	10.69	0.19	-0.03	0.11
GAL_10.47+00.03	C2H5CN	14.33	0.01	2.137e+14	2.770e+12	177.34	3.97	9.48	0.12	0.05	0.06
GAL_10.47+00.03	CH2NH	15.13	0.09	1.345e+15	2.848e+14	656.07	103.76	8.99	0.52	-0.13	0.26
GAL_10.47+00.03	CH3CCH	15.02	0.01	1.047e+15	2.816e+13	59.37	2.60	7.44	0.32	-0.51	0.13
GAL_10.47+00.03	CH3CN	14.73	0.03	5.385e+14	3.944e+13	671.73	38.83	11.61	0.17	-0.42	0.09
GAL_10.47+00.03	CH3CNv8	15.28	0.08	1.884e+15	3.340e+14	753.51	72.90	9.08	0.26	-0.69	0.14
GAL_10.47+00.03	CH3OH	15.23	0.00	1.687e+15	1.652e+13	20.60	0.19	7.43	0.06	-0.68	0.03
GAL_10.47+00.03	CH3OH	16.05	0.00	1.114e+16	1.119e+14	258.05	1.97	11.03	0.07	-0.91	0.04
GAL_10.47+00.03	CH3OCH3	15.70	0.01	4.987e+15	8.921e+13	130.78	2.23	11.30	0.19	-1.05	0.09
GAL_10.47+00.03	H2CCO	14.38	0.02	2.383e+14	1.169e+13	142.06	8.90	11.03	0.31	-0.74	0.19
GAL_10.47+00.03	H2CS	14.59	0.01	3.854e+14	1.280e+13	119.09	4.32	9.59	0.17	-0.94	0.09
GAL_10.47+00.03	HCCCN	13.69	0.06	4.927e+13	6.490e+12	65.34	5.74	10.87	0.27	-0.01	0.13
GAL_10.47+00.03	HCOOCH3	15.45	0.01	2.838e+15	7.965e+13	232.99	6.23	10.87	0.12	-1.14	0.07
GAL_10.47+00.03	NH2CHO	14.05	0.04	1.129e+14	1.047e+13	246.99	22.35	11.74	0.41	-0.08	0.22
GAL_10.47+00.03	OCS	15.52	0.10	3.324e+15	7.347e+14	30.67	2.35	10.07	0.28	-0.66	0.12
GAL_10.47+00.03	SO	14.26	0.01	1.799e+14	4.647e+12	39.94	7.04	9.26	0.19	-0.45	0.09
GAL_10.47+00.03	SO2	14.90	0.01	7.918e+14	2.676e+13	162.04	5.33	10.30	0.23	-0.22	0.11
GAL_10.47+00.03	t-HCOOH	14.04	0.14	1.106e+14	3.625e+13	148.50	58.38	8.59	1.79	1.78	0.55
GAL_10.47+00.03	C2H5OH	15.23	0.01	1.708e+15	4.514e+13	168.27	4.79	10.00	0.25	-1.15	0.10
GAL_10.47+00.03	CH3CHO	14.83	0.03	6.714e+14	5.336e+13	331.43	20.37	10.00	0.34	-0.27	0.16
GAL_10.47+00.03	CH3COCH3	14.32	0.02	2.095e+14	7.431e+12	62.08	2.96	10.00	0.41	-0.76	0.15
GAL_10.47+00.03	C-13-S-34	13.12	0.37	1.318e+13	1.130e+13	25.90	79.00	12.41	2.19	1.84	1.00
GAL_10.47+00.03	C-13-S	13.51	0.11	3.235e+13	7.843e+12	62.21	31.02	9.33	0.58	-0.89	0.28
GAL_10.47+00.03	CCH	14.54	0.85	3.479e+14	6.805e+14	13.46	26.72	6.89	0.62	-0.59	0.17
GAL_10.47+00.03	CN	14.89	0.03	7.686e+14	5.592e+13	4.97	0.08	7.22	0.23	-1.11	0.14
GAL_10.47+00.03	CS-33	13.22	0.07	1.662e+13	2.583e+12	49.92	18.39	9.30	0.92	-0.53	0.46
GAL_10.47+00.03	CS-34	13.50	0.17	3.162e+13	1.255e+13	86.83	66.79	11.13	2.10	0.90	2.64
GAL_10.47+00.03	CS-34	13.24	0.34	1.751e+13	1.368e+13	35.99	0.80	6.28	1.71	-2.11	0.55
GAL_10.47+00.03	CS	15.01	0.13	1.012e+15	3.103e+14	8.00	0.97	8.51	0.77	-0.21	0.28
GAL_10.47+00.03	CS	13.55	0.08	3.514e+13	6.326e+12	27.47	4.02	4.37	0.37	-3.39	0.12
GAL_10.47+00.03	CS	13.48	0.29	3.016e+13	1.988e+13	29.44	5.08	20.00	6.42	2.39	2.43
GAL_10.47+00.03	H2CO	13.66	0.12	4.567e+13	1.276e+13	49.95	19.14	5.15	1.07	-3.09	0.27
GAL_10.47+00.03	H2CO	13.81	0.12	6.501e+13	1.808e+13	28.85	2.36	9.57	0.95	0.89	1.26
GAL_10.47+00.03	HC-13-CCN	12.99	0.08	9.878e+12	1.713e+12	131.63	69.40	10.00	0.94	0.96	0.44
GAL_10.47+00.03	HC-13-N	13.03	0.38	1.083e+13	9.562e+12	100.00	138.75	13.72	2.58	2.41	2.65

GAL_10.47+00.03	HC-13-N	12.69	0.63	4.857e+12	7.064e+12	37.92	155.58	5.91	1.36	-3.08	0.31
GAL_10.47+00.03	HC-13-O+	12.61	0.06	4.029e+12	6.026e+11	39.63	14.95	7.23	0.42	-0.82	0.21
GAL_10.47+00.03	HCC-13-CN	13.49	0.45	3.123e+13	3.267e+13	1140.82	1388.25	10.99	0.89	-0.18	0.49
GAL_10.47+00.03	HCCC-13-N	13.52	0.43	3.332e+13	3.310e+13	1109.18	1293.12	12.00	1.09	0.61	0.45
GAL_10.47+00.03	HCN-15	12.57	0.32	3.715e+12	2.766e+12	15.99	19.50	8.94	1.69	-1.08	0.60
GAL_10.47+00.03	HDO	14.63	0.07	4.238e+14	6.778e+13	100.00	59.36	8.96	1.40	-0.92	0.61
GAL_10.47+00.03	HNC-13	12.61	0.16	4.092e+12	1.527e+12	36.70	40.24	7.37	0.93	-1.87	0.44
GAL_10.47+00.03	NO	15.93	0.13	8.565e+15	2.582e+15	100.00	33.33	7.90	0.81	-0.29	0.37
GAL_10.47+00.03	NS	14.01	1.23	1.027e+14	2.913e+14	13.59	18.92	8.25	0.62	0.13	0.26
GAL_10.47+00.03	OCS-34	14.44	0.60	2.744e+14	3.771e+14	100.00	519.54	8.85	0.87	-0.45	0.35
GAL_10.47+00.03	S-34-O	13.79	0.09	6.195e+13	1.300e+13	100.00	30.90	8.38	1.00	-0.24	0.41
GAL_10.47+00.03	SiO	12.99	0.11	9.849e+12	2.559e+12	29.23	15.96	18.94	3.28	3.88	1.10
GAL_12.21-0.10	C-13-S	13.00	1.46	1.000e+13	3.356e+13	75.68	459.42	7.73	1.04	0.27	0.44
GAL_12.21-0.10	CCH	14.55	0.16	3.511e+14	1.278e+14	11.67	3.29	6.56	0.31	0.98	0.11
GAL_12.21-0.10	CH3CCH	14.55	0.02	3.528e+14	1.756e+13	44.30	2.78	7.25	0.68	0.57	0.17
GAL_12.21-0.10	CH3CN	13.01	0.02	1.017e+13	4.384e+11	78.41	4.17	8.29	0.62	0.19	0.20
GAL_12.21-0.10	CH3OCH3	14.95	0.02	8.822e+14	3.968e+13	148.18	6.12	11.95	0.69	-0.07	0.24
GAL_12.21-0.10	CH3OH	14.93	0.01	8.434e+14	1.991e+13	161.98	3.57	8.76	0.25	0.18	0.09
GAL_12.21-0.10	CH3OH	14.98	0.00	9.621e+14	9.771e+12	15.76	0.17	7.59	0.08	0.41	0.03
GAL_12.21-0.10	CN	14.11	0.41	1.294e+14	1.215e+14	3.45	1.38	20.00	14.27	-2.00	1.95
GAL_12.21-0.10	CN	14.33	0.05	2.119e+14	2.414e+13	5.08	0.35	4.10	0.44	-1.52	0.07
GAL_12.21-0.10	CS	13.65	0.24	4.421e+13	2.469e+13	33.49	2.71	6.60	0.89	0.24	0.15
GAL_12.21-0.10	CS	13.67	0.25	4.698e+13	2.664e+13	42.53	13.08	9.86	0.75	0.25	0.24
GAL_12.21-0.10	CS-33	12.99	2.29	9.730e+12	5.120e+13	11.77	30.95	8.06	1.74	0.56	0.87
GAL_12.21-0.10	CS-34	13.24	0.36	1.746e+13	1.440e+13	25.80	56.73	7.40	0.43	0.89	0.18
GAL_12.21-0.10	H2CCO	13.41	0.04	2.567e+13	2.601e+12	76.80	10.39	9.50	1.30	-0.67	0.40
GAL_12.21-0.10	H2CO	13.83	0.36	6.753e+13	5.529e+13	31.59	58.09	7.45	0.22	-0.57	0.07
GAL_12.21-0.10	H2CS	13.88	0.01	7.588e+13	2.398e+12	64.77	2.90	8.02	0.20	0.72	0.08
GAL_12.21-0.10	HC-13-N	12.88	0.21	7.520e+12	3.632e+12	90.60	59.65	9.04	0.53	0.21	0.26
GAL_12.21-0.10	HC-13-O+	12.50	0.14	3.127e+12	1.034e+12	58.98	34.42	7.63	0.53	0.53	0.21
GAL_12.21-0.10	HCCCN	12.86	0.12	7.233e+12	2.050e+12	73.95	17.09	10.87	0.70	0.73	0.31
GAL_12.21-0.10	HCN	12.99	0.03	9.756e+12	6.959e+11	24.98	0.79	17.00	1.04	0.43	0.33
GAL_12.21-0.10	HCN	13.09	0.02	1.240e+13	7.089e+11	27.75	1.57	6.02	0.19	-1.54	0.06
GAL_12.21-0.10	HCN-15	11.93	0.35	8.467e+11	6.729e+11	30.63	107.62	10.08	3.53	0.51	1.71
GAL_12.21-0.10	HCO-18+	11.50	33.14	3.162e+11	2.413e+13	47.05	7853.66	4.75	10.51	0.29	4.65
GAL_12.21-0.10	HCS+	12.50	38.22	3.166e+12	2.787e+14	18.64	1253.43	5.91	4.10	1.77	1.32
GAL_12.21-0.10	HNC-13	12.09	0.29	1.236e+12	8.167e+11	16.08	15.50	7.52	3.33	-0.14	0.88
GAL_12.21-0.10	NO	15.28	0.27	1.925e+15	1.213e+15	89.25	58.92	7.85	3.05	0.37	0.90
GAL_12.21-0.10	NS	13.26	0.18	1.832e+13	7.764e+12	100.00	56.69	7.86	1.16	0.92	0.49
GAL_12.21-0.10	OCS	14.17	0.10	1.495e+14	3.498e+13	71.91	23.30	8.60	0.47	0.36	0.21
GAL_12.21-0.10	S-34-O	13.01	1.77	1.023e+13	4.168e+13	85.00	646.93	8.33	5.43	1.59	1.37
GAL_12.21-0.10	SO	13.93	0.03	8.437e+13	6.392e+12	26.09	2.71	8.00	0.15	0.95	0.07
GAL_12.21-0.10	SO2	13.90	0.04	7.859e+13	8.083e+12	127.76	14.22	10.64	0.79	-0.59	0.38
GAL_12.21-0.10	SiO	12.32	0.10	2.076e+12	4.758e+11	55.63	32.10	8.97	1.68	1.08	0.81
GAL_12.91-00.26	C-13-H3OH	13.79	0.07	6.168e+13	9.703e+12	99.02	12.68	3.04	0.42	1.70	0.16
GAL_12.91-00.26	C-13-S	12.62	0.11	4.194e+12	1.089e+12	47.23	26.56	4.05	0.69	0.38	0.36
GAL_12.91-00.26	CCH	14.58	0.34	3.807e+14	2.977e+14	11.35	6.34	4.43	0.23	0.28	0.08
GAL_12.91-00.26	CH2NH	13.16	0.05	1.441e+13	1.557e+12	38.87	5.76	5.48	0.58	1.28	0.26
GAL_12.91-00.26	CH3CCH	14.85	0.03	7.012e+14	4.513e+13	28.93	1.07	3.65	0.10	-0.10	0.05
GAL_12.91-00.26	CH3CN	13.18	0.02	1.500e+13	5.431e+11	116.96	5.26	5.23	0.16	0.91	0.09
GAL_12.91-00.26	CH3OCH3	14.70	0.02	4.967e+14	2.604e+13	111.88	5.77	4.74	0.29	1.09	0.12
GAL_12.91-00.26	CH3OH	14.95	0.01	8.972e+14	2.188e+13	178.20	4.79	5.10	0.07	1.25	0.04
GAL_12.91-00.26	CH3OH	14.98	0.01	9.549e+14	1.325e+13	13.89	0.19	5.12	0.03	-0.06	0.02
GAL_12.91-00.26	CN	13.25	5.98	1.798e+13	2.476e+14	10.94	217.52	4.90	10.53	5.88	5.25
GAL_12.91-00.26	CN	15.62	0.86	4.160e+15	8.198e+15	3.37	0.70	2.87	1.67	-0.09	0.56
GAL_12.91-00.26	CS	13.59	0.02	3.893e+13	2.066e+12	39.75	1.77	4.05	0.11	0.57	0.03
GAL_12.91-00.26	CS	13.90	0.02	7.933e+13	3.740e+12	99.94	3.28	11.01	0.30	-0.39	0.12
GAL_12.91-00.26	CS-33	12.12	23.10	1.334e+12	7.092e+13	50.94	8811.19	4.14	4.01	0.42	1.13
GAL_12.91-00.26	CS-34	12.20	1.25	1.575e+12	4.527e+12	35.14	3.93	3.91	7.47	4.24	5.26
GAL_12.91-00.26	CS-34	12.22	1.84	1.655e+12	7.029e+12	35.06	1.95	6.09	25.88	-4.75	11.26
GAL_12.91-00.26	CS-34	12.97	0.59	9.348e+12	1.260e+13	19.10	0.98	3.62	2.69	0.27	0.59
GAL_12.91-00.26	DNC	12.00	0.61	1.005e+12	1.403e+12	57.79	126.30	4.94	1.51	-0.25	0.75
GAL_12.91-00.26	H2CCO	13.17	0.05	1.481e+13	1.720e+12	68.15	20.92	3.68	0.54	0.83	0.24
GAL_12.91-00.26	H2CO	13.60	0.07	3.971e+13	6.542e+12	38.97	10.96	11.89	1.31	0.28	0.35
GAL_12.91-00.26	H2CO	14.02	0.50	1.053e+14	1.219e+14	100.00	102.04	4.11	0.25	0.20	0.07
GAL_12.91-00.26	H2CS	13.59	0.02	3.899e+13	1.794e+12	58.47	4.36	4.46	0.14	0.45	0.07
GAL_12.91-00.26	HC-13-N	12.14	0.27	1.395e+12	8.748e+11	26.05	3.04	3.36	1.01	0.58	0.27
GAL_12.91-00.26	HC-13-N	12.81	0.11	6.392e+12	1.691e+12	99.98	1.34	8.05	1.09	1.20	0.55
GAL_12.91-00.26	HC-13-O+	12.53	0.06	3.385e+12	4.700e+11	49.08	13.92	3.87	0.14	0.39	0.07
GAL_12.91-00.26	HCCCN	12.72	0.04	5.244e+12	5.036e+11	122.97	31.20	5.28	0.22	0.99	0.11
GAL_12.91-00.26	HCCCNv7	12.69	1.60	4.953e+12	1.828e+13	100.00	547.59	8.78	3.20	0.11	1.31
GAL_12.91-00.26	HCN	12.74	0.10	5.523e+12	1.301e+12	10.20	0.06	5.98	0.39	-5.71	0.32
GAL_12.91-00.26	HCN	13.26	0.05	1.819e+13	1.943e+12	99.94	0.24	5.49	0.24	3.39	0.06
GAL_12.91-00.26	HCN	13.27	0.04	1.860e+13	1.607e+12	26.02	0.11	19.93	1.31	1.26	0.34
GAL_12.91-00.26	HCN-15	12.01	0.19	1.025e+12	4.586e+11	38.79	38.32	5.32	1.24	0.87	0.61
GAL_12.91-00.26	HCO-18+	11.75	1.65	5.623e+11	2.140e+12	90.95	486.18	3.61	1.76	1.42	0.76
GAL_12.91-00.26	HCOOCH3	13.89	0.04	7.841e+13	8.027e+12	108.80	21.52	3.54	0.28	1.38	0.12
GAL_12.91-00.26	HCS+	12.19	0.32	1.564e+12	1.141e+12	56.09	132.76	6.00	3.35	1.12	1.87
GAL_12.91-00.26	HDCO	12.90	0.67	7.868e+12	1.213e+13	100.00	144.09	3.85	0.93	1.00	0.50
GAL_12.91-00.26	HDO	13.87	0.24	7.363e+13	4.048e+13	100.00	503.29	3.89	1.76	1.19	0.62
GAL_12.91-00.26	HNC-13	12.24	0.12	1.727e+12	4.949e+11	34.39	34.68	3.91	0.58	0.34	0.24
GAL_12.91-00.26	HNCO	13.52	0.04	3.276e+13	2.997e+12	35.95	3.86	5.00	0.46	0.72	0.16
GAL_12.91-00.26	NO	14.91	0.07	8.131e+14	1.274e+14	21.22	4.86	4.55	0.92	0.04	0.45
GAL_12.91-00.26	NS	13.02	0.35	1.040e+13	8.405e+12	20.45	17.06	4.66	1.20	0.60	0.42
GAL_12.91-00.26	OCS	14.24	0.16	1.735e+14	6.418e+13	50.27	12.92	5.74	0.38	0.68	0.17
GAL_12.91-00.26	S-34-O	13.13	0.78	1.338e+13	2.411e+13	16.55	17.22	3.41	1.37	0.97	0.48
GAL_12.91-00.26	SO	14.03	0.01	1.075e+14	2.964e+12	20.13	0.56	6.72	0.07	0.04	0.04
GAL_12.91-00.26	SO2	13.94	0.02	8.690e+13	4.380e+12	81.82	4.82	5.85	0.23	0.95	0.11
GAL_12.91-00.26	SiO	12.45	0.28	2.824e+12	1.824e+12	55.89	149.23	13.87	2.70	-0.38	1.40
GAL_19.61-0.23	C-13-H3OH	13.72	0.23	5.220e+13	2.780e+13	51.08	19.08	4.62	3.62	1.11	0.63
GAL_19.61-0.23	C-13-S	13.20	0.21	1.583e+13	7.798e+12	27.25	53.84	7.83	0.79	1.33	0.33
GAL_19.61-0.23	C2H3CN	13.52	0.02	3.344e+13	1.570e+12	129.34	8.79	8.77	0.50	0.77	0.22

GAL_19.61-0.23	C2H5CN	13.77	0.01	5.867e+13	1.454e+12	151.05	8.84	8.32	0.24	0.44	0.12
GAL_19.61-0.23	CCH	14.81	0.41	6.432e+14	6.027e+14	12.58	10.09	8.18	0.43	2.49	0.11
GAL_19.61-0.23	CH3CCH	14.88	0.01	7.582e+14	2.259e+13	47.08	1.71	5.79	0.18	1.91	0.09
GAL_19.61-0.23	CH3CN	14.09	0.04	1.223e+14	1.129e+13	467.33	35.68	9.32	0.24	0.79	0.11
GAL_19.61-0.23	CH3OCH3	14.61	0.06	4.062e+14	5.670e+13	137.87	24.38	4.80	0.59	0.69	0.26
GAL_19.61-0.23	CH3OH	14.61	0.02	4.053e+14	1.467e+13	14.29	0.42	6.98	0.21	2.21	0.10
GAL_19.61-0.23	CH3OH	15.25	0.01	1.787e+15	3.473e+13	176.85	2.99	7.40	0.12	0.90	0.05
GAL_19.61-0.23	CN	14.00	0.10	9.944e+13	2.220e+13	74.58	17.02	20.00	1.59	-2.80	0.95
GAL_19.61-0.23	CN	15.38	0.05	2.414e+15	2.768e+14	3.54	0.07	4.30	0.19	1.77	0.12
GAL_19.61-0.23	CS	14.00	0.07	1.001e+14	1.582e+13	52.47	24.89	7.33	0.19	2.24	0.04
GAL_19.61-0.23	CS	14.00	0.12	9.983e+13	2.657e+13	74.26	37.49	17.59	0.74	2.28	0.18
GAL_19.61-0.23	CS-33	12.86	0.20	7.176e+12	3.243e+12	46.20	76.40	7.45	1.22	1.36	0.62
GAL_19.61-0.23	CS-34	13.43	0.11	2.703e+13	6.684e+12	28.41	26.90	7.72	0.41	1.94	0.18
GAL_19.61-0.23	H2CCO	13.60	0.07	4.026e+13	6.756e+12	108.56	28.27	7.04	0.90	1.11	0.30
GAL_19.61-0.23	H2CO	13.79	0.63	6.191e+13	8.970e+13	99.98	111.61	5.41	0.67	1.43	0.23
GAL_19.61-0.23	H2CO	14.23	0.73	1.694e+14	2.860e+14	99.98	145.28	13.99	0.97	2.03	0.38
GAL_19.61-0.23	H2CS	13.95	0.02	8.833e+13	3.994e+12	70.19	4.26	7.12	0.22	1.55	0.10
GAL_19.61-0.23	HC-13-N	12.18	0.32	1.517e+12	1.101e+12	100.00	45.78	3.76	1.84	1.79	0.57
GAL_19.61-0.23	HC-13-N	12.94	0.05	8.628e+12	9.013e+11	23.28	14.87	13.40	1.30	1.32	0.38
GAL_19.61-0.23	HC-13-O+	12.70	0.04	4.969e+12	5.057e+11	44.72	9.48	7.98	0.33	2.08	0.17
GAL_19.61-0.23	HCCCN	13.31	0.03	2.040e+13	1.241e+12	114.26	14.59	11.52	0.24	0.78	0.13
GAL_19.61-0.23	HCN	12.81	0.05	6.418e+12	7.583e+11	29.54	3.21	7.58	0.51	-1.00	0.23
GAL_19.61-0.23	HCN	13.25	0.10	1.778e+13	3.908e+12	30.47	42.91	23.04	1.00	2.79	0.45
GAL_19.61-0.23	HCN-15	12.48	0.08	3.027e+12	5.269e+11	37.58	11.17	9.65	1.19	0.80	0.65
GAL_19.61-0.23	HCO-18+	11.74	0.77	5.546e+11	9.885e+11	67.63	86.59	4.65	10.10	3.89	1.55
GAL_19.61-0.23	HCOOCH3	14.28	0.05	1.902e+14	2.163e+13	138.46	19.88	4.25	0.26	0.76	0.11
GAL_19.61-0.23	HDO	14.02	0.15	1.051e+14	3.750e+13	100.00	315.82	5.34	2.47	0.63	0.91
GAL_19.61-0.23	HNC-13	12.48	0.09	3.003e+12	6.145e+11	37.41	11.73	11.85	2.04	0.90	1.09
GAL_19.61-0.23	HNCO	14.13	0.02	1.353e+14	7.024e+12	176.17	8.67	11.45	0.49	0.03	0.20
GAL_19.61-0.23	NO	15.28	0.38	1.905e+15	1.670e+15	69.27	67.69	7.05	3.68	1.49	0.93
GAL_19.61-0.23	NS	13.47	0.08	2.924e+13	5.333e+12	100.00	24.56	7.60	0.94	1.60	0.43
GAL_19.61-0.23	OCS	14.68	0.12	4.750e+14	1.293e+14	48.85	8.95	9.33	0.42	0.31	0.18
GAL_19.61-0.23	S-34-O	13.58	0.41	3.824e+13	3.612e+13	20.96	18.57	9.15	1.87	0.32	0.67
GAL_19.61-0.23	SO	14.35	0.00	2.251e+14	2.281e+12	44.44	2.01	14.05	0.12	1.33	0.07
GAL_19.61-0.23	SO2	14.83	0.01	6.722e+14	1.753e+13	150.12	3.66	11.90	0.23	0.07	0.09
GAL_19.61-0.23	SiO	13.03	0.31	1.066e+13	7.510e+12	54.51	196.14	20.00	1.59	1.96	0.75
GAL_24.78+0.08	C-13-H3OH	14.16	0.03	1.448e+14	1.139e+13	84.24	4.29	5.64	0.53	0.11	0.18
GAL_24.78+0.08	C-13-S	12.92	0.14	8.279e+12	2.624e+12	34.76	1.02	12.94	2.75	-0.87	1.37
GAL_24.78+0.08	C-13-S	13.06	0.09	1.139e+13	2.248e+12	34.55	1.15	4.22	0.51	-0.09	0.17
GAL_24.78+0.08	CCH	14.49	0.26	3.102e+14	1.822e+14	11.59	5.17	5.24	0.31	0.11	0.12
GAL_24.78+0.08	CH2NH	13.47	0.04	2.973e+13	2.692e+12	53.91	6.14	5.26	0.41	0.33	0.16
GAL_24.78+0.08	CH3CCH	14.88	0.02	7.600e+14	2.996e+13	38.24	1.34	4.74	0.13	-0.39	0.07
GAL_24.78+0.08	CH3CN	13.75	0.02	5.586e+13	2.043e+12	203.52	7.50	7.92	0.16	-0.15	0.07
GAL_24.78+0.08	CH3OCH3	15.12	0.01	1.329e+15	3.869e+13	124.81	3.55	6.47	0.20	0.12	0.09
GAL_24.78+0.08	CH3OH	15.16	0.00	1.433e+15	1.159e+13	16.99	0.17	7.81	0.04	0.01	0.03
GAL_24.78+0.08	CH3OH	15.19	0.01	1.554e+15	1.898e+13	140.87	1.87	5.85	0.05	0.28	0.03
GAL_24.78+0.08	CN	14.71	0.04	5.072e+14	4.918e+13	4.44	0.08	4.70	0.22	1.67	0.11
GAL_24.78+0.08	CS	13.92	0.05	8.234e+13	1.007e+13	23.00	3.12	20.00	0.97	-0.16	0.21
GAL_24.78+0.08	CS	14.04	0.06	1.094e+14	1.540e+13	17.75	2.48	7.47	0.26	0.07	0.05
GAL_24.78+0.08	CS-33	12.96	0.07	9.122e+12	1.558e+12	47.19	25.20	6.06	0.67	-0.00	0.31
GAL_24.78+0.08	CS-34	13.14	0.09	1.370e+13	2.912e+12	35.46	0.44	13.41	2.24	-0.40	0.79
GAL_24.78+0.08	CS-34	13.97	0.32	9.432e+13	6.887e+13	9.70	2.34	4.82	0.28	0.17	0.11
GAL_24.78+0.08	DNC	11.97	0.96	9.306e+11	2.056e+12	99.33	261.27	4.06	1.80	0.13	0.99
GAL_24.78+0.08	H2CO	13.80	0.14	6.378e+13	2.025e+13	49.94	19.19	17.09	1.44	0.02	0.62
GAL_24.78+0.08	H2CO	14.43	0.21	2.672e+14	1.283e+14	200.00	73.96	6.40	0.46	0.71	0.14
GAL_24.78+0.08	H2CS	14.06	0.01	1.149e+14	3.125e+12	69.90	2.63	6.03	0.10	0.04	0.05
GAL_24.78+0.08	HC-13-N	12.50	0.44	3.155e+12	3.231e+12	24.70	6.36	6.44	2.64	0.91	0.36
GAL_24.78+0.08	HC-13-N	12.92	0.22	8.410e+12	4.195e+12	49.94	6.81	13.62	2.65	0.49	0.65
GAL_24.78+0.08	HC-13-O+	12.50	0.69	3.173e+12	5.034e+12	35.74	213.94	5.07	0.32	0.32	0.11
GAL_24.78+0.08	HCCCN	13.30	0.06	2.014e+13	2.630e+12	70.28	6.88	8.61	0.20	0.06	0.11
GAL_24.78+0.08	HCCCNv7	12.97	0.11	9.235e+12	2.272e+12	106.70	47.88	7.90	0.66	0.05	0.29
GAL_24.78+0.08	HCN	13.00	0.07	1.000e+13	1.667e+12	48.73	12.77	13.90	0.93	-9.22	0.45
GAL_24.78+0.08	HCN	13.08	0.08	1.201e+13	2.218e+12	49.65	17.15	5.26	0.21	4.24	0.08
GAL_24.78+0.08	HCN	13.98	0.09	9.509e+13	1.976e+13	5.04	0.30	13.49	0.93	10.57	0.50
GAL_24.78+0.08	HCN-15	12.42	0.10	2.646e+12	6.145e+11	33.07	26.59	7.63	0.92	0.30	0.42
GAL_24.78+0.08	HCO-18+	11.76	0.65	5.798e+11	8.645e+11	100.00	166.47	2.63	1.03	0.84	0.59
GAL_24.78+0.08	HCOOCH3	14.49	0.02	3.074e+14	1.614e+13	132.89	9.84	5.90	0.20	0.15	0.09
GAL_24.78+0.08	HCS+	12.40	0.25	2.528e+12	1.446e+12	32.09	50.29	3.42	1.51	0.27	0.54
GAL_24.78+0.08	HNC-13	12.43	0.07	2.716e+12	4.401e+11	44.53	10.25	4.98	0.46	-0.30	0.27
GAL_24.78+0.08	HNCO	13.95	0.04	8.994e+13	9.210e+12	27.08	2.17	7.00	0.29	-0.97	0.15
GAL_24.78+0.08	NO	15.13	0.05	1.357e+15	1.656e+14	23.13	8.56	5.20	0.73	-0.39	0.36
GAL_24.78+0.08	NS	13.54	0.17	3.450e+13	1.336e+13	78.53	48.93	6.17	0.43	0.41	0.20
GAL_24.78+0.08	OCS	14.84	0.11	6.910e+14	1.756e+14	37.93	4.41	7.24	0.23	-0.11	0.11
GAL_24.78+0.08	SO	14.19	0.01	1.561e+14	2.415e+12	27.74	0.84	8.79	0.07	-0.59	0.04
GAL_24.78+0.08	SO2	14.18	0.03	1.531e+14	1.041e+13	102.10	8.48	8.70	0.31	-0.35	0.16
GAL_24.78+0.08	SiO	13.05	0.13	1.131e+13	3.497e+12	22.63	7.10	20.00	1.33	-0.88	0.72
GAL_31.41+0.31	C-13-H3CN	12.74	0.07	5.554e+12	8.834e+11	105.22	28.00	5.35	0.77	0.74	0.30
GAL_31.41+0.31	C-13-H3OH	14.07	0.15	1.184e+14	4.004e+13	37.76	11.62	7.48	0.97	0.78	0.42
GAL_31.41+0.31	C-13-H3OH	14.83	0.03	6.712e+14	4.597e+13	208.41	28.87	6.43	0.55	0.98	0.17
GAL_31.41+0.31	C-13-S	13.39	0.12	2.436e+13	6.764e+12	53.52	39.88	6.33	0.33	0.09	0.15
GAL_31.41+0.31	C2H3CN	13.34	0.05	2.206e+13	2.782e+12	167.81	22.22	9.26	1.74	1.42	0.39
GAL_31.41+0.31	C2H5CN	13.88	0.01	7.621e+13	1.386e+12	134.37	5.50	7.51	0.16	0.58	0.07
GAL_31.41+0.31	C2H5OH	14.76	0.02	5.697e+14	2.208e+13	127.12	6.28	6.71	0.27	0.54	0.11
GAL_31.41+0.31	CCH	14.54	1.44	3.469e+14	1.154e+15	13.53	45.48	5.31	0.80	1.44	0.10
GAL_31.41+0.31	CH2NH	13.67	0.06	4.686e+13	6.936e+12	77.32	13.15	6.65	0.61	0.64	0.24
GAL_31.41+0.31	CH3CCH	14.87	0.01	7.413e+14	1.824e+13	53.44	1.99	5.11	0.14	1.04	0.07
GAL_31.41+0.31	CH3CHO	13.80	0.04	6.356e+13	6.333e+12	102.62	10.86	6.95	0.53	0.25	0.19
GAL_31.41+0.31	CH3CN	14.08	0.02	1.206e+14	5.141e+12	320.97	12.30	8.92	0.14	0.07	0.07
GAL_31.41+0.31	CH3CNv8	13.67	0.08	4.651e+13	8.837e+12	179.84	23.84	7.12	0.93	0.08	0.27
GAL_31.41+0.31	CH3COCH3	14.28	0.33	1.885e+14	1.433e+14	137.10	39.64	6.02	0.40	0.33	0.16
GAL_31.41+0.31	CH3OCH3	15.41	0.01	2.553e+15	3.744e+13	95.32	1.30	7.26	0.11	0.70	0.06
GAL_31.41+0.31	CH3OH	15.08	0.01	1.214e+15	1.512e+13	38.41	0.45	7.74	0.06	0.73	0.03

GAL_31.41+0.31	CH3OH	15.57	0.01	3.708e+15	6.589e+13	268.05	4.63	7.00	0.07	0.62	0.04
GAL_31.41+0.31	CH3SH	13.71	0.19	5.173e+13	2.276e+13	20.60	7.06	5.00	0.99	0.86	0.43
GAL_31.41+0.31	CN	16.06	0.20	1.153e+16	5.432e+15	2.82	0.06	5.00	0.52	0.49	0.19
GAL_31.41+0.31	CS	13.92	0.06	8.288e+13	1.240e+13	23.48	5.14	5.38	0.09	-0.02	0.03
GAL_31.41+0.31	CS	14.00	0.10	1.009e+14	2.251e+13	16.67	2.89	14.76	0.36	1.29	0.17
GAL_31.41+0.31	CS-33	13.28	0.05	1.926e+13	2.063e+12	55.42	12.90	7.19	0.42	-0.05	0.21
GAL_31.41+0.31	CS-34	13.87	2.34	7.357e+13	3.960e+14	13.98	46.15	6.42	0.99	0.20	0.09
GAL_31.41+0.31	H2C-13-O	13.03	1.30	1.081e+13	3.226e+13	16.70	120.12	7.24	1.49	-0.87	0.59
GAL_31.41+0.31	H2CCO	14.04	0.02	1.092e+14	5.012e+12	126.42	7.60	7.12	0.26	0.36	0.12
GAL_31.41+0.31	H2CO	12.77	0.50	5.895e+12	6.853e+12	49.98	58.59	2.87	3.99	5.00	0.46
GAL_31.41+0.31	H2CO	13.39	0.19	2.458e+13	1.082e+13	26.05	31.59	5.46	1.13	-1.13	0.35
GAL_31.41+0.31	H2CO	13.61	0.12	4.086e+13	1.147e+13	49.98	34.28	15.70	8.87	1.11	0.98
GAL_31.41+0.31	H2CS	14.33	0.01	2.119e+14	4.859e+12	85.85	2.40	6.64	0.09	0.72	0.04
GAL_31.41+0.31	HC-13-N	13.01	0.07	1.030e+13	1.713e+12	70.93	17.18	8.47	0.37	-0.38	0.19
GAL_31.41+0.31	HC-13-O+	12.26	0.15	1.827e+12	6.120e+11	31.37	62.03	5.21	0.48	1.20	0.20
GAL_31.41+0.31	HCCCN	13.31	0.07	2.032e+13	3.353e+12	70.44	8.75	9.53	0.29	0.48	0.15
GAL_31.41+0.31	HCN	12.65	0.07	4.421e+12	6.851e+11	23.71	3.99	4.18	0.38	7.14	0.10
GAL_31.41+0.31	HCN	12.82	3.16	6.641e+12	4.825e+13	49.98	755.34	8.84	0.36	-7.71	0.25
GAL_31.41+0.31	HCN	12.89	2.65	7.756e+12	4.731e+13	49.98	640.19	15.66	1.60	15.00	1.05
GAL_31.41+0.31	HCN	12.93	0.04	8.505e+12	8.211e+11	23.52	8.80	3.89	0.14	-3.13	0.05
GAL_31.41+0.31	HCN-15	12.41	0.11	2.588e+12	6.792e+11	38.84	23.36	6.97	0.84	-0.06	0.43
GAL_31.41+0.31	HCOOCH3	15.14	0.01	1.392e+15	4.271e+13	223.97	6.59	6.06	0.07	0.55	0.04
GAL_31.41+0.31	HCS+	12.53	0.94	3.351e+12	7.287e+12	25.70	71.53	4.44	2.91	1.25	0.69
GAL_31.41+0.31	HDO	13.98	1.24	9.524e+13	2.711e+14	50.00	139.38	5.97	6.80	0.98	1.66
GAL_31.41+0.31	HNC-13	11.82	0.58	6.565e+11	8.695e+11	33.98	170.47	4.03	1.83	0.14	0.79
GAL_31.41+0.31	NH2CHO	12.85	0.06	7.096e+12	9.711e+11	53.36	9.64	6.63	1.43	0.32	0.42
GAL_31.41+0.31	NO	15.41	0.29	2.583e+15	1.701e+15	100.00	73.83	5.99	1.50	1.41	0.64
GAL_31.41+0.31	NS	13.36	0.39	2.303e+13	2.045e+13	23.65	31.63	6.45	0.75	0.79	0.30
GAL_31.41+0.31	OCS	15.07	0.10	1.170e+15	2.694e+14	35.86	3.52	7.39	0.19	0.32	0.09
GAL_31.41+0.31	S-34-O	14.74	1.26	5.544e+14	1.609e+15	6.67	3.31	8.49	3.60	0.09	1.34
GAL_31.41+0.31	SO	14.19	0.01	1.538e+14	3.428e+12	23.79	0.74	8.08	0.10	0.13	0.05
GAL_31.41+0.31	SO2	14.00	0.04	9.955e+13	9.880e+12	83.26	11.65	8.32	0.54	-0.07	0.23
GAL_31.41+0.31	SiO	12.99	2.66	9.752e+12	5.978e+13	21.25	122.26	19.51	2.14	1.76	1.04
GAL_45.47+0.05	C-13-S	12.50	46.37	3.162e+12	3.376e+14	12.56	798.33	4.94	4.35	0.15	1.11
GAL_45.47+0.05	CCH	14.30	0.05	2.014e+14	2.408e+13	14.24	1.95	4.60	0.28	0.84	0.08
GAL_45.47+0.05	CH3CCH	14.56	0.03	3.610e+14	2.435e+13	34.95	1.85	4.08	0.16	1.08	0.09
GAL_45.47+0.05	CH3OH	14.82	0.01	6.581e+14	1.120e+13	13.31	0.16	4.76	0.04	0.87	0.02
GAL_45.47+0.05	CN	13.08	0.06	1.201e+13	1.681e+12	19.25	0.49	5.32	0.42	1.37	0.27
GAL_45.47+0.05	CN	15.04	0.04	1.105e+15	9.371e+13	3.46	0.07	3.42	0.10	0.22	0.07
GAL_45.47+0.05	CS	14.12	0.08	1.315e+14	2.391e+13	13.51	1.27	5.18	0.06	0.76	0.02
GAL_45.47+0.05	CS-33	12.49	6.82	3.102e+12	4.868e+13	9.52	54.48	3.36	1.86	1.08	0.90
GAL_45.47+0.05	CS-34	12.55	0.07	3.564e+12	5.392e+11	48.25	12.90	5.21	0.64	1.51	0.33
GAL_45.47+0.05	DNC	12.08	2.35	1.198e+12	6.481e+12	6.95	15.91	6.25	3.57	1.31	1.46
GAL_45.47+0.05	H2CO	14.01	0.35	1.030e+14	8.333e+13	9.07	3.10	5.33	0.19	0.59	0.04
GAL_45.47+0.05	H2CS	13.22	0.02	1.664e+13	9.503e+11	39.63	6.65	3.96	0.24	1.25	0.11
GAL_45.47+0.05	HC-13-N	12.47	1.44	2.931e+12	9.725e+12	9.67	19.06	5.69	0.54	1.03	0.23
GAL_45.47+0.05	HC-13-O+	12.72	11.77	5.191e+12	1.406e+14	8.10	93.19	4.35	3.49	1.12	0.15
GAL_45.47+0.05	HCCCN	12.26	0.46	1.840e+12	1.940e+12	68.22	52.54	4.57	0.71	2.35	0.37
GAL_45.47+0.05	HCN	12.70	0.04	4.994e+12	4.445e+11	22.01	4.58	16.83	0.91	-4.13	0.53
GAL_45.47+0.05	HCN	12.71	0.05	5.165e+12	5.625e+11	26.95	0.61	5.10	0.43	-0.52	0.21
GAL_45.47+0.05	HCN	13.09	0.36	1.231e+13	1.016e+13	9.03	3.23	3.35	0.16	3.63	0.10
GAL_45.47+0.05	HCS+	12.75	76.90	5.625e+12	9.960e+14	10.43	594.17	3.88	10.47	2.54	3.87
GAL_45.47+0.05	HNC-13	12.00	0.28	1.000e+12	6.349e+11	70.78	56.97	4.00	1.24	0.64	0.34
GAL_45.47+0.05	HNCO	13.21	0.35	1.611e+13	1.286e+13	23.00	11.75	6.13	0.73	-0.06	0.42
GAL_45.47+0.05	NO	15.02	0.25	1.047e+15	6.126e+14	58.05	41.73	4.18	0.51	0.78	0.26
GAL_45.47+0.05	NS	13.34	0.87	2.212e+13	4.453e+13	9.92	6.40	7.55	1.97	1.98	1.10
GAL_45.47+0.05	OCS	14.17	1.15	1.496e+14	3.950e+14	25.15	17.92	3.96	1.33	1.88	0.55
GAL_45.47+0.05	SO	13.92	0.02	8.413e+13	4.066e+12	15.67	0.51	5.40	0.09	0.76	0.05
GAL_45.47+0.05	SO2	13.35	0.04	2.252e+13	2.209e+12	43.92	5.61	5.51	0.58	2.34	0.27
GAL_45.47+0.05	SiO	12.84	0.22	6.937e+12	3.458e+12	10.18	1.50	6.00	1.17	0.53	0.48
GAL_75.78+0.34	C-13-S	12.96	0.16	9.219e+12	3.299e+12	100.00	51.82	4.07	0.36	-3.94	0.18
GAL_75.78+0.34	CCH	14.95	0.12	8.977e+14	2.535e+14	8.17	0.92	4.55	0.13	-3.53	0.05
GAL_75.78+0.34	CH3CCH	14.60	0.02	3.997e+14	2.016e+13	34.55	1.25	3.12	0.09	-3.55	0.05
GAL_75.78+0.34	CH3CN	12.77	0.03	5.871e+12	3.545e+11	91.78	7.27	4.39	0.37	-3.72	0.14
GAL_75.78+0.34	CH3OH	14.67	0.01	4.718e+14	1.474e+13	159.96	9.06	3.43	0.07	-4.27	0.04
GAL_75.78+0.34	CH3OH	14.70	0.01	4.983e+14	1.066e+13	14.86	0.49	4.26	0.04	-4.00	0.03
GAL_75.78+0.34	CN	14.65	0.03	4.448e+14	2.938e+13	4.75	0.07	5.88	0.11	-3.13	0.07
GAL_75.78+0.34	CS	13.48	0.04	3.023e+13	2.931e+12	36.16	0.33	3.04	0.15	-3.46	0.03
GAL_75.78+0.34	CS	14.00	0.03	1.000e+14	5.888e+12	98.86	2.94	7.10	0.12	-2.92	0.07
GAL_75.78+0.34	CS-33	12.41	0.86	2.549e+12	5.038e+12	40.23	661.01	3.59	0.75	-3.40	0.33
GAL_75.78+0.34	CS-34	13.11	0.04	1.303e+13	1.230e+12	49.81	14.22	3.82	0.16	-3.66	0.08
GAL_75.78+0.34	DNC	11.54	0.69	3.449e+11	5.444e+11	13.93	29.31	2.67	2.03	-3.73	0.70
GAL_75.78+0.34	H2CCO	13.02	0.08	1.054e+13	2.005e+12	82.71	20.49	4.79	1.21	-3.33	0.36
GAL_75.78+0.34	H2CO	13.62	0.10	4.203e+13	9.293e+12	17.74	8.69	8.68	0.54	-4.50	0.15
GAL_75.78+0.34	H2CO	13.83	0.56	6.807e+13	8.793e+13	97.70	109.26	3.37	0.22	-3.69	0.07
GAL_75.78+0.34	H2CS	13.54	0.01	3.503e+13	1.099e+12	49.42	3.09	3.56	0.09	-3.71	0.05
GAL_75.78+0.34	HC-13-N	12.43	0.04	2.689e+12	2.762e+11	44.43	7.82	4.29	0.24	-3.03	0.13
GAL_75.78+0.34	HC-13-O+	12.52	0.06	3.333e+12	4.327e+11	57.10	12.84	3.87	0.11	-3.32	0.06
GAL_75.78+0.34	HCCCN	12.68	0.08	4.792e+12	8.892e+11	88.70	18.21	4.89	0.26	-3.21	0.11
GAL_75.78+0.34	HCCCNv7	12.64	0.40	4.414e+12	4.070e+12	79.10	66.66	4.43	0.98	-2.90	0.44
GAL_75.78+0.34	HCN	12.94	0.04	8.785e+12	7.528e+11	19.76	4.82	13.66	0.48	-4.61	0.28
GAL_75.78+0.34	HCN	13.00	0.06	1.000e+13	1.334e+12	96.02	15.32	3.80	0.12	-1.05	0.05
GAL_75.78+0.34	HCN-15	11.85	0.11	7.036e+11	1.852e+11	39.81	12.82	4.04	0.62	-3.37	0.43
GAL_75.78+0.34	HCO-18+	11.54	0.29	3.489e+11	2.352e+11	18.88	33.26	3.24	1.33	-2.08	0.50
GAL_75.78+0.34	HCS+	12.08	0.17	1.200e+12	4.823e+11	43.34	909.17	2.71	1.28	-3.10	0.51
GAL_75.78+0.34	HDCO	12.50	0.20	3.163e+12	1.473e+12	63.46	36.55	3.11	0.64	-3.64	0.25
GAL_75.78+0.34	HDO	14.01	0.46	1.034e+14	1.090e+14	31.22	18.85	5.69	5.26	-3.48	1.22
GAL_75.78+0.34	HNC-13	11.85	0.15	7.157e+11	2.472e+11	31.89	43.47	3.08	0.68	-3.59	0.30
GAL_75.78+0.34	HNCO	13.52	0.06	3.296e+13	4.450e+12	40.38	6.89	8.00	3.17	-1.00	0.91
GAL_75.78+0.34	NO	15.26	0.21	1.815e+15	8.603e+14	100.00	49.26	4.33	0.99	-3.72	0.37
GAL_75.78+0.34	NS	13.00	11.28	1.000e+13	2.597e+14	12.69	147.91	3.38	2.21	-3.37	0.48
GAL_75.78+0.34	OCS	14.00	0.25	1.011e+14	5.882e+13	47.26	17.51	4.64	0.40	-3.42	0.19

GAL_75.78+0.34	S-34-O	13.25	0.32	1.770e+13	1.314e+13	100.00	128.54	5.25	1.05	-3.19	0.36
GAL_75.78+0.34	SO	14.34	0.00	2.164e+14	2.381e+12	20.88	0.24	5.21	0.02	-3.68	0.01
GAL_75.78+0.34	SO2	14.17	0.01	1.463e+14	2.598e+12	59.08	1.43	5.70	0.10	-3.36	0.04
GAL_75.78+0.34	SiO	12.10	0.09	1.262e+12	2.506e+11	59.93	11.56	5.36	0.89	-3.97	0.54
GCM+0.693-0.027	CCH	14.57	0.03	3.696e+14	2.149e+13	42.15	5.37	13.45	0.40	4.61	0.20
GCM+0.693-0.027	CH2NH	14.21	0.01	1.625e+14	4.926e+12	27.77	2.33	22.87	0.78	1.92	0.32
GCM+0.693-0.027	CH3CCH	15.16	0.02	1.430e+15	5.559e+13	37.48	1.14	17.92	0.55	3.98	0.31
GCM+0.693-0.027	CH3OH	15.76	0.00	5.708e+15	5.202e+13	14.90	0.10	19.70	0.08	3.71	0.05
GCM+0.693-0.027	CS	12.84	0.11	6.978e+12	1.790e+12	92.86	42.44	4.72	1.86	-11.39	0.56
GCM+0.693-0.027	CS	14.04	0.23	1.087e+14	5.753e+13	10.78	0.65	13.10	1.32	4.00	1.50
GCM+0.693-0.027	CS	14.22	0.62	1.647e+14	2.342e+14	10.00	6.93	13.00	1.65	9.65	1.46
GCM+0.693-0.027	H2CO	13.90	11.85	7.950e+13	2.169e+15	15.79	699.15	11.29	13.88	9.67	0.43
GCM+0.693-0.027	H2CS	14.17	0.02	1.481e+14	7.520e+12	62.77	4.90	24.10	1.01	2.97	0.46
GCM+0.693-0.027	HC-13-N	15.28	0.68	1.896e+15	2.980e+15	2.87	0.17	9.45	3.42	9.75	0.88
GCM+0.693-0.027	HC-13-O+	13.53	0.21	3.383e+13	1.603e+13	4.68	0.40	10.23	2.66	6.54	0.85
GCM+0.693-0.027	NO	16.25	0.04	1.766e+16	1.759e+15	100.70	10.29	17.26	0.70	0.28	0.32
GCM+0.693-0.027	NS	13.35	0.13	2.237e+13	6.936e+12	23.25	9.61	14.16	1.32	4.70	0.69
GCM+0.693-0.027	OCS	14.92	0.13	8.348e+14	2.515e+14	49.93	10.47	23.53	1.07	-0.56	0.50
GCM+0.693-0.027	SiO	13.00	0.22	1.000e+13	5.084e+12	31.02	37.74	18.30	2.50	6.43	1.33
GCM+0.693-0.027	SiO	13.00	0.47	1.000e+13	1.076e+13	13.98	5.62	13.13	3.33	-9.65	1.63
HH_80-81	C-13-S	12.25	3.70	1.778e+12	1.517e+13	71.47	1152.70	2.11	0.69	-0.01	0.29
HH_80-81	CCH	14.65	0.08	4.481e+14	8.585e+13	9.93	1.03	2.15	0.05	0.08	0.03
HH_80-81	CH3CCH	14.49	0.12	3.107e+14	8.404e+13	20.03	1.91	1.48	0.10	-0.20	0.05
HH_80-81	CH3OH	14.32	0.01	2.091e+14	6.331e+12	14.73	0.35	2.97	0.06	0.73	0.03
HH_80-81	CN	13.47	0.16	2.936e+13	1.092e+13	36.16	26.17	5.60	0.47	-0.33	0.16
HH_80-81	CN	14.89	0.06	7.809e+14	1.118e+14	3.81	0.13	2.01	0.09	0.08	0.04
HH_80-81	CS	13.36	0.16	2.303e+13	8.734e+12	34.59	4.55	2.10	0.48	0.08	0.16
HH_80-81	CS	13.71	2.47	5.128e+13	2.915e+14	17.77	83.88	3.51	0.65	0.48	0.25
HH_80-81	CS-33	11.78	0.32	6.040e+11	4.454e+11	27.95	67.92	2.43	3.06	0.45	0.76
HH_80-81	CS-34	12.95	12.64	8.989e+12	2.617e+14	12.74	206.91	2.41	0.63	0.03	0.11
HH_80-81	H2CO	13.16	0.10	1.452e+13	3.229e+12	27.92	3.29	5.75	0.40	1.31	0.40
HH_80-81	H2CO	13.97	0.29	9.248e+13	6.086e+13	99.17	55.82	2.52	0.11	0.17	0.03
HH_80-81	H2CS	13.03	0.10	1.065e+13	2.529e+12	25.70	8.56	2.31	0.17	0.01	0.09
HH_80-81	HC-13-N	12.09	0.06	1.218e+12	1.691e+11	43.21	8.05	3.01	0.27	0.20	0.16
HH_80-81	HC-13-O+	12.33	0.04	2.154e+12	1.828e+11	100.00	7.94	2.00	0.08	-0.03	0.05
HH_80-81	HCN	13.76	0.10	5.816e+13	1.342e+13	7.70	0.44	4.52	0.16	0.34	0.03
HH_80-81	HCO-18+	11.19	0.59	1.532e+11	2.071e+11	19.58	77.80	2.99	3.73	1.24	1.18
HH_80-81	HNC-13	11.63	0.70	4.254e+11	6.885e+11	17.01	46.91	2.66	1.73	0.05	0.54
HH_80-81	NO	14.89	0.40	7.713e+14	7.139e+14	57.13	64.93	2.00	0.46	0.13	0.16
HH_80-81	NS	12.56	0.31	3.616e+12	2.614e+12	100.00	98.88	2.48	1.97	0.47	0.61
HH_80-81	S-34-O	12.84	1.24	6.929e+12	1.973e+13	100.00	494.05	2.37	0.45	-0.02	0.25
HH_80-81	SO	14.09	0.01	1.228e+14	2.086e+12	18.68	0.27	2.29	0.01	0.01	0.01
HH_80-81	SO2	13.65	0.01	4.503e+13	1.509e+12	46.93	2.36	3.13	0.10	0.12	0.06
L1157-MM	CH3OH	14.69	0.01	4.918e+14	1.036e+13	14.25	0.23	3.62	0.05	-1.34	0.04
L1157-MM	CH3OH	14.92	0.01	8.227e+14	1.476e+13	14.24	0.20	5.87	0.10	-3.70	0.03
L1157-MM	CN	13.38	0.85	2.383e+13	4.638e+13	9.76	23.15	6.08	0.61	-2.51	0.23
L1157-MM	CS	13.18	0.15	1.503e+13	5.167e+12	99.94	32.44	3.95	0.32	-1.71	0.13
L1157-MM	CS	13.28	0.03	1.898e+13	1.436e+12	23.40	2.22	6.96	0.31	-4.86	0.30
L1157-MM	H2CO	13.36	0.23	2.316e+13	1.218e+13	20.19	4.55	3.61	0.58	-0.90	0.11
L1157-MM	H2CO	13.65	0.15	4.519e+13	1.539e+13	31.57	10.72	6.47	0.56	-3.21	0.74
L1157-MM	HCN	13.28	0.91	1.905e+13	3.982e+13	7.11	5.80	11.25	3.71	-7.47	1.66
L1157-MM	HCN	13.86	0.57	7.280e+13	9.605e+13	6.43	1.81	6.45	1.23	-2.46	0.34
L1157-MM	SO	13.90	0.05	7.887e+13	8.777e+12	13.46	0.71	6.15	0.21	-3.95	0.17
L1157-MM	SO	14.00	0.07	9.974e+13	1.622e+13	9.79	0.60	3.02	0.14	-0.98	0.05
L1157-MM	SiO	12.48	0.10	3.036e+12	6.760e+11	40.31	4.73	11.75	2.06	-10.33	1.36
L1157-MM	SiO	13.03	3.41	1.070e+13	8.394e+13	15.05	60.12	5.90	0.56	-3.04	0.20
L1448_MM-1	CH3OH	13.10	0.13	1.264e+13	3.796e+12	17.71	2.79	1.28	0.55	5.80	0.14
L1448_MM-1	CN	14.65	0.06	4.455e+14	6.199e+13	2.90	0.05	1.07	0.06	5.27	0.03
L1448_MM-1	CS	12.66	0.03	4.620e+12	2.820e+11	25.80	3.27	1.43	0.04	5.56	0.02
L1448_MM-1	DNC	11.97	0.10	9.253e+11	2.104e+11	10.17	1.94	1.01	0.07	5.18	0.03
L1448_MM-1	H2CO	12.51	3.77	3.264e+12	2.836e+13	13.02	110.12	1.12	0.10	5.76	0.05
L1448_MM-1	HCN	11.77	0.03	5.925e+11	4.538e+10	24.13	7.11	1.86	0.17	3.18	0.07
L1448_MM-1	HCN	12.19	0.12	1.564e+12	4.287e+11	18.23	12.03	2.35	0.10	6.74	0.04
L1448_MM-1	HDCO	12.00	0.16	9.987e+11	3.617e+11	39.23	24.94	0.92	0.17	5.51	0.08
L1448_MM-1	N2D+	11.93	0.03	8.577e+11	6.043e+10	24.14	5.58	0.50	0.02	5.28	0.01
NGC6334-29	C-13-H3CN	12.38	0.11	2.386e+12	6.096e+11	83.49	57.63	4.02	0.97	-1.31	0.49
NGC6334-29	C-13-H3OH	13.94	0.06	8.750e+13	1.170e+13	54.30	7.23	4.12	0.67	-0.55	0.20
NGC6334-29	C-13-S	12.84	11.67	6.862e+12	1.843e+14	30.12	249.77	9.47	460.93	-2.73	95.26
NGC6334-29	C-13-S	13.12	10.25	1.327e+13	3.131e+14	28.76	137.01	3.59	35.74	-0.91	12.35
NGC6334-29	C2H5CN	13.38	0.03	2.380e+13	1.376e+12	147.07	18.61	5.49	0.34	-1.70	0.18
NGC6334-29	CCH	14.45	0.32	2.801e+14	2.065e+14	18.46	18.63	9.68	2.66	-1.04	0.81
NGC6334-29	CCH	14.69	0.32	4.881e+14	3.541e+14	16.22	17.25	3.05	0.58	-0.29	0.12
NGC6334-29	CH2NH	13.34	0.05	2.206e+13	2.542e+12	39.38	5.62	5.04	0.58	-1.34	0.26
NGC6334-29	CH3CCH	15.22	0.01	1.652e+15	3.281e+13	39.50	0.68	3.77	0.05	-0.89	0.03
NGC6334-29	CH3CHO	13.88	0.06	7.629e+13	1.138e+13	181.70	22.51	5.59	0.56	-1.23	0.24
NGC6334-29	CH3CN	13.83	0.01	6.818e+13	1.557e+12	169.74	4.27	5.48	0.07	-1.00	0.04
NGC6334-29	CH3OCH3	15.02	0.02	1.045e+15	5.070e+13	135.01	6.39	5.27	0.30	-0.89	0.12
NGC6334-29	CH3OH	15.22	0.00	1.641e+15	1.322e+13	18.69	0.22	5.49	0.03	-1.22	0.02
NGC6334-29	CH3OH	15.28	0.00	1.891e+15	2.154e+13	127.86	1.68	4.33	0.04	-0.70	0.02
NGC6334-29	CN	14.10	0.29	1.254e+14	8.431e+13	38.75	52.68	3.26	0.19	0.27	0.06
NGC6334-29	CN	15.43	0.06	2.711e+15	3.714e+14	4.53	0.14	7.22	0.23	-1.23	0.18
NGC6334-29	CS	14.32	0.05	2.097e+14	2.358e+13	30.52	7.96	4.08	0.16	-0.07	0.03
NGC6334-29	CS	14.50	0.06	3.145e+14	4.631e+13	99.18	23.36	11.21	0.20	-1.55	0.08
NGC6334-29	CS-33	12.73	2.09	5.312e+12	2.561e+13	28.35	224.40	3.34	4.99	-0.43	0.89
NGC6334-29	CS-33	12.96	1.24	9.035e+12	2.579e+13	100.00	188.79	8.46	14.94	-1.72	6.33
NGC6334-29	CS-34	13.25	0.20	1.781e+13	8.298e+12	32.35	56.63	10.24	3.53	-1.56	1.16
NGC6334-29	CS-34	13.50	0.34	3.165e+13	2.493e+13	58.50	107.90	3.69	0.51	-0.64	0.15
NGC6334-29	DNC	12.26	0.75	1.803e+12	3.112e+12	47.42	152.68	2.81	1.08	-1.52	0.48
NGC6334-29	H2CCO	13.69	0.02	4.873e+13	2.761e+12	65.06	7.13	4.63	0.28	-0.74	0.14
NGC6334-29	H2CO	14.04	0.09	1.095e+14	2.274e+13	28.64	8.31	10.77	1.03	-1.84	0.40
NGC6334-29	H2CO	14.11	0.14	1.294e+14	4.209e+13	21.25	36.56	4.00	0.77	-0.69	0.07
NGC6334-29	H2CS	13.84	0.05	6.972e+13	7.965e+12	25.77	3.34	9.38	0.89	-1.59	0.31

NGC6334-29	H2CS	14.02	0.03	1.040e+14	6.741e+12	69.98	4.18	3.42	0.15	-0.69	0.04
NGC6334-29	HC-13-N	12.96	0.13	9.078e+12	2.790e+12	28.65	54.34	12.91	2.47	-1.83	1.06
NGC6334-29	HC-13-N	13.25	0.45	1.780e+13	1.825e+13	50.72	108.96	4.51	0.38	-0.07	0.11
NGC6334-29	HC-13-O+	12.54	0.29	3.460e+12	2.334e+12	58.86	47.71	9.99	2.01	-1.87	1.26
NGC6334-29	HC-13-O+	12.86	0.05	7.267e+12	8.439e+11	26.83	10.01	3.34	0.25	-0.45	0.08
NGC6334-29	HCC-13-CN	12.55	0.76	3.541e+12	6.198e+12	243.00	1314.45	6.51	3.39	-2.32	1.41
NGC6334-29	HCCCN	13.65	13.79	4.453e+13	1.414e+15	44.75	532.30	3.62	2.89	-0.58	2.19
NGC6334-29	HCCCN	13.72	19.85	5.239e+13	2.395e+15	43.37	721.24	8.20	12.52	-3.01	7.64
NGC6334-29	HCCCNv7	13.47	0.49	2.945e+13	3.339e+13	68.12	56.84	6.19	1.16	-2.25	0.53
NGC6334-29	HCN-15	12.17	1.74	1.483e+12	5.945e+12	30.00	166.36	5.62	12.06	-4.67	8.34
NGC6334-29	HCN-15	12.98	0.47	9.645e+12	1.041e+13	100.00	50.04	4.38	1.35	-0.19	1.29
NGC6334-29	HCO-18+	12.08	0.65	1.196e+12	1.801e+12	13.69	21.56	3.16	1.57	0.29	0.65
NGC6334-29	HCOOCH3	14.78	0.05	6.037e+14	6.560e+13	285.40	28.51	5.94	0.21	-0.62	0.12
NGC6334-29	HCS+	12.99	2.80	9.772e+12	6.296e+13	14.02	44.00	4.05	2.29	-0.30	1.14
NGC6334-29	HDO	14.15	0.25	1.426e+14	8.086e+13	100.00	220.94	4.35	2.82	-1.54	1.15
NGC6334-29	HNC-13	12.41	0.64	2.570e+12	3.763e+12	30.75	168.64	11.35	6.93	-4.33	5.86
NGC6334-29	HNC-13	12.83	0.67	6.721e+12	1.035e+13	99.90	150.79	3.60	1.57	-1.07	0.34
NGC6334-29	HNCO	14.24	0.11	1.748e+14	4.621e+13	25.03	3.71	8.00	0.75	-0.82	0.39
NGC6334-29	NH2CHO	13.10	0.09	1.263e+13	2.611e+12	26.67	3.50	6.16	0.72	-1.85	0.34
NGC6334-29	NO	14.95	6.28	8.957e+14	1.296e+16	9.28	80.97	3.25	3.73	-0.90	1.37
NGC6334-29	NO	15.22	0.28	1.674e+15	1.085e+15	17.25	6.85	10.77	4.04	-3.51	3.37
NGC6334-29	NS	13.00	11.29	1.000e+13	2.599e+14	21.50	143.46	3.41	31.89	-0.67	11.55
NGC6334-29	NS	13.07	7.66	1.176e+13	2.073e+14	26.30	199.02	7.23	55.21	-2.15	19.45
NGC6334-29	OCS	14.45	0.47	2.812e+14	3.065e+14	46.28	27.14	3.72	0.73	-0.96	0.15
NGC6334-29	OCS	14.81	0.48	6.481e+14	7.203e+14	36.79	17.41	8.25	1.02	-2.67	0.74
NGC6334-29	S-33-O	13.19	1.22	1.566e+13	4.403e+13	24.10	80.55	4.93	3.88	-0.75	1.92
NGC6334-29	S-34-O	13.12	1.73	1.330e+13	5.307e+13	100.00	374.44	2.93	4.54	-0.66	1.26
NGC6334-29	S-34-O	13.60	0.29	3.943e+13	2.610e+13	44.85	115.33	8.35	4.36	-1.95	1.50
NGC6334-29	S-34-O2	14.18	0.03	1.526e+14	1.098e+13	109.48	8.75	6.30	0.27	-1.79	0.14
NGC6334-29	SO	14.54	0.12	3.446e+14	9.802e+13	204.86	73.50	4.32	0.07	-0.43	0.02
NGC6334-29	SO	14.56	0.34	3.651e+14	2.825e+14	191.72	191.31	13.49	0.25	-2.98	0.15
NGC6334-29	SO2	13.96	0.03	9.067e+13	7.208e+12	12.89	1.67	5.89	0.41	-1.58	0.29
NGC6334-29	SO2	14.95	0.01	8.995e+14	1.635e+13	137.77	2.90	6.95	0.08	-1.44	0.04
NGC6334-29	SiO	12.16	0.66	1.439e+12	2.201e+12	48.53	707.10	3.97	4.25	-0.29	1.33
NGC6334-29	SiO	13.00	1.22	9.901e+12	2.791e+13	17.53	34.44	16.08	5.09	-5.00	4.03
NGC6334-38	C-13-S	13.53	0.08	3.356e+13	6.550e+12	57.83	27.47	3.12	0.15	1.46	0.07
NGC6334-38	CCH	15.30	0.05	1.973e+15	2.359e+14	10.38	0.50	3.21	0.11	1.78	0.04
NGC6334-38	CH3CCH	14.98	0.01	9.544e+14	1.547e+13	43.62	0.66	2.88	0.04	2.14	0.02
NGC6334-38	CH3CN	13.02	0.03	1.044e+13	7.399e+11	33.20	1.72	4.15	0.23	1.66	0.11
NGC6334-38	CH3OH	14.94	0.00	8.681e+14	4.846e+12	21.74	0.15	3.72	0.02	1.48	0.01
NGC6334-38	CN	14.06	0.08	1.147e+14	1.999e+13	100.00	13.49	3.13	0.34	4.25	0.17
NGC6334-38	CN	15.00	0.02	1.001e+15	4.370e+13	7.58	0.16	3.65	0.08	1.60	0.06
NGC6334-38	CO+	12.15	0.72	1.420e+12	2.351e+12	34.79	102.77	5.08	8.37	2.45	1.48
NGC6334-38	CS	13.94	0.02	8.738e+13	4.529e+12	37.14	0.34	13.08	0.62	1.51	0.17
NGC6334-38	CS	14.45	0.03	2.839e+14	1.698e+13	30.89	3.45	3.89	0.10	1.56	0.01
NGC6334-38	CS-33	13.21	0.09	1.611e+13	3.366e+12	44.91	42.66	3.14	0.26	1.49	0.12
NGC6334-38	CS-34	13.80	0.04	6.310e+13	5.440e+12	50.30	16.46	3.29	0.08	1.55	0.04
NGC6334-38	DNC	11.57	0.58	3.701e+11	4.919e+11	30.19	87.11	2.35	2.34	1.78	1.21
NGC6334-38	H2C-13-O	12.76	3.50	5.700e+12	4.595e+13	53.83	475.36	4.33	7.93	1.62	2.36
NGC6334-38	H2CCO	13.20	0.05	1.591e+13	1.735e+12	45.25	6.60	3.51	0.30	1.51	0.17
NGC6334-38	H2CO	14.00	1.98	1.000e+14	4.558e+14	53.21	250.54	4.88	1.27	0.55	1.11
NGC6334-38	H2CO	14.00	6.56	1.000e+14	1.511e+15	68.68	1070.60	3.08	0.25	2.55	0.11
NGC6334-38	H2CS	14.02	0.01	1.044e+14	1.204e+12	47.58	1.24	3.23	0.03	1.73	0.02
NGC6334-38	H2CS-34	12.37	0.44	2.337e+12	2.378e+12	37.46	302.19	1.18	1.10	1.62	0.60
NGC6334-38	HC-13-N	12.64	0.35	4.364e+12	3.500e+12	22.58	20.94	9.53	4.74	2.30	0.80
NGC6334-38	HC-13-N	12.98	2.96	9.559e+12	6.512e+13	12.27	71.20	3.82	2.07	1.91	0.17
NGC6334-38	HC-13-O+	12.93	0.21	8.548e+12	4.136e+12	100.00	65.51	3.08	0.13	2.13	0.06
NGC6334-38	HCCCN	13.56	0.10	3.655e+13	8.681e+12	36.30	2.60	4.00	0.12	2.47	0.07
NGC6334-38	HCN	12.98	0.04	9.453e+12	8.477e+11	33.43	3.81	3.45	0.18	-2.00	0.07
NGC6334-38	HCN	13.21	0.04	1.637e+13	1.637e+12	47.34	9.03	2.80	0.09	4.45	0.03
NGC6334-38	HCN	13.91	0.06	8.058e+13	1.066e+13	99.98	15.90	13.71	0.23	1.63	0.15
NGC6334-38	HCN-15	12.28	0.18	1.915e+12	8.155e+11	36.44	40.31	3.32	0.64	2.00	0.32
NGC6334-38	HCO-18+	11.80	1.14	6.264e+11	1.638e+12	17.11	92.63	3.07	1.97	3.11	0.75
NGC6334-38	HCS+	12.98	3.15	9.539e+12	6.919e+13	18.96	106.46	2.78	0.64	1.64	0.28
NGC6334-38	HNC-13	12.23	0.25	1.692e+12	9.675e+11	43.22	46.95	2.75	1.12	2.03	0.37
NGC6334-38	HNCO	13.38	0.11	2.377e+13	5.835e+12	23.04	3.48	5.00	0.47	2.59	0.27
NGC6334-38	NO	15.42	0.71	2.639e+15	4.288e+15	5.27	1.63	3.06	6.83	1.53	1.05
NGC6334-38	NS	13.22	0.37	1.662e+13	1.399e+13	28.56	67.89	3.57	0.96	1.90	0.33
NGC6334-38	OCS	14.55	0.28	3.552e+14	2.301e+14	30.52	6.81	4.11	0.36	1.57	0.14
NGC6334-38	S-34-O	13.12	1.76	1.304e+13	5.270e+13	16.86	41.57	3.23	2.83	1.44	0.94
NGC6334-38	SO	14.38	0.00	2.386e+14	2.612e+12	21.42	0.24	3.58	0.01	1.64	0.01
NGC6334-38	SiO	12.98	0.90	9.487e+12	1.968e+13	14.56	15.17	9.46	1.89	1.75	1.08
NGC6334-43	C-13-S	13.28	25.85	1.898e+13	1.130e+15	16.33	866.28	2.62	4.81	2.43	0.14
NGC6334-43	CCH	14.84	0.04	6.939e+14	6.583e+13	100.00	10.45	2.59	0.57	2.21	0.18
NGC6334-43	CH3CCH	14.86	0.02	7.308e+14	3.281e+13	31.25	0.87	3.04	0.08	2.05	0.03
NGC6334-43	CH3CN	13.17	0.15	1.472e+13	5.162e+12	17.64	2.03	4.00	0.57	2.58	0.28
NGC6334-43	CH3OH	14.80	0.01	6.369e+14	7.358e+12	16.83	0.18	3.12	0.03	2.57	0.01
NGC6334-43	CN	14.49	0.05	3.098e+14	3.663e+13	7.59	0.13	2.36	0.09	1.80	0.05
NGC6334-43	CN	15.67	0.14	4.625e+15	1.460e+15	3.81	0.22	2.85	0.28	2.05	0.14
NGC6334-43	CS	13.89	0.05	7.774e+13	8.226e+12	61.58	5.27	4.14	0.11	2.96	0.15
NGC6334-43	CS	14.07	0.03	1.165e+14	7.231e+12	47.63	5.19	2.77	0.03	1.55	0.02
NGC6334-43	CS-33	13.04	1.56	1.098e+13	3.941e+13	14.44	34.99	2.80	0.51	2.33	0.18
NGC6334-43	CS-34	13.63	0.05	4.231e+13	5.072e+12	17.50	1.87	2.74	0.12	2.20	0.04
NGC6334-43	DNC	11.85	0.30	7.155e+11	4.930e+11	11.65	4.34	2.34	2.48	2.06	0.57
NGC6334-43	H2CCO	13.65	0.35	4.452e+13	3.599e+13	17.55	4.99	4.35	0.75	1.93	0.45
NGC6334-43	H2CO	13.25	0.90	1.798e+13	3.713e+13	24.05	37.27	2.86	1.79	4.15	2.10
NGC6334-43	H2CO	14.00	0.20	1.000e+14	4.613e+13	35.75	8.01	2.89	0.47	1.76	0.49
NGC6334-43	H2CS	13.75	0.01	5.669e+13	1.176e+12	33.54	1.76	2.89	0.06	2.18	0.03
NGC6334-43	HC-13-N	12.74	0.12	5.499e+12	1.580e+12	87.87	29.32	2.99	0.49	2.20	0.16
NGC6334-43	HC-13-O+	13.11	0.35	1.286e+13	1.023e+13	6.90	1.38	2.05	0.41	2.03	0.09
NGC6334-43	HCCCN	13.12	0.40	1.320e+13	1.209e+13	33.98	8.48	3.80	0.52	2.32	0.21
NGC6334-43	HCN	14.53	0.07	3.408e+14	5.859e+13	8.23	0.05	3.96	0.17	2.18	0.04

NGC6334-43	HCN-15	11.97	0.34	9.228e+11	7.171e+11	13.92	13.99	2.69	1.32	2.11	0.41
NGC6334-43	HCO-18+	11.48	0.35	3.034e+11	2.433e+11	31.81	43.90	3.56	4.70	2.73	1.32
NGC6334-43	HCS+	12.41	1.13	2.560e+12	6.675e+12	26.15	80.63	2.58	3.52	2.33	0.86
NGC6334-43	HNC-13	12.24	0.36	1.735e+12	1.431e+12	61.89	76.84	2.04	0.58	1.61	0.20
NGC6334-43	NO	14.65	1.55	4.483e+14	1.603e+15	13.19	59.94	2.69	3.44	1.80	1.03
NGC6334-43	NS	13.14	0.34	1.371e+13	1.075e+13	29.25	73.56	2.58	0.62	2.28	0.23
NGC6334-43	OCS	14.31	1.36	2.024e+14	6.339e+14	30.66	32.38	3.67	1.70	2.85	0.62
NGC6334-43	SO	14.70	0.02	4.994e+14	2.467e+13	10.18	0.16	3.02	0.03	2.52	0.01
NGC6334-I(N)	C-13-H3OH	14.11	0.07	1.299e+14	2.200e+13	14.67	2.59	4.73	0.39	-1.28	0.17
NGC6334-I(N)	C-13-S	13.04	0.68	1.102e+13	1.720e+13	43.36	317.19	2.89	0.30	-1.81	0.13
NGC6334-I(N)	CCH	15.72	0.07	5.205e+15	8.499e+14	6.00	0.13	2.53	0.16	-1.14	0.06
NGC6334-I(N)	CH2NH	13.05	0.05	1.134e+13	1.427e+12	22.08	4.78	3.40	0.44	-1.71	0.23
NGC6334-I(N)	CH3CCH	15.44	0.03	2.763e+15	1.694e+14	20.69	0.45	2.79	0.05	-1.75	0.03
NGC6334-I(N)	CH3CHO	13.88	0.07	7.540e+13	1.174e+13	19.48	1.10	3.54	0.35	-1.55	0.15
NGC6334-I(N)	CH3CN	13.33	0.06	2.132e+13	3.171e+12	22.94	1.57	3.95	0.27	-1.33	0.15
NGC6334-I(N)	CH3OCH3	14.50	0.03	3.134e+14	2.072e+13	35.18	3.17	3.26	0.30	-1.43	0.14
NGC6334-I(N)	CH3OH	15.18	0.03	1.515e+15	1.094e+14	20.42	0.76	3.39	0.12	-2.18	0.02
NGC6334-I(N)	CH3OH	15.25	0.02	1.792e+15	8.260e+13	16.49	1.08	6.90	0.10	-0.89	0.16
NGC6334-I(N)	CN	15.66	0.04	4.548e+15	4.076e+14	4.24	0.04	2.92	0.07	-1.90	0.06
NGC6334-I(N)	CS	13.50	0.07	3.166e+13	4.891e+12	99.22	10.45	2.00	0.14	-3.77	0.04
NGC6334-I(N)	CS	13.53	0.03	3.417e+13	2.045e+12	20.15	1.85	9.45	0.48	5.00	0.29
NGC6334-I(N)	CS	13.97	0.05	9.311e+13	1.082e+13	19.87	2.93	4.76	0.26	0.13	0.07
NGC6334-I(N)	CS-33	12.98	288.98	9.599e+12	6.387e+15	13.13	5051.55	2.51	17.21	-1.69	0.33
NGC6334-I(N)	CS-34	13.46	0.04	2.907e+13	2.812e+12	57.64	13.47	3.23	0.12	-1.89	0.05
NGC6334-I(N)	DNC	11.89	0.68	7.688e+11	1.200e+12	18.33	113.65	2.52	0.89	-1.90	0.40
NGC6334-I(N)	H2C-13-O	13.16	0.37	1.455e+13	1.236e+13	30.98	55.49	3.46	0.46	-1.49	0.20
NGC6334-I(N)	H2CCO	13.97	0.11	9.422e+13	2.312e+13	21.33	2.27	4.04	0.27	-1.65	0.14
NGC6334-I(N)	H2CO	13.97	4.81	9.248e+13	1.025e+15	77.88	804.99	2.68	0.29	-4.07	0.04
NGC6334-I(N)	H2CO	14.00	1.95	1.000e+14	4.483e+14	81.81	336.46	3.25	0.15	1.12	0.05
NGC6334-I(N)	H2CO	14.04	0.03	1.102e+14	6.706e+12	26.00	3.59	13.41	0.55	-0.53	0.23
NGC6334-I(N)	H2CS	14.04	0.01	1.099e+14	1.506e+12	36.40	1.31	3.16	0.04	-1.63	0.02
NGC6334-I(N)	HC-13-N	12.94	1.89	8.647e+12	3.754e+13	99.67	586.51	6.37	0.53	-1.43	0.25
NGC6334-I(N)	HC-13-O+	12.51	0.25	3.249e+12	1.887e+12	17.88	20.17	3.24	0.23	-1.45	0.08
NGC6334-I(N)	HCCCN	14.38	0.33	2.416e+14	1.818e+14	22.16	2.88	6.64	0.49	-1.17	0.29
NGC6334-I(N)	HCN	12.90	7.44	7.986e+12	1.369e+14	99.98	2497.39	3.65	5.27	4.14	1.66
NGC6334-I(N)	HCN	13.04	0.06	1.087e+13	1.431e+12	43.71	23.46	3.32	0.58	-5.60	0.07
NGC6334-I(N)	HCN	13.41	0.36	2.570e+13	2.149e+13	22.71	79.01	26.19	9.52	0.94	0.87
NGC6334-I(N)	HCN-15	11.83	1.33	6.835e+11	2.101e+12	15.03	70.34	2.56	1.37	-1.57	0.47
NGC6334-I(N)	HCO-18+	11.42	0.36	2.624e+11	2.200e+11	33.19	67.04	2.47	1.60	-0.78	0.81
NGC6334-I(N)	HCS+	13.00	36.31	1.000e+13	8.361e+14	14.40	598.44	2.79	1.31	-1.91	0.30
NGC6334-I(N)	HDCS	13.95	0.57	8.994e+13	1.184e+14	10.06	3.38	3.51	0.45	-1.54	0.31
NGC6334-I(N)	HNC-13	12.29	116.58	1.968e+12	5.284e+14	17.11	9374.82	2.94	17.08	-1.88	0.23
NGC6334-I(N)	HNCO	14.35	0.12	2.219e+14	5.993e+13	16.31	1.67	7.00	0.52	-0.50	0.20
NGC6334-I(N)	N2D+	11.74	0.86	5.530e+11	1.091e+12	33.17	201.16	3.98	3.82	-2.81	1.53
NGC6334-I(N)	NO	15.18	0.08	1.496e+15	2.702e+14	25.43	15.38	2.85	0.36	-1.72	0.18
NGC6334-I(N)	NS	14.50	1.48	3.161e+14	1.075e+15	8.20	6.50	2.74	0.31	-1.87	0.11
NGC6334-I(N)	OCS	14.74	0.23	5.506e+14	2.863e+14	31.20	5.72	3.56	0.25	-1.73	0.10
NGC6334-I(N)	S-34-O	12.98	0.29	9.606e+12	6.357e+12	34.72	84.62	3.25	0.93	-1.77	0.47
NGC6334-I(N)	SO	14.30	0.04	2.000e+14	1.751e+13	13.76	0.62	8.56	0.14	0.49	0.14
NGC6334-I(N)	SO	14.69	0.03	4.940e+14	3.012e+13	14.25	0.37	2.91	0.03	-1.75	0.01
NGC6334-I(N)	SO2	13.57	0.04	3.693e+13	3.134e+12	34.72	4.03	4.62	0.37	-1.79	0.21
NGC6334-I(N)	SiO	13.04	0.07	1.086e+13	1.675e+12	63.40	25.41	13.13	0.87	0.76	0.47
NGC_1333_IRAS_2A	CCH	13.56	0.09	3.655e+13	7.444e+12	82.12	19.73	2.00	0.15	0.14	0.24
NGC_1333_IRAS_2A	CH3OH	13.65	0.02	4.482e+13	2.431e+12	26.01	1.55	2.79	0.13	0.06	0.09
NGC_1333_IRAS_2A	CN	14.80	0.05	6.276e+14	7.009e+13	3.00	0.04	1.30	0.06	-0.24	0.03
NGC_1333_IRAS_2A	CS	12.74	0.21	5.484e+12	2.643e+12	47.30	97.72	6.25	3.36	0.49	0.34
NGC_1333_IRAS_2A	CS	12.98	509.73	9.572e+12	1.124e+16	100.00	183359.46	2.22	5.35	-0.05	0.34
NGC_1333_IRAS_2A	DNC	12.00	0.08	1.011e+12	1.957e+11	83.90	9.70	2.00	0.17	-0.62	0.21
NGC_1333_IRAS_2A	H2CO	12.86	0.13	7.226e+12	2.218e+12	35.95	18.21	2.64	0.11	0.00	0.07
NGC_1333_IRAS_2A	HC-13-N	11.51	0.13	3.231e+11	9.412e+10	43.31	21.56	2.71	0.56	-0.19	0.30
NGC_1333_IRAS_2A	HC-13-O+	12.19	0.03	1.546e+12	9.333e+10	100.00	3.33	2.00	0.05	0.27	0.07
NGC_1333_IRAS_2A	HCN	12.24	1.41	1.757e+12	5.698e+12	16.95	47.81	5.00	5.93	-1.72	8.33
NGC_1333_IRAS_2A	HCN	12.33	1.72	2.128e+12	8.418e+12	39.41	18.49	5.00	5.97	1.95	7.05
NGC_1333_IRAS_2A	HCN-15	11.29	0.15	1.934e+11	6.781e+10	34.57	17.71	2.96	1.07	1.00	0.58
NGC_1333_IRAS_2A	HDCO	12.48	0.12	3.032e+12	8.674e+11	48.46	19.24	3.18	0.34	-0.19	0.21
NGC_1333_IRAS_2A	HNC-13	11.43	0.22	2.669e+11	1.380e+11	51.23	19.63	2.00	0.95	-0.49	0.34
NGC_1333_IRAS_2A	NO	14.31	0.55	2.019e+14	2.545e+14	11.74	15.36	2.13	0.85	0.32	0.32
NGC_1333_IRAS_2A	SO	13.31	0.04	2.022e+13	1.806e+12	18.79	1.55	4.03	0.13	-0.21	0.09
NGC_1333_IRAS_4A	C-13-S	12.24	0.12	1.730e+12	4.717e+11	44.62	12.14	5.92	1.25	1.89	0.79
NGC_1333_IRAS_4A	CCH	13.75	0.37	5.646e+13	4.812e+13	90.84	106.57	5.07	0.68	1.25	0.32
NGC_1333_IRAS_4A	CH3OH	14.05	0.14	1.128e+14	3.716e+13	17.64	7.19	2.98	0.17	0.61	0.07
NGC_1333_IRAS_4A	CH3OH	14.71	0.06	5.076e+14	7.072e+13	16.48	2.65	11.79	0.26	-0.78	0.16
NGC_1333_IRAS_4A	CN	14.45	0.12	2.789e+14	7.837e+13	3.03	0.11	2.19	0.21	0.54	0.11
NGC_1333_IRAS_4A	CS	13.02	0.02	1.035e+13	5.589e+11	51.19	5.38	2.53	0.07	0.24	0.03
NGC_1333_IRAS_4A	CS	13.75	0.02	5.623e+13	3.212e+12	78.53	7.70	13.89	0.21	0.40	0.09
NGC_1333_IRAS_4A	CS-34	12.55	0.09	3.540e+12	7.625e+11	45.05	33.60	7.83	1.10	0.36	0.56
NGC_1333_IRAS_4A	DNC	11.83	0.15	6.785e+11	2.304e+11	30.16	37.79	2.36	0.32	0.98	0.15
NGC_1333_IRAS_4A	H2CO	13.48	0.67	3.035e+13	4.691e+13	94.32	126.14	2.74	0.13	0.25	0.05
NGC_1333_IRAS_4A	H2CO	13.62	0.09	4.217e+13	8.579e+12	33.12	13.00	13.19	0.44	0.58	0.16
NGC_1333_IRAS_4A	H2CS	12.65	0.10	4.497e+12	1.065e+12	41.41	18.92	2.85	0.53	0.58	0.23
NGC_1333_IRAS_4A	H2CS	13.34	0.29	2.177e+13	1.439e+13	14.38	4.22	11.99	2.82	-1.25	1.05
NGC_1333_IRAS_4A	HC-13-N	12.06	0.07	1.157e+12	1.912e+11	35.43	8.53	11.04	1.58	1.58	0.86
NGC_1333_IRAS_4A	HC-13-O+	11.84	0.05	6.983e+11	7.591e+10	35.70	10.10	2.74	0.19	0.41	0.09
NGC_1333_IRAS_4A	HCN	12.52	0.05	3.289e+12	3.515e+11	100.00	13.17	2.00	0.07	-0.17	0.04
NGC_1333_IRAS_4A	HCN	13.14	0.17	1.365e+13	5.318e+12	28.91	110.68	17.74	0.53	0.29	0.11
NGC_1333_IRAS_4A	HCO-18+	11.29	0.47	1.930e+11	2.069e+11	15.95	32.92	2.71	2.34	1.93	0.70
NGC_1333_IRAS_4A	HDCO	12.78	0.02	6.002e+12	3.045e+11	30.83	2.90	3.56	0.16	0.82	0.08
NGC_1333_IRAS_4A	HNC-13	11.75	0.20	5.595e+11	2.524e+11	33.34	53.58	9.23	2.91	0.92	1.46
NGC_1333_IRAS_4A	N2D+	12.26	0.14	1.803e+12	5.733e+11	51.60	26.17	3.05	0.26	0.87	0.13
NGC_1333_IRAS_4A	OCS	13.48	0.12	3.000e+13	8.012e+12	100.00	85.33	6.96	1.32	0.70	0.80
NGC_1333_IRAS_4A	SO	13.44	0.03	2.744e+13	2.061e+12	18.01	1.19	2.59	0.08	0.69	0.03
NGC_1333_IRAS_4A	SO	14.04	0.16	1.089e+14	4.010e+13	145.35	73.91	20.94	0.61	1.20	0.22

NGC_1333_IRAS_4A	SiO	11.84	0.22	6.967e+11	3.551e+11	44.88	6.24	5.01	2.21	4.80	0.83
NGC_1333_IRAS_4A	SiO	12.25	0.64	1.778e+12	2.637e+12	94.22	262.64	9.01	2.01	14.06	0.77
NGC_1333_IRAS_4A	SiO	12.38	0.07	2.419e+12	4.033e+11	46.00	3.37	13.54	2.73	-7.15	1.18
NGC_1333_IRAS_4B	CH3OH	13.94	0.06	8.769e+13	1.298e+13	23.90	1.20	5.45	0.91	-4.01	0.40
NGC_1333_IRAS_4B	CH3OH	14.68	0.01	4.827e+14	1.352e+13	18.45	0.24	4.92	0.11	2.42	0.07
NGC_1333_IRAS_4B	CN	14.14	0.18	1.387e+14	5.760e+13	3.46	0.26	2.82	0.25	1.60	0.11
NGC_1333_IRAS_4B	CS	13.14	0.06	1.367e+13	1.943e+12	100.00	17.76	3.06	0.12	2.43	0.05
NGC_1333_IRAS_4B	CS	13.47	0.02	2.951e+13	1.373e+12	50.99	5.85	13.11	0.35	1.44	0.14
NGC_1333_IRAS_4B	CS-34	12.83	0.11	6.747e+12	1.676e+12	52.26	30.39	25.00	2.37	2.22	1.55
NGC_1333_IRAS_4B	DNC	11.97	0.07	9.354e+11	1.527e+11	33.49	12.44	2.79	0.27	1.91	0.14
NGC_1333_IRAS_4B	H2CO	13.53	0.37	3.372e+13	2.854e+13	44.02	48.68	12.16	0.63	1.54	0.23
NGC_1333_IRAS_4B	H2CO	13.75	0.08	5.617e+13	1.044e+13	100.00	16.02	3.59	0.15	1.87	0.05
NGC_1333_IRAS_4B	H2CS	12.99	1.55	9.875e+12	3.530e+13	11.63	20.91	2.67	6.89	2.16	1.50
NGC_1333_IRAS_4B	H2CS	13.42	0.09	2.648e+13	5.568e+12	75.78	21.17	15.00	3.76	2.08	0.78
NGC_1333_IRAS_4B	HC-13-O+	11.64	0.07	4.346e+11	6.985e+10	43.96	9.58	2.65	0.20	2.77	0.15
NGC_1333_IRAS_4B	HDCO	13.05	0.08	1.110e+13	2.148e+12	64.19	14.12	6.26	0.29	2.92	0.22
NGC_1333_IRAS_4B	HNCO	13.38	0.03	2.397e+13	1.914e+12	50.24	11.38	10.00	2.21	3.00	0.26
NGC_1333_IRAS_4B	N2D+	12.51	0.17	3.203e+12	1.236e+12	57.38	35.44	3.05	0.16	2.12	0.08
NGC_1333_IRAS_4B	SO	13.39	0.02	2.449e+13	1.341e+12	35.45	6.47	12.37	0.52	-4.93	0.34
NGC_1333_IRAS_4B	SO	13.77	0.03	5.948e+13	3.887e+12	14.91	0.60	3.73	0.07	2.43	0.05
NGC_1333_IRAS_4B	SiO	12.62	0.04	4.173e+12	4.146e+11	25.26	1.87	20.00	1.59	-2.33	0.87
NGC_2264	C-13-S	12.46	0.18	2.892e+12	1.221e+12	43.60	40.04	7.14	2.15	0.78	1.22
NGC_2264	CCH	14.84	0.17	6.881e+14	2.757e+14	9.93	2.09	3.38	0.14	0.95	0.04
NGC_2264	CH3CCH	14.28	0.03	1.892e+14	1.381e+13	49.28	4.38	4.04	0.21	1.24	0.14
NGC_2264	CH3OH	14.90	0.00	7.929e+14	7.416e+12	17.49	0.16	4.66	0.03	0.27	0.02
NGC_2264	CN	15.10	0.03	1.263e+15	7.787e+13	4.14	0.04	3.31	0.08	1.04	0.05
NGC_2264	CS	13.32	0.05	2.070e+13	2.261e+12	47.03	8.44	18.51	1.32	1.78	0.69
NGC_2264	CS	13.81	0.37	6.391e+13	5.418e+13	18.64	15.04	4.03	0.21	0.38	0.03
NGC_2264	CS-33	12.44	0.20	2.759e+12	1.266e+12	47.49	39.87	8.75	2.47	-0.08	1.62
NGC_2264	CS-34	12.96	0.51	9.225e+12	1.088e+13	15.21	13.64	3.83	0.43	0.61	0.22
NGC_2264	DNC	12.01	0.23	1.025e+12	5.486e+11	35.40	47.13	3.29	0.66	0.75	0.31
NGC_2264	H2CO	13.76	0.00	5.716e+13	4.675e+11	19.56	0.32	5.11	0.04	0.38	0.02
NGC_2264	H2CS	13.42	0.03	2.604e+13	1.769e+12	56.42	6.46	5.30	0.23	0.79	0.14
NGC_2264	HC-13-N	12.33	0.10	2.137e+12	4.901e+11	39.63	22.28	4.20	0.39	0.74	0.20
NGC_2264	HC-13-O+	12.51	0.19	3.199e+12	1.372e+12	61.63	45.61	3.38	0.14	0.78	0.06
NGC_2264	HCN	12.48	0.19	3.039e+12	1.303e+12	49.85	21.29	2.71	0.85	3.99	0.22
NGC_2264	HCN	12.91	0.02	8.140e+12	4.510e+11	47.92	5.87	3.14	0.13	-1.81	0.04
NGC_2264	HCN	12.97	0.04	9.233e+12	7.962e+11	32.27	17.98	28.92	3.20	1.75	0.75
NGC_2264	HCN-15	11.77	0.25	5.886e+11	3.380e+11	27.51	132.37	4.05	1.51	0.05	0.65
NGC_2264	HCO+	12.42	0.11	2.609e+12	6.312e+11	12.33	2.06	2.48	0.34	3.78	0.09
NGC_2264	HCO+	12.69	0.03	4.870e+12	3.196e+11	32.05	16.29	17.50	1.21	1.27	0.35
NGC_2264	HCO+	13.00	0.42	1.000e+13	9.645e+12	60.02	112.32	2.61	0.09	-1.25	0.01
NGC_2264	HCO-18+	11.60	0.18	3.952e+11	1.669e+11	33.57	27.73	3.29	1.07	1.64	0.56
NGC_2264	HCS+	12.34	0.15	2.186e+12	7.654e+11	51.47	19.45	4.61	1.35	1.31	0.82
NGC_2264	HDCO	12.89	0.05	7.675e+12	9.669e+11	44.81	8.38	4.39	0.20	0.18	0.13
NGC_2264	HNC-13	12.08	0.13	1.209e+12	3.526e+11	36.64	21.94	4.52	0.84	0.47	0.44
NGC_2264	N2D+	11.87	0.29	7.426e+11	5.001e+11	30.83	51.79	5.37	2.00	0.53	1.11
NGC_2264	NO	14.83	0.80	6.739e+14	1.246e+15	9.51	12.59	3.82	1.09	0.81	0.67
NGC_2264	SO	13.71	0.01	5.187e+13	1.156e+12	30.21	1.70	4.24	0.06	0.31	0.03
NGC_2264	SiO	12.34	0.05	2.184e+12	2.319e+11	38.23	26.22	7.00	0.79	-0.56	0.39
NGC_7538	C-13-S	12.88	102.54	7.499e+12	1.770e+15	93.03	34518.18	3.26	1.14	-0.09	0.23
NGC_7538	CCH	14.98	0.14	9.625e+14	3.162e+14	8.45	1.10	3.62	0.14	-0.41	0.06
NGC_7538	CH3CCH	15.21	0.19	1.617e+15	7.210e+14	14.37	1.58	3.12	0.39	-0.38	0.13
NGC_7538	CH3CN	12.89	0.08	7.755e+12	1.451e+12	244.44	42.66	3.95	0.51	-1.35	0.20
NGC_7538	CH3OH	14.38	0.01	2.417e+14	4.486e+12	24.30	0.87	3.09	0.06	-0.44	0.03
NGC_7538	CH3OH	14.59	0.04	3.864e+14	3.335e+13	256.81	20.51	3.26	0.19	-2.34	0.09
NGC_7538	CN	13.96	0.29	9.222e+13	6.239e+13	8.53	5.46	14.55	1.44	-0.27	0.42
NGC_7538	CN	14.51	0.05	3.263e+14	3.541e+13	5.28	0.24	2.71	0.19	-0.56	0.05
NGC_7538	CS	14.00	0.02	9.894e+13	3.960e+12	56.00	5.41	3.20	0.04	0.46	0.01
NGC_7538	CS	14.01	0.04	1.022e+14	1.053e+13	12.55	0.71	8.59	0.29	0.12	0.12
NGC_7538	CS-33	12.38	0.17	2.401e+12	9.489e+11	50.58	36.41	3.55	0.88	0.38	0.54
NGC_7538	CS-34	13.21	0.04	1.628e+13	1.648e+12	57.16	12.99	3.31	0.15	0.17	0.07
NGC_7538	DNC	11.41	1.28	2.560e+11	7.558e+11	22.52	11432.55	3.23	3.29	-0.90	1.29
NGC_7538	H2CCO	12.93	0.07	8.590e+12	1.443e+12	66.06	14.15	2.70	0.59	-1.06	0.22
NGC_7538	H2CO	13.91	1.70	8.086e+13	3.171e+14	86.34	300.99	11.64	2.37	-0.96	0.63
NGC_7538	H2CO	14.00	0.73	1.000e+14	1.687e+14	64.04	109.58	3.79	0.25	-0.52	0.05
NGC_7538	H2CS	13.54	0.02	3.444e+13	1.409e+12	47.77	4.05	3.72	0.15	-0.12	0.06
NGC_7538	HC-13-N	12.88	0.56	7.524e+12	9.731e+12	94.25	168.07	4.23	0.24	-0.26	0.10
NGC_7538	HC-13-O+	12.50	0.19	3.197e+12	1.403e+12	71.34	48.89	3.50	0.19	-0.38	0.08
NGC_7538	HCCCN	13.40	0.48	2.498e+13	2.756e+13	28.13	7.01	4.08	0.49	-0.68	0.27
NGC_7538	HCN	13.34	0.08	2.192e+13	3.866e+12	15.65	4.29	4.92	0.30	-0.55	0.04
NGC_7538	HCN	13.37	0.06	2.329e+13	3.306e+12	59.55	8.13	14.60	1.01	0.60	0.19
NGC_7538	HCN-15	12.07	198.89	1.173e+12	5.373e+14	29.09	93868.02	3.76	27.11	-0.37	0.40
NGC_7538	HNC-13	11.60	0.25	4.017e+11	2.349e+11	33.00	86.19	2.95	2.09	-1.21	0.81
NGC_7538	NS	12.49	0.59	3.071e+12	4.162e+12	25.35	54.80	2.39	3.22	-2.03	0.80
NGC_7538	SO	14.34	0.01	2.189e+14	7.362e+12	13.31	0.23	3.92	0.04	0.05	0.02
NGC_7538	SO2	13.51	0.04	3.262e+13	3.094e+12	60.25	11.34	4.51	0.34	-0.99	0.18
NGC_7538	SiO	11.74	0.51	5.530e+11	6.529e+11	51.77	219.03	3.47	3.60	-1.12	0.98
Orion-KL	C-13-H3OH	15.95	0.03	8.994e+15	6.768e+14	140.00	8.22	5.69	0.19	-0.64	0.11
Orion-KL	C-13-S	13.69	0.37	4.925e+13	4.236e+13	99.98	48.13	4.31	1.27	-0.25	0.50
Orion-KL	C-13-S	13.96	0.11	9.027e+13	2.238e+13	35.92	3.89	11.96	2.80	-0.31	0.87
Orion-KL	C-13-S-34	12.81	6.82	6.396e+12	1.004e+14	16.32	98.97	3.75	56.52	6.95	7.64
Orion-KL	C-13-S-34	13.50	0.28	3.162e+13	2.014e+13	54.76	64.58	8.69	8.57	-1.66	3.76
Orion-KL	C2H3CN	14.96	0.02	9.057e+14	4.269e+13	202.61	9.62	11.47	0.36	-4.04	0.24
Orion-KL	C2H5CN	15.11	0.03	1.281e+15	8.667e+13	236.70	14.88	7.06	0.27	-3.64	0.08
Orion-KL	C2H5CN	15.38	0.01	2.395e+15	7.348e+13	115.20	4.33	21.69	0.54	-5.47	0.23
Orion-KL	CH2NH	14.70	0.13	4.994e+14	1.454e+14	79.50	30.55	10.00	1.42	-0.96	0.64
Orion-KL	CH3CCH	15.54	0.05	3.438e+15	3.819e+14	95.53	15.41	4.35	0.51	0.37	0.26
Orion-KL	CH3CN	15.64	0.01	4.328e+15	9.292e+13	229.57	4.99	13.84	0.11	-1.82	0.06
Orion-KL	CH3COCH3	16.37	0.16	2.344e+16	8.465e+15	308.39	42.89	8.50	0.49	-1.39	0.34
Orion-KL	CH3OCH3	16.43	0.01	2.687e+16	8.063e+14	125.19	3.84	4.13	0.10	-0.80	0.05
Orion-KL	CH3OH	16.60	0.01	3.949e+16	9.852e+14	131.13	1.87	4.34	0.04	-0.25	0.02

Orion-KL	CH3OH	16.91	0.01	8.106e+16	1.545e+15	194.21	2.55	11.67	0.11	-1.81	0.07
Orion-KL	CN	14.19	0.07	1.556e+14	2.344e+13	15.20	3.11	3.29	0.41	0.22	0.19
Orion-KL	CN	15.00	0.02	1.009e+15	5.508e+13	61.63	1.02	35.06	1.79	-0.12	0.89
Orion-KL	CS	14.68	0.15	4.751e+14	1.614e+14	99.93	60.55	4.17	0.18	1.10	0.05
Orion-KL	CS	15.14	0.07	1.384e+15	2.194e+14	99.93	12.67	16.04	0.72	-1.12	0.19
Orion-KL	CS	15.24	0.03	1.749e+15	1.289e+14	35.92	3.70	30.65	1.12	0.59	0.29
Orion-KL	CS-33	13.88	0.21	7.533e+13	3.620e+13	40.16	1.11	14.19	4.83	-1.35	2.07
Orion-KL	CS-33	14.00	0.35	1.000e+14	8.153e+13	12.57	0.92	4.63	2.00	-0.14	0.44
Orion-KL	CS-34	14.17	0.10	1.493e+14	3.531e+13	70.52	30.11	4.44	0.33	0.07	0.12
Orion-KL	CS-34	14.46	0.06	2.903e+14	3.789e+13	68.61	12.96	17.73	1.08	-1.70	0.57
Orion-KL	H2CCO	14.80	0.08	6.318e+14	1.225e+14	138.42	34.00	5.84	0.53	-0.87	0.31
Orion-KL	H2CO	15.00	0.02	1.000e+15	5.112e+13	47.54	2.60	4.58	0.11	0.44	0.05
Orion-KL	H2CO	15.00	0.04	1.000e+15	8.651e+13	22.30	0.55	25.00	0.63	0.61	0.45
Orion-KL	H2CO	15.00	0.07	1.000e+15	1.523e+14	43.74	4.15	16.92	0.48	-1.80	0.34
Orion-KL	H2CS	15.12	0.02	1.332e+15	6.248e+13	95.30	5.45	5.27	0.12	-0.05	0.07
Orion-KL	HCCCN	14.12	8.42	1.320e+14	2.559e+15	481.60	11802.56	10.01	15.40	12.36	9.83
Orion-KL	HCCCN	14.33	0.70	2.117e+14	3.425e+14	55.18	19.76	4.84	3.14	0.21	0.68
Orion-KL	HCCCN	14.91	0.25	8.120e+14	4.754e+14	120.95	47.82	17.62	5.37	-4.18	4.59
Orion-KL	HCCCNv7	14.41	0.40	2.570e+14	2.381e+14	734.49	461.61	6.11	1.65	-3.70	0.36
Orion-KL	HCCCNv7	14.86	0.15	7.244e+14	2.581e+14	655.09	235.03	17.59	2.98	-3.30	0.49
Orion-KL	HCOOCH3	16.24	0.01	1.720e+16	4.662e+14	182.12	5.11	5.35	0.06	-0.83	0.03
Orion-KL	HDCO	14.25	0.19	1.763e+14	7.792e+13	16.31	6.31	4.21	0.51	0.13	0.24
Orion-KL	HDO	15.99	0.02	9.681e+15	3.794e+14	107.62	9.10	9.48	0.31	-2.45	0.16
Orion-KL	HNCO	15.37	0.02	2.327e+15	8.539e+13	40.70	1.83	10.00	0.23	-1.90	0.10
Orion-KL	NO	16.70	0.03	5.048e+16	3.320e+15	17.66	0.46	22.10	1.66	-1.14	0.78
Orion-KL	NO	16.79	0.14	6.098e+16	1.971e+16	7.30	0.69	5.27	0.70	-0.32	0.30
Orion-KL	OCS	15.26	0.16	1.839e+15	6.690e+14	99.98	53.58	7.95	2.12	-4.78	1.86
Orion-KL	OCS	15.54	0.11	3.487e+15	9.085e+14	99.98	23.12	5.00	0.46	-0.34	0.18
Orion-KL	OCS	15.91	0.06	8.168e+15	1.105e+15	99.98	40.10	21.87	1.58	-2.01	0.45
Orion-KL	S-33-O	15.44	0.04	2.745e+15	2.713e+14	100.00	11.63	40.00	4.47	4.22	1.36
Orion-KL	S-33-O2	14.66	27.24	4.524e+14	2.837e+16	126.62	362.35	10.01	87.81	8.00	187.02
Orion-KL	S-33-O2	15.13	8.88	1.337e+15	2.735e+16	100.18	352.43	16.00	251.32	-4.20	164.96
Orion-KL	S-34-O	15.99	0.03	9.818e+15	7.296e+14	112.00	13.95	24.11	0.36	0.13	0.17
Orion-KL	S-34-O2	14.95	0.17	8.945e+14	3.485e+14	39.57	9.78	8.82	2.06	-3.45	0.46
Orion-KL	S-34-O2	16.06	0.02	1.147e+16	5.830e+14	148.98	9.45	26.00	1.20	1.01	0.48
Orion-KL	SO	17.30	2.87	1.981e+17	1.308e+18	56.99	476.05	30.10	4.10	-0.97	2.26
Orion-KL	SO2	16.10	0.02	1.268e+16	4.830e+14	15.36	0.44	22.02	0.42	-0.01	0.21
Orion-KL	SO2	16.22	0.07	1.656e+16	2.729e+15	246.30	18.47	8.90	1.53	-2.55	0.25
Orion-KL	SO2	16.97	0.01	9.301e+16	2.823e+15	113.11	2.09	29.59	0.47	1.63	0.13
Orion-KL	t-HCOOH	14.73	0.08	5.327e+14	9.639e+13	39.14	9.66	6.55	0.93	-0.22	0.50
W3(H2O)	C-13-H3OH	14.20	0.12	1.578e+14	4.305e+13	116.96	7.66	6.14	1.30	-2.49	0.81
W3(H2O)	C-13-H3OH	14.27	0.10	1.851e+14	4.199e+13	100.80	5.48	4.54	0.43	2.54	0.30
W3(H2O)	C-13-S	12.75	0.47	5.586e+12	6.041e+12	40.83	6.61	12.69	8.05	-1.27	3.61
W3(H2O)	C-13-S	13.19	0.16	1.542e+13	5.674e+12	33.34	2.00	5.28	1.03	0.38	0.32
W3(H2O)	C-13-S-34	12.34	0.45	2.171e+12	2.265e+12	33.60	1279.52	10.28	12.80	0.53	4.99
W3(H2O)	C2H5CN	13.41	0.02	2.557e+13	9.655e+11	112.83	7.18	9.23	0.30	-0.11	0.18
W3(H2O)	CCH	14.86	0.14	7.294e+14	2.354e+14	15.34	5.89	5.14	0.22	-0.27	0.06
W3(H2O)	CH3CCH	14.84	0.01	6.875e+14	8.347e+12	80.78	2.28	5.13	0.07	0.68	0.04
W3(H2O)	CH3CN	13.70	0.01	4.977e+13	1.031e+12	152.50	3.71	8.56	0.14	0.31	0.06
W3(H2O)	CH3OCH3	14.55	0.05	3.517e+14	3.975e+13	22.51	3.18	8.64	0.68	0.50	0.48
W3(H2O)	CH3OCH3	14.83	0.24	6.794e+14	3.740e+14	156.50	13.92	5.36	1.54	-3.24	1.34
W3(H2O)	CH3OCH3	14.99	0.16	9.840e+14	3.681e+14	108.32	13.41	5.77	0.87	1.73	0.84
W3(H2O)	CH3OH	14.96	0.00	9.071e+14	6.042e+12	16.74	0.12	4.36	0.03	0.65	0.01
W3(H2O)	CH3OH	15.24	0.01	1.745e+15	4.619e+13	151.50	1.72	4.09	0.05	2.20	0.02
W3(H2O)	CH3OH	15.44	0.01	2.784e+15	4.855e+13	149.92	1.29	9.66	0.08	0.12	0.05
W3(H2O)	CN	14.60	0.03	4.026e+14	2.751e+13	6.19	0.12	4.80	0.13	-1.33	0.07
W3(H2O)	CS	13.70	0.14	5.025e+13	1.613e+13	34.11	2.21	3.27	0.37	-1.82	0.16
W3(H2O)	CS	13.97	0.10	9.369e+13	2.232e+13	99.93	5.75	4.46	0.42	1.56	0.26
W3(H2O)	CS	13.97	0.16	9.306e+13	3.426e+13	19.78	0.39	8.54	0.77	-0.58	0.48
W3(H2O)	CS-33	12.55	1.27	3.515e+12	1.025e+13	67.90	249.81	3.51	2.30	0.94	0.85
W3(H2O)	CS-33	13.09	0.18	1.226e+13	4.955e+12	35.96	1.80	7.31	1.49	-0.09	0.83
W3(H2O)	CS-34	13.91	14.55	8.212e+13	2.752e+15	14.27	296.93	5.72	7.07	0.39	0.18
W3(H2O)	DNC	11.84	0.63	6.849e+11	9.930e+11	15.10	36.08	4.95	4.64	0.42	1.46
W3(H2O)	H2CCO	13.57	0.02	3.734e+13	1.943e+12	83.08	8.60	6.85	0.37	1.02	0.17
W3(H2O)	H2CO	13.25	0.32	1.774e+13	1.327e+13	22.23	1.01	3.61	1.24	2.34	0.70
W3(H2O)	H2CO	14.00	0.38	1.000e+14	8.830e+13	89.24	107.66	3.75	0.98	-1.44	0.36
W3(H2O)	H2CO	14.00	0.46	1.000e+14	1.071e+14	83.62	134.23	9.24	2.95	-0.18	0.68
W3(H2O)	H2CS	14.20	0.01	1.592e+14	1.981e+12	71.79	1.20	5.49	0.05	0.42	0.02
W3(H2O)	HC-13-N	13.17	0.05	1.473e+13	1.534e+12	46.74	10.45	6.74	0.21	0.48	0.10
W3(H2O)	HC-13-O+	12.73	138.99	5.425e+12	1.736e+15	13.59	4339.87	4.97	68.77	-0.22	0.43
W3(H2O)	HCCCN	13.06	0.01	1.160e+13	2.048e+11	178.68	23.23	6.90	0.11	0.14	0.06
W3(H2O)	HCCCNv7	12.72	0.20	5.225e+12	2.427e+12	82.87	37.12	8.33	1.39	0.95	0.45
W3(H2O)	HCN-15	12.88	0.82	7.530e+12	1.430e+13	92.58	240.61	6.18	0.60	0.47	0.27
W3(H2O)	HCO-18+	11.77	0.57	5.922e+11	7.761e+11	18.21	57.09	4.93	2.98	1.48	1.12
W3(H2O)	HCOOCH3	14.62	0.05	4.181e+14	4.501e+13	162.53	6.24	4.78	0.20	2.46	0.16
W3(H2O)	HCOOCH3	14.70	0.04	5.002e+14	4.681e+13	239.20	12.76	6.16	0.41	-2.68	0.34
W3(H2O)	HCS+	12.27	8.19	1.856e+12	3.499e+13	24.05	1945.34	2.89	93.04	-2.69	34.02
W3(H2O)	HCS+	13.15	2.26	1.406e+13	7.316e+13	50.58	220.32	4.35	14.88	0.98	9.93
W3(H2O)	HDCO	12.91	0.04	8.139e+12	7.173e+11	38.87	5.29	5.88	0.38	0.76	0.16
W3(H2O)	HDCS	12.95	0.25	8.902e+12	5.143e+12	47.27	61.58	4.26	2.54	1.21	1.29
W3(H2O)	HNC-13	12.03	0.72	1.071e+12	1.767e+12	21.28	195.32	5.00	1.92	-0.23	0.88
W3(H2O)	HNCO	13.65	0.11	4.438e+13	1.074e+13	36.58	9.70	8.00	1.21	1.00	0.55
W3(H2O)	NO	15.12	0.53	1.304e+15	1.602e+15	16.17	57.54	6.05	1.58	-0.30	0.67
W3(H2O)	NS	13.57	0.17	3.692e+13	1.441e+13	100.00	52.17	6.13	0.72	0.89	0.32
W3(H2O)	OCS	14.55	0.01	3.563e+14	6.335e+12	131.95	21.50	7.42	0.12	0.38	0.05
W3(H2O)	S-33-O	14.07	1.91	1.185e+14	5.200e+14	9.58	11.15	7.49	4.10	0.35	1.64
W3(H2O)	S-34-O	13.66	0.04	4.591e+13	4.240e+12	41.99	36.42	6.88	0.66	-0.27	0.31
W3(H2O)	SO	14.74	0.00	5.551e+14	5.133e+12	65.19	1.97	6.29	0.01	0.02	0.01
W3(H2O)	SO+	13.33	0.39	2.141e+13	1.932e+13	61.32	143.10	4.81	2.13	0.60	0.81
W3(H2O)	SO2	13.82	0.12	6.659e+13	1.900e+13	70.09	17.18	3.58	0.63	-0.74	0.10
W3(H2O)	SO2	13.97	0.04	9.320e+13	9.525e+12	16.52	1.98	6.52	0.28	0.24	0.28
W3(H2O)	SO2	14.67	0.01	4.688e+14	1.497e+13	148.08	6.17	8.90	0.23	0.03	0.13

W3(H2O)	SiO	13.01	0.04	1.021e+13	1.001e+12	65.53	13.51	7.60	0.46	-0.23	0.24
W51	C-13-H3OH	14.55	0.02	3.553e+14	1.710e+13	159.39	5.93	9.93	0.41	1.47	0.22
W51	C-13-S	13.24	0.08	1.729e+13	3.028e+12	47.52	25.41	8.98	0.68	1.98	0.32
W51	C-13-S-34	12.30	0.80	2.011e+12	3.716e+12	37.47	447.01	8.22	8.94	3.86	4.01
W51	CCH	14.05	1.51	1.134e+14	3.949e+14	16.61	105.82	4.61	1.61	3.73	0.24
W51	CCH	14.30	3.92	2.017e+14	1.822e+15	18.87	440.39	13.68	3.32	4.28	0.53
W51	CH2NH	13.22	0.07	1.653e+13	2.529e+12	53.44	10.88	9.00	1.19	3.88	0.56
W51	CH3CCH	14.68	0.01	4.766e+14	1.094e+13	62.45	2.72	7.45	0.27	3.49	0.11
W51	CH3CN	13.45	0.03	2.841e+13	1.660e+12	226.37	12.53	9.51	0.33	1.85	0.15
W51	CH3OCH3	15.11	0.02	1.282e+15	4.792e+13	146.32	5.20	8.99	0.29	0.98	0.16
W51	CH3OH	14.87	0.00	7.393e+14	6.368e+12	22.88	0.26	7.75	0.07	2.18	0.03
W51	CH3OH	15.33	0.01	2.162e+15	4.124e+13	257.17	4.02	9.32	0.13	1.99	0.06
W51	CN	14.93	0.04	8.500e+14	8.097e+13	3.83	0.06	6.04	0.28	2.76	0.14
W51	CS	13.13	0.41	1.358e+13	1.283e+13	35.67	0.34	5.56	3.04	-2.33	1.35
W51	CS	13.60	0.12	4.013e+13	1.068e+13	35.89	0.07	17.10	2.06	2.99	1.17
W51	CS	14.00	0.10	1.000e+14	2.385e+13	13.35	0.64	6.40	0.77	4.01	0.58
W51	CS-33	11.83	0.85	6.792e+11	1.336e+12	39.09	111.19	2.78	3.67	3.96	1.40
W51	CS-33	13.00	9.93	9.973e+12	2.280e+14	14.44	227.30	10.02	2.29	2.02	1.44
W51	CS-34	12.61	6.07	4.067e+12	5.684e+13	31.81	65.50	5.04	25.28	4.11	3.57
W51	CS-34	13.34	2.91	2.207e+13	1.477e+14	15.63	34.06	9.09	7.80	2.38	7.68
W51	H2CCO	13.70	0.03	4.959e+13	3.730e+12	91.42	11.16	11.02	0.61	2.14	0.33
W51	H2CO	13.10	0.16	1.263e+13	4.771e+12	22.44	1.40	4.80	0.94	4.47	0.30
W51	H2CO	14.06	0.12	1.143e+14	3.108e+13	63.38	18.15	11.42	0.49	1.90	0.36
W51	H2CS	14.08	0.01	1.192e+14	3.406e+12	87.74	3.02	8.27	0.14	2.26	0.07
W51	HC-13-N	12.64	0.16	4.336e+12	1.645e+12	39.01	41.80	10.04	0.87	3.03	0.40
W51	HCCCN	13.51	0.08	3.270e+13	5.807e+12	44.53	3.05	11.38	0.32	3.46	0.18
W51	HCN	12.83	0.19	6.762e+12	2.947e+12	25.66	1.33	6.95	0.86	-4.16	0.85
W51	HCN	12.90	0.10	7.986e+12	1.875e+12	20.00	0.74	35.00	9.81	-1.34	3.38
W51	HCN	13.28	0.18	1.894e+13	7.708e+12	99.88	1.26	8.77	2.02	1.90	1.03
W51	HCN-15	12.15	0.15	1.409e+12	4.881e+11	35.75	33.59	8.70	1.97	2.99	0.94
W51	HCOOCH3	15.32	0.03	2.067e+15	1.269e+14	472.55	23.66	10.79	0.16	1.47	0.10
W51	HCS+	12.00	5.96	1.007e+12	1.382e+13	22.41	345.86	2.87	4.77	2.23	1.27
W51	HCS+	12.50	0.28	3.151e+12	2.051e+12	37.46	45.39	12.10	5.43	2.68	2.76
W51	HNC-13	11.86	0.27	7.167e+11	4.426e+11	33.42	48.95	7.61	3.13	1.98	1.75
W51	HNCO	13.52	0.02	3.294e+13	1.885e+12	45.94	4.27	10.00	1.07	4.00	0.24
W51	NO	15.40	0.32	2.510e+15	1.866e+15	100.00	79.84	9.84	2.37	2.10	1.18
W51	NS	13.32	0.11	2.067e+13	5.322e+12	100.00	35.46	9.28	1.28	2.97	0.66
W51	OCS	15.21	0.10	1.621e+15	3.876e+14	26.77	1.86	9.20	0.28	2.01	0.14
W51	S-34-O	13.23	0.11	1.679e+13	4.439e+12	40.15	78.13	9.91	2.54	3.19	1.21
W51	SO	14.52	0.04	3.330e+14	3.413e+13	14.41	0.67	9.54	0.10	2.76	0.05
W51	SO2	14.44	0.02	2.752e+14	1.182e+13	192.76	7.77	10.32	0.31	3.30	0.15
W51	SiO	12.50	0.96	3.162e+12	6.959e+12	21.85	61.74	8.74	5.97	3.85	1.79
W51	SiO	12.57	0.19	3.743e+12	1.678e+12	37.75	16.32	30.35	40.26	0.05	4.19
W75N	C-13-S	13.12	0.19	1.310e+13	5.601e+12	52.03	50.44	5.13	0.94	0.39	0.51
W75N	CCH	14.88	0.26	7.633e+14	4.647e+14	13.20	6.83	4.54	0.33	-0.35	0.11
W75N	CH3CCH	14.88	0.02	7.541e+14	2.718e+13	54.00	2.63	4.66	0.14	-0.10	0.09
W75N	CH3CN	13.73	0.02	5.426e+13	2.066e+12	169.26	7.14	8.06	0.20	0.04	0.10
W75N	CH3OH	15.17	0.00	1.494e+15	1.116e+13	19.18	0.19	4.18	0.03	-0.27	0.01
W75N	CH3OH	15.50	0.01	3.187e+15	4.742e+13	206.76	2.89	8.24	0.08	-0.66	0.04
W75N	CN	14.80	0.03	6.329e+14	4.963e+13	6.77	0.15	4.73	0.14	0.59	0.10
W75N	CS	13.92	0.04	8.316e+13	8.254e+12	38.54	0.66	10.72	0.63	0.42	0.21
W75N	CS	14.36	0.02	2.303e+14	9.157e+12	39.74	4.81	4.32	0.10	0.25	0.02
W75N	CS-33	12.98	2.77	9.572e+12	6.107e+13	14.49	63.38	5.17	2.22	0.08	1.05
W75N	CS-34	13.46	0.08	2.879e+13	5.628e+12	60.31	24.51	4.61	0.39	0.16	0.19
W75N	DNC	12.23	0.22	1.700e+12	8.553e+11	27.78	46.99	4.15	1.62	-0.24	0.76
W75N	H2CCO	13.84	0.03	6.941e+13	4.269e+12	80.03	8.69	10.21	0.46	-0.18	0.32
W75N	H2CO	13.86	0.14	7.299e+13	2.292e+13	23.86	1.59	8.91	0.94	0.13	0.58
W75N	H2CO	14.14	0.08	1.382e+14	2.502e+13	20.78	3.58	4.41	0.30	0.95	0.09
W75N	H2CS	14.09	0.01	1.217e+14	3.292e+12	65.88	2.61	4.78	0.08	-0.32	0.04
W75N	HC-13-N	13.26	0.06	1.811e+13	2.705e+12	59.59	14.54	5.71	0.27	-0.09	0.14
W75N	HC-13-O+	13.16	0.09	1.451e+13	2.886e+12	58.52	21.76	4.32	0.14	-0.18	0.06
W75N	HCCCN	13.36	0.06	2.276e+13	3.370e+12	66.76	6.77	7.57	0.20	0.13	0.11
W75N	HCN	13.27	0.83	1.873e+13	3.599e+13	13.48	27.93	3.23	2.15	-3.71	0.21
W75N	HCN	13.46	0.16	2.907e+13	1.058e+13	41.26	13.30	3.32	0.33	2.21	0.08
W75N	HCN	13.86	1.83	7.267e+13	3.065e+14	99.70	524.34	14.22	2.72	-0.15	0.74
W75N	HCN-15	12.89	0.18	7.778e+12	3.225e+12	100.00	45.11	5.78	0.75	0.03	0.46
W75N	HCO-18+	12.28	0.24	1.920e+12	1.075e+12	45.08	42.23	5.46	1.41	1.00	0.82
W75N	HCS+	12.52	0.84	3.296e+12	6.375e+12	27.58	84.59	4.12	5.10	-0.35	1.66
W75N	HDCO	13.13	4.07	1.341e+13	1.258e+14	50.00	750.66	8.06	6.18	-0.36	2.89
W75N	HDO	14.31	0.20	2.052e+14	9.379e+13	100.00	112.79	8.24	3.68	0.45	2.09
W75N	HNC-13	12.50	2.15	3.149e+12	1.555e+13	73.14	550.39	4.02	1.49	-0.81	0.61
W75N	HNCO	13.91	0.05	8.174e+13	9.718e+12	49.56	9.32	8.00	1.60	1.32	0.57
W75N	NO	15.74	0.31	5.504e+15	3.895e+15	100.00	73.82	6.18	1.35	0.30	0.78
W75N	NS	13.24	0.27	1.743e+13	1.064e+13	100.00	84.57	6.13	2.22	-0.29	1.24
W75N	OCS	14.54	0.10	3.498e+14	7.822e+13	60.26	12.99	7.43	0.27	-0.23	0.15
W75N	S-33-O	13.27	1.04	1.882e+13	4.528e+13	69.73	431.56	7.05	4.18	-0.20	2.11
W75N	S-34-O	13.68	0.12	4.808e+13	1.358e+13	36.95	50.36	6.48	0.99	0.43	0.53
W75N	SO	14.68	0.01	4.781e+14	1.035e+13	32.84	1.61	5.47	0.02	0.24	0.01
W75N	SO2	14.85	0.01	7.087e+14	1.033e+13	112.93	1.70	7.39	0.07	0.63	0.04
W75N	SiO	13.03	0.10	1.067e+13	2.421e+12	81.31	28.97	7.74	0.85	0.55	0.49

Bibliography

1. Oró, J. Mechanism of Synthesis of Adenine from Hydrogen Cyanide under Possible Primitive Earth Conditions. *Nature* **191,** 1193–1194 (09/1961).
2. Chyba, C., Thomas, P., Brookshaw, L. & Sagan, C. Cometary delivery of organic molecules to the early Earth. *Science* **249,** 366–373. ISSN: 0036-8075 (1990).
3. Raymond, S. N., Quinn, T. & Lunine, J. I. Making other earths: dynamical simulations of terrestrial planet formation and water delivery. *Icarus* **168,** 1–17. ISSN: 0019-1035 (2004).
4. Indriolo, N. & McCall, B. J. Investigating the cosmic-ray ionization rate in the galactic diffuse interstellar medium through observations of H_3^+. *Astrophys. J.* **745,** 91 (2012).
5. Ferrière, K. M. The interstellar environment of our galaxy. *Rev. Mod. Phys.* **73,** 1031–1066 (2001).
6. Bergin, E. A. & Tafalla, M. Cold dark clouds: the initial conditions for star formation. *Annu. Rev. Astron. Astrophys.* **45,** 339–396 (2007).
7. Ceccarelli, C. *The hot corinos of solar type protostars* in *Star Formation in the Interstellar Medium: In Honor of David Hollenbach* (eds Johnstone, D., Adams, F. C., Lin, D. N. C., Neufeeld, D. A. & Ostriker, E. C.) **323** (2004), 195.
8. Kurtz, S., Cesaroni, R., Churchwell, E., Hofner, P. & Walmsley, C. M. Hot Molecular Cores and the Earliest Phases of High-Mass Star Formation. *Protostars and Planets IV,* 299–326 (05/2000).
9. Herbst, E. & van Dishoeck, E. F. Complex organic interstellar molecules. *Annu. Rev. Astron. Astrophys.* **47,** 427–480 (2009).
10. Horn, A. *et al.* The gas-phase formation of methyl formate in hot molecular cores. *Astrophys. J.* **611,** 605–614 (2004).
11. Smith, I. W. Laboratory astrochemistry: gas-phase processes. *Annu. Rev. Astron. Astrophys.* **49,** 29–66 (2011).
12. Garrod, R., Wakelam, V. & Herbst, E. Non-thermal desorption from interstellar dust grains via exothermic surface reactions. *Astron. Astrophys.* **467,** 1103–1115 (2007).
13. Garrod, R. T. & Widicus Weaver, S. L. Simulations of hot-core chemistry. *Chem. Rev.* **113,** 8939–8960 (2013).
14. Garrod, R., Park, I. H., Caselli, P. & Herbst, E. Are gas-phase models of interstellar chemistry tenable? The case of methanol. *Faraday Discuss.* **133,** 51–62 (2006).

15. Garrod, R. T., Weaver, S. L. W. & Herbst, E. Complex chemistry in star-forming regions: an expanded gas-grain warm-up chemical model. *Astrophys. J.* **682,** 283–302 (2008).

16. Laas, J. C., Garrod, R. T., Herbst, E. & Widicus Weaver, S. L. Contributions from grain surface and gas phase chemistry to the formation of methyl formate and its structural isomers. *Astrophys. J.* **728,** 71–79 (2011).

17. Cernicharo, J. *et al.* Discovery of the methoxy radical, CH_3O, toward B1: dust grain and gas-phase chemistry in cold dark clouds. *Astrophys. J. Lett.* **759,** L43 (2012).

18. Bacmann, A. & Faure, A. The origin of gas-phase HCO and CH_3O radicals in prestellar cores. *Astron. Astrophys.* **587,** A130 (2016).

19. Oesterling, L. C., Albert, S., Lucia, F. C. D., Sastry, K. V. L. N. & Herbst, E. The millimeter- and submillimeter-wave spectrum of methyl formate. *Astrophys. J.* **521,** 255 (1999).

20. Medvedev, I. *et al.* The millimeter- and submillimeter-wave spectrum of the trans–gauche conformer of diethyl ether. *J. Mol. Spectrosc.* **228,** 314–328 (2004).

21. Carroll, P. B., Drouin, B. J. & Weaver, S. L. W. The submillimeter spectrum of glycolaldehyde. *Astrophys. J.* **723,** 845 (2010).

22. Mesko, A., Zou, L., Carroll, P. B. & Widicus Weaver, S. L. Millimeter and submillimeter spectrum of propylene oxide. *J. Mol. Spectrosc.* (2017).

23. McCarthy, M. C., Chen, W., Travers, M. J. & Thaddeus, P. Microwave spectra of 11 polyyne carbon chains. *Astrophys. J. Suppl. Ser.* **129,** 611–623 (2000).

24. Grabow, J.-U., Palmer, E. S., McCarthy, M. C. & Thaddeus, P. Supersonic-jet cryogenic-resonator coaxially oriented beam-resonator arrangement Fourier transform microwave spectrometer. *Rev. Sci. Instrum.* **76,** 093106/1–11 (2005).

25. Kaur, D. *et al.* Multipass cell for molecular beam absorption spectroscopy. *Appl. Opt.* **29,** 119–124 (1990).

26. Laas, J. C., Hays, B. M. & Widicus Weaver, S. L. Multipass millimeter-submillimeter spectrometer to probe dissociative reaction dynamics. *J. Phys. Chem. A* **117,** 9548–9554 (2013).

27. Zou, L., Hays, B. M. & Widicus Weaver, S. L. Weakly bound clusters in astrochemistry? Millimeter and submillimeter spectroscopy of trans-HO_3 and comparison to astronomical observations. *J. Phys. Chem. A* **120,** 657–667 (2016).

28. Brown, G. G. *et al.* A broadband Fourier transform microwave spectrometer based on chirped pulse excitation. *Rev. Sci. Instrum.* **79.** doi:`http://dx.doi.org/10.1063/1.2919120` (2008).

29. Petkie, D. T. *et al.* A fast scan submillimeter spectroscopic technique. *Rev. Sci. Instrum.* **68,** 1675–1683 (1997).

30. Melnik, D. G., Gopalakrishnan, S., Miller, T. A., De Lucia, F. C. & Belov, S. Submillimeter wave vibration–rotation spectroscopy of Ar·CO and Ar·ND_3. *J. Chem. Phys.* **114,** 6100–6106 (2001).

31. Park, G. B., Steeves, A. H., Kuyanov-Prozument, K., Neill, J. L. & Field, R. W. Design and evaluation of a pulsed-jet chirped-pulse millimeter-wave spectrometer for the 70–102 GHz region. *J. Chem. Phys.* **135,** 024202/1–10 (2011).

32. Hays, B. M. *Rotational spectroscopy of O(^1D) insertion products* PhD thesis (Emory University, 2015).

33. Goldsmith, P. F. & Langer, W. D. Population diagram analysis of molecular line emission. *Astrophys. J.* **517,** 209 (1999).

34. Pickett, H. M. *et al.* Submillimeter, millimeter, and microwave spectral line catalog. *J. Quant. Spectrosc. Radiative Trans.* **60,** 883–890 (1998).

35. Agilent Technologies. *Agilent E8257D PSG microwave analog signal generator data sheet* (01/06/2012), 21.

36. QMC Instruments Ltd. *Magnetically enhanced indium antimonide (InSb) hot-electron bolometer models QFI/XBI and QFI/XB* (2011).

37. Goldsmith, P. F. *et al.* Herschel measurements of molecular oxygen in Orion. *Astrophys. J.* **737,** 96 (2011).

38. Liseau, R. *et al.* Multi-line detection of O_2 toward ρ Ophiuchi A. *Astron. Astrophys.* **541,** A73 (2012).

39. Melnick, G. J. *et al.* Herschel search for O_2 toward the Orion Bar. *Astrophys. J.* **752,** 26 (2012).

40. Chen, J.-H. *et al.* Herschel HIFI observations of O_2 toward Orion: special conditions for shock enhanced emission. *Astrophys. J.* **793,** 111 (2014).

41. Wirström, E. S., Charnley, S. B., Cordiner, M. A. & Ceccarelli, C. A search for O_2 in CO-depleted molecular cloud cores with Herschel. *Astrophys. J.* **830,** 102 (2016).

42. Wilson, T. L. & Rood, R. Abundances in the interstellar medium. *Annu. Rev. Astron. Astrophys.* **32,** 191–226 (1994).

43. Whittet, D. C. B. Oxygen depletion in the interstellar medium: implications for grain models and the distribution of elemental oxygen. *Astrophys. J.* **710,** 1009 (2010).

44. Klemperer, W. & Vaida, V. Molecular complexes in close and far away. *Proc. Nat. Acad. Sci.* **103,** 10584–10588 (2006).

45. Cooper, P. D., Moore, M. H. & Hudson, R. L. Infrared detection of HO_2 and HO_3 radicals in water ice. *J. Phys. Chem. A* **110,** 7985–7988 (2006).

46. Zheng, W., Jewitt, D. & Kaiser, R. I. Mechanistical studies on the formation of isotopomers of hydrogen peroxide (HOOH), hydrotrioxy (HOOO), and dihydrogentrioxide (HOOOH) in electron-irradiated $H_2^{18}O/O_2$ ice mixtures. *Phys. Chem. Chem. Phys.* **9,** 2556–2563 (2007).

47. Le Picard, S. D., Tizniti, M., Canosa, A., Sims, I. R. & Smith, I. W. M. The thermodynamics of the elusive HO_3 radical. *Science* **328,** 1258–1262 (2010).

48. Suma, K., Sumiyoshi, Y. & Endo, Y. Force-field calculation and geometry of the HOOO radical. *J. Chem. Phys.* **139,** 094301/1–8 (2013).

49. Varandas, A. J. C. Ab Initio treatment of bond-breaking reactions: Accurate course of HO_3 dissociation and revisit to isomerization. *J. Chem. Theory Comput.* **8,** 428–441 (2012).

50. Suma, K., Sumiyoshi, Y. & Endo, Y. The rotational spectrum and structure of the HOOO radical. *Science* **308,** 1885–1886 (2005).

51. Murray, C., Derro, E. L., Sechler, T. D. & Lester, M. I. Weakly bound molecules in the atmosphere: a case study of HOOO. *Acc. Chem. Res.* **42,** 419–427 (2009).

52. Speranza, M. Structure, stability, and reactivity of cationic hydrogen trioxides and thermochemistry of their neutral analogs. A Fourier-transform ion cyclotron resonance study. *Inorg. Chem.* **35,** 6140–6151 (1996).

53. Speranza, M. Stable vs metastable HOOO. An experimental solution for an evergreen theoretical dilemma. *J. Phys. Chem. A* **102,** 7535–7536 (1998).

54. Derro, E. L., Sechler, T. D., Murray, C. & Lester, M. I. Observation of $\nu_1+\nu_n$ combination bands of the HOOO and DOOO radicals using infrared action spectroscopy. *J. Chem. Phys.* **128,** 244313/1–9 (2008).

55. Cacace, F., de Petris, G., Pepi, F. & Troiani, A. Experimental detection of hydrogen trioxide. *Science* **285,** 81–82 (1999).

56. Nelander, B., Engdahl, A. & Svensson, T. The HOOO radical. A matrix isolation study. *Chem. Phys. Lett.* **332,** 403–408 (2000).

57. Derro, E. L., Murray, C., Sechler, T. D. & Lester, M. I. Infrared action spectroscopy and dissociation dynamics of the HOOO radical. *J. Phys. Chem. A* **111,** 11592–11601 (2007).

58. Murray, C., Derro, E. L., Sechler, T. D. & Lester, M. I. Stability of the hydrogen trioxy tadical via infrared action spectroscopy. *J. Phys. Chem. A* **111,** 4727–4730 (2007).

59. Derro, E. L., Sechler, T. D., Murray, C. & Lester, M. I. Infrared action spectroscopy of the OD stretch fundamental and overtone transitions of the DOOO radical. *J. Phys. Chem. A* **112,** 9269–9276 (2008).

60. McCarthy, M. C., Lattanzi, V., Kokkin, D., Oscar Martinez, J. & Stanton, J. F. On the molecular structure of HOOO. *J. Chem. Phys.* **136,** 034303/1–10 (2012).

61. Liang, T., Magers, D. B., Raston, P. L., Allen, W. D. & Douberly, G. E. Dipole moment of the HOOO radical: resolution of a structural enigma. *J. Phys. Chem. Lett.* **4,** 3584–3589 (2013).

62. Raston, P. L., Liang, T. & Douberly, G. E. Infrared spectroscopy of HOOO and DOOO in ^4He nanodroplets. *J. Chem. Phys.* **137,** 184302/1–7 (2012).

63. Varandas, A. J. C. & Yu, H. G. Double many-body expansion potential energy surface for ground-state HO_3. *Mol. Phys.* **91,** 301–318 (1997).
64. Denis, P. A., Kieninger, M., Ventura, O. N., Cachau, R. E. & Diercksen, G. H. Complete basis set and density functional determination of the enthalpy of formation of the controversial HO_3 radical: a discrepancy between theory and experiment. *Chem. Phys. Lett.* **365,** 440–449 (2002).
65. Mansergas, A., Anglada, J. M., Olivella, S., Ruiz-Lopez, M. F. & Martins-Costa, M. On the nature of the unusually long OO bond in HO_3 and HO_4 radicals. *Phys. Chem. Chem. Phys.* **9,** 5865–5873 (2007).
66. Braams, B. J. & Yu, H.-G. Potential energy surface and quantum dynamics study of rovibrational states for HO_3 (X^2A''). *Phys. Chem. Chem. Phys.* **10,** 3150–3155 (2008).
67. Varner, M. E., Harding, M. E., Gauss, J. & Stanton, J. F. On the geometry of the HO_3 radical. *Chem. Phys.* **346,** 53–55 (2008).
68. Denis, P. A. & Ornellas, F. R. Theoretical characterization of hydrogen polyoxides: HOOH, HOOOH, HOOOOH, and HOOO. *J. Phys. Chem. A* **113,** 499–506 (2009).
69. Varner, M. E., Harding, M. E., Vázquez, J., Gauss, J. & Stanton, J. F. Dissociation energy of the HOOO radical. *J. Phys. Chem. A* **113,** 11238–11241 (2009).
70. Anglada, J. M., Olivella, S. & Solé, A. On the dissociation of ground state trans-HOOO radical: a theoretical study. *J. Chem. Theory Comput.* **6,** 2743–2750 (2010).
71. Beames, J. M., Lester, M. I., Murray, C., Varner, M. E. & Stanton, J. F. Analysis of the HOOO torsional potential. *J. Chem. Phys.* **134,** 044304/1–9 (2011).
72. Varandas, A. J. C. Is HO_3 minimum cis or trans? An analytic full-dimensional ab initio isomerization path. *Phys. Chem. Chem. Phys.* **13,** 9796–9811 (2011).
73. Varandas, A. J. C. On the stability of the elusive HO_3 radical. *Phys. Chem. Chem. Phys.* **13,** 15619–15623 (2011).
74. Hoy, E. P., Schwerdtfeger, C. A. & Mazziotti, D. A. Relative energies and geometries of the cis- and trans-HO_3 radicals from the parametric 2-electron density matrix method. *J. Phys. Chem. A* **117,** 1817–1825 (2013).
75. Pickett, H. M. The fitting and prediction of vibration-rotation spectra with spin interactions. *J. Mol. Spectrosc.* **148,** 371–377 (1991).
76. Sears, T. J., Radford, H. E. & Moore, M. A. b–dipole transitions in trans-HOCO observed by far infrared laser magnetic resonance. *J. Chem. Phys.* **98,** 6624–6631 (1993).
77. Cohen, R. C. *et al.* Tunable far infrared laser spectroscopy of van der Waals bonds: vibration–rotation–tunneling spectra of Ar–H_2O. *J. Chem. Phys.* **89,** 4494–4504 (1988).

78. Cohen, R. C., Busarow, K. L., Lee, Y. T. & Saykally, R. J. Tunable far infrared laser spectroscopy of van der Waals bonds: the intermolecular stretching vibration and effective radial potentials for Ar–H_2O. *J. Chem. Phys.* **92,** 169–177 (1990).

79. Cohen, R. C. & Saykally, R. J. Multidimensional intermolecular dynamics from tunable far-infrared laser spectroscopy: angular-radial coupling in the intermolecular potential of Argon–H_2O. *J. Chem. Phys.* **95,** 7891–7906 (1991).

80. Fraser, G., Lovas, F., Suenram, R. & Matsumura, K. Microwave spectrum of Ar–H_2O: Dipole moment, isotopic studies, and ^{17}O quadrupole coupling constants. *J. Mol. Spectrosc.* **144,** 97–112 (1990).

81. Germann, T. C. & Gutowsky, H. S. Nuclear hyperfine interactions and dynamic state of H_2O in Ar–H_2O. *J. Chem. Phys.* **98,** 5235–5238 (1993).

82. Buckingham, A. D., Fowler, P. W. & Hutson, J. M. Theoretical studies of van der Waals molecules and intermolecular forces. *Chem. Rev.* **88,** 963–988 (1988).

83. Hutson, J. M. Intermolecular forces from the spectroscopy of van der Waals molecules. *Annu. Rev. Phys. Chem.* **41,** 123–154 (1990).

84. Nesbitt, D. J. & Lascola, R. Vibration, rotation, and parity specific predissociation dynamics in asymmetric OH stretch excited Ar–H_2O: A half collision study of resonant V–V energy transfer in a weakly bound complex. *J. Chem. Phys.* **97,** 8096–8110 (1992).

85. Kuma, S., Slipchenko, M. N., Momose, T. & Vilesov, A. F. Infrared spectra and intensities of Ar–H_2O and O_2–H_2O complexes in the range of the ν_3 band of H_2O. *J. Phys. Chem. A* **114,** 9022–9027 (2010).

86. Weida, M. J. & Nesbitt, D. J. High resolution mid-infrared spectroscopy of Ar–H_2O: The ν_2 bend region of H_2O. *J. Chem. Phys.* **106,** 3078–3089 (1997).

87. Verdes, D. & Linnartz, H. Depletion modulation of Ar–H_2O in a supersonic planar plasma. *Chem. Phys. Lett.* **355,** 538–542 (2002).

88. Liu, X. & Xu, Y. New rovibrational bands of the Ar$-$$H_2O$ complex at the ν_2 bend region of H_2O. *J. Mol. Spectrosc.* **301,** 1–8 (2014).

89. Hutson, J. M. Atom–asymmetric top van der Waals complexes: Angular momentum coupling in Ar–H_2O. *J. Chem. Phys.* **92,** 157–168 (1990).

90. Zwart, E. & Meerts, W. The submillimeter rotation-tunneling spectrum of Ar–D_2O and Ar–NH_3. *Chem. Phys.* **151,** 407–418 (1991).

91. Didriche, K. & Földes, T. High resolution spectroscopy of the Ar–D_2O and Ar–HDO molecular complexes in the near-infrared range. *J. Chem. Phys.* **138.** doi:`http://dx.doi.org/10.1063/1.4794161` (2013).

92. Li, S., Zheng, R., Zhu, Y. & Duan, C. Rovibrational spectra of the Ar–D_2O and Kr–D_2O van der Waals complexes in the ν_2 bend region of D_2O. *J. Mol. Spectrosc.* **272,** 27–31 (2012).

93. Stewart, J. T. & McCall, B. J. Additional bands of the Ar–D_2O intramolecular bending mode observed using a quantum cascade laser. *J. Mol. Spectrosc.* **282,** 34–38 (2012).

94. Cohen, R. C. & Saykally, R. J. Determination of an improved intermolecular global potential energy surface for Ar–H_2O from vibration-rotation-tunneling spectroscopy. *J. Chem. Phys.* **98,** 6007–6030 (1993).

95. Zou, L. & Widicus Weaver, S. L. Direct measurement of additional Ar–H_2O vibration–rotation–tunneling bands in the millimeter–submillimeter range. *J. Mol. Spectrosc.* **324,** 12–19 (2016).

96. Suzuki, S., Bumgarner, R. E., Stockman, P. A., Green, P. G. & Blake, G. A. Tunable far-infrared laser spectroscopy of deuterated isotopomers of Ar–H_2O. *J. Chem. Phys.* **94,** 824–825 (1991).

97. Rad, M. L., Zou, L., Sanders III, J. L. & Widicus Weaver, S. L. Global optimization and broadband analysis software for interstellar chemistry (GOBASIC). *Astron. Astrophys.* **585,** A23 (2016).

98. Blake, G. A., Masson, C. R., Phillips, T. G. & Sutton, E. C. The rotational emission-line spectrum of Orion A between 247 and 263 GHz. *Astrophys. J. Suppl. Ser.* **60,** 357–374 (1986).

99. Müller, H., Schlöder, F., Stutzki, J. & Winnewisser, G. The cologne database for molecular spectroscopy, CDMS: a useful tool for astronomers and spectroscopists. *J. Mol. Struct.* **742,** 215–227 (2005).

100. Geppert, W. D. *et al.* Dissociative recombination of protonated methanol. *Faraday Discuss.* **133,** 177–190 (2006).

101. Snyder, L. E. Interferometric observations of large biologically interesting interstellar and cometary molecules. *Proc. Nat. Acad. Sci.* **103,** 12243–12248 (2006).

102. Kaul, A. B. *et al.* Fabrication of wide-IF 200–300 GHz superconductor-insulator-superconductor mixers with suspended metal beam leads formed on silicon-on-insulator. *JVSTB* **22,** 2417–2422 (2004).

103. Rice, F. *et al.* SIS mixer design for a broadband millimeter spectrometer suitable for rapid line surveys and redshift determinations. *Proc. SPIE* **4855,** 301–311 (2003).

104. Kooi, J. W. *et al.* A 275–425 GHz tunerless waveguide receiver based on AlN-barrier SIS technology. *IEEE Trans. Microw. Theory Techn.* **55,** 2086–2096 (2007).

105. Nummelin, A. *et al.* A three-position spectral line survey of Sagittarius B2 between 218 and 263 GHz. I. The observational data. *Astrophys. J. Suppl. Ser.* **117,** 427 (1998).

106. Sutton, E. C., Blake, G. A., Masson, C. R. & Phillips, T. G. Molecular line survey of Orion A from 215 to 247 GHz. *Astrophys. J. Suppl. Ser.* **58,** 341–378 (1985).

107. Blake, G. A., Sutton, E., Masson, C. & Phillips, T. Molecular abundances in OMC-1 – The chemical composition of interstellar molecular clouds and the influence of massive star formation. *Astrophys. J.* **315,** 621–645 (1987).

108. Mangum, J. G., Wootten, A., Wadiak, E. J. & Loren, R. B. Observations of the formaldehyde emission in Orion-KL-Abundances, distribution, and kinematics of the dense gas in the Orion molecular ridge. *Astrophys. J.* **348,** 542–556 (1990).

109. Minh, Y., Ohishi, M., Roh, D., Ishiguro, M. & Irvine, W. M. Interferometric observations for oxygen-containing organic molecules toward Orion-KL. *Astrophys. J.* **411,** 773–777 (1993).

110. Liu, S.-Y., Girart, J. M., Remijan, A. & Snyder, L. E. Formic Acid in Orion KL from 1 Millimeter Observations with the Berkeley-Illinois-Maryland Association Array. *Astrophys. J.* **576,** 255 (2002).

111. Beuther, H. *et al.* Subarcsecond Submillimeter Continuum Observations of Orion KL. *Astrophys. J. Lett.* **616,** L31 (2004).

112. Friedel, D. N., Snyder, L. E., Remijan, A. J. & Turner, B. E. Detection of interstellar acetone toward the Orion-KL hot core. *Astrophys. J. Lett.* **632,** L95 (2005).

113. Beuther, H. *et al.* Submillimeter Array 440 µm/690 GHz Line and Continuum Observations of Orion KL. *Astrophys. J.* **636,** 323–331 (2006).

114. Persson, C. M. *et al.* A spectral line survey of Orion KL in the bands 486-492 and 541-577 GHz with the Odin satellite. *Astron. Astrophys.* **476,** 807–828 (2007).

115. Friedel, D. N. & Snyder, L. E. High-Resolution $\lambda = 1$ mm CARMA Observations of Large Molecules in Orion-KL. *Astrophys. J.* **672,** 962 (2008).

116. Crockett, N. R. *et al.* Herschel observations of EXtra-Ordinary Sources (HEXOS): The Terahertz spectrum of Orion KL seen at high spectral resolution. *Astron. Astrophys.* **521,** L21 (2010).

117. Gupta, H. *et al.* Detection of OH^+ and H_2O^+ towards Orion KL. *Astron. Astrophys.* **521,** L47 (2010).

118. Margulès, L. *et al.* Rotational Spectrum and Tentative Detection of $DCOOCH_3$–Methyl Formate in Orion. *Astrophys. J.* **714,** 1120 (2010).

119. Favre, C. *et al.* $HCOOCH_3$ as a probe of temperature and structure in Orion-KL. *Astron. Astrophys.* **532,** A32 (2011).

120. Favre, C. *et al.* High-resolution Expanded Very Large Array Image of Dimethyl Ether $(CH_3)_2O$ in Orion-KL. *Astrophys. J. Lett.* **739,** L12 (2011).

121. Zapata, L. A., Schmid-Burgk, J. & Menten, K. M. Orion KL: the hot core that is not a "hot core". *Astron. Astrophys.* **529,** A24 (2011).

122. Friedel, D. N. & Widicus Weaver, S. L. Complex organic molecules at high spatial resolution toward ORION-KL. II. Kinematics. *Astrophys. J. Suppl. Ser.* **201,** 17 (2012).

123. Brouillet, N. *et al.* CH_3OCH_3 in Orion-KL: a striking similarity with $HCOOCH_3$? *Astron. Astrophys.* **550,** A46 (2013).

124. Crockett, N. R. *et al.* Herschel Observations of Extraordinary Sources: Analysis of the HIFI 1.2 THz Wide Spectral Survey toward Orion KL. I. Methods. *Astrophys. J.* **787,** 112 (2014).

125. Favre, C. *et al.* ^{13}C-Methyl formate: observations of a sample of high-mass star-forming regions Including Orion-KL and spectroscopic characterization. *Astrophys. J. Suppl. Ser.* **215,** 25 (2014).

126. Frayer, D. T. *et al.* The GBT 67-93.6 GHz Spectral Line Survey of Orion-KL. *Astron. J.* **149,** 162 (2015).

127. Morris, P. W. *et al.* Herschel/HIFI Spectral Mapping of C^+, CH^+, and CH in Orion BN/KL: The Prevailing Role of Ultraviolet Irradiation in CH^+ Formation. *Astrophys. J.* **829,** 15 (2016).

128. Tahani, K. *et al.* Analysis of the Herschel/Hexos Spectral Survey Toward Orion South: A Massive Protostellar Envelope with Strong External Irradiation. *Astrophys. J.* **832,** 12 (2016).

129. Nummelin, A. *et al.* A Three-Position Spectral Line Survey of Sagittarius B2 between 218 and 263 GHz. II. Data Analysis. *Astrophys. J. Suppl. Ser.* **128,** 213 (2000).

130. Snyder, L. E. *et al.* Confirmation of interstellar acetone. *Astrophys. J.* **578,** 245 (2002).

131. Friedel, D. N., Snyder, L. E., Turner, B. E. & Remijan, A. A Spectral Line Survey of Selected 3 Millimeter Bands toward Sagittarius B2(N-LMH) Using the National Radio Astronomy Observatory 12 Meter Radio Telescope and the Berkeley-Illinois-Maryland Association Array. I. The Observational Data. *Astrophys. J.* **600,** 234 (2004).

132. Leigh, D., Remijan, A. & Turner, B. *Complete 2mm Spectral Line Survey (130-170 GHz) Of Sgr B2N, Sgr B2 OH, IRC+10 216, Orion (KL), Orion-S, W51M And W3(IRS5)* in *American Astronomical Society Meeting Abstracts* **39** (12/2007), 961.

133. Belloche, A., Müller, H. S. P., Menten, K. M., Schilke, P. & Comito, C. Complex organic molecules in the interstellar medium: IRAM 30 m line survey of Sagittarius B2(N) and (M). *Astron. Astrophys.* **559,** A47 (2013).

134. Neill, J. L. *et al.* Herschel Observations of Extraordinary Sources: Analysis of the Full Herschel/HIFI Molecular Line Survey of Sagittarius B2(N). *Astrophys. J.* **789,** 8 (2014).

135. Miao, Y. & Snyder, L. E. Full Synthesis Observations of CH_3CH_2CN in Sagittarius B2: Further Evidence for Grain Chemistry. *Astrophys. J. Lett.* **480,** L67 (1997).

136. Mehringer, D. M., Snyder, L. E., Miao, Y. & Lovas, F. J. Detection and Confirmation of Interstellar Acetic Acid. *Astrophys. J. Lett.* **480,** L71 (1997).

137. Hollis, J. M., Lovas, F. J. & Jewell, P. R. Interstellar glycolaldehyde: the first sugar. *Astrophys. J.* **540,** L107–L110 (2000).

138. Remijan, A., Snyder, L. E., Liu, S.-Y., Mehringer, D. & Kuan, Y.-J. Acetic Acid in the Hot Cores of Sagitarrius B2(N) and W51. *Astrophys. J.* **576,** 264 (2002).

139. Hollis, J. M. *et al.* Detection of Acetamide (CH_3CONH_2): The Largest Interstellar Molecule with a Peptide Bond. *Astrophys. J. Lett.* **643,** L25 (2006).

140. Halfen, D. T., Apponi, A. J., Woolf, N., Polt, R. & Ziurys, L. M. A Systematic Study of Glycolaldehyde in Sagittarius B2(N) at 2 and 3 mm: Criteria for Detecting Large Interstellar Molecules. *Astrophys. J.* **639,** 237 (2006).

141. Apponi, A. J. *et al.* Investigating the Limits of Chemical Complexity in Sagittarius B2(N): A Rigorous Attempt to Confirm 1,3-Dihydroxyacetone. *Astrophys. J. Lett.* **643,** L29 (2006).

142. Belloche, A. *et al.* Detection of amino acetonitrile in Sgr B2(N). *Astron. Astrophys.* **482,** 179–196 (2008).

143. Belloche, A. *et al.* Increased complexity in interstellar chemistry: detection and chemical modeling of ethyl formate and n-propyl cyanide in Sagittarius B2(N). *Astron. Astrophys.* **499,** 215–232 (2009).

144. Martín-Pintado, J., Rizzo, J. R., de Vicente, P., Rodríguez-Fernández, N. J. & Fuente, A. Large-Scale Grain Mantle Disruption in the Galactic Center. *Astrophys. J. Lett.* **548,** L65 (2001).

145. Halfen, D. T., Ilyushin, V. & Ziurys, L. M. Formation of Peptide Bonds in Space: A Comprehensive Study of Formamide and Acetamide in Sgr B2(N). *Astrophys. J.* **743,** 60 (2011).

146. Halfen, D. T., Ilyushin, V. V. & Ziurys, L. M. Insights into Surface Hydrogenation in the Interstellar Medium: Observations of Methanimine and Methyl Amine in Sgr B2(N). *Astrophys. J.* **767,** 66 (2013).

147. Furuya, R. S., Cesaroni, R. & Shinnaga, H. Infall, outflow, and rotation in the G19.61-0.23 hot molecular core. *Astron. Astrophys.* **525,** A72 (2011).

148. Minh, Y. C. *et al.* Submillimeter array observations toward the massive starforming core MM1 of W75N. *Astrophys. J.* **723,** 1231 (2010).

149. Charnley, S. B. Sulfuretted molecules in hot cores. *Astrophys. J.* **481,** 396 (1997).

150. Hatchell, J., Thompson, M. A., Millar, T. J. & MacDonald, G. Sulphur chemistry and evolution in hot cores. *Astron. Astrophys.* **338,** 713–722 (1998).

151. Buckle, J. V. & Fuller, G. A. Sulphur-bearing species as chemical clocks for low mass protostars? *Astron. Astrophys.* **399,** 567–581 (2003).

152. Kuiper, T. B. H., Kuiper, E. N. R., Dickinson, D. F., Turner, B. E. & Zuckerman, B. Methyl acetylene as a temperature probe for dense interstellar clouds. *Astrophys. J.* **276,** 211–220 (1984).

153. Wakelam, V., Caselli, P., Ceccarelli, C., Herbst, E. & Castets, A. Resetting chemical clocks of hot cores based on S-bearing molecules. *Astron. Astrophys.* **422,** 159–169 (2004).

154. Hincelin, U. *et al.* Oxygen depletion in dense molecular clouds: a clue to a low O_2 abundance? *Astron. Astrophys.* **530,** A61 (2011).